DEMOCRATIC AND POPULAR REPUBLIC OF ALGERIA
MINISTRY OF HIGHER EDUCATION AND SCIENTIFIC RESEARCH

Abdelhamid Ibn Badis University of Mostaganem
Faculty of Exact Sciences and Computer Science
Department of Physics

Laboratory for the Development and Physico-Mechanical and Metallurgical Characterization of Materials

THESIS

To obtain the degree of Doctorate in Physics
Specialty: Condensed Matter Physics
Option: Materials Physics

Presented by

MEZILET Oum Keltoum

Piezoelectric and Thermoelectric Properties of Transition Metal-Doped Compounds: An Ab-initio Study

---

Defended on 03/07/2025 in front of the Jury :

Pr. BOUKORTT Abdelkader	President	Univ- Abdelhamid Ibn Badis Mostaganem
Pr. ABBES Charef	Examiner	Univ- Abdelhamid Ibn Badis Mostaganem
Pr. BENNACER Hamza	Examiner	Univ-Djilali Liabes Sidi-Bel-Abbes
Pr. ASSALI Abdenacer	Thesis Director	UROP – Setif , CDTA
Pr. MESKINE Said	Thesis Co-Director	Univ- Abdelhamid Ibn Badis Mostaganem

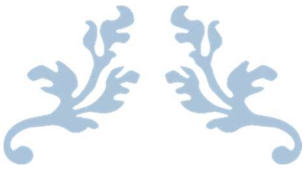

"Beyond the discoveries of those before you lies an uncharted path for your own genius— and thus the odyssey of research begins."

Dedication

I dedicate this modest work with heartfelt gratitude

To my entire family

To those who believed in me.

Acknowledgments

Pursuing a PhD can be difficult and challenging. First and foremost, I want to express my deepest gratitude to my supervisor, DR. Assali Abdenacer, for his unwavering support throughout my Ph.D. journey. I grateful to the opportunity to work with him. I appreciate his guidance, sharing his knowledge, expertise that made this experience enjoyable. He was always patient, never losing his temper or his humbleness over mistakes or missing points in my studies, and continuously encouraged me by recognizing my efforts and maintaining confidence in my ability to complete this Ph.D. His useful and valuable advice greatly improved my research and writing skills. This experience will remain extremely valuable to me, and I will cherish it for the rest of my life.

I am also grateful to my co-supervisor, Pr. Meskine Said, for his scientific guidance and insightful discussions. Working with him was always lively and I have learned a lot from him. His encouragement during challenging times was invaluable. I will be thankful for his mentorship in shaping me as a researcher.

Additionally, I extend my thanks to Pr. Boukortt Abdelkader, director of the ECP3M research laboratory, where this work was carried out, for warmly welcoming me and offering sincere advice. He was always available to discuss my ideas, ask thoughtful questions, and help me navigate problems.

I would also like to acknowledge my thesis committee for their time, feedback, and insightful comments that broadened my research from different angles.

My heartfelt thanks go to all my fellow members at the ECP3M laboratory for keeping my mind always refreshed, which helped me to concentrate in work.

Above all, I must thank my parents and my siblings for their unwavering support through both good and tough times. I love them dearly and could not have come this far without them. Thanks for everything that helped me get to this day.

Abstract

In this work, advanced *ab initio* DFT calculations using GGA-PBsol and *n*KTB-mBJ functionals within the full-potential linear augmented plane wave (FP-LAPW) method were employed to investigate key characteristics, such as the structural, electronic, elastic, piezoelectric, dielectric, thermodynamic, and thermoelectric properties of two eco-friendly materials: the perovskite $Na_{0.5}Bi_{0.5}TiO_3$ (NBT) and $Y_xAl_{1-x}N$ (with $0 \leq x \leq 0.375$) to explore their potential for application in piezoelectric and thermoelectric technologies.

The first part of the study focused on perovskite $Na_{0.5}Bi_{0.5}TiO_3$ (NBT), crystalized in rhombohedral (*R*3*c*), tetragonal (*Pb*4*m*), and cubic ($Pm\bar{3}m$) phases. These crystals exhibited indirect bandgaps of 3.05–3.29 eV, elastic stability, and high piezoelectric coefficients in the tetragonal phase [d_{15} = 101.1 pC/N, d_{31} = -51.3 pC/N, and d_{33} = 81.1 pC/N]. The thermoelectric properties of NBT included Seebeck coefficients of up to 201.42 µV/K at 500 K and ZT values reaching 2.76 at 700 K.

In the second part of the study, DFT simulations revealed a near-linear variation in lattice parameters with increasing yttrium content for $Y_xAl_{1-x}N$ ($0 \leq x \leq 0.375$) alloys, and tunable bandgaps ranging from 6.10 eV to 3.85 eV, making these alloys suitable for ultraviolet emission applications. Additionally, BoltzTraP calculations indicated promising electronic transport properties, including Seebeck coefficients up to 213.9 µV/K and a figure of merit (ZT) of ~0.72 at x = 0.25 (600 K). Thermal conductivity per relaxation time was also low, at κ/τ ~9.9×10^{13} $W.m^{-1}.K^{-1}.s^{-1}$. Piezoelectric coefficients for $Y_xAl_{1-x}N$ at x = 0.375 were significantly enhanced, with d_{33} = 17.5 pC/N, d_{15} = 11.07 pC/N, and d_{31} = 8.65 pC/N, representing increases of ~300%, ~400%, and ~370%, respectively, compared to pure AlN crystals.

Finally, the results highlight the potential of $Na_{0.5}Bi_{0.5}TiO_3$ and $Y_xAl_{1-x}N$ for green energy applications, optoelectronics, high-performance piezoelectric devices, and high-power thermoelectric technologies.

Keywords:

Ab initio DFT calculations, Piezoelectric performances, Thermoelectrics, Lead-free perovskite $Na_{0.5}Bi_{0.5}TiO_3$, $Y_xAl_{1-x}N$ alloys, Green energy and Microtechnology applications.

Résumé

Dans ce travail, des calculs DFT ab initio avancés utilisant les fonctionnels GGA-PBsol et nKTB-mBJ dans la méthode des ondes planes augmentées linéaires à potentiel complet (FP-LAPW) ont été employés pour étudier des caractéristiques clés, telles que les propriétés structurelles, électroniques, élastiques, piézoélectriques, diélectriques, thermodynamiques et thermoélectriques de deux matériaux écologiques : le pérovskite $Na_{0.5}Bi_{0.5}TiO_3$ (NBT) et $Y_xAl_{1-x}N$ (avec $0 \leq x \leq 0{,}375$) afin d'explorer leur potentiel pour des applications dans les technologies piézoélectriques et thermoélectriques.

La première partie de l'étude s'est concentrée sur la pérovskite $Na_{0.5}Bi_{0.5}TiO_3$ (NBT), cristallisée dans des phases rhomboédriques (R3c), tétraédriques (Pb4m) et cubiques ($Pm\bar{3}m$). Ces cristaux ont présenté des bandes interdites indirectes de 3,05 à 3,29 eV, une stabilité élastique et des coefficients piézoélectriques élevés dans la phase tétraédrique [d_{15} = 101,1 pC/N, d_{31} = -51,3 pC/N, et d_{33} = 81,1 pC/N]. Les propriétés thermoélectriques du NBT comprenaient des coefficients de Seebeck allant jusqu'à 201,42 µV/K à 500 K et des valeurs de ZT atteignant 2,76 à 700 K.

Dans la deuxième partie de l'étude, les simulations DFT ont révélé une variation quasi-linéaire des paramètres de réseau avec l'augmentation de la concentration de l'yttrium pour les alliages $Y_xAl_{1-x}N$ ($0 \leq x \leq 0.375$), et des gaps ajustables allant de 6,10 eV à 3,85 eV, rendant ces alliages adaptés aux applications d'émission ultraviolette. De plus, les calculs de BoltzTraP ont indiqué des propriétés de transport électronique prometteuses, y compris des coefficients de Seebeck allant jusqu'à 213,9 µV/K et un facteur de mérite (ZT) d'environ 0,72 à x = 0,25 (600 K). La conductivité thermique par temps de relaxation était également faible, à κ/τ ~$9{,}9 \times 10^{13}$ $W.m^{-1}.K^{-1}.s^{-1}$. Les coefficients piézoélectriques pour $Y_xAl_{1-x}N$ à x = 0,375 ont été considérablement améliorés, avec d_{33} = 17,5 pC/N, d_{15} = 11,07 pC/N, et d_{31} = 8,65 pC/N, représentant des augmentations d'environ 300 %, 400 %, et 370 %, respectivement, par rapport aux cristaux d'AlN pur.

Enfin, les résultats mettent en évidence le potentiel de $Na_{0.5}Bi_{0.5}TiO_3$ et $Y_xAl_{1-x}N$ pour les applications en énergie verte, l'optoélectronique, les dispositifs piézoélectriques haute performance et les technologies thermoélectriques haute puissance.

Mots-clés:
Calculs DFT ab initio, Performances piézoélectriques, Thermoélectriques, Pérovskite sans plomb $Na_{0.5}Bi_{0.5}TiO_3$, Alliages $Y_xAl_{1-x}N$, Énergie verte et applications en micro-technologie.

ملخص

في هذا العمل، تم استخدام حسابات DFT (GGA-PBEsol , nKTB−mBj) ضمن طريقة الأمواج المستوية الخطية المعززة ذات الجهد الكامل (FP−LAPW) ، لدراسة الخصائص الرئيسية مثل الخصائص البنيوية والإلكترونية والمرنة والكهربائية الحرارية والديناميكية الحرارية لمادتين صديقتين للبيئة: البيروفسكايت الخالي من الرصاص $Na_{0.5}Bi_{0.5}TiO_3$ و خليط شبه ناقل $Y_xAl_{1-x}N$ ، للاستخدام في التقنيات الكهروإجهادية والكهروحرارية.

ركز الجزء الاول من الدراسة على بلورات $Na_{0.5}Bi_{0.5}TiO_3$ (NBT) ، التي تشكلت في (R3c) ، (Pb4m) ، (Pm3̄m) أظهرت هذه البلورات وفجوة الطاقة غير مباشرة تتراوح بين 3.05 إلكترون فولت إلى 3.29 إلكترون فولت، واستقرارًا مرنًا، ومعاملات كهروإجهادية عالية في الطور الرباعي [d_{15} = 101.1 بيكوكلون/نيوتن، و d_{31} = - 51.3 بيكوكلون/نيوتن، و d_{33} = 81.1 بيكوكلون/نيوتن]. تضمنت الخصائص الكهربائية الحرارية لل NBT معاملات سيبيك تصل إلى 201.42 ميكروفولت/كلفن عند 500 كلفن وقيم ZT تصل إلى 2.76 عند 700كلفن.

في الجزء الثاني من الدراسة، كشفت محاكاة DFT عن تغير شبه خطي في معلمات الشبكة مع زيادة محتوى الإيتريوم في سبائك $Y_xAl_{1-x}N$ $(0 \le x \le 0.375)$ ، وفجوة الطاقة قابلة للتعديل تتراوح من 6.10 إلكترون فولت إلى3.85 إلكترون فولت، مما يجعل هذه السبائك مناسبة لتطبيقات الانبعاث فوق البنفسجي .بالإضافة إلى ذلك، أشارت حسابات BoltzTraP إلى خصائص نقل إلكتروني واعدة، بما في ذلك معاملات سيبيك تصل إلى 213.9 ميكروفولت/كلفن وقيمة شكل (ZT) تبلغ حوالي 0.72 عند x = 0.25 (600 كلفن) . كما كانت التوصيلية الحرارية لكل زمن استرخاء منخفضة، حيث $\kappa/\tau \sim 9.9\times10^{13}$ واط/متر/كلفن/ثانية .كما كانت معاملات الكهروإجهادية لسبائك $Y_xAl_{1-x}N$ عند x = 0.375 مرتفعة بشكل ملحوظ، حيث كانت d_{33} = 17.5 بيكوكلون/نيوتن، وd_{15} = 11.07 بيكوكلون/نيوتن، و d_{31} = 8.65 بيكوكلون/نيوتن، مما يمثل زيادة قدرها حوالي 300 % ، و 400 %، و370 % ، على التوالي، مقارنةً ببلورات AlN النقية.

وأخيرًا، تُبرز النتائج إلى الإمكانيات الواعدة لكل من المادتين في تطبيقات الطاقة الخضراء، والبصريات الإلكترونية، والتطبيقات الكهروإجهادية عالية الأداء، والأجهزة الحرارية الكهربائية عالية الطاقة.

الكلمات المفتاحية:

حسابات DFT ، الخواص الكهربائية الكهروإجهادية ، الخواص الكهربائية الحرارية ، البيروفسكايت الخالي من الرصاص $Na_{0.5}Bi_{0.5}TiO_3$ ، سبائك $Y_xAl_{1-x}N$ ، تطبيقات الطاقة الخضراء و التكنولوجيا الدقيقة.

Table of Contents

Abstract ..... *iv*
Table of Contents ..... *v*
List of Figures ..... *vii*
List of Tables ..... *viii*
Introduction *16*

CHAPTER I: Piezoelectric and Thermoelectric Materials: An Overview of Recent Advances and Properties

I.1. Introduction 22
I.2. III–V semiconductors 22
I.2.1. Crystal Structure of III–V Semiconductors and their Physical Properties 23
I.2.2. Advanced III–V Semiconductor Alloys: Case of $Y_xAl_{1-x}N$ System 27
I.2.2.1. Properties and Technological Interest 27
I.3. Perovskite Materials: Low-cost and Potential Applications 29
I.3.1. Perovskite Structure 31
I.3.2. Lead-free Perovskite $Na_{0.5}Bi_{0.5}TiO_3$ (NBT) 32
I.3.3. Stability in Perovskite Structures 35
I.3.4. Electric and Thermoelectric Phenomena in Perovskite Materials 37
I.3.4.1. Paraelectricity 37
I.3.4.2. Ferroelectricity 37
I.3.4.3. Pyroelectricity 38
I.3.4.4. Thermoelectricity 39
I.3.4.4.1. Thermoelectricity Technology Applications 40
I.3.4.5. Piezoelectricity 43
I.3.4.5.1. Fundamentals and Mechanism of the Piezoelectric Effect 43
I.3.4.5.2. Piezoelectricity Technology Applications 49
I.4.3. Categories of Piezoelectric Materials 51
I.5. Conclusion 54
References 55

CHAPTER II: DFT Methodologies: Advancements in Computational Techniques for Precise Material Property Prediction

II.1. Introduction 63
II.2. Overview of Quantum Simulation Methods 64
II.2.1.The Many-Body Hamiltonian 64
II.2.2.The Born-Oppenheimer Approximation 65
II.2.3. Density Functional Theory 65
II.2.3.1.The Hohenberg and Kohn Theorems 66
II.2.3.2.The Kohn-Sham Equations 67

II.2.3.3.Approximations to the Exchange-Correlation Functional 69
II.2.3.3.1.Generalized Gradient Approximation (GGA) 70
II.2.3.4.Corrections to Density Functional Theory 70
II.2.3.4.1.The Modified Becke-Johnson (mBJ) Exchange-Correlation (XC) Potential 71
II.2.4. Simulation Software Packages 71
II.2.4.1.WIEN2K Package 71
II.2.4.1.1.BerryPi Code 72
II.2.4.1.2.BoltzTrap Code 72
II.2.4.1.3.Gibbs Code 73
II.2.4.2.CASTAP Package 74
II.3. Conclusion 75
References 76

CHAPTER III: Exploring the Piezoelectric and Thermoelectric Performance of Lead-Free $Na_{0.5}Bi_{0.5}TiO_3$ Perovskites for Sustainable Energy

III.1. Introduction 79
III.2. Computational Details 79
III.3. Structural Property 81
A. Geometry Optimization 81
B. Lattice Stability 84
III.4. Electronic Structure 85
A. Band Structure 85
B. Density of States 87
C. Electronic Charge Density 89
III.5. Elastic and Mechanical Properties 90
A. Elastic Stiffness Constants (Cij) 90
B. Mechanical Behavior 92
C. Sound Wave Velocities 96
III.6. Piezoelectric Properties Analysis 97
A. Piezoelectric and Dielectric Parameters 97
B. Directional Dependence of the Piezoelectric Coefficient 101
III.7. Thermodynamic Properties 103
A. Pressure and Temperature Effects on Volume (V) and Bulk Modulus (B) . 104
B. Specific Heat (*Cv*) 105
C. Thermal Expansion (α) 106
D. Entropy (S) 106
E. Debye Temperature (θ_D) 107
III.8. Thermoelectric Properties 109
A. Seebeck Coefficient (S) 110
B. Electrical Conductivity (σ/τ) 110

C. Thermal Conductivity (κ/τ) 111
D. Power Factor 111
E. Figure of Merit (ZT) 111
III.9. Conclusion 114
References 115

CHAPTER IV: Insights into the Emergent Piezoelectric and Thermoelectric Properties of Novel YAlN Semiconductor Alloys for Promising Microtechnology and Energy Conversion

IV.1. Introduction 121
IV.2. Methodological Details 121
IV.3. Structural Properties and Lattice Stabilities 124
A. Ground-State Structural Parameters 124
B. Lattice Stability 127
IV.4. Electronic Structure 128
A. Bandgap 128
B. Density of States (DOS) 132
C. Charge Density Map 134
IV.5 Elastic and Mechanical Properties 134
IV.6. Piezoelectric Properties 142
IV.7. Thermodynamic Properties 145
IV.8. Thermoelectric Properties 151
IV.9. Conclusion 156
References 157

General Conclusion 165
Recommendations for Future Work ix
Appendix x
Scientific production xi

List of Figures

CHAPTER I

Figure I.1: The three crystalline structures of AlN: (a) zinc blende, (b) rock salt, and (c) wurtzite 24

Figure I.2: Schematic representation of the wurtzite lattice structure 24

Figure I.3: Relationships between crystal classes and their corresponding symmetries 27

Figure I.4: Tetrahedral geometry of AlN, with B1 and B2 representing different Al–N bond lengths 28

Figure I.5: Illustration of unit cell of the ABO_3 perovskite structure 31

Figure I.6: Displacement of cation B within the octahedron BO_6 of certain directions (on axis 2π/n): (a) an axis of tetrad π/2, (b) an axis oftriad 2π/3, (c) a dyad axis π. 32

Figure I.7: Illustration of perovskite $Na_{0.5}Bi_{0.5}TiO_3$ in pseudo-cubic structure.. 34

Figure I.8: Polarization as a function of the electric field for a single crystal (gray-dashed line) and polycrystalline (blue solid line) ferroelectric materials. The direction of the electric field change is indicated by arrows 38

Figure I.9: (a) Schematic representation of the Multi-Mission Radioisotope Thermoelectric Generator (MMRTG) [102]; (b) & (c) The MMRTG on the Perseverance rover during its Mars mission, (Image credit: NASA/JPL/Caltech) 41

Figure I.10: **(a)** NASA curiosity rover equipped with Multi-Mission Radioisotope Thermoelectric Generator (MMRTG) on mars, demonstrating thermoelectric power in harsh environments. **(b)** Image of a vehicle with a thermoelectric power generator (TEG) harnessing wasted heat from the engine. **(c)** Image illustrating low-power applications like small portable electronic devices, wireless sensors, and medical equipment powered by a thermoelectric generator (TEG) 42

Figure I.11: Schematics of direct piezoelectric effects: **(a)** at applied compressive stress, **(d)** at applied tension 43

Figure I.12: Operating modes of a piezoelectric material, 33-mode and 31-mode 45

Figure I.13: Piezoelectric charge coefficient as a function of the angle away from the polar axis for tetragonal single crystals, calculated by T.O.

Hooper et al. [106]. The d_{33}^{*} illustrates the distinction between rotator and extender behavior in tetragonal materials 46

Figure I.14: Domain alignment mechanisms before, during, and after the poling process 48

Figure I.15: Schematic of the diverse range of piezoelectricity applications 49

Figure I.16: Illustration of the categories of piezoelectric materials. The inset image shows barium titanate (BT) in powder form 52

CHAPTER II

Figure II.1: The diagram illustrates the self-consistent cycle employed to iteratively solve the Kohn-Sham equations 68

CHAPTER III

Figure III.1: Crystallographic structures of $Na_{0.5}Bi_{0.5}TiO_3$ (NBT): (a) rhombohedral (R3c) (hexagonal axes), (b) tetragonal P4bm) and (c) cubic ($Pm\bar{3}m$) phases 81

Figure III.2: Total energy as a function of volume for $Na_{0.5}Bi_{0.5}TiO_3$ (NBT) crystals crystalizing in *R3c*, *P4bm* and *Pm$\bar{3}$m* symmetries using PBEsol. The most stable energetically structure corresponds to rhombohedral symmetry 83

Figure III.3: Phonon dispersion curves for (a) rhombohedral, (b) tetragonal and (c) cubic phases of $Na_{0.5}Bi_{0.5}TiO_3$ (NBT) crystals 85

Figure III.4: Electronic band structures and total density of states (PDOS) of (a) rhombohedral, (b) tetragonal and (c) cubic phases of $Na_{0.5}Bi_{0.5}TiO_3$ (NBT) crystalsobtained by KTB–mBJ+so functional 87

Figure III.5: Total DOS and partial PDOS of $Na_{0.5}Bi_{0.5}TiO_3$ (NBT) for (a) rhombohedral, (b) tetragonal and (c) cubic phases obtained by KTB–mBJ+so functional 88

Figure III.6: Charge density distributions for $Na_{0.5}Bi_{0.5}TiO_3$ (NBT) in (a) (120)-plane for R3c, (b) (100)-plane for P4bm, and (c) (110)-plane for $Pm\bar{3}m$ symmetriesobtained by KTB–mBJ+so functional 89

Figure III.7: Directional dependence of bulk modulus, shear modulus and Young modulus for $Na_{0.5}Bi_{0.5}TiO_3$ (NBT) crystals for (a) R3c, b) P4bm, (c) and $Pm\bar{3}m$ symmetries 96

Figure III.8: Orientation dependence of $d_{33}^{*}(\theta,\phi)$ in (a) rhombohedral and (b) tetragonal phases of $Na_{0.5}Bi_{0.5}TiO_3$ (NBT) crystals. Note that the

minimum and maximum piezoelectric constants appear along the [010] direction. The coordinate system represents crystallographic axes 103

Figure III.9: Dependence of (a) volume V and (b) compressibility modulus B as a function of temperature for different pressures for rhombohedral $Na_{0.5}Bi_{0.5}TiO_3$ crystal 105

Figure III.10: Dependence of (a) the thermal capacity C_v, (b) thermal expansion α, (c) entropy S, and (d) Debye temperature Θ_D as a function of temperature for different pressures for rhombohedral $Na_{0.5}Bi_{0.5}TiO_3$ crystal 108

Figure III.11: Temperature dependence of (a) Seebeck coefficient S, (b) the ratio of electrical conductivity to relaxation time σ/τ, (c) the ratio of thermal conductivity to relaxation time κ/τ, (d) thermal power, and (e) figure of merit ZT for R3c, P4bm, and $Pm\bar{3}m$ phases of $Na_{0.5}Bi_{0.5}TiO_3$ crystals 113

CHAPTER IV

Figure IV.1: Crystalline structures of wurtzite $Y_xAl_{1-x}N$ alloys for x= 0 (a) (unit cell), 0.062 (b), 0.125 (c), 0.25 (d), and 0.375 (e) (2a×2b×2c supercell) 123

Figure IV.2: Variation of lattice parameters a_0 (a) and c_0 (b) as a function of yttrium composition for wurtzite $Y_xAl_{1-x}N$ alloys 126

Figure IV.3: Variation of total energy as a function of volume for wurtzite $Y_xAl_{1-x}N$ alloys with x values of 0, 0.062, 0.125, 0.25, and 0.375. The solid lines denote the fit of Murnaghan's equation of state to the data 126

Figure IV.4: Computed phonon dispersions for wurtzite $Y_xAl_{1-x}N$ alloys with concentrations x = 0, 0.125, 0.25, and 0.375 along high-symmetry directions 128

Figure IV.5: Calculated band structures for wurtzite $Y_xAl_{1-x}N$ alloys with concentrations x = 0 (a), 0.125 (b), 0.25 (c), and 0.375 (d) along high-symmetry directions using nKTB–mBJ functional 131

Figure IV.6: Calculated direct $E_{\Gamma-\Gamma}$ and indirect $E_{M-\Gamma}$, $E_{K-\Gamma}$ bandgaps as a function of yttrium composition for wurtzite $Y_xAl_{1-x}N$ alloys using nKTB–mBJ functional. The bandgap transitions from direct to indirect at x = 0.029 and then back to direct at x = 0.29 131

Figure IV.7: Calculated partial density of states (PDOS) and total density of states (TDOS) for wurtzite $Y_xAl_{1-x}N$ alloys with x = 0.125 (a), 0.25 (b), and 0.375 (c) using nKTB–mBJ functional 133

Figure IV.8: Charge density maps in the (4-20) plane for wurtzite $Y_xAl_{1-x}N$ alloys for compositions: (a) x= 0, (b) x= 0.125, (c) x= 0.25, and (d) x= 0.375 from nKTB–mBJ functional 133

Figure IV.9: Dependency of elastic constants (C_{ij}) on yttrium composition in $Y_xAl_{1-x}N$ alloys 136

Figure IV.10: 3D anisotropic surface plots of bulk modulus, shear modulus, and Young's modulus for wurtzite $Y_xAl_{1-x}N$ alloys with compositions x = 0 (a), 0.125 (b), and (c) 0.375 139

Figure IV.11: Debye temperature (Θ_D), and density (ρ) (a), and sound velocities (ν_l, ν_t, ν_m) (b), versus yttrium composition in wurtzite $Y_xAl_{1-x}N$ alloys 141

Figure IV.12: Piezoelectric stress constants (e_{ij}) (a), and piezoelectric strain constants (d_{ij}) as a function of yttrium content in wurtzite $Y_xAl_{1-x}N$ alloys 145

Figure IV.13: Dependence of volume (V_0) (a), and compressibility modulus (B_0) (b) on temperature under pressure for wurtzite $Y_xAl_{1-x}N$ crystals 147

Figure IV.14: Calculated thermal capacity (C_v) (a), thermal expansion (α) (b), entropy (S) (c), and Debye temperature (Θ_D) (d) as a function of temperature under pressure for wurtzite $Y_xAl_{1-x}N$ alloys 150

Figure IV.15: Calculated Grüneisen parameter (γ) as a function of pressure (a), and temperature (b) for wurtzite $Y_xAl_{1-x}N$ crystals 151

Figure IV.16 : Dependence of Calculated Seebeck coefficient (S) (a), electrical conductivity (σ/τ) (b), electronic thermal conductivity (κ_{el}/τ) (c), power factor (PF) (d), and figure of merit (ZT) (e) as a function of temperature for wurtzite $Y_xAl_{1-x}N$ crystals 156

List of Tables

CHAPTER I

Table I.1: Indicates the values of δ and its equivalent bonds 36

Table I.2: Piezoelectric equations 44

CHAPTER III

Table III.1: Equilibrium lattice parameters (a_0, c_0) (Å), cell volume V_0 (Å^3), energy of formation ΔE_f (eV/atom) and fractional coordinates (x,y,z) for different phases of $Na_{0.5}Bi_{0.5}TiO_3$ (NBT) along with available experimental data and theoretical values 83

Table III.2: Band gap energies (Eg) for different phases of $Na_{0.5}Bi_{0.5}TiO_3$ (NBT) crystals obtained by the improved TB–mBJ and KTB–mBJ functionals with and without spin-orbit interaction 87

Table III.3: Calculated elastic constants C_{ij} (GPa), bulk modulus B (GPa), shear modulus G (GPa), Young modulus Y (GPa), Poisson's ratio ν, and Frantesvich ratio G/B forperovskite$Na_{0.5}Bi_{0.5}TiO_3$ (NBT) in rhombohedral, tetragonal and cubic phases using GGA–PBEsol and GGA–WC approximations along to experimental values and other theoretical works 92

Table III.4: Calculated densityρ (g/cm^3), longitudinal υ_l (m/s), transverse υ_t (m/s), and average υ_m acoustic wave velocities (m/s) for rhombohedral, tetragonal and cubic phases of perovskite $Na_{0.5}Bi_{0.5}TiO_3$ (NBT) 97

Table III.5: Calculated piezoelectric coefficients d_{ij} (in pC/N), e_{ij} (in C/m^2) and dielectric constants (ϵ_{ij}) for ferroelectric $Na_{0.5}Bi_{0.5}TiO_3$ (NBT) crystal 100

CHAPTER IV

Table IV.1: Calculated equilibrium latticesparameters (Å), c_0/a_0 ratio, volume (Å^3), bulk modulus, and formation energy (ΔE_f) (eV) for wurtzite $Y_xAl_{1-x}N$ alloys with yttrium contents ($0 \leq x \leq 0.375$) 125

Table IV.2: Calculated direct {$E_{\Gamma-\Gamma}$} and indirect {$E_{M-\Gamma}$, $E_{K-\Gamma}$} bandgaps for wurtzite $Y_xAl_{1-x}N$ alloys with yttrium contents ($0 \leq x \leq 0.375$) using *n*KTB–mBJ functional 129

Table IV.3: indicates the values of δ and its equivalent bonds 135

Table IV.4: Computed piezoelectric strain constants (d_{ij}) in pC/N, piezoelectric stress constants (e_{ij}) in C/m^2, and static dielectric constants (ε_{ij}) for wurtzite $Y_xAl_{1-x}N$ crystal 143

Table IV.5: Computed thermodynamic parameters—bulk modulus (B_0, in GPa), heat capacity at constant volume (C_V, in J·mol^{-1}·K^{-1}), entropy (S, in J·mol^{-1}·K^{-1}), Debye temperature (Θ_D, in K), and thermal expansion coefficient (α, in K^{-1})—at 300 K and various pressures for $Y_xAl_{1-x}N$ crystals 146

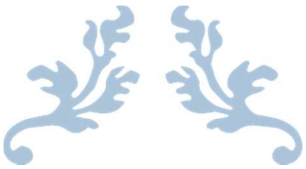

INTRODUCTION

The field of piezoelectric devices is undergoing significant advancements, propelled by innovations in materials science, nanotechnology, and sensor technology. In the twenty-first century, research is focused on the development of novel piezoelectric materials, enhancing device efficiency, and exploring emerging applications in areas such as wearable electronics, renewable energy, and smart infrastructure. According to a recent report by IMIR Market Research, the global market for piezoelectric devices was valued at USD 31.8 billion in 2023 and is projected to grow at a compound annual growth rate (CAGR) of 5.6%, reaching USD 41.93 billion by 2032.

Piezoelectric devices harness the piezoelectric effect to measure physical factors, such as mechanical stress, by converting them into electrical charges and vice versa (via the converse effect). Common types of piezoelectric devices include sensors, actuators, transducers, motors, and generators, which are developed using various materials such as ceramics, crystals, polymers, and composites. These devices are widely employed for process management, quality control, and research and development across numerous industrial sectors, including manufacturing, defense and aerospace, automotive, healthcare, information and communication, and consumer electronics. Since 2020, there has been increasing interest in piezoelectric micro-electromechanical systems (MEMS), which are miniaturized devices built from bulk piezoelectric materials for use in actuators or sensors. This area of development is expected to be a key focus for new business ventures.

Piezoelectric materials offer innovative applications by generating renewable energy from everyday activities, requiring minimal maintenance, and providing scalability across various industries. They also enable real-time monitoring in smart systems. However, these materials face challenges, including limited energy conversion efficiency, complex and costly integration into existing systems, and ensuring long-term durability in harsh environments.

In advancing the use of piezoelectricity, researchers are continually developing and engineering new, more efficient, and environmentally friendly materials. Lead-based materials such as Lead Zirconate Titanate (PZT), Lead Magnesium Niobate (PMN), and Lead Iron Niobate (PFN) have been extensively used due to their exceptional electromechanical properties [1–4]. Over the past fifty years, perovskite-type lead zirconate titanate (PZT) has been a dominant choice in commercial and industrial piezoelectric applications because of its outstanding electrical and piezoelectric properties

and its high Curie temperature [5]. However, due to the toxicity of lead (Pb), there is a growing demand for lead-free perovskites as sustainable alternatives to PZT-based piezoceramics [6, 7]. Recent developments have seen the adoption of lead-free materials, such as Barium Titanate (BaTiO3, BT), Potassium Sodium Niobate (KNN), Bismuth Ferrite (BiFeO3, BFO), Bismuth Potassium Titanate (BKT), Lithium Tantalate (LiTaO3, LT), and Lithium Niobate (LiNbO3, LNb) [8–11].

Among the lead-free materials, the perovskite oxide Sodium Bismuth Titanate ($Na_{0.5}Bi_{0.5}TiO_3$), is a promising candidate to replace lead-based materials. This material has garnered attention due to its exceptional ferroelectric properties, such as a remnant polarization (Pr) of 38 μC/cm² and relatively high piezoelectric coefficients (d_{33} = 72−79 pC/N). It stands out from most ABO_3 systems by having its A site equally occupied by two different cations—Na^+ and Bi^{3+}. This unique arrangement induces hetero-polar activity and relaxor behavior, distinguishing NBT from the more common B-site substituted perovskite systems, and contributing to its rarity and specialized properties. However, despite the excellent properties of lead-free piezoelectric NBT compounds, their lower recommended operating temperature (around 200 °C, though still superior to that of PZT with a recommended Tc of ≈180 °C) and low thermal conductivity limit their application in high-temperature-resistant devices, such as sensors or actuators designed for extreme conditions.

The III–V semiconductors, such as aluminum nitride (AlN), with a non-centrosymmetric crystalline structure, effectively address many of the challenges mentioned earlier due to their non-toxicity, high thermal stability (approximately 450 °C), wide direct bandgap (6.2 eV), high thermal conductivity (320 W/m•K), and high electrical resistivity (10^{14} Ω) [12]. These properties make AlN highly suitable for various applications, including short-wavelength light emitters and detectors, as well as high-temperature devices [13]. Additionally, AlN's low dielectric permittivity, efficient transduction, high stiffness, and high sound velocity, combined with its compatibility with complementary metal-oxide-semiconductor (CMOS) technology, offer great potential for nano/micro-electromechanical systems (NEMS/MEMS), such as surface acoustic wave (SAW) and bulk acoustic wave (BAW) technologies. However, despite its many advantages, AlN exhibits a relatively low piezoelectric response (d_{33} = 6.5 Introduction pm/V), which is lower than

that of other promising piezoelectric materials, limiting its use in high-performance electroacoustic and piezoelectric devices.

Doping aluminum nitride (AlN) with transition metals such as yttrium (Y) to form modern III-nitride materials like Yttrium Aluminum Nitride ($Y_xAl_{1-x}N$) alloys offers a promising solution for enhancing piezoelectric performance, comparable to $Sc_xAl_{1-x}N$ alloys, with a dramatic increase in the piezoelectric coefficient d_{33}, reaching up to 400% in $Al_{0.57}Sc_{0.43}N/Si$ [14]. This makes them highly suitable for advanced microelectromechanical systems (MEMS) used in the development of RF filters and resonators operating at high frequencies (in the GHz range), which are highly sought after for modern mobile communication technologies, such as 5th and 6th generation [15].

Environmental concerns regarding refrigerant fluids, along with the demand for non-toxic and cost-effective materials, have driven the search for high-performance thermoelectric materials suitable for small-scale power generation and refrigeration, including applications such as cooling electronic devices and flat-panel solar thermoelectric generators. Thermoelectric materials possess the unique ability to directly convert heat into electricity and vice versa. In recent years, dominant materials for thermoelectric applications have included Bi_2Te_3, PbTe, SiGe, and Half-Heusler alloys due to their excellent thermoelectric properties. However, new non-toxic systems such as $Na_{0.5}Bi_{0.5}TiO_3$ and $Y_xAl_{1-x}N$ offer promising alternatives as thermoelectric materials.

In condensed matter theory and materials science, Ab initio computational methods based on density functional theory (DFT) are ideal for modeling and understanding phenomena at the atomic and electronic scales. These methods have been increasingly used to extract, with high precision, all the ground-state properties of solids. The DFT formalism, grounded in the Hohenberg-Kohn theorem (1964), solves the Schrödinger equation by considering that the total energy of a system is a functional of the electron density, using only atomic constants as input parameters. These computational techniques provide powerful tools for designing new materials with tailored properties, driving efforts to guide the synthesis of novel thermoelectric and piezoelectric materials.

The present thesis aims to discover novel eco-friendly piezoelectric and thermoelectric materials as alternatives to lead-based materials (like $Na_{0.5}Bi_{0.5}TiO_3$) and to enhance the properties of existing aluminum nitride (AlN) materials to make them technologically attractive.

This dissertation summarizes the research done, which is divided into four chapters:

- **Chapter I** includes brief introductions to each topic covered in the dissertation, covering fundamental concepts of physical properties such as ferroelectric, piezoelectric, and thermoelectric properties. It also presents comprehensive information about piezoelectric (PE) and thermoelectric (TE) materials and their technological applications.
- **Chapter II** describes the principles of the computational methods used to understand the physical properties of the studied compounds, including the density functional theory (DFT) and its derived method (Full-Potential Linearized Augmented Plane Wave, FP-LAPW), as well as the approximations (GGA, mBJ) applied in various simulation packages such as Wien2K and CASTEP.
- **Chapter III** provides in-depth insights into the structural, electronic, elastic, piezoelectric, thermodynamic, and thermoelectric characteristics of lead-free Na0.5Bi0.5TiO3 perovskite systems crystallized in rhombohedral (R3c), tetragonal (P4bm), and cubic ($Pm\bar{3}m$) phases, as derived from ab initio calculations.
- **Chapter IV** discusses the computed structural, electronic, elasto-mechanical, piezoelectric, thermodynamic, and thermoelectric properties of wurtzite YxAl1−xN semiconductor alloys with ($0 \leq x \leq 0.375$), highlighting their potential for new optoelectronic applications and energy conversion, based on ab initio DFT investigations.

References

[1] K. Uchino, Ferroelectric Devices, Marcel Dekker, New York, NY, 2000.

[2] R. Zachariasz, D. Bochenek, Properties of the PZT type ceramics admixed with barium and niobium, Archives of Metallurgy and Materials 54 (2009) 895-902.

[3] R. Skulski, P. Wawrzała, K. Ćwikiel, D. Bochenek, Dielectric and electromechanical behaviors of PMN-PT ceramic samples, Journal of Intelligent Material Systems and Structures 18 (2007) 1049-1056, https://doi.org/10.1177/1045389XO6072356.

[4] D. Bochenek, Magnetic and ferroelectric properties of PbFe1/2Nb1/2O3 synthesized by solution precipitation method, Journal of Alloys and Compounds 504 (2010) 508-513, https://doi.org/10.1016/j.jallcom.2010.05.153.

[5] D. Damjanovic, Contributions to the piezoelectric effect in ferroelectric single crystals and ceramics, Journal of the American Ceramic Society 88 (2005) 2663-2676, https://doi.org/10.1111/j.1551-2916.2005.00671.x.

[6] T. Takenaka, H. Nagata, Current status and prospects of lead-free piezoelectric ceramics, Journal of the European Ceramic Society 25 (2005) 2693-2700, https://doi.org/10.1016/j.jeurceramsoc.2005.03.125.

[7] T.R. Shrout, S.J. Zhang, Lead-Free piezoelectric ceramics: alternatives for PZT? Journal of Electroceramics 19 (2007) 111, https://doi.org/10.1007/s10832-007-9047-0.

[8] Wu, Perovskite lead-free piezoelectric ceramics, Journal of Applied Physics 127 (2020) 190901, https://doi.org/10.1063/5.0006261.

[9] H. Mgbemere, G. Schneider, M. Hoelzel, M. Hintersteind, Neutron diffraction study of (KxNa1-x)NbO3-based ceramics from low to high temperatures, Journal of Applied Crystallography 49 (2016) 891-901, http://doi.org/10.1107/S1600576716005197.

[10] Y. Guan, S. Fukao, K. Ito, Y. Nakanishi, Y. Sato, Y. Ito, S. Yoshikado, Improvement of compact X-rays source using uniaxially polarized LiNbO3 single crystal, Key Engineering Materials 445 (2010) 43–46, https://doi.org/10.4028/www.scientific.net/kem.445.43.

[11] D.Y. Zhang, D. Yin, W. Qian, K. Li, J.S. Xie, Ferroelectric property of ion beam enhanced deposited lithium tantalate thin film, Advanced Materials Research 335–336 (2011) 1418–1423, https://doi.org/10.4028/www.scientific.net/amr.335-336.1418.

[12] A.M. Alsaad, I.A. Qattan, A.A. Ahmad, A. Ababneh, Z. Albataineh, I.A. Aljarrah, A. Telfah, Measurement and ab initio investigation of structural, electronic, optical, and mechanical properties of sputtered aluminum nitride thin films, Frontiers in Physics 8 (2020) 115, https://doi.org/10.3389/fphy.2020.00115.

[13] H. Morkoc, Handbook of Nitride Semiconductors and Devices, Vol. 1: Materials Properties, Physics and Growth, Wiley-VCH, 2008.

[14] M. Akiyama, T. Kamohara, K. Kano, A. Teshigahara, Y. Takeuchi, N. Kawahara, Enhancement of piezoelectric response in scandium aluminum nitride alloy thin films prepared by dual reactive cosputtering, Advanced Materials 21 (2009) 593, https://doi.org/10.1002/adma.200802611.

[15] Y. Lu, Development and Characterization of Piezoelectric AlScN-Based Alloys for Electroacoustic Applications, Thesis, Albert-Ludwigs-Universität Freiburg im Breisgau, 2019.

Piezoelectric and Thermoelectric Materials: An Overview of Recent Advances and Properties

Chapter I

I.1. Introduction

The majority of crystalline solid properties are intrinsically linked to their structure. Piezoelectricity, a fundamental physical property, arises only in materials with a non-centrosymmetric structure—where there is no inversion center. In such materials, the centers of gravity of positive and negative charges are spatially separated within the crystal lattice, generating a dipole moment. When mechanical stress or an electric field is applied to this structure, it induces either electrical polarization or mechanical deformation, referred to as the direct and converse piezoelectric effects, respectively.

A diverse range of materials, including ceramics, crystals, polymers, and composites, exhibit this polarity-driven phenomenon. Each class of materials presents unique advantages and limitations, which make them valuable in industries that rely on piezoelectricity. Among these, perovskites have garnered significant attention due to their exceptional and versatile properties. However, due to concerns regarding environmental pollution and toxicity—particularly from lead-based perovskites such as PZT—the scientific community has increasingly focused on the development of non-toxic, lead-free alternatives to safeguard both human health and the environment. In addition to perovskites, III–V semiconductor materials also play a prominent role in piezoelectric applications, contributing to technological advancements in the field.

This chapter provides a comprehensive overview of these materials, with a particular emphasis on Sodium Bismuth Titanate (NBT) and Yttrium Aluminum Nitride (YAlN). Detailed discussions of their physical properties and their current and potential technological applications are explored, shedding light on their growing relevance in future piezoelectric technologies.

I.2. III–V Semiconductors

III–V materials are semiconductor compounds typically crystallizing in zinc blende, rock salt, or hexagonal/wurtzite structures. Composed of elements from groups III and V of the periodic table, these materials are primarily characterized by a direct bandgap, making them well-suited for optoelectronic applications such as lasers (LDs), light-emitting diodes (LEDs),

and solar cells (photovoltaic cells). In some cases, these materials may exhibit an indirect bandgap in their ternary or quaternary alloys.

Among III–V compounds, III-nitrides—including AlN, GaN, InN, and their alloys—stand out due to their unique optoelectronic and piezoelectric properties. These polar materials crystallize in either the wurtzite or zinc blende structure and have garnered increasing scientific and technological interest in recent years. Their exceptional characteristics include a high melting point, high thermal conductivity, large bulk moduli, low dielectric permittivity, efficient transduction, high stiffness, and high sound velocity. Additionally, their compatibility with complementary metal–oxide semiconductor (CMOS) technology enables their integration into micro- and nanoelectromechanical systems (MEMS/NEMS), facilitating the development of devices such as surface acoustic wave (SAW) and bulk acoustic wave (BAW) sensors. These technologies are employed in the fabrication of mass and gas sensors, biosensors, ultrasound transducers, filters, and digital logic circuits [1−4].

The remarkable optoelectronic properties of III-nitrides are directly associated to their lattice constants, which are 20–40% smaller than those of other III–V semiconductors, such as GaAs or InAs, due to the smaller size of nitrogen atoms [5].

I.2.1. Crystal Structure of III–V Semiconductors and their Physical Properties

III–V materials are mineral compounds with the general chemical formula AB or $(TM_x)A_{1-x}B$. The A-site is occupied by group III elements (e.g., B, Al, Ga, In), and the B-site by group V elements (e.g., N, P, As, Sb) from the periodic table. In ternary alloys, the TM-site can also be occupied by transition metals (e.g., Sc, Y, V, Cr), with *x* representing the concentration of the transition metal in the alloy. These III–V compounds can crystallize in various structures, including cubic, hexagonal, triclinic, and orthorhombic, as illustrated in Figure I.1 for the case of AlN. However, the most common structures are cubic and hexagonal, with the zinc blende, rock salt, and wurtzite structures being the most prevalent. Of these, the wurtzite (WZ) structure is particularly significant in piezoelectric studies, as it is typically

associated with enhanced piezoelectric properties. In contrast, the zinc blende (ZB) structure is more commonly observed in bulk materials [6].

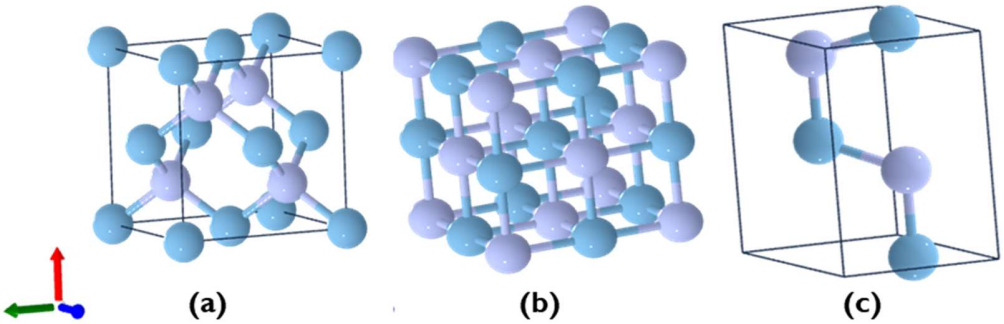

Figure I.1: The three crystalline structures of AlN: (a) zinc blende, (b) rock salt, and (c) wurtzite.

The wurtzite crystal structure belongs to the hexagonal crystal system and is characterized by two lattice constants: *a* (the length of the sides of the base) and *c* (the height of the unit cell). In an ideal case, the *c*/*a* ratio is equal to $\sqrt{(8/3)}$, and the internal parameter *u* (representing the bond length between anion and cation) takes its ideal value of 3/8. In the wurtzite structure of III–V materials, each lattice site consists of two atoms—one from group III and one from group V. As shown in Figure I.2, each cation (gray sphere) is surrounded by four nearest neighbor anions (yellow sphere) arranged at the corners of a tetrahedron, and vice versa [7]. The point group of the wurtzite structure is 6mm, while the space group is $P6_3mc$ [8].

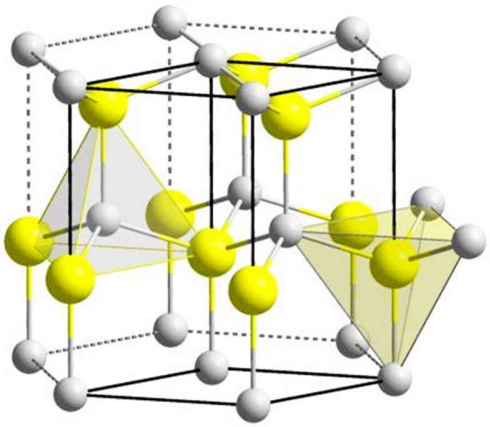

Figure I.2: Schematic representation of the wurtzite lattice structure.

Recent research on wurtzite III–V materials has surged in the field of piezoelectricity due to their promising applications in technological devices. Among III–V semiconductors, nitride-based compounds are unique in that they exhibit spontaneous polarization (P_s) without the influence of an external electric field, making them pyroelectric materials [9–12].

In wurtzite structures, crystallographic polarity is observed along the [0001] and [000$\bar{1}$] c-directions in noncentrosymmetric compound crystals. This noncentrosymmetry leads to spontaneous polarization, which is sensitive to structural parameters. The nonideal nature of the crystal structure in aluminum nitride (AlN) results in a significantly larger spontaneous polarization, with values reaching up to $|P_s| = 0.09$ cm^{-2}, compared to other III-nitrides [9, 13]. Notably, the spontaneous polarization values for (Al, In, Ga)N materials are approximately one-third of those found in typical perovskite ferroelectrics, such as $BaTiO_3$ [14].

In addition to spontaneous polarization, these materials also exhibit piezoelectric polarization (P_{px}) when subjected to mechanical stress. The variation of spontaneous polarization with temperature defines the pyroelectric coefficients; for instance, AlN has a coefficient of $dP_s/d*T = 7.5$ μC K^{-1} m^{-2} at room temperature [13]. This characteristic makes these materials particularly advantageous for high-power and high-temperature applications, such as surface acoustic wave (SAW) devices, high-frequency high-power transistors (HEMTs), and microwave amplifiers [13]. While, the total polarization, which encompasses both piezoelectric and spontaneous components, responds to applied stress and strain, with piezoelectric coefficients in III-nitrides being significantly higher than those in InAs, GaAs, and AlAs [9].

Generally, the physical properties of crystals are directly linked to their symmetry, specifically their point group (macroscopic symmetry). Figure I.3 summarizes the relationships between various properties and the macroscopic symmetries of different compounds. Depending on the symmetry of the crystals and external effects such as electric fields, temperature, or strain, various types of polarization can occur in materials. The differences in polarization have physical significance and can be used to describe measurable physical quantities [15, 16].

Materials are classified into 32 crystalline classes:

1. *Centrosymmetric Classes:*
    - There are eleven centrosymmetric classes, which possess a center of inversion. These crystals do not exhibit piezoelectric properties and are classified as paraelectric. The eleven paraelectric crystal classes are: $\bar{1}$, 2/m, mmm, 4/m, 4/mmm, $\bar{3}$, $\bar{3}$m, 6/m, 6/mmm, m$\bar{3}$, and m$\bar{3}$m.
2. *Non-Centrosymmetric Classes:*
    - Twenty-one classes are non-centrosymmetric, meaning they do not have a center of inversion and generate electrical charges when subjected to mechanical stress (the direct piezoelectric effect), with the exception of one class (the cubic class 432, which has more complex symmetry). The twenty piezoelectric crystal classes are: 1, 2, m, mm2, 4, 4mm, 3, 3m, 6, 6mm, 222, $\bar{4}$, 422, $\bar{4}$2m, 32, $\bar{6}$, 622, $\bar{6}$2m, 23, and $\bar{4}$3m.
3. *Pyroelectric Classes:*
    - Among the piezoelectric classes, ten exhibit pyroelectric behavior, characterized by changes in polarization due to thermal effects. These classes have a single polar axis along which spontaneous polarization (P_s) occurs, with its value varying according to temperature. The ten pyroelectric classes are: 1, 2, m, mm2, 4, 4mm, 3, 3m, 6, and 6mm.
4. *Ferroelectric Materials:*
    - Within the group of pyroelectric materials, some crystals have the ability to reverse their polarization when an electric field is applied in the opposite direction. These crystals are known as ferroelectric materials. Ferroelectric materials are a subgroup of pyroelectric materials, which in turn are a subgroup of piezoelectric materials.

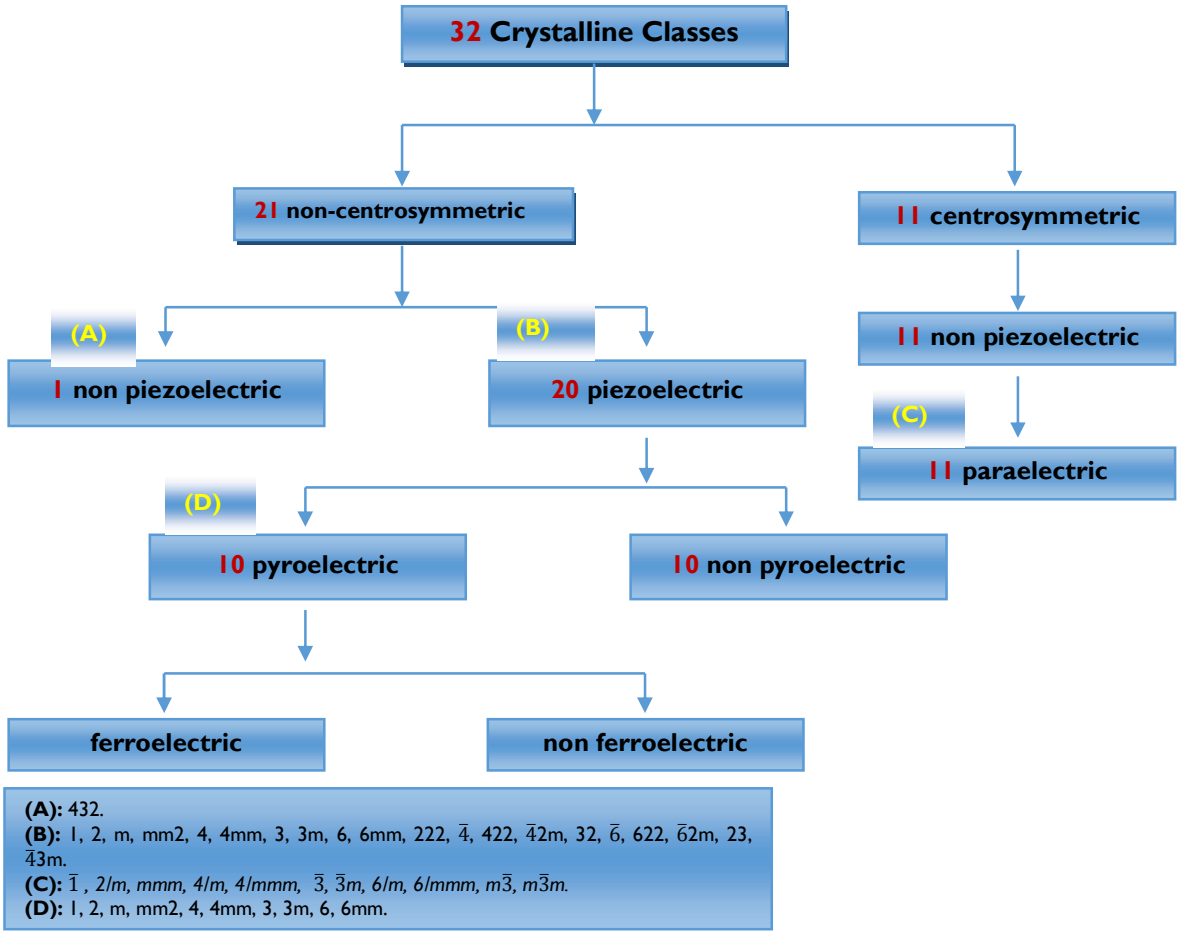

Figure I.3: Relationships between crystal classes and their corresponding symmetries.

I.2.2. Advanced III–V Semiconductor Alloys: Case of $Y_xAl_{1-x}N$ System

I.2.2.1. Properties and Technological Interest

Particularly, aluminum nitride (AlN) has garnered significant interest due to its exceptional properties, including a wide direct bandgap of 6.2 eV, high thermal conductivity of 320 W/m·K, and high electric resistivity of 1014 Ω [17]. These characteristics make AlN promising for various applications, particularly in short-wavelength light emitters, detectors, and high-temperature devices [18, 19]. Moreover, AlN exhibits a reasonably good piezoelectric response (d_{33} ≈ 6.5 pm/V [20]), low dielectric permittivity, high stiffness, and high sound velocity. Consequently, AlN crystals are highly desirable in the piezoelectric industry

and are extensively utilized in the fabrication of high-quality micromechanical resonators and filters for MEMS technology and biosensing applications [21, 22].

The atomic structure of AlN features a close-packed hexagonal arrangement (see in Figure I.2) with a space group of P63mc. The lattice parameters are a = 3.11 Å and c = 4.98 Å, with an internal parameter u = 0.38. Each aluminum atom is tetrahedrally coordinated to four nitrogen atoms, as depicted in Figure I.4. Due to the asymmetry in the wurtzite structure, where the Al–N bond B_2 along the c-axis (0001 direction) is slightly longer than the other three bonds B_1, AlN possesses a polar axis along the c-axis, resulting in spontaneous polarization in that direction. Furthermore, variations in physical conditions, such as temperature, strain, or voltage, can alter this polarization, leading to various physical phenomena including pyroelectricity and piezoelectricity.

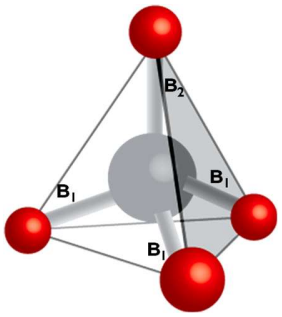

Figure I.4: Tetrahedral geometry of AlN, with B1 and B2 representing different Al–N bond lengths.

Yttrium aluminum nitride ($Y_xAl_{1-x}N$) alloys recently emerged as promising alternatives to traditional III–V semiconductor materials for advanced optoelectronics [23]. The incorporation of yttrium (Y) into AlN crystals enables bandgap engineering, allowing for a range from 6.2 eV for AlN (in the wurtzite phase) [24] to 0.498 eV for YN (in the rock-salt phase) [25]. This flexibility opens avenues for extending the spectral range from infrared (IR) and visible light to the deep ultraviolet spectrum. $Y_xAl_{1-x}N$ also exhibits enhanced piezoelectric properties, making it an ideal candidate for the development of high-frequency surface acoustic wave (SAW) and bulk acoustic wave (BAW) devices, which are crucial for future mobile communication technologies, including 5G [26, 27]. $Y_xAl_{1-x}N$ crystals maintain stability in the hexagonal wurtzite phase for yttrium contents up to $x \approx 0.56$ [28] and $x \approx 0.75$

[29], after which they transition to the cubic rock-salt phase at higher yttrium concentrations. However, it has been observed that the crystalline quality of similar $Sc_xAl_{1-x}N$ films degrades significantly when x approaches approximately 0.3 [30].

The first growth of $Y_xAl_{1-x}N$ films on sapphire and silicon substrates using reactive magnetron sputtering epitaxy (MSE) was demonstrated by Žukauskaite et al. in 2012 [29]. Sedrine et al. later (in 2013) analyzed the effect of Y doping on the bandgap energies and optical constants of $Y_xAl_{1-x}N$ (where $0 \leq x \leq 0.22$) epitaxial films on silicon (100) substrates, employing spectroscopic ellipsometry (SE). They observed a decrease in the bandgap energy (Eg = 6.2 to 4.5 eV) and a shift in the refractive index (n=1.93 to 2.20) in the transparent region as the composition x varied within the range of 0 to 0.22 [23]. Extensive studies on $Y_xAl_{1-x}N$ have been reported in recent years. Notably, in 2023, Pandit et al. synthesized $Y_xAl_{1-x}N$ thin films with x = 15% using a standard DC magnetron sputtering system [31].

Similarly, AlN doping with transition metals such as scandium (Sc) and chromium (Cr) to form new alloys (ScAlN, CrAlN) has shown increased interest in recent years due to offering the best raw materials to significantly enhance the performance of AlN-based components [32, 33]. Sc doping can dramatically increase the piezoelectric coefficient d_{33} up to about 400% in $Al_{0.57}Sc_{0.43}N$/Si thin films [34], and a d_{33} of 31.6 pC/N in $Al_{0.59}Sc_{0.41}N$ was achieved [35], which permits improved transducer losses in ScAlN/Sapphire-based SAW devices [36]. AlN allowing with Ga-dilute leads to more interesting applications in UV–LED (*l*~ 210–375 *n*m) and radio-frequency UV sensors [37, 38].

I.3. Perovskite Materials: Low-cost and Potential Applications

One of the most exciting applications of perovskites is in next-generation solar cells, where they have demonstrated unprecedented improvements in efficiency. Moreover, their integration into flexible electronics, MEMS systems, and biomedical devices further highlights their adaptability and potential for future technological breakthroughs.

In the past decade, perovskite ferroelectric piezo-ceramics have garnered significant attention due to their broad range of technological applications in electronic and photonic devices. These include transducers, actuators, acoustic sensors, filters, optical signal

processing systems, highly sensitive photodetectors, second harmonic generators (SHGs), light sensors, and medical imaging tools [39–42]. Among perovskite materials, lead zirconate titanate (PZT) has been one of the most widely used materials for piezoelectric applications in both commercial and industrial sectors over the past half-century. PZT is renowned for its exceptional electrical and piezoelectric properties as well as its high Curie temperature, which have made it the material of choice for numerous applications [43]. However, due to the toxicity of lead (Pb), there has been a growing demand for lead-free alternatives to PZT-based piezo-ceramics in recent years [44, 45].

Several lead-free piezo-ceramics have emerged as promising replacements for PZT, including Barium Titanate ($BaTiO_3$, BT), Barium Titanate Potassium Sodium Niobate [$(K,Na)NbO_3$, KNN], Bismuth Ferrite ($BiFeO_3$, BFO), Bismuth Potassium Titanate [$(Bi,K)TiO_3$, BKT], Lithium Titanate ($LiTaO_3$, LT), and Lithium Niobate ($LiNbO_3$, LNb) [46–49]. These materials have been employed in the creation of multifunctional prototype devices such as integrated circuits, energy storage systems, and MEMS systems [50, 51].

The perovskite structure is highly versatile, allowing for the incorporation of various elements at the A or B sites, which results in a wide array of materials and applications. In recent years, perovskite materials have garnered significant attention as promising piezoelectric materials due to their properties that align with modern technological demands.

Among these materials are:

- **Lead Zirconate Titanate ($Pb_{1-x}Zr_xTiO_3$, PZT):**

  PZT has long been considered one of the best piezoelectric materials, with extensive research focused on optimizing PZT-based compositions for specific applications. However, due to the toxicity of lead oxide, recent efforts have shifted toward the development of lead-free piezoceramics.

- **Lead-Free Perovskites:**

  Lead-free perovskites, such as $BaTiO_3$, $SrTiO_3$, and $CaTiO_3$, along with their mixed compositions like $Ba_{1-x}Sr_xTiO_3$ (BST), are widely used in the development of piezoelectric devices. Barium titanate ($BaTiO_3$), the first piezoelectric ceramic developed,

remains in widespread use today [52]. The demand for lead-free perovskites is growing due to their environmentally friendly nature, as they serve as alternatives to conventional lead-based PZT ceramics and offer enhanced performance for electromechanical devices.

I.3.1. Perovskite Structure

Perovskite is a naturally occurring mineral with the general chemical formula ABX_3. In this formula:

- **A-site cations** are typically alkali or alkaline-earth metals, with ionic radii ranging from 1.2 to 1.6 Å [53]. These cations have valences between +1 and +3 (e.g., Na^+, Bi^{3+}, Ca^{2+}, Pb^{2+}, K^+), and they are surrounded by twelve anions, giving them a coordination number of 12.
- **B-site cations** are usually transition elements, with smaller ionic radii in the range of 0.6 to 0.7 Å [53]. Their valence varies from +3 to +6 (e.g., Cr^{3+}, Ti^{4+}, Zr^{4+}, Nb^{5+}, Mn^{4+}), and they are coordinated by six anions, resulting in a coordination number of 6.
- **X-site anions** are commonly oxygen but can also be other anions such as fluoride, chloride, bromide, iodide, sulfide, or hydride [54]. In this structure, each X-site anion is coordinated by six nearest neighbors, comprising four A-site cations and two B-site cations.

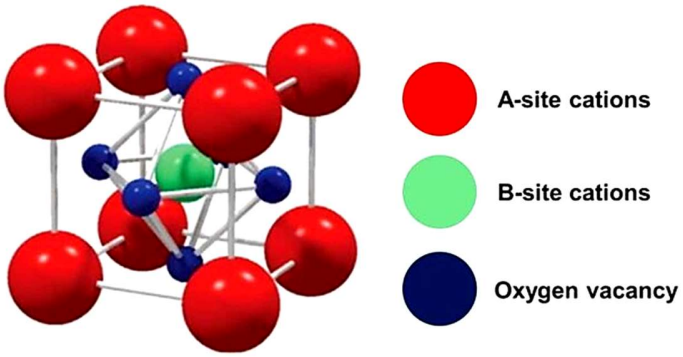

Figure I.5: Illustration of unit cell of the ABO_3 perovskite structure [55].

In deformed (non-ideal) perovskites, modifications such as changes in lattice parameters or interatomic bond strengths can lead to the displacement of the small-sized B cation within the octahedron. This displacement causes the cation to occupy a position offset from the center along specific crystallographic directions (axes of symmetry of order 2, 3, or 4), as illustrated in Figure I.6. Consequently, the material acquires a non-centrosymmetrical structure. The non-centrosymmetry results in the development of electrical polarization within the material, which induces a permanent dipole moment. This dipole moment is the origin of various physical phenomena in the material, including ferroelectricity [53]. The ability to maintain this polarization under an external electric field is crucial for the functionality of ferroelectric materials in a range of applications, including sensors, actuators, and memory devices.

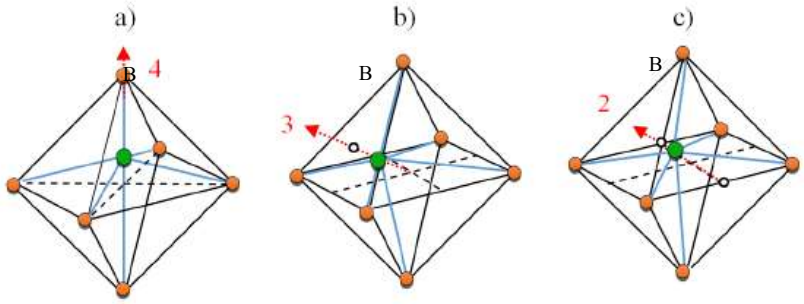

Figure I.6: Displacement of cation B within the octahedron BO_6 of certain directions (on axis 2π/n): (a) an axis of tetrad π/2, (b) an axis oftriad 2π/3, (c) a dyad axis π [56].

I.3.2. Lead-free Perovskite $Na_{0.5}Bi_{0.5}TiO_3$ (NBT)

Among the lead-free piezo-ferroelectrics, *Sodium Bismuth Titanate* ($Na_{0.5}Bi_{0.5}TiO_3$) has gained prominence as a modern alternative for eco-friendly piezoelectric applications. Sodium Bismuth Titanate (NBT) was first discovered by Smolensky et al. in the 1960s [57], and it has since become an important material in the realm of lead-free piezoelectric ceramics. NBT has attracted considerable attention due to its high remnant polarization (Pr = 38 μC/cm²) [58] and relatively high piezoelectric coefficients (d_{33} = 72–79 pC/N) [59, 60], positioning it as one of the most promising candidates for lead-free piezoelectric applications [61, 62]. In addition

to its high conductivity, NBT is characterized by a high coercive field (Ec = 73 kV/cm) [58], which presents a challenge for the poling process of NBT ceramics [63]. This difficulty in poling contributes to its relatively modest piezoelectric performance compared to lead-based materials like PZT. Despite these challenges, NBT properties make it a strong contender for various technological applications, particularly in the quest for eco-friendly piezoelectric materials.

Sodium Bismuth Titanate (NBT) single crystals have been successfully grown using various techniques, each with its own set of advantages and specific applications. These methods include: a spontaneous crystallization [64], Bridgman [65], solid-state reaction [66], metalorganic solution deposition [67], top-seeded solution [68], laser ablation [69] and sol-gel [70]. These methods highlight the versatility of NBT crystal growth and the various approaches used to optimize its properties for different technological applications.

At room temperature (5–528 K), the crystallographic structure of Sodium Bismuth Titanate ($Na_{0.5}Bi_{0.5}TiO_3$, or NBT) adopts a rhombohedral structure with R3c symmetry [71, 72]. As temperature increases, NBT undergoes two successive phase transitions. The first transition occurs between the rhombohedral and tetragonal phase (P4bm) at approximately 573–593 K [73]. The second transition is from the tetragonal to the cubic phase ($Pm\bar{3}m$) at 773–823 K [73]. It has been demonstrated that the tetragonal distortion of NBT increases with rising temperature, peaking around 673 K [74]. Additionally, NBT exhibits two-phase coexistence regions at the phase boundaries: a pseudo-rhombohedral/tetragonal coexistence between 528–673 K and a tetragonal/cubic coexistence between 773–813 K [71].

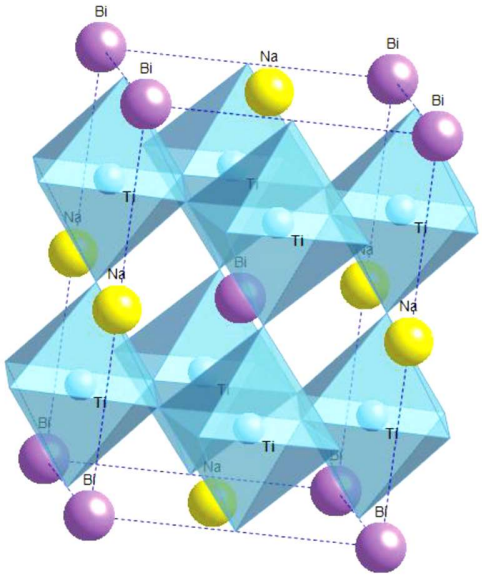

Figure I.7: Illustration of perovskite $Na_{0.5}Bi_{0.5}TiO_3$ in pseudo-cubic structure [75].

Perovskite Sodium Bismuth Titanate (NBT) exhibits a unique property not commonly found in most ABO_3 systems: it shares the A-site cation equally between two different elements, sodium (Na) and bismuth (Bi). This cation disorder within the NBT crystal structure is associated with hetero-polar activity at both the A and B sites, contributing to its relaxor behavior [76]. A-site substituted perovskite systems, like NBT, are considered much rarer than their B-site substituted counterparts. Other examples of A-site substituted perovskite systems include [64]: $Ag_{0.5}Nd_{0.5}TiO_3$, $Ag_{0.5}Bi_{0.5}TiO_3$, and $K_{0.5}Bi_{0.5}TiO_3$. The presence of two different cations at the A site enhances the material's complexity and contributes to its intriguing physical properties, making NBT a significant candidate for applications in piezoelectric devices and other advanced technologies.

$Na_{0.5}Bi_{0.5}TiO_3$ has been extensively investigated to date : Niranjan et al. [76] observed a significant dielectric response in Sodium Bismuth Titanate (NBT) crystals, which can be attributed to phonon modes associated with the Bi-O (109 cm^{-1}) and Ti-O (246, 276 cm^{-1}) vibrations. Additionally, Andriyevsky et al. [77] detected anomalies in the temperature dependence of dielectric susceptibility and the intensity of reflected light within the temperature range of 180–320 °C, which are linked to the complex phase transformations occurring in NBT ceramics. Meanwhile, Bousquet et al. [69] determined the optical constants

of $Na_{0.5}Bi_{0.5}TiO_3$ powders, which suggested an optical band gap of 3.26 eV and a refractive index of 2.346.

Furthermore, Thanh et al. [70] measured a band gap of 3.12 eV for pure $Bi_{0.5}Na_{0.5}TiO_3$ nanopowders, noting a decrease to 1.71 eV as the concentration of Mn doping increased to 9 mol%. These findings highlight the tunable electronic properties of NBT-based materials through composition and doping, making them promising candidates for various electronic applications. Recently, Khatua et al. [78] observed a drastic reduction in the piezoelectric response of bulk Sodium Bismuth Titanate (NBT) ceramics when the grain size is submicron. This reduction is attributed to the grains' inability to collectively transform into a long-range rhombohedral ferroelectric state, which is essential for maintaining strong piezoelectric properties. In another study, Takagi et al. [79] demonstrated that controlling the quenching rate in the temperature range of 1100°C to 800°C during the preparation of lead-free piezoelectric $(Bi_{0.5}Na_{0.5})TiO_3$ ceramics can significantly enhance both the depolarization temperature (T_e) and the mechanical strength of the materials. This finding highlights the importance of processing conditions in optimizing the performance of NBT-based ceramics for various applications in piezoelectric devices

I.3.3. Stability in Perovskite Structures

In an ideal perovskite crystal (typically cubic), any intrinsic changes in symmetry can lead to structural distortions, resulting in non-ideal atomic positions for the A or B cations. The stability of the perovskite structure primarily depends on two key factors: the Goldschmidt tolerance factor (*t*) and the ionic character of the anion-cation bonds.

The Goldschmidt Tolerance Factor

The Goldschmidt tolerance factor is a crucial metric for determining the deviation from the ideal cubic structure in perovskites (ABX_3) [80]. It is calculated using the following relationship:

$$t = \frac{r_A + r_X}{\sqrt{2}(r_B + r_X)} \quad (1)$$

Where: r_A, r_B and r_X represent the ionic radii of the A-site cation, B-site cation, and the X-site ion, respectively.

This factor quantifies the compactness and stability of the perovskite structure, accounting for possible distortions. The stability limits for the perovskite phase (whether distorted or ideal) occur when *t* ranges between 0.75 and 1.06 [81, 82]. For cubic structures, *t* values are typically close to 1 [53, 54, 83].

The following structural distinctions can be made based on *t*:

- 0.75 < t < 0.95: Orthorhombic/Tetragonal distortion (e.g., $CaTiO_3$, $GdFeO_3$).
- 0.96 < t < 0.99: Rhombohedral distortion (e.g., $Na_{0.5}Bi_{0.5}TiO_3$, $BiFeO_3$).
- 0.99 < t < 1.06: Cubic structure (e.g., $SrTiO_3$, $BaZrO_3$).

The Ionicity of Anion-Cation Bonds

The stability of the perovskite structure also depends on the ionic character of the bonds between the cations and the anions. Generally, the perovskite structure is more stable when the bonds have a strong ionic character. According to Miller et al. [84], covalent bonds (e.g., in lead-based perovskites) tend to reduce stability compared to more ionic perovskites like $BaTiO_3$. The ionicity of these bonds can be quantified using the differences in electronegativities, as measured on the Pauling scale [85]:

$$\delta = \frac{|\chi_{A-X} - \chi_{B-X}|}{2} \quad (2)$$

Where: χ_{A-X} and χ_{B-X} are the electronegativity differences between A and X, and B and X, respectively.

The following table summarizes the values of δ and its corresponding bond types [86]:

Electronegativity Difference	Type of Bond Formed
0.0 to 0.2	nonpolar covalent
0.3 to 1.4	polar covalent
> 1.5	ionic

I.3.4. Electric and Thermoelectric Phenomena in Perovskite Materials

I.3.4.1. Paraelectricity

Paraelectric materials exhibit dielectric polarization when an electric field is applied and lose this polarization once the electric field is removed. There are three main types of polarization in paraelectric materials: electronic polarization, ionic polarization, and orientational polarization. In electronic polarization, electrons are displaced relative to the atomic nucleus. In ionic polarization, positive and negative ions shift against each other, while in orientational polarization, molecules with permanent dipole moments realign their orientations in response to an external electric field. The phenomenon of paraelectricity was first observed in $ATiO_3$ perovskite oxides, where the A site is occupied by two different cations [87]. Most dielectric materials exhibit paraelectric behavior, with strontium titanate ($SrTiO_3$) being a prominent example due to its high dielectric constant. Paraelectricity has also been explored as a potential mechanism for refrigeration, offering an alternative to traditional heat pump systems and potentially useful for cooling electronic devices, such as computer chips.

I.3.4.2. Ferroelectricity

Ferroelectric materials possess two distinct, non-zero spontaneous polarization states that can be switched by applying an external electric field. This switching behavior, characterized by the polarization change between these states, produces a hysteresis loop, a hallmark of ferroelectricity. These materials exhibit unique pyroelectric and piezoelectric properties, with perovskites being among the most notable ferroelectric materials.

In the past two decades, significant efforts have been made to develop lead-free perovskite ferroelectrics with comparable dielectric, ferroelectric, piezoelectric, and pyroelectric properties to conventional lead-based perovskites. These materials hold great promise for energy harvesting from diverse sources, including solar, thermal, magnetic, wind, and mechanical vibrations [88].

The key characteristics of ferroelectric materials include [89, 90] (refer to Figure I.8):

- Hysteresis behavior (P ~ E curve),
- Spontaneous polarization,
- Reversible polarization,
- Curie temperature (T_C), marking the transition between ferroelectric and paraelectric phases.

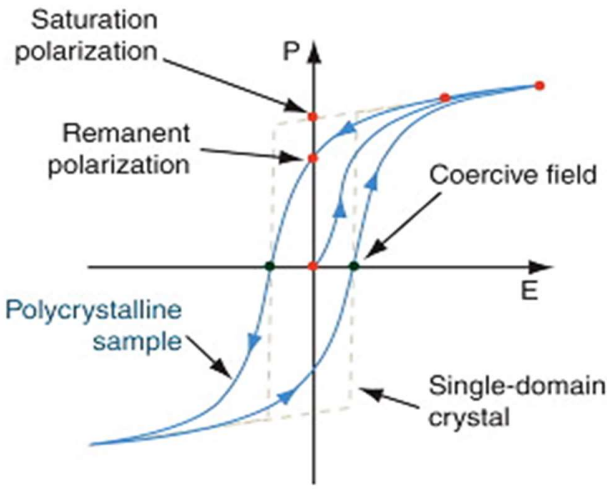

Figure I.8: Polarization as a function of the electric field for a single crystal (gray-dashed line) and polycrystalline (blue solid line) ferroelectric materials. The direction of the electric field change is indicated by arrows [91].

I.3.4.3. Pyroelectricity

Pyroelectricity is a property of polar crystals that enables these materials to generate electrical charges when subjected to temperature changes. As the material heats up or cools down, the positions of atoms within the crystal structure shift slightly, altering the material's polarization. This change in polarization results in a temporary voltage across the crystal. Once the temperature stabilizes, the pyroelectric voltage gradually dissipates. It is important to distinguish the pyroelectric effect from the thermoelectric effect, as the latter involves a constant temperature gradient leading to a permanent voltage. Certain perovskite piezo-ceramics have proven suitable for vibration energy harvesters [92, 93], as well as for

pyroelectric energy conversion, which has enabled the development of self-powered, battery-free devices [94, 95].

I.3.4.4. Thermoelectricity

Thermoelectric (TE) technology has gained increasing interest due to its wide range of applications, including cooling, power generation, and energy conversion. A key focus in recent research has been the development of affordable and non-toxic thermoelectric materials, such as lead-free perovskites, to enhance energy conversion efficiency in TE devices. Thermoelectric materials are capable of converting thermal energy into electrical energy, with electrons and phonons acting as charge and heat carriers, respectively. The efficiency of this conversion process is determined by the figure of merit (ZT), which is influenced by several parameters: electrical conductivity (σ), Seebeck coefficient (S), electronic thermal conductivity (κ_e), and lattice thermal conductivity (κ_{latt}). The figure of merit can be expressed as:

$$ZT = S\sigma^2 T / (\kappa_{el} + \kappa_{latt}) \quad (3)$$

- **Seebeck Coefficient (S in V/K)**:

  The Seebeck coefficient provides information on the dominant charge carriers (n-type or p-type) in the material. It can be calculated using:

$$S = (8\pi^2 k_B^2/3eh^2).m^*T(\pi/3n)^{2/3} \quad (4)$$

- **Electrical Conductivity (σ in $\Omega^{-1}.m^{-1}$)**:

  Electrical conductivity represents the material's ability to conduct an electrical current and is related to the charge carrier density (n or p) and mobility (μ):

$$\sigma = ne\mu_n + pe\mu_p \quad (5)$$

  Where mobility (μ in $cm^2/V \cdot s$) is:

$$\mu = e\tau / m^* \quad (6)$$

  Here, m is the effective mass of the carriers, and τ is the scattering time between collisions.

- **Thermal Conductivity (κ in W/m·K)**:

  Thermal conductivity refers to the material's ability to conduct heat, given by:

$$\kappa = \kappa_{el} + \kappa_{latt} \quad (7)$$

  Where the electronic component is:

$$\kappa_{el} = L\sigma T \quad (8)$$

  and the lattice component is:

$$\kappa_{latt} = A(M_a V \Theta_D n^{1/3} / \gamma^2 T) \quad (9)$$

  In this equation, A is a constant, M_a is the average atomic mass, V is the volume per atom, Θ^D is the acoustic Debye temperature, γ is the Grüneisen parameter, n is the number of atoms per unit cell, and T is the temperature.

- **Power Factor (PF in W/m·K²)**:

  The power factor is a key parameter in assessing the thermoelectric potential of materials, given by:

$$PF = S^2 \sigma \quad (10)$$

To analyze thermoelectric performance, various parameters, including the ones mentioned above, can be calculated using computational tools such as the BoltzTrap code. These parameters are crucial in determining the efficiency and potential of thermoelectric materials.

I.3.4.4.1. Thermoelectricity Technology Applications

- **Thermoelectric Generator:** Thermoelectric devices are highly promising for a wide range of applications due to their ability to operate without mechanical moving parts and with minimal maintenance. Their applications span from large-scale space missions [96–98] to micropower energy harvesting [99]. One notable example is the Radioisotope Thermoelectric Generator (RTG), which has been instrumental in several missions conducted by the United States National Aeronautics and Space Administration (NASA). The most recent RTG configuration, known as the Multi-Mission Radioisotope Thermoelectric Generator (MMRTG) (Figure I.9-(a)), was deployed on NASA's Mars

Science Laboratory rovers, Curiosity (Figure I.10-(a)) and Perseverance (Figure I.9-(b), (c)). Usually, this MMRTG uses TE materials (like lead telluride (PeTe) or bismuth telluride (BiTe) based alloys) to generate electricity by harnessing the heat from the decay of plutonium-238 (or americium Am-241), making it ideal for environments where solar power is impractical [100–102]. In addition to their use in space exploration, RTGs are employed in select terrestrial applications that demand reliable, long-term power supplies capable of delivering up to several hundred watts. These systems are particularly valuable in remote and extreme environments where conventional power sources are impractical. Examples include autonomous weather stations, navigation beacons, lighthouses, and scientific research installations, such as those used for volcanic and geothermal monitoring, as well as deep-sea and ocean floor investigations. [101]

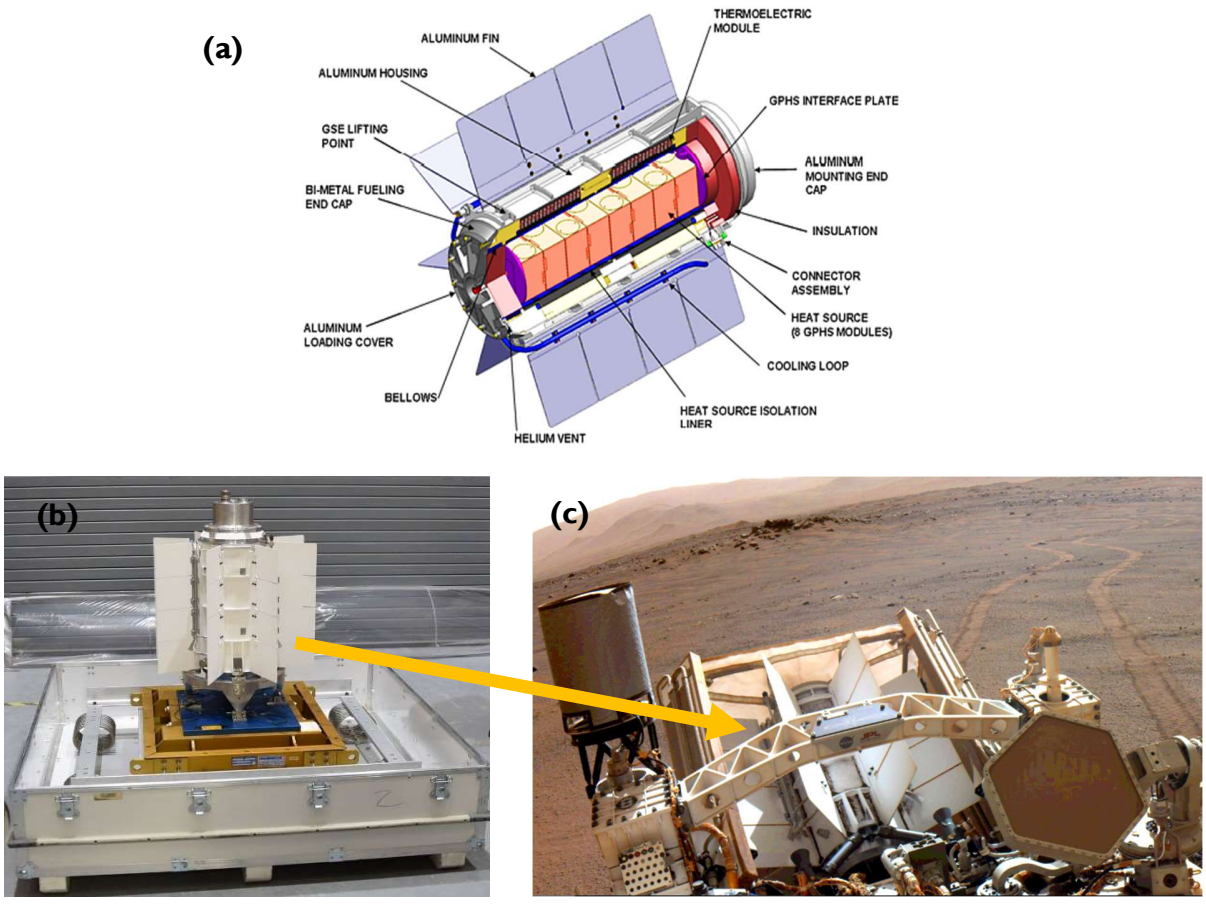

Figure I.9: (a) Schematic representation of the Multi-Mission Radioisotope Thermoelectric Generator (MMRTG) [102]; (b) & (c) The MMRTG on the Perseverance rover during its Mars mission, (Image credit: NASA/JPL/Caltech).

- **Automotive industry:** The automotive industry represents one of the most active fields for thermoelectric applications. In vehicles powered by internal combustion engines, approximately 75% of the energy is wasted as heat. Thermoelectric power generators (TEGs) can harness this wasted heat to recharge the battery, potentially reducing or even eliminating the need for an alternator (Figure I.10-(b)). This can lead to a significant improvement in fuel efficiency, with gains of up to 10% [99].

- **Small Portable Devices:** Thermoelectric generators (TEGs) offer a viable alternative to traditional batteries for small portable electronic devices that require lighter and more compact power sources. By utilizing small-scale heat generation, TEGs are ideal for low-power applications, including wireless sensor networks, mobile devices, and medical equipment (Figure I.10-(c)) [99].

- **Other Applications:** Thermoelectric technology has become increasingly common in everyday life, with practical applications such as portable mini coolers, refrigerators, and coffee warmers. Thermoelectric heat pumps are also utilized in temperature control devices, including cooled seats, weather vests, semiconductor laser temperature regulators, and medical equipment [99]. Current research in the field of thermoelectrics is driven by the quest to develop and discover advanced thermoelectric materials for use in higher-power thermoelectric devices.

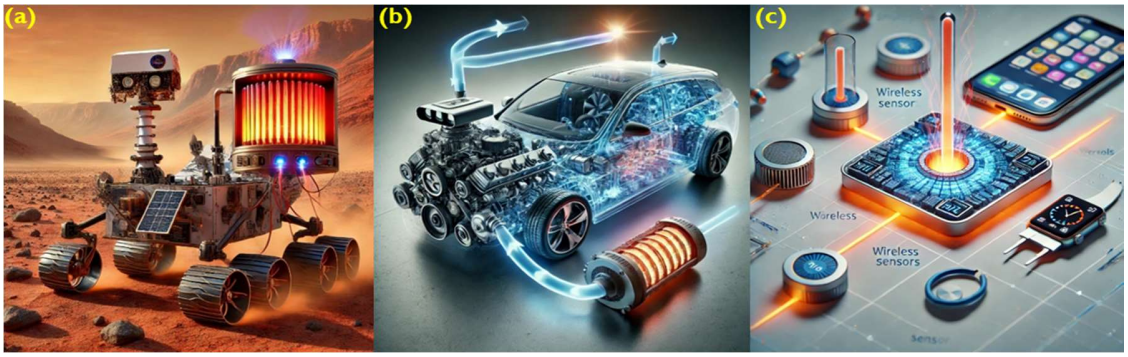

Figure I.10: (a) NASA curiosity rover equipped with Multi-Mission Radioisotope Thermoelectric Generator (MMRTG) on mars, demonstrating thermoelectric power in harsh environments. **(b)** Image of a vehicle with a thermoelectric power generator (TEG) harnessing wasted heat from the engine. **(c)** Image illustrating low-power applications like small portable electronic devices, wireless sensors, and medical equipment powered by a thermoelectric generator (TEG).

I.3.4.5. Piezoelectricity

I.3.4.5.1. Fundamentals and Mechanism of the Piezoelectric Effect

Piezoelectricity was first discovered by the Curie brothers, Jacques and Pierre, in 1880 during experiments with natural crystals such as quartz. The term "piezo" comes from the Greek word *piezein*, meaning "to press." Piezoelectricity can be defined as the generation of an electric charge in certain materials when mechanical pressure is applied. This phenomenon occurs in materials that lack a center of symmetry (non-centrosymmetric materials).

Piezoelectric materials are characterized by their ability to generate a voltage when subjected to mechanical stress, a property attributed to their atomic structure. This effect also works in reverse; applying a voltage across the material induces strain or deformation (see Figure I.11). Direct piezoelectricity is commonly utilized in sensing devices, while the reverse piezoelectric effect is applied in actuators.

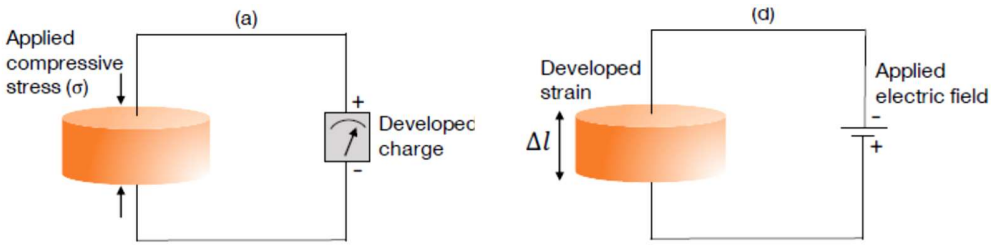

Figure I.11: Schematics of direct piezoelectric effects: **(a)** at applied compressive stress, **(d)** at applied tension [103].

A. Piezoelectric Constants and Equations

Piezoelectricity arises from the coupling of electrical and mechanical energies within a material. When the pyroelectric effect is negligible, the piezoelectric equations describe the relationship between mechanical variables (strain S or stress T) and electrical variables (electric displacement D or electric field E) [104]. This leads to a linear system of eight tensor equations, as illustrated in Table I.2.

Table I.2: Piezoelectric equations.

Independent Variables	Electrical Quantities	*Mechanical Quantities*
E, T	$D = dT + \varepsilon^T E$	$S = S^E T + d^t E$
D, T	$E = \beta^T D - gT$	$S = S^D T + g^t D$
E, S	$D = e^S E + eS$	$T = c^E S - e^t T$
D, S	$E = \beta^S D - hS$	$T = c^D S - h^t D$

Where:

- *S:* Deformation (strain)
- *D* (C/m²): Dielectric displacement
- *T* (N/m²): Mechanical stress (stress)
- *E* (V/m): Electric field
- *S* (m²/N): Compliance or elastic susceptibility
- *c* (N/m²): Stiffness or elastic constant
- *ϵ* (F/m): Electrical permittivity
- *β* (m/F): Dielectric impermeability constant
- *d* (C/N or m/V): Piezoelectric constant (load constant), indicating the proportionality between the load and the stress under constant or zero fields [$d_{ij} = \left(\frac{\partial D_i}{\partial T_j}\right)_E = \left(\frac{\partial S_j}{\partial E_i}\right)_T$]
- e (C/m² or N/V·m): Piezoelectric constant reflecting the proportionality between the load and deformation under constant or zero fields [$e_{ij} = -\left(\frac{\partial T_j}{\partial E_i}\right)_S = \left(\frac{\partial D_i}{\partial S_j}\right)_E$]
- *g* (V·m/N or m²/C): Piezoelectric coefficient that represents the proportionality between stress and the resulting electric field under constant or zero induction [$g_{ij} = -\left(\frac{\partial E_i}{\partial T_j}\right)_D = \left(\frac{\partial S_j}{\partial D_i}\right)_T$]
- *h* (V/m or N/C): Piezoelectric coefficient indicating the proportionality between deformation and the resulting electric field under constant or zero induction [$h_{ij} = -\left(\frac{\partial E_i}{\partial S_j}\right)_D - \left(\frac{\partial T_j}{\partial D_i}\right)_S$].

B. Piezoelectric Charge (Strain) Constant d_{ij}

The piezoelectric constant, denoted as d_{ij}, is a matrix of elements that characterizes the behavior of a piezoelectric material under an applied electric field or mechanical stress. The indices *i* and *j* refer to the direction of polarization or applied electric field (first subscript) and the direction of applied stress or induced strain (second subscript) [105]. This constant is

commonly used to evaluate the quality of piezoelectric materials, serving as a critical figure of merit in piezoelectric devices

The piezoelectric constant can be expressed as follows:

$$d_{ij} = \frac{deformation\ (strain)}{electric\ field} = \frac{1}{\text{Newtons}/\text{Coulombs}} = \frac{1}{N/C} = \frac{C}{N},$$

Or:

$$d_{ij} = \frac{polarisation}{stress} = \frac{\text{Coulombs}/m^2}{\text{Newtons}/m^2} = \frac{C/m^2}{N/m^2} = \frac{C}{N}.$$

C. Operating Modes of a Piezoelectric Material

In the 33-mode, the applied stress and the generated voltage are in the same direction. In contrast, in the 31-mode, the stress is applied axially, while the voltage is generated perpendicularly. The two common modes are illustrated in Figure I.12, commonly utilized in piezoelectric energy harvesting [106]. The 33-mode generates a higher voltage output, while the 31-mode excels in delivering high current output [107].

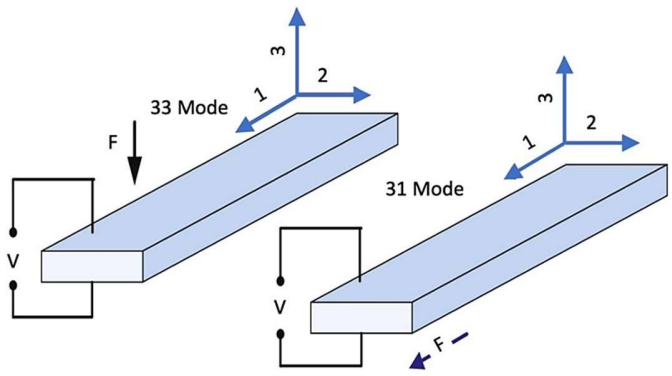

Figure I.12: Operating modes of a piezoelectric material, 33-mode and 31-mode.

D. Longitudinal Charge Coefficient (d_{33}^*)

The calculation of piezoelectric properties as a function of the angle relative to the polar axis helps determine whether a ferroelectric material exhibits '*extender*' or '*rotator*' behavior.

- **Rotator ferroelectrics** are characterized by higher d_{15}/d_{33} ratios, where a significant shear component contributes to the d_{31} value, reducing their hydrostatic properties [108].
- **Extender ferroelectrics** have lower d_{15}/d_{33} ratios, with a smaller shear component affecting the d_{31} value, leading to higher piezoelectric anisotropy and hydrostatic coefficients.

By transforming to different coordinate systems (such as spherical coordinates), the orientational dependence of the piezoelectric coefficient can be calculated, as illustrated in Figure I.13 (an example from T.O. Hooper et al. [108]). The longitudinal charge coefficient (d_{33}^{*}) as a function of the angle away from the polar axis (θ) can be determined using Equation 9:

$$d_{33}^{*} = \cos\theta\,(d_{31}\sin 2\theta + d_{15}\sin 2\theta + d_{33}\cos 2\theta) \qquad (11)$$

Piezoelectric charge coefficient as a function of the angle away from the polar axis, calculated using Equation 9 for tetragonal single crystals by T.O. Hooper et al. [108].

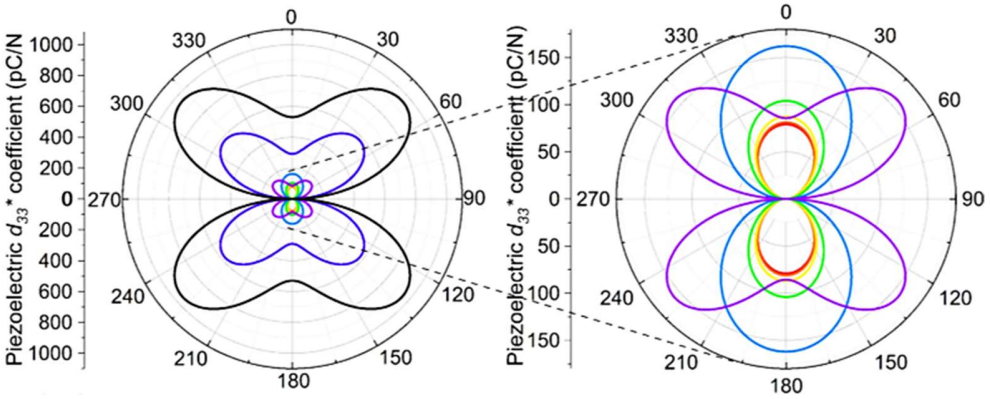

Figure I.13: Piezoelectric charge coefficient as a function of the angle away from the polar axis for tetragonal single crystals, calculated by T.O. Hooper et al. [108]. The d_{33}^{*} illustrates the distinction between rotator and extender behavior in tetragonal materials.

E. Poling Process

In polycrystalline materials, dipole arrangements vary among the different domains. Consequently, the random orientation of these dipoles results in a cancellation of their overall effect, leading to depolarization of the material. To achieve polarization, it is essential to orient the dipoles in a specific direction, which is accomplished through the poling process. Ferroelectric polycrystalline materials must undergo poling to be effectively used as piezoelectric materials. Electrical poling is a crucial procedure for ferroelectric piezoelectric materials, involving the application of a strong electric field across the material. This field causes the majority of domains to switch from their pristine polarization and align along the direction of the electric field. A schematic representation of the poling process is illustrated in Figure I.14.

If a material is not fully poled, even if the same material is used, the resulting piezoelectric properties—particularly the piezoelectric charge coefficient (d_{33})—will be significantly reduced. It is important to note that the poling process is not applicable to non-ferroelectric materials; thus, high-performance piezoelectric materials must be ferroelectric.

Several methods of poling are employed, including:

- DC electrode poling
- Corona discharge poling
- AC electrode poling

Among these, DC electrode poling and corona discharge poling are the most commonly utilized methods, while AC electrode poling has been introduced more recently.

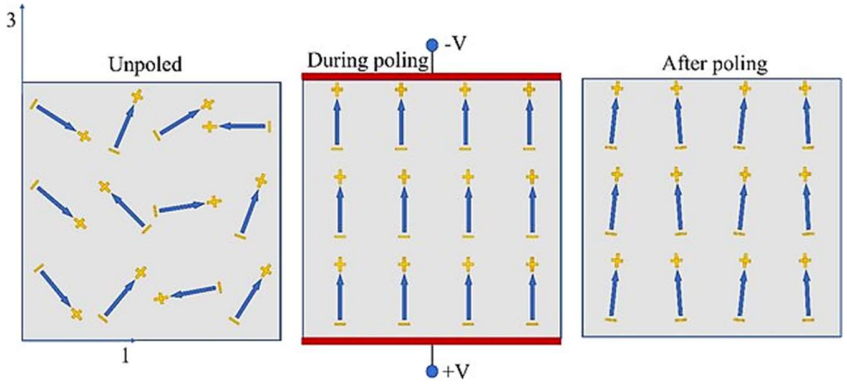

Figure I.14: Domain alignment mechanisms before, during, and after the poling process [109].

F. Electromechanical Coupling Factor (K^2)

The electromechanical coupling factor, denoted as K^2, is a key parameter that determines the effectiveness of piezoelectric materials in converting electrical energy into mechanical energy and vice versa in piezoelectric devices. It is expressed as:

$$k^2 = \frac{stored\ mechanical\ energy}{input\ electrical\ energy}\ or\ \ k^2 = \frac{stored\ electrical\ energy}{input\ mechanical\ energy}$$

G. Energy Transmission Coefficient (λ_{max})

The energy transmission coefficient λ_{max} represents the efficiency of energy transmission in piezoelectric devices. It is the ratio of output mechanical energy to input electrical energy, defined as:

$$\lambda_{max} = \frac{\text{output mechanical enegy}}{\text{input electrical energy}}$$

H. Mechanical Quality Factor (Q_M)

The mechanical quality factor (Q_M) describes the sharpness of the electromechanical resonance spectrum in piezoelectric devices. It is crucial for evaluating the magnitude of resonant displacement and strain, determining the efficiency of energy conversion.

I. Acoustic Impedance (Z)

Acoustic impedance (Z) assesses the transfer of acoustic energy between two materials. It is defined as:

$$Z^2 = \frac{pressure}{volume\ .velocity}$$

In solid materials, acoustic impedance is given by:

$$Z = \sqrt{\rho C}$$

Where ρ is the density, and C is the elastic stiffness of the material.

I.3.4.4.2. Piezoelectricity Technology Applications

The following diagram (Figure I.15) illustrates various applications of piezoelectricity. Piezoelectric devices can be classified into several key areas, including sensors, actuators, ultrasonic transducers, resonators and filters, transformers, energy harvesters, and more specialized sectors such as NEMS/MEMS systems, automotive technology, and piezo-based microrobots. Currently, there is significant interest in certain applications, owing to remarkable advancements that have enhanced device performance, providing both precision and convenience.

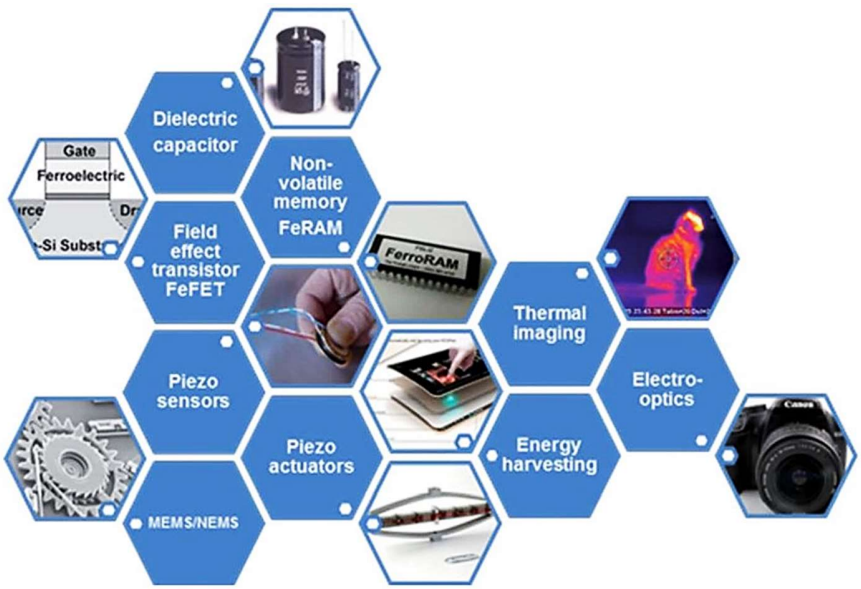

Figure I.15: Schematic of the diverse range of piezoelectricity applications [110].

- **NEMS/MEMS Systems**

  Magnetoelectric-based Nano- and Micro-Electromechanical Systems (NEMS/MEMS) have attracted considerable attention due to their wide range of innovative applications. These include RF front-end filters, infrared (IR) sensors, non-reciprocal microwave devices, microwave-quantum transducers, mechanical antennas, energy harvesters, and magnetic field sensors. These technologies are impacting sectors like communication, computing, healthcare, and defense [111–115]. The growing use of NEMS/MEMS in commercial electronics is propelling market growth, particularly with the adoption of the Internet of Things (IoT) and wearable medical devices for healthcare diagnostics and treatments [116, 117].

- **Automotive Technology**

  The automotive sector is currently one of the largest markets for piezoelectric products. Piezoelectric technologies are used in actuators, fuel injectors, sensors, and safety systems. Piezoelectric actuators adjust mirrors, lenses, and other automotive components by converting electrical signals into mechanical movement. Fuel injectors based on piezo technology provide greater accuracy, resulting in improved fuel efficiency and lower emissions. Other applications include fuel atomizers, keyless door entry systems, seat belt alerts, airbag sensors, airflow sensors, audible alarms, knock sensors, and tire pressure monitors [118].

- **Piezo-based Microrobots**

  Advances in precision manufacturing, leveraging piezoelectric properties, have led to the development of micro-robotic systems. These robots can operate in environments inaccessible to conventional robots. For example, piezo-based microrobots mimic biological systems, such as using tactile sensing similar to that of insects [119]. Piezoelectric sensors are also being explored for various applications, including in human health monitoring [120], which could further inspire innovations in microrobotics [121].

- **Medical Devices**

Piezoelectric biosensors, typically made from materials with high acoustic velocities, such as aluminum nitride (AlN), are capable of detecting a variety of molecules, microorganisms, and biological structures. These piezoceramic sensors exhibit high reproducibility, a linear response, and a low detection limit. AlN piezoelectric biosensors can effectively detect protein-ligand interactions and antigen-antibody binding [122]. Additionally, basic life functions such as breathing and pulse can be monitored using nanowire-shaped piezoelectric sensors made from highly aligned polyvinylidene fluoride-trifluoroethylene (P(VDF–TrFE)), which offers excellent sensitivity [123]. Piezoelectric energy harvesting systems are also ideal candidates for biomedical electronics [124, 125]. Various piezo-energy harvesters constructed from materials such as lead magnesium niobate-lead titanate (PMN-PT), zinc oxide (ZnO), lead zirconate titanate (PZT), and barium titanate ($BaTiO_3$) have been developed to capture and store energy from heartbeats, organ movements, body movements, and other mechanical deformations [126]. Due to their unique properties, nanogenerators based on piezoelectric materials such as gallium nitride (GaN) and zinc oxide (ZnO) are increasingly used as biomechanical energy harvesters [127]. Many applications of piezoelectric technology in the medical field can be developed using smart piezoelectric materials to design and enhance medical devices. A deeper understanding of piezoelectricity is essential for addressing future challenges in the medical industry.

I.4. Categories of Piezoelectric Materials

The piezoelectric effect occurs in non-centrosymmetric materials, which are of significant interest due to their inherent electric polarization properties. This polarization arises from the application of stress or strain in conjunction with an electric field. The piezoelectric materials can be classified along with the in the diagram shown in Figure I.16.

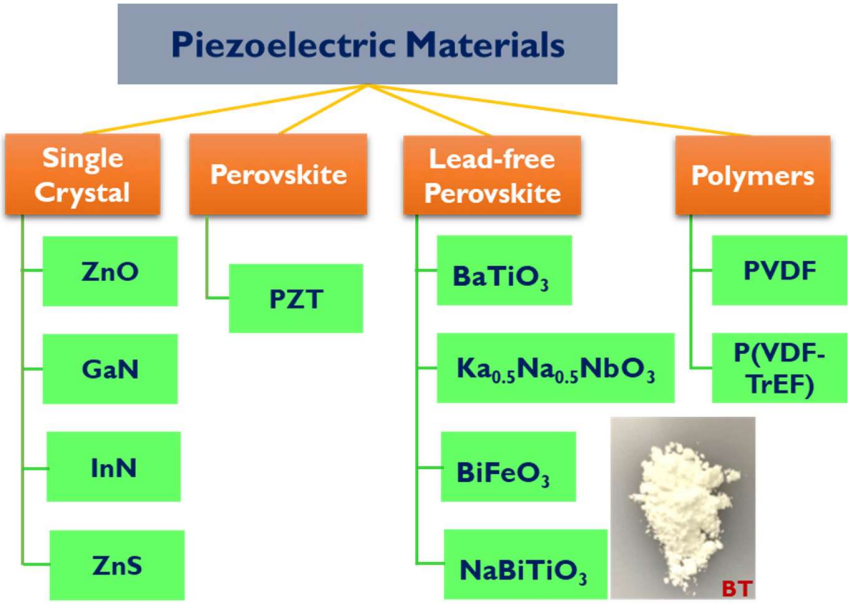

Figure I.16: Illustration of the categories of piezoelectric materials [128]. The inset image shows barium titanate (BT) in powder form.

Some examples of these piezoelectric materials, include:

- **Piezoceramics**

  Piezoceramics are the most widely used piezoelectric materials in the technology industry, occupying the largest share of the piezoelectric devices market [103], like Potassium niobate ($KNbO_3$), barium titanate ($BaTiO_3$), lead zirconate titanate (PZT), bismuth ferrite ($BiFeO_3$), etc.. Their cost-effectiveness and adaptability to specific applications have made them a focal point for researchers. Piezoceramics can be categorized based on their form of use: single crystals, polycrystalline materials, and thin films.

- **Polymers**

  Cellulose and its derivatives, polylactic acid (PLA), polyvinylidene fluoride (PVDF), etc.

- **Materials Based on Single Crystals**

  Single crystals offer advantages over polycrystalline ceramics, primarily due to the absence of grain boundaries and the potential for non-ferroelectric piezoelectricity. The piezoelectric activity in single crystals differs from that in polycrystalline materials of the

same composition. For instance, $Ba(Ti_{0.8}Zr_{0.2})O_3$–$(Ba_{0.7}Ca_{0.3})TiO_3$ was recently reported by Liu et al. [129] to have a d_{33} greater than 620 pC/N in polycrystalline form, while predictions suggest that single crystals could achieve d_{33} values of up to 2000 pC/N. Other notable single crystal piezoelectric materials include quartz ($d_{11} \sim 2.3$ pC/N) [130–133], $LiTaO_3$ [132], $GaPO_4$ [134], and members of the Langasite family [132]. The d_{33} value of $Li_2B_4O_7$ is reported as 19.5 pC/N [135], while $BaTiO_3$ has a d_{33} of approximately 86 pC/N [133], which is significantly lower than its polycrystalline counterpart. Relaxor-based perovskite ferroelectrics, such as single crystals of PMN-PT, exhibit remarkable piezoelectric coefficients exceeding 2.000 pC/N and electromechanical coupling factors greater than 0.9, far surpassing PZT ceramics [136].

- **Materials Based on Polycrystalline**

For polycrystalline materials to exhibit piezoelectricity, they must be ferroelectric through a process known as "poling." Generally, piezoelectric coefficients in ferroelectrics are higher than in non-ferroelectrics. For instance, in perovskites, the d_{33} value can reach 160 pC/N for $K_{0.5}Na_{0.5}NbO_3$ (KNN) [137] and 190 pC/N for $BaTiO_3$ (BT) [133], while non-ferroelectric single crystal AlN has a d_{33} of only 6.5 pC/N [133], and $Ba_2TiSi_2O_8$ has a d_{33} of approximately 17.5 pC/N [133]. Important polycrystalline piezoceramic materials include solid solutions of $PbZrO_3$, $PbTiO_3$, and $(Pb(Zr,Ti)O_3$ or PZT), which exhibit a high piezoelectric response of 410 pC/N [138]; however, they are limited by their maximum operating temperature of 250°C. Recently, some perovskite single crystals have demonstrated superior piezoelectric properties compared to PZT [139]. Due to their easier and less expensive preparation, ferroelectric perovskites in polycrystalline form are widely used in various piezoelectric applications [140, 141].

- **Materials Based on Thin Films**

Both aluminum nitride (AlN) and zinc oxide (ZnO) are simple binary compounds with a Wurtzite structure, and their thin films are widely employed in bulk acoustic wave (BAW) and surface acoustic wave (SAW) devices. However, the performance of these Wurtzite-based devices is limited due to their low piezoelectric coupling. PZT thin films, on the other hand, exhibit higher piezoelectric properties and are used in micro-transducers and

micro-actuators [141]. Although AlN and ZnO have much higher mechanical quality factors than PZT, they are easier to grow in thin film form compared to $LiNbO_3$. The defect dynamics and grain boundaries within polycrystalline perovskite thin films pose significant challenges for improving the efficiency and stability of devices [142]. The use of relatively simple Wurtzite materials facilitates integration and process compatibility with the rest of the device, as the strong polarity of the Wurtzite structure allows for polar growth and a stable piezoelectric response over time, while ferroelectrics always face the risk of depoling [103].

I.6. Conclusion

In conclusion, this chapter has provided a comprehensive overview of the structural characteristics of perovskite and III-V semiconductors, with a particular focus on $Na_{0.5}Bi_{0.5}TiO_3$ (NBT) and $YxAl_1-xN$. These materials were chosen due to their exceptional properties such as environmental compliance, high thermal conductivity, and enhanced piezoelectric performance, which made it promising materials for future green energy including manufacturing high-performance piezoelectric devices and developing high power thermoelectric generators. We also taken insight into the physical properties, including thermoelectric and piezoelectric properties, and their broad range of technological applications. To investigate the physical properties of the selected materials, we utilized software packages such as WIEN2K and CASTEP, as detailed in Chapters 3 and 4. The subsequent chapter will delve into these Density Functional Theory (DFT) codes, exploring their programming aspects and mathematical frameworks.

References

[1] J. Bjurström, I. Katardjiev, V. Yantchev, Lateral-field-excited thin-film Lamb wave resonator, Appl. Phys. Lett. 86 (2005) 154103, https://doi.org/10.1063/1.1900312.

[2] C.E. Dreyer, A. Janotti, C.G. Van de Walle, and D. Vanderbilt, Correct implementation of polarization constants in wurtzite materials and impact on III-Nitrides, Phys. Rev. X 6 (2016) 021038, https://doi.org/10.1103/PhysRevX.6.021038.

[3] C.-M. Lin, Y.-Y. Chen, V.V. Felmetsger, D.G. Senesky, and A.P. Pisano, AlN/3C–SiC composite plate enabling high-frequency and high-q micromechanical resonators, Adv. Mater. 24 (2012) 2722–2727, https://doi.org/10.1002/adma.201104842.

[4] C.-M. Lin, T.-T. Wu, Y.-Y. Chen, T.-T. Chou, AlN/3C–SiC Composite plate enabling high-frequency and high-q micromechanical resonators, J. Mech. 23 (2007) 253, https://doi.org/10.1002/adma.201104842.

[5] K. Karch, F. Bechstedt, Ab initio lattice dynamics of BN and AlN: Covalent versus ionic forces, Physical Review B 56 (1997) 7404–7415, https://doi.org/10.1103/PhysRevB.56.7404.

[6] Y. Calahorra, X. Guan, N. N. Halder, M. Smith, S. Cohen, D. Ritter, ... S. Kar-Narayan, Exploring piezoelectric properties of III–V nanowires using piezo-response force microscopy, Semiconductor Science and Technology 32 (2017) 074006, https://doi.org/10.1088/1361-6641/aa6c85.

[7] Dahal, Rajendra Prasad. Fabrication and characterization of III-nitride nanophotonic devices. Kansas State University, 2009.

[8] S. Adachi, Properties of Group-IV, III–V and II–VI Semiconductors, John Wiley & Sons Ltd., Chichester, UK, 2005.

[9] F. Bernardini, V. Fiorentini, D. Vanderbilt, Spontaneous polarization and piezoelectric constants of III-V nitrides, Phys. Rev. B 56(16) (1997) R10024–R10027, https://doi.org/10.1103/PhysRevB.56.R10024.

[10] A. Zoroddu, F. Bernardini, P. Ruggerone, V. Fiorentini, First-principles prediction of structure, energetics, formation enthalpy, elastic constants, polarization, and piezoelectric constants of AlN, GaN, and InN, Phys. Rev. B 64(4) (2001), https://doi.org/10.1103/PhysRevB.64.045208.

[11] O. Ambacher, J. Smart, J. R. Shealy, N. G. Weimann, K. Chu, M. Murphy, ... J. Hilsenbeck, Two-dimensional electron gases induced by spontaneous and piezoelectric polarization charges in N- and Ga-face AlGaN/GaN heterostructures, Journal of Applied Physics 85(6) (1999) 3222–3233, https://doi.org/10.1063/1.369664.

[12] M.-A. Dubois, P. Muralt, Properties of aluminum nitride thin films for piezoelectric transducers and microwave filter applications, Applied Physics Letters 74(20) (1999) 3032–3034, https://doi.org/10.1063/1.124055.

[13] O. Ambacher, J. Majewski, C. Miskys, A. Link, M. Hermann, M. Eickhoff, ... L. F. Eastman, Pyroelectric properties of Al(In)GaN/GaN hetero- and quantum well structures, Journal of Physics: Condensed Matter 14(13) (2002) 3399–3434, https://doi.org/10.1088/0953-8984/14/13/302.

[14] J. S. Speck, S. F. Chichibu, Nonpolar and Semipolar Group III Nitride-Based Materials, MRS Bulletin 34(05) (2009) 304–312, https://doi.org/10.1557/mrs2009.91.

[15] R. Resta, Macroscopic polarization in crystalline dielectrics: the geometric phase approach, Rev. Mod. Phys. 66 (1994) 899.

[16] R. Resta, D. Vanderbilt, Theory of Polarization: A Modern Approach, Top. Appl. Phys., 105 (2007).

[17] A.M. Alsaad, I.A. Qattan, A.A. Ahmad, A. Ababneh, Z. Albataineh, I.A. Aljarrah, A. Telfah, Measurement and ab initio investigation of structural, electronic, optical, and mechanical properties of sputtered aluminum nitride thin films, Frontiers in Physics 8 (2020) 115, https://doi.org/10.3389/fphy.2020.00115.

[18] H. Morkoc, Handbook of Nitride Semiconductors and Devices, Vol. 1: Materials Properties, Physics and Growth (Wiley-VCH, 2008).

[19] N. Matsunami, H. Kakiuchida, M. Sataka, and S. Okayasu, XRD characterization of AlN thin films prepared by reactive RF-sputter deposition, Advances in Materials Physics and Chemistry 3(2013) 101, https://doi.org/10.4236/ampc.2013.31A012.

[20] K. Hasegawa, K. Inagawaand M. Koshiba, Coefficients of coupled-mode equations for a natural-single-phase-unidirectional transducer and an electrode-width-difference-reversal-of-directivity transducer on a 50° Y-24° X $La_3Ga_5SiO_{14}$ Substrat, Jpn. J. Appl. Phys. 39 (2000) 3020, https://doi.org/10.1143/JJAP.39.3020.

[21] C.E. Dreyer, A. Janotti, C.G. Van de Walle, and D. Vanderbilt, Correct Implementation of polarization constants in wurtzite materials and impact on III-Nitrides, Phys. Rev. X6 (2016) 021038, https://doi.org/10.1103/PhysRevX.6.021038.
[22] C.-M. Lin, Y.-Y. Chen, V.V. Felmetsger, D.G. Senesky, and A.P. Pisano, AlN/3C–SiC Composite plate enabling high-frequency and high-Q micromechanical resonators, Adv. Mater. 24 (2012) 2722–2727, https://doi.org/10.1002/adma.201104842.
[23] N.B. Sedrine, A. Zukauskaite, J. Birch, J. Jensen, L. Hultman, S. Schöche, M. Schubert and V. Darakchieva, Infrared dielectric functions and optical phonons of wurtzite $Y_xAl_{1-x}N$ ($0 \leqslant x \leqslant 0.22$), J. Phys. D: Appl. Phys. 48 (2015) 415102, https://doi.org/10.1088/0022-3727/48/41/415102.
[24] S. Adachi, Properties of Group-IV, III–V and II–VI Semiconductors, John Wiley & Sons Ltd., Chichester, UK, 2005.
[25] C.N Zoita, M. Braic and V. Braic, Structural, optical and electronic properties of $In_{1-x}Y_xN$ thin films, Dig. J. Nanomater. Biostruct. 6(2011) 1877–86.
[26] A. Assali, F. Laidoudi, R. Serhane, F. Kanouni, O. Mezilet, highly enhanced electro-acoustic properties of YAlN/sapphire based surface acoustic wave devices for next generation of microelectromechanical systems, Mater. Today Commun. 26 (2021), 102067, https://doi.org/10.1016/j.mtcomm.2021.102067.
[27] P.M. Mayrhofer, H. Riedl, H. Euchner, M. Stöger-Pollach, P.H. Mayrhofer, A. Bittner, Microstructure and piezoelectric response of $Y_xAl_{1-x}N$ thin films, Acta Materialia 100 (2015) 81–89, https://doi.org/10.1016/j.actamat.2015.08.019.
[28] D.I. Bilc, R. Orlando, R. Shaltaf, G.-M. Rignanese, J. Íñiguez, and P. Ghosez, Hybrid exchange-correlation functional for accurate prediction of the electronic and structural properties of ferroelectric oxides, Phys. Rev. 77 (2008) 165107, https://doi.org/10.1103/PhysRevB.77.165107.
[29] A. Žukauskaite, C. Tholander, J. Palisaitis, P.O. Persson, V. Darakchieva, N. Ben Sedrine, F. Tasnádi, B. Alling, J. Birch, L. Hultman, $Y_xAl_{1-x}N$ thin films, J. Phys. D. Appl. Phys. 45 (2012) 422001, https://doi.org/10.1088/0022-3727/45/42/422001.
[30] A. Zukauskaite, G. Wingqvist, J. Palisaitis, J. Jensen, Per O. A. Persson, R. Matloub, P. Muralt, Y. Kim, J. Birch, and L. Hultman, Microstructure and dielectric properties of piezoelectric magnetron sputtered w-$Sc_xAl_{1-x}N$ thin films, Journal of Applied Physics 111 (2012) 093527, https://doi.org/10.1063/1.4714220
[31] S. Pandit, M. Schneider, C. Berger, S. Schwarz, U. Schmid, Impact of AlN Seed Layer on Microstructure and Piezoelectric Properties of YxAl1−xN (x = 15%) Thin Films, Adv. Electron. Mater. 9 (2023) 2200789, https://doi.org/10.1002/aelm.202200789.
[32] F. Kanouni, S. Amara, A. Assali, F. Arab, Z. Qin, A P-matrix-based model for the frequency analysis of IDT/AlScN/Sapphire SAW-delay line, Sensors and Actuators A 307 (2020) 111980, https://doi.org/10.1016/j.sna.2020.111980.
[33] S. Manna, K.R. Talley, P. Gorai, J. Mangum, A. Zakutayev, G.L. Brennecka, V. Stevanović, and C.V. Ciobanu, Enhanced Piezoelectric Response of AlN via CrN Alloying, Phys. Rev. Appl. 9 (2018) 34026, https://doi.org/10.1103/PhysRevApplied.9.034026.
[34] M. Akiyama, T. Kamohara, K. Kano, A. Teshigahara, Y. Takeuchi, N. Kawahara, Enhancement of piezoelectric response in scandium aluminum nitride alloy thin films prepared by dual reactive cosputtering, Adv. Mater. 21 (2009) 593, https://doi.org/10.1002/adma.200802611.
[35] Y. Lu, M. Reusch, N. Kurz, A. Ding, T. Christoph, M. Prescher, L. Kirste, O. Ambacher, A. Žukauskaitė, Elastic modulus and coefficient of thermal expansion of piezoelectric Al1−xScxN (up to x = 0.41) thin films, Appl. Mater. 6 (2018) 076105, https://doi.org/10.1063/1.5040190.
[36] A. Kochhar, Y. Yamamoto, A. Teshigahara, K.-y. Hashimoto, S. Tanaka and M. Esashi, Wave propagation direction and c-axistilt angle influence on the performance of ScAlN/Sapphire-based SAW devices, IEEE Transactions on Ultrasonics, Ferroelectrics, and Frequency Control 63 (2016) 7, https://doi.org/10.1109/TUFFC.2016.2539226.
[37] P. Panda, R. Ramaseshan, S. Tripura Sundari, and H. Suematsu, Anisotropic optical properties of a-axis AlN films: a spectroscopic ellipsometry study, OSA Continuum 1(4) (2018) 1241–1250, https://doi.org/10.1364/OSAC.1.001241.
[38] V. Chivukula, D. Ciplys, A. Sereika, M. Shur, J. Yang, and R. Gaska, AlGaN based highly sensitive radio-frequency UV sensor, Appl. Phys. Lett. 96(2010) 163504, https://doi.org/10.1063/1.3405692.
[39] K. Hashimoto, RF Bulk Acoustic Wave Filters for Communications, Artech House Microwave Library, Norwood, MA, 2009.

[40] V. Fuflyigin, H. Jiang, F.Wang, P. Yip, P. Vakhutinsky, J. Zhao, Sol-Gel Synthesis of $BaTiO_3$ Based Films for Photonic Applications, Mater. Res. Soc. 606 (2000) 169, https://doi.org/10.1557/PROC-606-169.
[41] D.Y. Kim, S.E. Moon, E.K. Kim, S.J. Lee, J.J. Choi, H.E. Kim, Electro-Optic Characteristics Of (001)-Oriented $Ba_{0.6}Sr_{0.4}tio_3$ Thin Films, Appl. Phys. Lett. 82 (2003) 1455, https://doi.org/10.1063/1.1556962.
[42] J.F. Scott, A.Q. Jiang, S.A.T. Redfern, M. Zhang, M. Dawber, Infrared Spectra And Second-Harmonic Generation In Barium Strontium Titanate And Lead Zirconate-Titanate Thin Films:"Polaron" Artifacts, J. Appl. Phys. 94 (2003) 3333, https://doi.org/10.1063/1.1596715.
[43] D. Damjanovic, Contributions to the Piezoelectric Effect in Ferroelectric Single Crystals and Ceramics, Journal of the American Ceramic society 88 (2005) 2663–2676, https://doi.org/10.1111/j.1551-2916.2005.00671.xT.
[44] Takenaka and H. Nagata,Current Status and Prospects of Lead-Free Piezoelectric Ceramics, Journal of the European Ceramic Society 25 (2005) 2693-2700, https://doi.org/10.1016/j.jeurceramsoc.2005.03.125.
[45] T.R. Shrout and S.J. Zhang: Lead-Free Piezoelectric Ceramics: Alternatives for PZT? J. Electroceram. 19 (2007) 111, https://doi.org/10.1007/s10832-007-9047-0.
[46] J. Wu, Perovskite Lead-Free Piezoelectric Ceramics, Journal of Applied Physics 127 (2020) 190901, https://doi.org/10.1063/5.0006261.
[47] H. Mgbemere, G. Schneider, M. Hoelzel and M. Hintersteind, Neutron diffraction study of $(K_xNa_{1-x})NbO_3$-based ceramics from low to high temperatures, Journal of applied crystallography, 49 (2016) 891–901, http://dx.doi.org/10.1107/S1600576716005197.
[48] Y. Guan, S. Fukao, K. Ito, Y. Nakanishi, Y. Sato, Y. Ito, & S. Yoshikado, Improvement of Compact X-Rays Source Using Uniaxially Polarized $LiNbO_3$ Single Crystal, Key Engineering Materials 445 (2010) 43–46, https://doi.org/10.4028/www.scientific.net/kem.445.43.
[49] D.Y. Zhang, D. Yin, W. Qian, K. Li, and J.S. Xie, Ferroelectric Property of Ion Beam Enhanced Deposited Lithium Tantalate Thin Film, Advanced Materials Research 335–336 (2011) 1418–23, https://doi.org/10.4028/www.scientific.net/amr.335-336.1418.
[50] S.S. Parizi, A. Mellinger, and G. Garuntu, Ferroelectric Barium Titanate Nanocubes as Capacitive Building Blocks for Energy Storage Applications, ACS Appl. Mater. Interfaces. 6 (2014) 17506, https://doi.org/10.1021/am502547h.
[51] S.S. Gevorgian, A.K. Tagantsev, and A.K. Vorobiev, Tuneable Film Bulk Acoustic Wave Resonators, Springer, 2013.
[52] K. Uchino, The development of piezoelectric materials and the new perspective, in Advanced Piezoelectric Materials (Second Edition), pages 1–92, Elsevier, 2017.
[53] R. Roukos, Phase transitions in complex oxides of perovskite structure: case of the system (1-x)Na0.5Bi0.5TiO3 -xCaTiO3, Thesis, University of Burgundy, France, 2015.
[54] Y. Benaissa Cherif, Magnetic Structures of ABC3-type Perovskites Study of the first principle, Thesis, University of Mostaganem, Algeria, 2016.
[55] H.U. Habermeier, Thin films of perovskite-type complex oxides, Materials Today 10(10) (2007) 34-43, https://doi.org/10.1016/S1369-7021(07)70243-2.
[56] F. Bouchareb, Etude ab-initio des propriétés électroniques et magnétiques de l'hétérostructure SrMnO3/SrVO3 , thesis University of Tlemcen, Algeria, 2017.
[57] G.A. Smolenskii, V.A. Isupov, A.I. Agranovskaya, and N.N. Krainik, New Ferroelectrics of Complex Composition IV, Sov. Phys. Solid. State. 2 (1961) 2651–2654.
[58] M. Spreitzer, M. Valant, and D. Suvorov, Sodium Deficiency in $Na_{0.5}Bi_{0.5}TiO_3$, J. Mater. Chem. 17 (2007) 185–192, https://doi.org/10.1039/B609606A.
[59] Y. Hiruma, H. Nagata, and T. Takenaka, Thermal Depoling Process and Piezoelectric Properties of Bismuth Sodium Titanate Ceramics, Journal of Applied Physics 105 (2009) 084112, https://doi.org/10.1063/1.3115409.
[60] N. Yasuda, S. Hashimoto, H. Ohwa, O. Sakurada, K. Fujita, Y. Yamashita, M. Iwata, and Y. Ishibashi, Electrical properties of lead-free relaxor ferroelectric solid solution single crystal (Na1/2Bi1/2)TiO3–BaTiO3 grown by Bridgman method, Japanese Journal of Applied Physics 48 (2009) 09KC06, https://doi.org/10.1143/JJAP.48.09KC06.
[61] H. Qi and R. Zuo, Linear-Like Lead-Free Relaxor Antiferroelectric (Bi0.5Na0.5) TiO3–NaNbO3 with Giant Energy-Storage Density/Efficiency And Super Stability Against Temperature And Frequency. Journal of Materials Chemistry A 7 (2019) 3971–3978, https://doi.org/10.1039/C8TA12232F.

[62] J. Yin, Y. Zhang, X. Lv, and J.G. Wu, Ultrahigh Energy-Storage Potential Under Low Electric Field In Bismuth Sodium Titanate-Based Perovskite Ferroelectrics, Journal of Materials Chemistry A 6 (2018) 9823–9832, https://doi.org/10.1039/C8TA00474A.

[63] T. Zheng, J. Wu, D. Xiao, J. Zhu, Recent Development in Lead-Free Perovskite Piezoelectric Bulk Materials, Progress in Materials Science 98 (2018) 552–624, https://doi.org/10.1016/j.pmatsci.2018.06.002

[64] G.O. Jones and P.A. Thomas, Investigation of The Structure and Phase Transitions in the Novel A-Site Substituted Distorted Perovskite Compound $Na_{0.5}Bi_{0.5}TiO_3$, Acta Crystallographica Section B: Structural Science 58 (2002) 168–178, https://doi.org/10.1107/S0108768101020845.

[65] G. Xu, Z. Duan, X. Wang, & D. Yang, Growth And Some Electrical Properties of Lead-Free Piezoelectric Crystals (Na1/2Bi1/2)TiO3 and (Na1/2Bi1/2)TiO3–BaTiO3 Prepared by a Bridgman Method, Journal of Crystal Growth 275 (2005) 113–119, https://doi.org/10.1016/j.jcrysgro.2004.10.074.

[66] W. Ge, H. Liu, X. Zhao, W. Zhong, X. Pan, T. He, et al., Growth, Optical and Electrical Properties of Pure and Mn-doped Na0.5Bi0.5TiO3 Lead-Free Piezoelectric Crystals, Journal of Alloys and Compounds 462 (2008) 256–261, https://doi.org/10.1016/j.jallcom.2007.08.006.

[67] Y. Wang, Z. Wang, H. Xu, & D. Li, Properties of (1−x)Bi0.5Na0.5TiO3–xSrTiO3 Ferroelectric Thin Films Prepared by Metalorganic Solution Deposition, Journal of Alloys and Compounds 484 (2009) 230–232, https://doi.org/10.1016/j.jallcom.2009.03.172.

[68] C.He, Y. Zhang, L. Sun, J. Wang, T. Wu, F. Xu, et al., Electrical and Optical Properties of Nd3+-doped Na0. 5Bi0.5TiO3 Ferroelectric Single Crystal, Journal of Physics D: Applied Physics, 46 (2013) 245104, https://doi.org/10.1088/0022-3727/46/24/245104.

[69] M. Bousquet, J.-R. Duclère, E. Orhan, A. Boulle, C. Bachelet, et al., Optical Properties of an Epitaxial Na0.5Bi0.5TiO3 Thin Film Grown by Laser Ablation: Experimental Approach And Density Functional Theory Calculations, Journal of Applied Physics 107 (2010) 104107, https://doi.org/10.1063/1.3400095

[70] L.T.H.Thanh, N.B. Doan, L.H. Bac, D.V. Thiet, S. Cho, P.Q. Bao, & D.D. Dung, Making Room-Temperature Ferromagnetism in Lead-Free Ferroelectric Bi0.5Na0.5TiO3 Material. Materials Letters 186 (2017) 239–242, https://doi.org/10.1016/j.matlet.2016.09.105.

[71] S.B. Vakrushev, B.G. Ivanitsky, B.E. Kvyatkovsky, A.N. Maystrenko, R.S. Malysheva, N.M. Okuneva, N.N. Parfenova, Sov. Phys. Solid State 25 (1983) 1504.

[72] I.G. Siny, C.-S. Tu, V.H. Schmidt, Critical acoustic behavior of the relaxor ferroelectric Na1/2Bi1/2TiO3 in the intertransition region, Phys. Rev. B 51 (1995) 5659–5665, https://doi.org/10.1103/PhysRevB.51.5659.

[73] G.O. Jones, P.A. Thomas, The tetragonal phase of Na0.5Bi0.5TiO3–a new variant of the perovskite structure, Acta Crystallogr. Sect. B Struct. Sci. 56 (2000) 426–430, https://doi.org/10.1107/S0108768100001166.

[74] A. O'Brien, D.I. Woodward, K. Sardar, R.I. Walton, P.A. Thomas, Inference of oxygen vacancies in hydrothermal Na0.5Bi0.5TiO3, Appl. Phys. Lett. 101 (2012), 142902, https://doi.org/10.1063/1.4755882.

[75] E. Aksel, J.L. Jones, Advances in Lead-Free Piezoelectric Materials for Sensors and Actuators, Sensors 10 (2010) 1935-1954, https://doi.org/10.3390/s100301935.

[76] M.K. Niranjan, T. Karthik, S. Asthana, J. Pan, and Umesh V. Waghmare, Theoretical and Experimental Investigation of Raman Modes, Ferroelectric and Dielectric Properties of Relaxor $Na_{0.5}Bi_{0.5}TiO_3$, Journal of Applied Physics 113 (2013) 194106, https://doi.org/10.1063/1.4804940.

[77] B. Andriyevsky, J. Suchanicz, C. Cobet, A. Patryn, N. Esser and B. Kosturek, Manifestation of Phase Transformations in Optical Spectra of $Na_{0.5}Bi_{0.5}TiO_3$ Crystals Between 25°C and 350°C, Phase Transitions: A Multinational Journal 82 (2009) 567–575, http://dx.doi.org/10.1080/01411590903092899.

[78] D.K. Khatua, T. Mehrotra, A. Mishr, B. Majumdar, A. Senyshyn, R. Ranjan, Anomalous influence of grain size on the global structure, ferroelectric and piezoelectric response of Na0.5Bi0.5TiO3, Acta Mater. 134 (2017) 177–187, https://doi.org/10.1016/j.actamat.2017.05.068.

[79] Y. Takagi, H. Nagata, T. Takenaka, Effects of quenching on bending strength and piezoelectric properties of (Bi0.5Na0.5)TiO3 Ceramics, J. Asian Ceram. Soc. (2020), https://doi.org/10.1080/21870764.2020.1732020.

[80] V. M. Goldshmidt, Geochemische Verteilungsgesetetze de Element VII, VIII, (1927/1928).

[81] J.B. Philipp, P. Majewski, L. Alff, A. Erb, R. Gross, Structural and doping effects in the half-metallic double perovskite A2CrWO6 (A=Sr, Ba, and Ca), Phys. Rev. B 68(13) (2003), https://doi.org/10.1103/PhysRevB.68.144431.

[82] K. S. Song, H. Xing-Cui, S-D. Kim, S-K. Kang, Catalytic combustion of CH_4 and CO on $La_{1-x}M_xMnO_3$ perovskites, Catal. Today 47 (1999) 155, https://doi.org/10.1016/S0920-5861(98)00295-8.

[83] H. Mohammed, Study of the Structural, Optoelectronic and Thermodynamic properties of Perovskites and Double Perovskites materials based on halogens, Thesis, University of Mostaganem, Algeria, (2019).
[84] S. C. Miller, W. F. Love, Tables of Irreducible Representations of Space Groups, (1967).
[85] Pauling, The nature of chemical bonds. Cornell University Press, New York, (1967): p. 267.
[86] M. Matson, A.W. Orbaek. Inorganic Chemistry for Dummies. John Wiley & Sons, 2013.
[87] Y. Inaguma, J.H. Sohn, I.S. Kim, M. Itoh, T. Nakamura, Quantum paraelectricity in a perovskite La1/2Na1/2TiO3, Journal of the Physical Society of Japan 61 (1992) 3831-3832, https://doi.org/10.1143/JPSJ.61.3831.
[88] S. Gupta, D. Maurya, A. Pramanick, D. Viehland, Introduction to ferroelectrics and related materials, in Ferroelectric Materials for Energy Harvesting and Storage, Woodhead Publishing Series in Electronic and Optical Materials, (2021), Pages 1-41, ISBN 9780081028025, https://doi.org/10.1016/B978-0-08-102802-5.00001-7.
[89] F. Jona, G. Shirane, Ferroelectric crystals, Volume 1, Pergamon, 1962.
[90] B. Jaffe, Piezoelectric ceramics, Volume 3, Elsevier, 2012.
[91] R. Wördenweber, Ferroelectric thin layers, in Comprehensive Semiconductor Science and Technology (2011) 177–205, https://doi.org/10.1016/b978-0-44-453153-7.00096-1.
[92] S. Rong, B. Faheem, Y. Li, Perovskite single crystals: synthesis, properties, and applications, Journal of Electronic Science and Technology 19 (2021) 100081, https://doi.org/10.1016/j.jnlest.2021.100081.
[93] K. Hashimoto, RF bulk acoustic wave filters for communications, Artech House Microwave Library, Norwood, MA, 2009.
[94] A.E. Crawford, Lead zirconate-titanate piezoelectric ceramics, British Journal of Applied Physics 12 (1961) 529.
[95] S. Trolier-McKinstry, P. Muralt, Thin film piezoelectrics for MEMS, Journal of Electroceramics 12 (2004) 7–17.
[96] NASA, Radioisotope power systems for space exploration (2011), NASA facts.
[97] New horizons mission powered by space radioisotope power systems, https://www.energy.gov/ne/articles/new-horizons-mission-powered-space-radioisotope-power-systems.
[98] R. R. Furlong and E. J. Wahlquist, Nuclear News 42, 2635 (1999).
[99] G. J. Snyder, The Electrochemical Society Interface p. 54 (2008), and there in references.
[100] D. Dat Thanh, Electronic structure and thermoelectric properties of narrow band gap semiconductors and pseudo-gap systems, Thesis, Michigan State University, (2013), ISBN 9781303348013, https://doi.org/10.25335/M58X2M.
[101] Ambrosi, R. M., Williams, H., Watkinson, E. J., Barco, A., Mesalam, R., Crawford, T., … Foxcroft, B. (2019). European Radioisotope Thermoelectric Generators (RTGs) and Radioisotope Heater Units (RHUs) for Space Science and Exploration. Space Science Reviews, 215(8). doi:10.1007/s11214-019-0623-9.
[102] D. Palaporn, S. A .Tanusilp, Y. Sun, S. Pinitsoontorn, & K. Kurosaki. Thermoelectric materials for radioisotope thermoelectric generators. Materials Advances , 2024, 5, 5351. DOI:10.1039/D4MA00309H.
[103] S. Manna, Design and Discovery of New Piezoelectric Materials Using Density Functional Theory, Thesis, Department of Mechanical Engineering, Colorado, USA, 2018.
[104] M. Saidi, Effets des conditions de synthèse sur les propriétés diélectriques, ferroélectriques et piézoélectriques de la composition (Na0.535 K0.480)0.966Li0.058O3, Thèse, Université Mouloud Mammeri, Tizi-Ouzou, 2017.
[105] J.A. Hooper, Ab-Initio Studies into Intrinsic Piezoelectric Properties, University of Leeds, Thesis (2018).
[106] N. Sezer, M. Koç, A comprehensive review on the state-of-the-art of piezoelectric energy harvesting, Nano Energy 80 (2021) 105567, https://doi.org/10.1016/j.nanoen.2020.105567.
[107] H. Liu, J. Zhong, C. Lee, S.W. Lee, L. Lin, A comprehensive review on piezoelectric energy harvesting technology: materials, mechanisms, and applications, Applied Physics Reviews 5 (4) (2018) 041306, https://doi.org/10.1063/1.5074184.
[108] T.O. Hooper, J.I. Roscow, A. Mathieson, H. Khanbareh, A.J. Goetze-Barral, and A.J. Bell, High voltage coefficient piezoelectric materials and their applications, Journal of the European Ceramic Society (2021), ISSN 0955-2219, https://doi.org/10.1016/j.jeurceramsoc.2021.06.022.

[109] S. Sharma, et al., Design of spatially varying electrical poling for enhanced piezoelectricity in Pb(Mg1/3Nb2/3)O3–0.35PbTiO3, Int. J. Mech. Mater. Des., 2021, 17(1), 99–118, https://doi.org/10.1007/s10999-020-09514-w.

[110] J. Varghese, R.W. Whatmore, J.D. Holmes, Ferroelectric nanoparticles, wires and tubes: synthesis, characterization and applications, Journal of Materials Chemistry C 1 (2013) 2618-2638, https://doi.org/10.1039/C3TC00597F.

[111] J. Zhu, X. Liu, Q. Shi, T. He, Z. Sun, X. Guo, W. Liu, O.B. Sulaiman, B. Dong, and C. Lee, Development Trends and Perspectives of Future Sensors and MEMS/NEMS, Micromachines 11 (2020) 7, https://doi.org/10.3390/mi11010007.

[112] L. Wei, X. Kuai, Y. Bao, J. Wei, L. Yang, P. Song, M. Zhang, F. Yang, and X. Wang, The Recent Progress of MEMS/NEMS Resonators, Micromachines 12 (2021) 724, https://doi.org/10.3390/mi12060724.

[113] X. Liang, A. Matyushov, P. Hayes, V. Schell, C. Dong, H. Chen, Y. He, A. Will-Cole, E. Quandt, P. Martins, Roadmap on Magnetoelectric Materials and Devices, IEEE Trans. Magn. 57 (2021) 8, https://doi.org/10.1109/TMAG.2021.3086635.

[114] C.C. W. Ruppel, Acoustic Wave Filter Technology – A Review, IEEE Trans. Ultrason. Ferroelectr. Freq. Control. 64 (2017) 9, https://doi.org/10.1109/TUFFC.2017.2690905.

[115] G. Pillai and S.-S. Li, Piezoelectric MEMS Resonators: A Review, IEEE Sensors Journal, 21, 11 (2021), pp. 12589-12605, https://doi.org/10.1109/JSEN.2020.3039052.

[116] J. Bryzek, in Proceedings of the 10th Annual MEMS Technology Symposium (Microelectronics Packaging and Test Engineering Council (MEPTEC), 2012), Vol. 23, pp. 1–9.

[117] A. K. Basu, A. Basu, S. Ghosh, and S. Bhattacharya, MEMS applications in biology and healthcare, AIP Publishing, Melville, NY, 2021, pp. 7-1–7-14, https://doi.org/10.1063/9780735423954_007.

[118] H. Kulkarni, K. Zohaib, A. Khusru, K. Shravan Aiyappa, (2018). Application of piezoelectric technology in automotive systems. Materials Today: Proceedings, 5(10), 21299–21304. doi:10.1016/j.matpr.2018.06.532.

[119] I.M. Koç and E. Akça, Design of a piezoelectric based tactile sensor with bio-inspired micro/nano-pillars, Tribol. Int. 59 (2013) pp. 321–331, https://doi.org/10.1016/j.triboint.2012.06.003.

[120] R. Sun, S.C. Carreira, Y. Chen, C. Xiang, L. Xu, B. Zhang, M. Chen, I. Farrow, F. Scarpa, and J. Rossiter, Stretchable piezoelectric sensing systems for self-powered and wireless health monitoring, Adv. Mater. Technol. 4 (2019) 1900100, https://doi.org/10.1002/admt.201900100.

[121] A. Fath, T. Xia, and W. Li, Recent Advances in the application of piezoelectric materials in microrobotic systems, Micromachines 13 1422 (2022), https://doi.org/10.3390/mi13091422.

[122] Z. Angelika, G. Arkadiusz, and S. Paweł, Progress in the applications of smart piezoelectric materials for medical devices, polymers 12 2754 (2020), https://doi.org/10.3390/polym12112754.

[123] L. Su, Z. Jiang, Z. Tian, H. Wang, H. Wang, and Y. Zi, Self-powered, ultrasensitive, and high-resolution visualized flexible pressure sensor based on color-tunable triboelectrification-induced electroluminescence, Nano Energy 79 (2021) 105431, https://doi.org/10.1016/j.nanoen.2020.105431.

[124] R. Caliò, U.B. Rongala, D. Camboni, M. Milazzo, C. Stefanini, G. De Petris, and C.M. Oddo, Piezoelectric energy harvesting solutions, Sensors 14 (2014) 4755–4790, https://doi.org/10.3390/s140304755.

[125] H. Zhou, Y. Zhang, Y. Qiu, H. Wu, W. Qin, Y. Liao, and H. Cheng, Stretchable piezoelectric energy harvesters and self-powered sensors for wearable and implantable devices, Biosens. Bioelectron. 165 (2020) 112569, https://doi.org/10.1016/j.bios.2020.112569.

[126] M.A.P. Mahmud, N. Huda, S.H. Farjana, M. Asadnia, and C. Lang, Recent advances in nanogenerator-driven self-powered implantable biomedical devices, Adv. Energy Mater. 8 (2018) 1701210, https://doi.org/10.1002/aenm.201701210.

[127] N. Jamond, P. Chrétien, L. Gatilova, E. Galopin, L. Travers, J.C. Harmand, F. Glas, F. Houzé, and N. Gogneau, Energy harvesting efficiency in GaN nanowire-based nanogenerators: The critical influence of the Schottky nanocontact, Nanoscale 9 (2017) 4610–4619, https://doi.org/10.1039/C7NR00647K.

[128] O.Y. Pawar, S.L. Patil, R.S. Redekar, S.B. Patil, S. Lim, N.L. Tarwal, Strategic development of piezoelectric nanogenerator and biomedical applications, Applied Sciences 13 (2023) 2891, https://doi.org/10.3390/app13052891.
[129] W. Liu and X. Ren, Large piezoelectric effect in Pb-free ceramics, Phys. Rev. Lett. 103 (2009) 257602, https://doi.org/10.1103/PhysRevLett.103.257602.
[130] L.A.O. Araujo, C.R. Foschini, and C.A. Fortulan, Piezoelectric energy harvesting device based on quartz as a power generator, in: Magnetic, Ferroelectric, and Multiferroic Metal Oxides, Elsevier, 2018, pp. 265–274.
[131] Y. Saigusa, Quartz-based piezoelectric materials, in: Advanced Piezoelectric Materials (Second Edition), Elsevier, 2017, pp. 197–233.
[132] S. Ang, J.L. Uo, T. Out, High-performance, high-Tc piezoelectric crystals, in Handbook of Advanced Dielectric, Piezoelectric and Ferroelectric Materials: Synthesis, Properties and Applications, page 130, 2008.
[133] S. Trolier-McKinstry, Sh. Zhang, A. J. Bell, and X. Tan, High-Performance Piezoelectric Crystals, Ceramics, and Films, Annu. Rev. Mater. Res. 2018. 48:6.1–6.27, https://doi.org/10.1146/annurev-matsci-070616-124023.
[134] P. Krempl, G. Schleinzer, W. Wallno, et al., Gallium phosphate, GaPO4: a new piezoelectric crystal material for high-temperature sensorics, Sensors and Actuators A: Physical, 61(1-3) (1997) 361–363.
[135] S. Zhang, F. Yu, Piezoelectric materials for high temperature sensors, Journal of the American Ceramic Society 94 (2011) 3153–3170, https://doi.org/10.1111/j.1551-2916.2011.04792.xCitations.
[136] S.E. Park, T.R. Shrout, Ultrahigh strain and piezoelectric behavior in relaxor based ferroelectric single crystals, J. Appl. Phys. 82 (1997) 1804–11.
[137] H. Du, Zh. Li, F.Tang, S. Qu ,Zh. Pei, W. Zhou, Preparation and piezoelectric properties of (K0.5Na0.5)NbO3 lead-free piezoelectric ceramics with pressure-less sintering, Materials Science and Engineering B 131 (2006) 83–87, https://doi.org/10.1016/j.mseb.2006.03.039.
[138] M. Akiyama, T. Kamohara, K. Kano, A. Teshigahara, Y. Takeuchi, N. Kawahara, Enhancement of piezoelectric response in scandium aluminum nitride alloy thin films prepared by dual reactive cosputtering, Advanced Materials 21 (2009) 593–596, https://doi.org/10.1002/adma.200802611.
[139] X Ming Lu and TL Proulx. Single crystals vs. PZT ceramics for medical ultrasoundapplications, In Ultrasonics Symposium, 2005 IEEE, volume 1, pages 227–230. IEEE, 2005.
[140] AE Crawford, Lead zirconate-titanate piezoelectric ceramics. British Journal of Applied Physics, 12(10):529, 1961.
[141] S. Trolier-McKinstry and P. Muralt. Thin film piezoelectrics for MEMS, Journal of Electroceramics 12(1-2) (2004) 7–17, https://doi.org/10.1023/B:JECR.0000033998.72845.51.
[142] S. Rong, B. Faheem, Y Li, Perovskite single crystals: Synthesis, properties, and applications, Journal of Electronic Science and Technology, Vol. 19, Issue 2, June 2021, 100081, https://doi.org/10.1016/j.jnlest.2021.100081.

DFT- Based Computational Techniques for Material Modeling

Chapter II

II.1. Introduction

Ab initio Density Functional Theory (DFT) is a promising approach that addresses the increasing demand for high-quality results in contemporary ab initio quantum chemistry. The advent of high-speed, large-memory computers has made extensive electronic structure simulations feasible, supported by a variety of well-established quantum simulation methods and versatile codes. The origins of electronic structure calculations trace back to the development of quantum theory in the first half of the 20th century, which not only enhanced our understanding of physics but also provided precision and predictive capabilities. Quantum mechanical methods are distinctive for several reasons:

- They are based on first principles or ab initio approaches, meaning they do not rely on empirical models or prior experimental data, enabling the examination of any system.
- The equations of quantum mechanics can effectively model real-world processes.
- Importantly, electronic structure calculations allow researchers to determine physical properties—such as the binding energy of atoms or molecules—that may be difficult or impossible to measure directly.
- These methods can also aid in discovering new compounds with specific properties, facilitating comparisons with existing materials and conserving experimental resources and time.
- Overall, material simulations offer insights that may not be attainable through experimental methods alone.

However, solving quantum mechanical equations, such as the Schrödinger equation, for many-body systems is challenging due to their complexity and large scale, as it necessitates finding the eigenvalues and eigenvectors of a large matrix representing the system's energy levels. This often requires sophisticated numerical methods along with various approximations. Popular electronic structure methods include DFT [1–3], Hartree-Fock (HF) [4,5], Quantum Monte Carlo [6–8], coupled cluster [9,10], and multireference configuration interaction [11]. The choice of method depends on the properties being studied. These methods can be applied through various simulation packages tailored to specific challenges; for example, software like GAMESS [12] and Gaussian [13] address molecular structure issues, while plane-wave basis set

codes such as VASP [14] and Quantum Espresso [15] are suited for metals and materials where band structure is significant. Hybrid approaches, like CP2K [16], are also used, while codes such as WIEN2K [17] and ELK [18] are designed to handle heavy elements where pseudopotential methods may fail, necessitating the use of all-electron potentials.

II.2. Overview of Quantum Simulation Methods

II.2.1. The Many-Body Hamiltonian

The Many-Body Hamiltonian is a mathematical representation of the total energy of a system of interacting particles, utilized in quantum mechanics to describe the behavior of collections of particles, such as atoms or molecules, that interact through forces like the electromagnetic force. Quantum mechanical simulations aim to calculate the electronic structure of a system by solving the many-body Schrödinger equation. For a solid, the many-particle Hamiltonian of electromagnetically interacting particles can be expressed as:

$$\hat{H} = \hat{T}_{nucl} + \hat{T}_{elec} + \hat{V}_{n-e} + \hat{V}_{e-e} + \hat{V}_{n-n}, \quad (1)$$

where:

- The first two terms represent the kinetic energy operators for the nuclei and the electrons:

$$\hat{T}_{nucl} = -\frac{h^2}{2}\sum_i \frac{\nabla_{Ri}^2}{M_i} \ , \quad (2)$$

$$\hat{T}_{elec} = -\frac{h^2}{2}\sum_i \frac{\nabla_{ri}^2}{m_i} \ , \quad (3)$$

- The last three terms describe the Coulomb interactions between nuclei-electron, electron-electron, and nuclei-nuclei, respectively:

$$\hat{V}_{n-e} = -\frac{1}{4\pi\epsilon_0}\sum_{i,j} \frac{Z_i e^2}{|R_i - r_i|} \ , \quad (4)$$

$$\hat{V}_{e-e} = -\frac{1}{8\pi\epsilon_0}\sum_{i\neq j} \frac{e^2}{|r_i - r_j|} \ , \quad (5)$$

$$\hat{V}_{n-n} = -\frac{1}{8\pi\epsilon_0}\sum_{i\neq j} \frac{e^2 Z_i Z_j}{|R_i - R_j|} \ , \quad (6)$$

- The M_i and m_i represent the masses of the nuclei and electrons located at positions R_i and r_i, respectively.

This Hamiltonian is used to obtain the eigenstates (the wave functions the wave functions $\psi(R_n; r_e)$) of the many-particle system by solving the corresponding Schrödinger equation:

$$\hat{H}\psi\{R_n, r_e\} = E\psi\{R_n, r_e\}, \tag{7}$$

However, it is well known that solving such an equation is impossible without making several approximations at various levels to obtain approximate eigenstates.

II.2.2. The Born-Oppenheimer Approximation

Due to the significantly smaller mass of electrons compared to that of nuclei, electronic motion is much faster than nuclear motion. Since the velocities of the nuclei are much lower, we can assume that they are effectively frozen in fixed positions. This approximation allows us to neglect the kinetic energy of the nuclei in the Hamiltonian, making the last term constant. Consequently, the Hamiltonian of a many-electron system takes the following form:

$$\hat{H} = \hat{T}_{elec} + \hat{V}_{e-e} + \hat{V}_{ext}\ , \tag{8}$$

where, $\hat{T}_{elec}$ represents the kinetic energy of the electrons, $\hat{V}_{e-e}$ is the potential due to electron-electron interactions, and $\hat{V}_{ext}$ is the potential of the electrons interacting with the external nuclei.

II.2.3. Density Functional Theory

Density Functional Theory (DFT) is a computational method in quantum mechanics used to calculate the electronic structure of atoms, molecules, and solids. Developed in 1964, it is based on the theorems of Hohenberg and Kohn [19], followed by a set of equations introduced by Walter Kohn and Lu Jeu Sham [20]. DFT is the most widely used and effective quantum mechanical method for addressing real-world materials, offering faster and more accurate results than other approaches. It finds applications in various fields, including condensed matter physics, materials science, chemistry, biology, geoscience, and mineralogy. Regarded as a significant achievement in computational physics, DFT is valued for its precision and feasibility, and it is implemented through several simulation packages.

II.2.3.1. The Hohenberg and Kohn Theorems

The two theorems of Hohenberg and Kohn are as follows:

- **1st Theorem:** There is a one-to-one correspondence between the ground-state density $\rho(\vec{r})$ of a many-electron system (such as an atom, molecule, or solid) and the external potential $\hat{V}_{ext}$. An immediate consequence is that the ground-state expectation value of any observable $\hat{O}$ is a unique functional of the exact ground-state electron density [21] :

$$\langle\psi|\hat{O}|\psi\rangle = O[\rho], \tag{9}$$

The first theorem states that the ground-state energy of a many-electron system can be uniquely determined by its electron density. Furthermore, the electron density that minimizes the energy corresponds to the true ground-state density.

- **2nd Theorem:** When the observable $\hat{O}$ is the Hamiltonian $\hat{H}$, the ground-state total energy functional is given by [21]:

$$H\,[\rho] = EV_{ext}[\rho]\,, \tag{10}$$

which takes the form:

$$EV_{ext}[\rho] = \langle\psi|\hat{T} + \hat{V}|\psi\rangle + \langle\psi|\hat{V}_{ext}|\psi\rangle, \tag{11}$$

$$= F_{HK[\rho]} + \int \rho(\vec{r})V_{ext}(\vec{r})d\vec{r}, \tag{12}$$

The second theorem states that there exists a functional of the electron density that can be used to determine the potential energy of the system, and this functional is unique for a given system. Together, the Hohenberg-Kohn (HK) theorems provide a framework for predicting the properties and behavior of many-electron systems based solely on their electron density, eliminating the need to solve the Schrödinger equation for the entire system. This reduces the N-electron many-body problem with 3N spatial coordinates to one with just three spatial coordinates.

However, these theorems are difficult to apply in practice because the form of F_{HK} is not known. To make DFT applicable, Kohn and Sham introduced equations that can be used to construct a suitable energy functional.

II.2.3.2. The Kohn-Sham Equations

The primary aim of Kohn and Sham was to create a fictional system of non-interacting particles that would exhibit the same ground-state properties as the real system of interacting electrons. They achieved this by defining the Hamiltonian of the system as follows:

$$\hat{H}_{KS} = \hat{T}_0 + \hat{V}_H + \hat{V}_{XC} + \hat{V}_{ext}, \tag{13}$$

where, $\hat{T}_0$ is the kinetic energy operator, and $\hat{V}_H$, $\hat{V}_{XC}$ *and* $\hat{V}_{ext}$ represent the Hartree, exchange-correlation, and external potentials, respectively.

The electron density of the non-interacting system of *N* electrons is defined as:

$$\rho(\vec{r}) = \sum_{i=1}^{N} \psi_i^*(\vec{r})\psi_i(\vec{r}) \, , \tag{14}$$

and the kinetic energy functional is given by:

$$T_0(\rho) = -\frac{\hbar^2}{2m_e}\sum_{i=1}^{N}\langle\psi_i|\nabla^2|\psi_i\rangle \, , \tag{15}$$

where $|\psi_i >$ represents the one-electron orbitals, and the electron density is obtained by summing all the occupied orbitals, following the Pauli exclusion principle. Furthermore, the energy functional can be expressed as:

$$EV_{ext}[\rho] = \underbrace{T_0[\rho] + E_H[\rho] + E_{xc}[\rho]}_{\mathrm{F_{HK[\rho]}}} + \int \rho(\vec{r})V_{ext}(\vec{r})d\vec{r} \ , \tag{16}$$

where $F_{HK[\rho]}$ is defined as the sum of the first three terms, with $T_0[\rho]$, $E_H[\rho]$, and $E_{xc}[\rho]$ representing the kinetic energy, Hartree, and exchange-correlation functionals, respectively.
The ground-state density can be calculated by evaluating Eq. (11) as follows:

$$\left[-\frac{\hbar^2}{2m_e}\nabla + \hat{V}_{eff}(\vec{r})\right]\psi_i(\vec{r}) = \varepsilon_i\psi_i(\vec{r}) \, , \tag{17}$$

where Ψi and εi are the single-particle wave function and the single-particle energy, respectively. Here,

$$\hat{V}_{eff}(\vec{r}) = \hat{V}_H + \hat{V}_{XC} + \hat{V}_{ext} \, , \tag{18}$$

and $\hat{V}_H$ and $\hat{V}_{XC}$ are defined as:

$$\hat{V}_H = \frac{e^2}{4\pi\epsilon_0}\int\frac{\rho(\overrightarrow{r'})}{|\vec{r}-\overrightarrow{r'}|}d\overrightarrow{r'} \ , \quad \hat{V}_{XC} = \frac{\delta E_{xc}[\rho]}{\delta n} \ , \tag{19}$$

Given the above, the exchange function $E_{xc}(\rho)$ is the only unknown, which can be determined using approximations for the Exchange-Correlation Functional (see the following section). By employing a self-consistent procedure (as illustrated in Figure II.1), the ground-state energy can be calculated iteratively through the evaluation of the Hartree potential and the exchange-correlation potential, both of which depend on the electron density. The initial electron density $\rho_0(\vec{r})$ serves as a starting guess for constructing the Kohn-Sham Hamiltonian H_{KS}. Using Ψ_i, if the final density $\rho_k(\vec{r})$ differs from the initial density, the procedure is restarted by constructing a new Hamiltonian and determining the next density value. This iterative process continues until convergence is achieved, at which point a self-consistent solution for the Kohn-Sham equations is obtained.

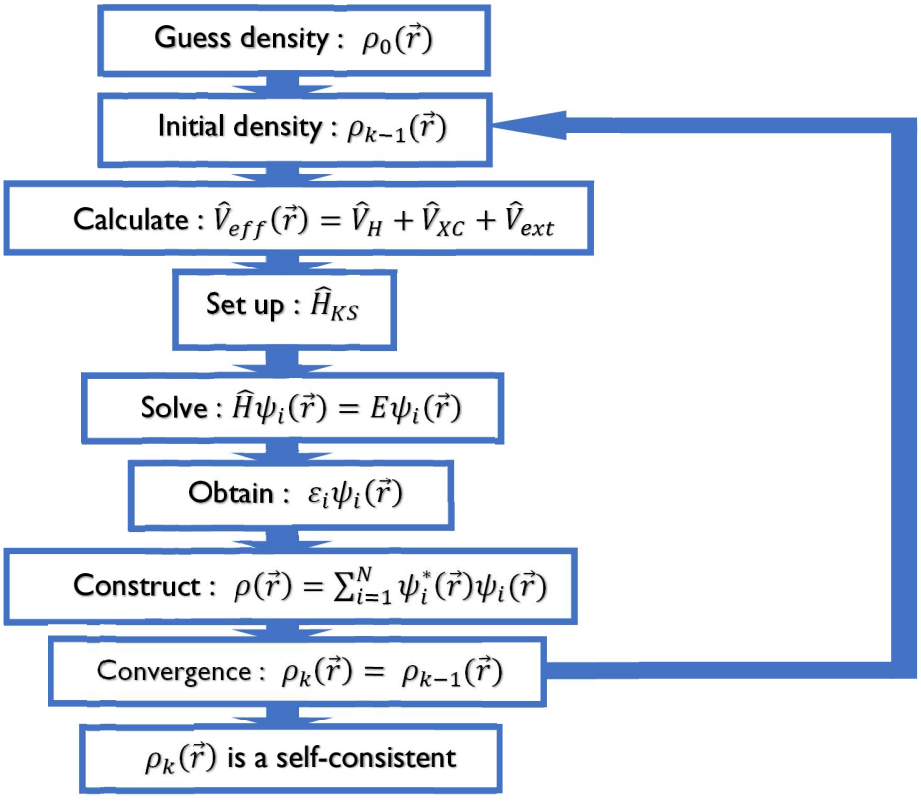

Figure II.1: The flowchart illustrates the self-consistent cycle employed to iteratively solve the Kohn-Sham equations.

II.2.3.3. Approximations to the Exchange-Correlation Functional

The exchange-correlation functional is a crucial element of density functional theory (DFT), a widely employed computational method in materials science, chemistry, and physics. This functional characterizes the interactions between electrons in a system and is typically approximated in DFT calculations due to its inherent complexity. There are several different approximations to the exchange-correlation functional, each with its own strengths and weaknesses.

Some common approximations include:

- **Local Density Approximation (LDA):** This approximation assumes that the exchange-correlation energy depends solely on the local electron density at each point in space. LDA is relatively simple and computationally efficient, but it can have limited accuracy for systems exhibiting strong electron correlations.
- **Generalized Gradient Approximation (GGA):** This approach incorporates not only the local electron density but also the gradient of the density. GGA is often more accurate than LDA for many systems; however, it may still face limitations in strongly correlated systems.
- **Hybrid Functionals:** These approximations combine elements of LDA or GGA with additional terms that include some amount of exact exchange energy, specifically the Hartree–Fock (HF) exchange energy. Hybrid functionals are widely used in quantum chemistry calculations and can provide greater accuracy than LDA or GGA alone, albeit at a higher computational cost.
- **Meta-GGA:** This approximation includes the local density, its gradient, and the Laplacian of the density. Meta-GGA accounts for the local kinetic energy density, allowing for a more accurate treatment of various chemical bonds (e.g., covalent, metallic, and weak) compared to LDA and GGA. However, it is also more computationally demanding.

Overall, the choice of exchange-correlation functional approximation depends on the specific system being studied and the level of accuracy required for the research question at hand.

II.2.3.3.1. Generalized Gradient Approximation (GGA)

The most popular XC functionals are those that use the generalized gradient approximation (GGA) to approximate the XC energy and potential.

Some of the most popular GGA forms include:

- ***Becke 88 (B88):*** This is an early GGA functional that was proposed by John Becke in 1988. It is based on the gradient expansion of the XC energy and has been used extensively in DFT calculations.
- ***Perdew-Wang 91 (PW91):*** This is another early GGA functional that was proposed by Perdew and Wang in 1991. It is based on the gradient expansion of the XC energy and has been used in a variety of DFT calculations.
- ***Perdew-Burke-Ernzerhof (PBE):*** This is one of the most widely used GGA functionals, which was proposed by Perdew, Burke, and Ernzerhof in 1996. It is a parameterized functional that is based on the gradient expansion of the XC energy.
- ***Revised Perdew-Burke-Ernzerhof (RPBE or WC-PBE):*** This is a modified version of the PBE functional that was proposed in 2008. It includes an additional correction term that improves the description of the exchange energy.
- ***Perdew-Burke-Ernzerhof for solids (PBEsol):*** This is a modified version of the PBE functional that was proposed in 2008. It includes an additional correction term that improves the description of solids.

These GGA functionals have been used in a wide range of DFT calculations, including studies of molecules, surfaces, and solids. However, it is important to note that the choice of XC functional can have a significant impact on the accuracy of the results, and different functionals may be more appropriate for different types of systems.

II.2.3.4. Corrections to Density Functional Theory

While Kohn-Sham Density Functional Theory (DFT) using Local Density Approximation (LDA) and even Generalized Gradient Approximation (GGA) has proven effective, it has limitations in accurately predicting certain properties of systems, particularly bandgaps, which are often underestimated due to the lack of self-interaction correction. To achieve more

accurate descriptions, several alternative approaches can be employed. These include the application of Hubbard correction (Local Density Approximation + U (LDA + U) [22], hybrid functionals [23], GW methods [24], and the Tran and Blaha modified Becke-Johnson (TB-mBJ) (2009) [25] and KTB-mBJ (2012) [26].

II.2.3.4.1. The Modified Becke-Johnson (mBJ) Exchange-Correlation (XC) Potential

The modified Becke-Johnson (mBJ) exchange-correlation (XC) potential and its variant, KmBJ, are corrections to the standard density functional theory (DFT) XC functional.

- The mBJ potential was proposed by Tran and Blaha in 2009 to enhance the description of electronic band gaps in semiconductors and insulators, which are often underestimated by standard DFT functionals. It introduces an additional term in the XC potential that depends on both the local density and the gradient of the density. This term aims to improve the description of the exchange interaction between electrons, particularly in systems with localized electrons.
- The KmBJ potential, introduced by Koller et al. in 2012, modifies the mBJ potential by incorporating an additional parameter that allows for a more accurate description of the electronic structure of solids, especially in systems exhibiting strong electron correlation effects.

Both the mBJ and KmBJ potentials have been shown to enhance the accuracy of electronic band gaps and other properties across a variety of materials, including semiconductors, insulators, transition metal compounds, and rare earth compounds.

II.2.4. Simulation Software Packages

II.2.4.1. WIEN2K Package

WIEN2k [17] is a powerful software package designed for electronic structure calculations and simulations of solids. It is widely utilized by researchers in solid-state physics, materials science, and related fields to investigate a diverse range of materials, including metals, semiconductors, insulators, and complex compounds. Specifically developed for studying crystalline materials using density functional theory (DFT), WIEN2k is valued for its accuracy and flexibility. The package is based on the scalar relativistic full-potential linearized augmented

plane wave (FP-LAPW) method, which is known for its high accuracy due to the consideration of the full electronic structure.

Major versions of the WIEN2k package have been released over the years, including:

- WIEN: The original version of the code, developed by Peter Blaha and Karlheinz Schwarz in the late 1980s.
- WIEN92 (1992)
- WIEN97 (1997)
- WIEN2k: The successor to the earlier versions, which continues to be the focus of ongoing development.

Since the initial release of WIEN2k, subsequent updates and patches have been issued to enhance stability, address bugs, and introduce new features. These updates are typically denoted by the release year and version number, such as WIEN2k_19.1, WIEN2k_20.10, etc. The most recent update is WIEN2k_23.2 [17]. In this work, we utilized the WIEN2k_18.2 and WIEN2k_21 versions.

II.2.4.1.1. BerryPi Code

BerryPi [27] is a Python script developed for calculating the Berry phase and related properties of solids, particularly topological materials, using the WIEN2k density functional package. The software requires only one input parameter: the k-mesh for Berry phase integration. By analyzing WIEN2k output files, BerryPi automatically extracts essential information, including the number of occupied bands, cell geometry, ionic charges, and their relative positions. It then performs calculations to determine the electronic, ionic, and total phases, along with the polarization components along the Cartesian axes. The latest update for BerryPi was released in July 2022 [28].

II.2.4.2. BoltzTrap Code

Boltzmann Transport Properties (BoltzTraP) [29] is a program that employs a smoothed Fourier interpolation algorithm for electronic bands to calculate the electronic transport

properties of materials. The code utilizes a mesh of band energies and can interface with various computational packages, including WIEN2k, ABINIT, SIESTA, VASP, and QuantumEspresso. One of the primary applications of BoltzTraP is calculating thermoelectric transport coefficients as functions of temperature and chemical potential within the rigid-band approximation. Additionally, it enables the generation of 3D plots of Fermi surfaces based on reconstructed bands. These calculations and predictions facilitate the understanding and design of materials for a variety of electronic and energy-related applications, such as thermoelectric materials, semiconductor devices, and energy conversion systems.

BoltzTraP2 [30] is an updated version of BoltzTraP that addresses certain limitations and provides enhanced functionalities. It extends the original capabilities by incorporating more advanced algorithms, including the treatment of spin-orbit coupling and the inclusion of anisotropic scattering. Furthermore, BoltzTraP2 introduces improved parallelization and efficiency, enabling it to handle large-scale calculations on modern high-performance computing systems.

II.2.4.37. Gibbs Code

The Gibbs program [31], developed within the Fortran77 framework, employs a quasi-harmonic Debye model to calculate the Debye temperature Θ(V)\Theta(V)Θ(V) based on the energy of a solid (EEE) in relation to its molecular volume (VVV). It is designed to analyze the thermodynamic properties of solids while accounting for dependencies on pressure and temperature. The primary goal of the program is to extract comprehensive thermodynamic information from a minimal set of (E,V)(E, V)(E,V) data, facilitating the analysis of costly electronic structure calculations while incorporating thermal effects at a low computational cost. Gibbs2 [32] is a reimplementation of the original Gibbs program in Fortran90. This updated code includes new models that address temperature effects, extending from the simple Debye model of the original code to a comprehensive quasi-harmonic model that necessitates the phonon density of states at each calculated volume. Notably, Gibbs2 introduces empirical energy corrections to mitigate systematic errors stemming from the choice of exchange-correlation functional in equilibrium volume calculations. Additionally, it accounts for electronic contributions to the free energy and enables automatic computation of phase diagrams. The

code is accompanied by extensive documentation, including a user guide, a complete set of tests, sample data, and the source code.

1.4.2. CASTAP Package

The CASTAP (CAS-Transport-Applications) package [33] is a computational software tool designed for simulating and analyzing atomic-scale transport phenomena in materials. It focuses on electronic structure calculations and transport properties of solids, making it particularly suitable for applications in nanoscale devices and materials. CASTAP can simulate a wide range of material properties, including energetics, atomic-level structure, vibrational properties, and electronic response characteristics. Additionally, it features various spectroscopic capabilities that link directly to experimental techniques, such as infrared and Raman spectroscopies, nuclear magnetic resonance (NMR), and core-level spectra. CASTAP is based on density functional theory (DFT) and performs calculations using plane-wave basis sets and pseudopotentials, treating the nucleus and core electrons as a single ion that acts on the outer electrons. This approach allows for efficient and accurate simulations of complex materials. The package provides a user-friendly interface, enabling researchers and scientists to set up and execute calculations efficiently. It also includes post-processing tools for analyzing and visualizing the obtained results, facilitating the interpretation of computational data.

II.3. Conclusion

Quantum simulation methods are essential for understanding and predicting the behavior of quantum systems. These methods provide valuable insights into the properties and dynamics of quantum systems, with the potential to revolutionize various fields, including condensed matter physics. A significant advantage of quantum simulations is their ability to accurately model complex systems, offering detailed descriptions of electronic structures that allow researchers to investigate a wide range of physical properties. Among these methods, density functional theory (DFT), particularly the widely used Kohn-Sham DFT, strikes a favorable balance between accuracy and computational efficiency, making it suitable for studying larger systems. Quantum simulation methods empower researchers to explore and design new materials while deepening our understanding of fundamental quantum phenomena. As these methods continue to advance alongside developments in quantum computing technology, they are expected to profoundly affect various scientific and technological domains. This progress will drive innovation and open new avenues for exploration in the quantum realm.

References

[1] R. Martin, Density functional theory: foundations, Electr. Struct (2004) 119-134, https://doi.org/10.1017/CBO9780511805769.008.

[2] K. Capelle, A bird's-eye view of density-functional theory, Br. J. Phys. 36 (2006) 1318-1343, 10.1590/S0103-97332006000700035.

[3] N. Argaman, G. Makov, Density functional theory: An introduction, Am. J. Phys. 68 (2000) 69-79, https://doi.org/10.1119/1.19375.

[4] I. Mayer, The Hartree-Fock method, Simple Theorems, Proofs, and Derivations in Quantum Chemistry, Springer, Boston, MA, 2003, pp. 165-225.

[5] Thijssen, The Hartree-Fock method, Computational Physics, Cambridge University Press, 2007, pp. 43-88.

[6] W. Foulkes, L. Mitas, R. Needs, G. Rajagopal, Quantum Monte Carlo simulations of solids, Rev. Modern Phys. 73 (2001) 33-83, https://doi.org/10.1103/RevModPhys.73.33.

[7] B. Hammond, W. Lester, P. Reynolds, Monte Carlo methods in ab initio quantum chemistry, World Scientific Publishing Co, Singapore, 1994.

[8] J. Kolorenc, L. Mitas, Applications of quantum Monte Carlo methods in condensed systems, Rep. Progr. Phys. 74 (2011) 026502, https://doi.org/10.1088/0034-4885/74/2/026502.

[9] I. Shavitt, R. Bartlett, Many-Body Methods in Chemistry and Physics, Cambridge University Press, Cambridge, 2010.

[10] B. Jeziorski, H. Monkhorst, Coupled-cluster method for multideterminantal reference states, Phys. Rev. A. 24 (1981) 1668-1681.

[11] C. David Sherrill, H. Schaefer, The configuration interaction method: advances in highly correlated approaches, Adv. Quant. Chem. (1999) 143-269, https://doi.org/10.1016/S0065-3276(08)60532-8.

[12] GAMESS: Open Source Quantum Chemistry Software | Ames Laboratory [WWW Document], n.d. URL https://www.ameslab.gov/gamess-open-source-quantum-chemistry-software (accessed 7.14.25).

[13] Gaussian.com | Expanding the limits of computational chemistry [WWW Document], n.d. URL https://gaussian.com/ (accessed 7.14.25).

[14] VASP - Vienna Ab initio Simulation Package [WWW Document], n.d. URL https://www.vasp.at/ (accessed 7.14.25).

[15] Home Page - Quantum Espresso [WWW Document], n.d. URL https://www.quantum-espresso.org/ (accessed 7.14.25).

[16] J. Hutter, M. Iannuzzi, F. Schiffmann, and J. Vandevondele, J. (2014). Cp2k: atomistic simulations of condensed matter systems. WIREs Comput Mol Sci 4, 15–25. https://doi.org/10.1002/wcms.1159

[17] P. Blaha, K. Schwarz, F. Tran, R. Laskowski, G.K.H. Madsen, L.D. Marks, WIEN2k: an APW+ lo program for calculating the properties of solids, J. Chem. Phys. 152 (2020), 074101, https://doi.org/10.1063/1.5143061.

[18] The Elk Code - The Elk Code [WWW Document], n.d. URL http://elk.sourceforge.net/ (accessed 7.14.25).

[19] P. Hohenberg, W. Kohn, Inhomogeneous electron gas, Phys. Rev. 136 (1964) B864-B871.

[20] W. Kohn, L. Sham, Self-consistent equations including exchange and correlation effects, Phys. Rev. 140 (1965) A1133-A1138.

[21] Chakraborty, B. Electronic Structure and Theoretical Aspects on Sensing Application of 2D Materials. Fundamentals and Sensing Applications of 2D Materials (2019) 145–203, https://doi.org/10.1016/b978-0-08-102577-2.00005-1.

[22] V.I. Anisimov, J. Zaanen, O.K. Andersen, Band theory and Mott insulators: Hubbard U instead of Stoner I, Phys. Rev. B (1991) 943-954.

[23] A.D. Becke, A new mixing of Hartree–Fock and local density-functional theories, The Journal of Chemical Physics 98(2) (1993) 1372–1377, https://doi.org/10.1063/1.464304.

[24] F. Bechstedt, F. Fuchs, G. Kresse, Ab-initio theory of semiconductor band structures: New developments and progress, Phys. Status Solidi B (2009) 1877-1892, https://doi.org/10.1002/pssb.200945074.

[25] F. Tran, P. Blaha, Accurate band gaps of semiconductors and insulators with a semilocal exchange-correlation potential, Phys. Rev. Lett. (2009) 226401, https://doi.org/10.1103/physrevlett.102.226401.

[26] D. Koller, F. Tran, P. Blaha, Improving the modified Becke-Johnson exchange potential, Phys. Rev. B (2012) 155109, https://doi.org/10.1103/physrevb.85.155109.

[27] S.J. Ahmed, J. Kivinen, B. Zaporzan, L. Curiel, S. Pichardo, O. Rubel, BerryPI: A software for studying polarization of crystalline solids with WIEN2k density functional all-electron package, Comput. Phys. Commun. (2013) 647-651, https://doi.org/10.1016/j.cpc.2012.10.028.

[28] Ahmed, S. J., Kivinen, J., Zaporzan, B., Curiel, L., Pichardo, S., & Rubel, O. (2013). BerryPI: A software for studying polarization of crystalline solids with WIEN2k density functional all-electron package. Computer Physics Communications, 184(3), 647–651, https://doi.org/10.1016/j.cpc.2012.10.028.

[29] G.K.H. Madsen, D.J. Singh, BoltzTraP: A code for calculating band-structure dependent quantities, Comput. Phys. Commun. (2006) 67-71, https://doi.org/10.1016/j.cpc.2006.03.007.

[30] G.K.H. Madsen, J. Carrete, M.J. Verstraete, BoltzTraP2: A program for interpolating band structures and calculating semi-classical transport coefficients, Comput. Phys. Commun. (2018) 140-145, https://doi.org/10.1016/j.cpc.2018.05.010.

[31] M.A. Blanco, E. Francisco, V. Luaña, GIBBS: Isothermal-isobaric thermodynamics of solids from energy curves using a quasi-harmonic Debye model, Comput. Phys. Commun. (2004) 57-72, https://doi.org/10.1016/j.comphy.2003.12.001.

[32] A. Otero-de-la-Roza, D. Abbasi-Pérez, V. Luaña, Gibbs2: A new version of the quasiharmonic model code. II. Models for solid-state thermodynamics, features and implementation, Comput. Phys. Commun. (2011) 2232-2248, https://doi.org/10.1016/j.cpc.2011.05.009.

[33] S. J. Clark, , M. D. Segall, , C. J. Pickard, P. J. Hasnip, M. I. J. Probert., Refson, K., & M. C. Payne, (2005). First principles methods using CASTEP. Zeitschrift Für Kristallographie - Crystalline Materials, 220(5/6). https://doi.org/10.1524/zkri.220.5.567.65075.

DFT Insights into the Thermoelectric and Piezoelectric Properties in Lead-Free Perovskites: A Case Study of $Na_{0.5}Bi_{0.5}TiO_3$

Chapter III

III.1. Introduction

$Na_{0.5}Bi_{0.5}TiO_3$ (NBT), a lead-free perovskite, stands out for its valuable properties that make it a promising material for high-performance eco-friendly piezoelectric devices and high-power thermoelectric generators. This chapter presents a comprehensive investigation of NBT's elastic, piezoelectric, thermodynamic, and thermoelectric properties across its rhombohedral (*R*3*c*), tetragonal (*Pb*4*m*) and cubic ($Pm\bar{3}m$) phases using Ab Initio Density Functional Theory (DFT) calculations. We analyze the stability of these phase structures through formation energy and phonon dispersion studies.

To accurately describe the electronic band structures and chemical bonds, the advanced *n*KTB–mBJ+so functional within FP–LAPW method is employed. This study provides a detailed examination of the elasticity and piezoelectricity of NBT crystals, along with an in-depth analysis of thermodynamic quantities and thermoelectric parameters using the quasi-harmonic Debye model and BoltzTraP2 code, respectively.

III.2. Computational Methods

The electronic structure of $Na_{0.5}Bi_{0.5}TiO_3$ (NBT) crystals in the rhombohedral (R3c), tetragonal (P4bm), and cubic ($Pm\bar{3}m$) phases was explored using the Full Potential Linear Augmented Plane Wave (FP–LAPW) method [1], as implemented in the WIEN2K program package [3], based on Density Functional Theory (DFT) [2]. For structural optimization, we utilized the Perdew-Burke-Ernzerhof Generalized Gradient Approximation (GGA-PBE) [4] and its newer parameterized versions, GGA–PBEsol [5] and GGA–WC [6], to describe the exchange-correlation (*XC*) potential. These functionals are known for their efficiency in material geometry optimization [7, 8]. To analyze the electronic properties, including the band structure, density of states, and bonding charge, we used the advanced modified Becke-Johnson exchange potential of Koller-Tran-Blaha (*n*KTB–mBJ) [9], along with the original Tran-Blaha-mBJ (TB–mBJ) [10], incorporating spin-orbit (so) interaction. These approximations are essential for accurately describing the band gaps of semiconductors and insulators [11]. The Muffin-Tin radius (R_{MT}) values for Na, Ba, Ti, and O were set at 2.4, 2.5, 1.9, and 1.7 a.u., respectively, with charge density and potential inside the Muffin-Tin spheres

expanded with an angular momentum up to l_{max} = 10. To ensure energy convergence, wave functions were expanded in plane waves (PWs) with a cut-off of $R_{MT}K_{max}$ = 7 in the interstitial regions, where R_{MT} is the smallest muffin-tin radius and K_{max} is the maximum wave vector value. Valence electron configurations used were (*2s 2p 3s*) for Na, (*5d 6s 6p*) for Bi, (*3d 4s*) for Ti, and (*2s 2p*) for O. Integrations over the Brillouin zone employed Monkhorst-Pack grids [12] of 25 (5×5×2), 30 (8×8×5), and 45 (10×10×5) special *k*-points for R3c, P4bm, and $Pm\bar{3}m$ NBT symmetry crystals, respectively.

Additionally, the elastic properties were calculated using the Ultrasoft Vanderbilt pseudopotential [13] with GGA–PBEsol approaches [5] based on the Cambridge Serial Total Energy package [14]. A self-consistent field tolerance of 5.0×10^{-6} eV/atom, residual force less than 0.01 eV/Å, residual bulk stress less than 0.02 GPa, atomic displacement less than 0.001 Å, and plane-wave cutoff energy of 520 eV were adopted to ensure calculation convergence. Density functional perturbation theory (DFPT) [15] was employed to study piezoelectric and dielectric responses using the GGA–PBE method for the exchange-correlation potential. At room temperature, $Na_{0.5}Bi_{0.5}TiO_3$ (NBT) crystallizes in a rhombohedral structure with the space group *R*3*c*, characterized by lattice parameters a = b = 5.488 Å, c = 13.50 Å, and angles α = β = 90°, γ = 120° [16]. Between 673 and 773 K, NBT undergoes a phase transition to a tetragonal structure with space group P4bm, where the lattice parameters are a = b = 5.517 Å, c = 3.907 Å, and all angles α = β = γ = 90°. At temperatures exceeding 813 K, NBT adopts a cubic symmetry with space group $Pm\bar{3}m$, featuring lattice parameters a = b = c = 3.913 Å and angles α = β = γ = 90° [16].

For modeling $Na_{0.5}Bi_{0.5}TiO_3$ (NBT) crystals, we utilized supercells with 30 atoms for the rhombohedral (*R*3*c*) phase (using hexagonal axes), 20 atoms for the tetragonal (*P*4*bm*) phase, and 10 atoms for the cubic ($Pm\bar{3}m$) phase. Figure III.1 illustrates the crystalline structures of NBT in the *R*3*c*, *P*4*bm* and $Pm\bar{3}m$ symmetries. All were fully relaxed, allowing the atoms to move to their equilibrium positions during the FP–LAPW calculations.

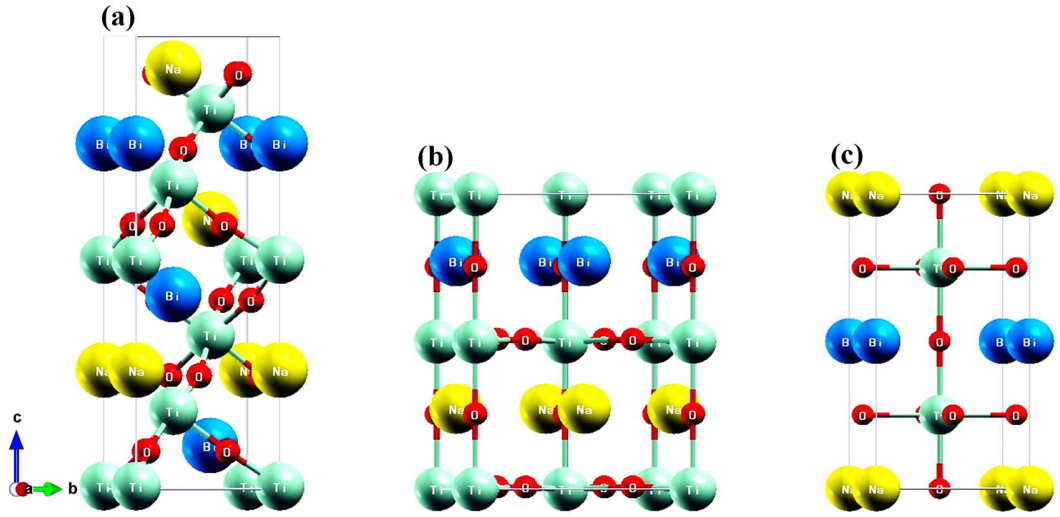

Figure III.1: Crystalline structures of $Na_{0.5}Bi_{0.5}TiO_3$ (NBT): (a) rhombohedral (*R*3*c*) (hexagonal axes) phase, (b) tetragonal (*P*4*bm*) phase, and (c) cubic ($Pm\bar{3}m$) phase.

III.3. Structural Property

A. Geometry Optimization

We initially employed FP–LAPW technique to obtain equilibrium structural parameters of $Na_{0.5}Bi_{0.5}TiO_3$ (NBT) in its rhombohedral (*R*3*c*), tetragonal (*P*4*bm*), and cubic ($Pm\bar{3}m$) phase structures. Various approximations for the exchange-correlation potential were used, including GGA–PBE, GGA–WC, and GGA–PBEsol. These parameters were optimized by minimizing the total energy as a function of the unit cell volume, and the results were then fitted to Murnaghan's equation of state [17]:

$$E(V) = \left\{ E_0 + \left[\frac{B_0 V}{B_0 (B_0) - 1} \right] \times \left[B_0' \left(1 - \frac{V_0}{V} \right) + \left(\frac{V_0}{V} \right)^{B'} - 1 \right] \right\} \quad (1)$$

where E_0 is the equilibrium total energy, B_0 is the bulk modulus, and B' is the first pressure derivative of B_0.

Figure III.2 depicts the variation in total energy as a function of volume for the rhombohedral, tetragonal, and cubic phases of $Na_{0.5}Bi_{0.5}TiO_3$ (NBT) crystals, calculated using the PBEsol, WC, and PBE approximations.

Table III.1 listen the results of lattice constants (a_0, c_0), ratio c_0/a_0, cell volume V_0, and fractional coordinates (x, y, z) of $Na_{0.5}Bi_{0.5}TiO_3$ (NBT) in the *R*3*c*, *P*4*bm*, and $Pm\bar{3}m$ symmetries, compared to available experimental data and previously reported computational values. Our calculated (a_0, c_0) are (5.446, 13.54) Å using GGA–PBEsol and (5.448, 13.54) Å using GGA–WC for the *R*3*c*-NBT crystal, which are very close to the experimental values (5.488, 13.50) Å [16] and (5.498, 13.50) [18]. These results are also more accurate than those calculated using classical approximations, such as LDA (5.680, 14.03) Å [18] and GGA–PBE (5.68, 14.03) Å [18], (5.359, 13.27) Å [19]. The obtained (a_0, c_0) values for *P*4*bm*-NBT, (5.359, 3.938) Å using PBEsol and (5.362, 3.940) Å using WC, are also found to be in good agreement with the measured values of (5.517, 3.907) Å [16]. The predicted lattice constant a_0 for $Pm\bar{3}m$-NBT is equal to 3.851 Å using PBEsol and 3.853 Å using WC, which are slightly underestimated compared to the experimental value of 3.913 Å [16]. The atomic positions in three phases of NBT crystals are well predicted by both GGA–PBEsol and GGA–WC approaches, as shown in Table III.1. Therefore, we find that both the novel GGA–PBEsol and GGA–WC approximations [20,21] can estimate the structural parameters of the studied structures with precision compared to classical approximations, such as GGA–PBE and LDA. It is worth noting that the lattice parameters derived from GGA–PBE and LDA often deviate from experimental measurements due to their limitations within DFT theory [22,23].

Furthermore, the phase stability of $Na_{0.5}Bi_{0.5}TiO_3$ perovskites in the rhombohedral, tetragonal, and cubic crystallographic phases under conditions of zero pressure (P = 0 GPa) and absolute zero temperature (T = 0 K) was analyzed by evaluating the total energy as a function of volume using the GGA–PBEsol functional. The results are presented in Figure III.3.

It is well-established that the most stable structure is the one with the lowest energy. Based on this principle, we determined that the rhombohedral (*R*3*c*) phase is the most energetically stable, followed by the tetragonal (*P*4*bm*) phase, and finally the cubic ($Pm\bar{3}m$) structure. Our prediction of the NBT crystals being most stable in the *R*3*c* phase is in good agreement with experimental observations [16].

Table III.1: Calculated lattice parameters (a_0, c_0) (Å), cell volume V_0 (Å^3), formation energy (ΔE_f) (eV/atom) and fractional coordinates (x, y, z) for $Na_{0.5}Bi_{0.5}TiO_3$ perovskites crystallizing in *R*3*c*, *P*4*bm*, and *Pm*$\bar{3}$*m* symmetries using different approximations (PBEsol, WC, PBE).

Crystals (NBT)		a_0	c_0	c_0/a_0	V_0	ΔE_f	Na/Bi (x)	Na/Bi (y)	Na/Bi (z)	Ti (x)	Ti (y)	Ti (z)	O (x)	O (y)	O (z)
Rhombohedral (*R*3*c*)	PBEsol	5.446	13.54	2.486	346.94	−6.906	0.0	0.0	0.2685	0.0	0.0	0.0142	0.102	0.333	0.0824
	WC	5.448	13.54	2.486	347.83		0.0	0.0	0.2683	0.0	0.0	0.0104	0.102	0.333	0.0825
	PBE	5.496	13.89	2.528	362.50		0.0	0.0	0.2751	0.0	0.0	0.0166	0.100	0.333	0.0801
	Expt.[16]	5.488	13.50	2.460	352.33		0.0	0.0	0.2627	0.0	0.0	0.0063	0.126	0.336	0.0833
	[18]	5.498	13.50	2.455	350.29										
	LDA [18]	5.359	13.27		333.47										
	PBE [19]	5.680	14.03												
Tetragonal (*P*4*bm*)	PBEsol	5.359	3.938	0.734	113.13	−6.874	0.0	0.5	0.4971	0.0	0.0	0.0207	0.301	0.198	0.0023
	WC	5.362	3.940	0.734	113.31		0.0	0.5	0.4975	0.0	0.0	0.0208	0.301	0.198	0.0032
	PBE	5.406	3.969	0.734	116.03		0.0	0.5	0.4970	0.0	0.0	0.0207	0.301	0.198	0.0023
	Expt.[16]	5.517	3.907		118.96		0.0	0.5	0.5450	0.0	0.0	0.0000	0.271	0.229	0.0150
	Theo.[24]	5.505	3.925				0.0	0.5	0.5230	0.0	0.0	0.0000	0.270	0.230	0.0260
Cubic (*Pm*$\bar{3}$*m*)	PBEsol	3.851			57.38	−6.856	0.0	0.0	0.0000	0.5	0.5	0.2566	0.500	0.500	0.0000
	WC	3.853			57.47		0.0	0.0	0.0000	0.5	0.5	0.2566	0.500	0.500	0.0000
	PBE	3.886			58.88		0.0	0.0	0.0000	0.5	0.5	0.2565	0.500	0.500	0.0000
	Expt.[16]	3.913			59.94		0.0	0.0	0.0000	0.5	0.5	0.5000	0.500	0.500	0.0000

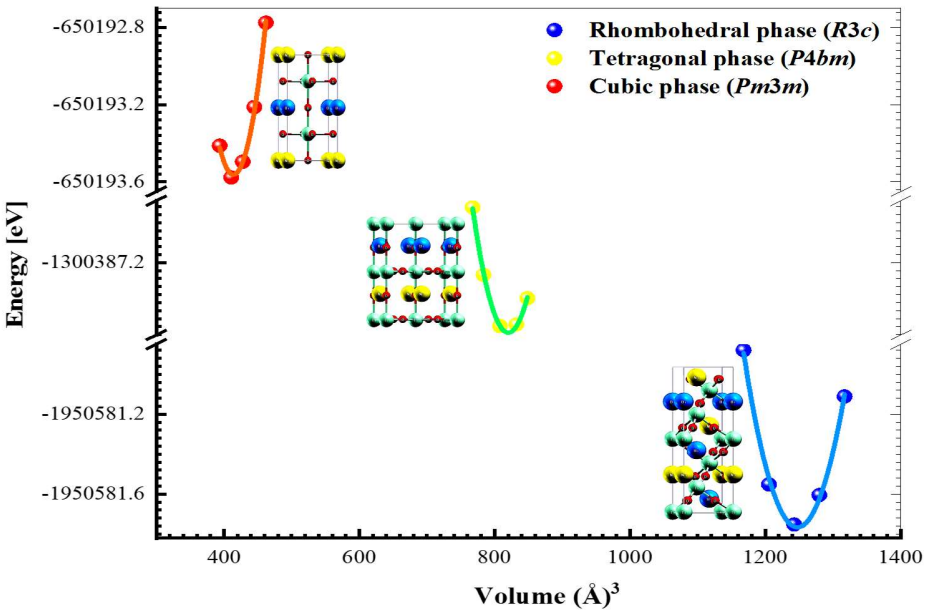

Figure III.2: Total energy as a function of volume for $Na_{0.5}Bi_{0.5}TiO_3$ (NBT) crystals crystalizing in *R*3*c*, *P*4*bm* and *Pm*$\bar{3}$*m* symmetries using PBEsol. The most stable energetically structure corresponds to rhombohedral symmetry.

B. Lattice Stability

The lattice stability of $Na_{0.5}Bi_{0.5}TiO_3$ crystals can be assessed by analyzing their thermodynamic and dynamic stabilities, which are determined through the calculated formation energy and phonon analysis [25].

The formation energy (ΔE_f) is obtained using the following equation [26,27]:

$$\Delta E_f = \frac{E_{crystal} - n_{Na} E_{solid}^{Na} - n_{Bi} E_{solid}^{Bi} - n_{Ti} E_{solid}^{Ti} - n_O E_{solid}^{O}}{n_{Na} + n_{Bi} + n_{Ti} + n_O} \quad (2)$$

Here, n_{Na}, n_{Bi}, n_{Ti} and n_O represent the numbers of Na, Bi, Ti, and O atoms in the unit cell, respectively. $E_{crystal}$ is the total energy of the NBT unit cell, while $E_{solid}^{Na}, E_{solid}^{Bi}, E_{solid}^{Ti}$ and E_{solid}^{O} are the energies per Na, Bi, Ti, and O atom in their respective solid states.

The negative values of ΔE_f signify stronger atomic bonding and greater structural stability within a crystal. We obtained energies of –324.77, –43163.06, –1707.15 and –150.00 eV/atom for Na, Bi, Ti, and O atoms, respectively, using GGA–PBEsol approximation. Thus, the calculated formation energy (ΔE_f) per atom for the rhombohedral, tetragonal and cubic phases are –6.9069, –6.8742, and –6.8564 eV/atom, respectively, all of which are negative. These results indicate the thermodynamic stability of NBT crystals. Given its lower formation energy compared to the tetragonal and cubic structures, the rhombohedral structure is expected to exhibit greater thermodynamic stability. Consequently, we assume that the $Na_{0.5}Bi_{0.5}TiO_3$ in the rhombohedral (*R*3*c*) phase is more likely to form during experimental growth.

Regarding dynamic stability, the phonon frequencies for NBT crystals in the rhombohedral, tetragonal, and cubic symmetries were computed using density functional perturbation theory (DFPT) [28], with the exchange-correlation potential treated using the Local Density Approximation (LDA). LDA is a reliable approach for phonon calculations that align well with experiments [29,30]. The absence of imaginary phonon frequencies indicates dynamic stability within a crystal [31], whereas negative phonon frequencies signify unstable modes [32]. Figure III.4 illustrates the spectra of phonon frequencies along high-symmetry

directions. Figure III.4(a) shows no imaginary phonon frequencies for the rhombohedral (*R*3*c*) phase, confirming its dynamic stability. In contrast, Figure III.4(b) and III.4(c) depict unstable modes at Γ-point and M-point, respectively, corresponding to the ferroelectric (FE) phase transitions. Experimentally, NBT crystal undergoes a sequence of ferroelectric (FE) phase transitions from the most stable rhombohedral symmetry to tetragonal and cubic structures as the temperature increases [33,34].

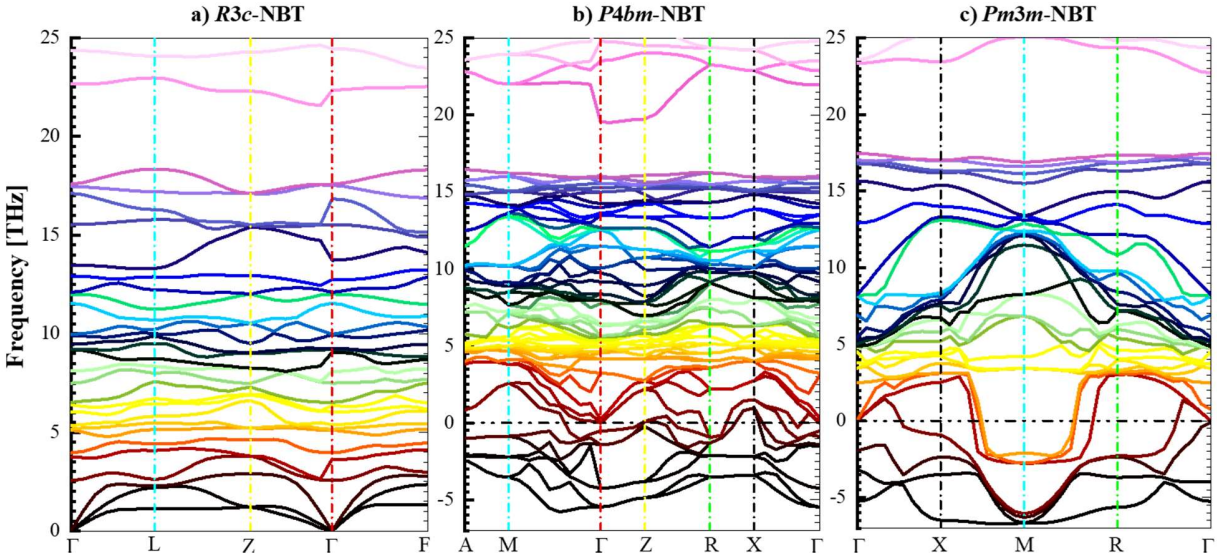

Figure III.3: Calculated phonon frequencies along high-symmetry directions for (a) rhombohedral, (b) tetragonal, and (c) cubic phases of $Na_{0.5}Bi_{0.5}TiO_3$ (NBT) crystals.

III.4. Electronic Properties

A. Band Structure

In this section, we investigate the electronic band structure, density of states, and bonding charge of $Na_{0.5}Bi_{0.5}TiO_3$ (NBT) crystals in rhombohedral (*R*3*c*), tetragonal (*P*4*bm*), and cubic ($Pm\bar{3}m$) symmetries. We employ the recent modified Becke-Johnson (mBJ) exchange potential proposed by Koller-Tran-Blaha [9], as well as its original mBJ version by Tran-Blaha [10], incorporating spin-orbit interaction (SO).

The results for bandgap energies are listed in Table III.2, along with the experimental data and previous theoretical reports.

Figure III.5 shows the band structures and partial density of states (PDOS) plots for NBT crystals in the three phases, along high-symmetry lines in the first Brillouin zone (BZ), using KTB–mBJ+so functional.

As shown in Figure III.5(a), the *R*3*c*-NBT crystal exhibits an indirect bandgap of 3.292 eV, calculated using the KTB–mBJ+so method, which is in excellent agreement with the observed value of 3.30 eV reported by Bousquet et al. [35]. This energy gap forms between the valence band maximum (VBM), located between the Z and Γ points, and the conduction band minimum (CBM) near the Γ point. The original TB–mBJ+so method also predicts a bandgap of 3.212 eV, which is closer to the experimental data of 3.18 eV reported by Selvadurai et al. [36], and is more accurate than the 3.30 eV reported by Chatta et al. [19], who used the same TB–mBJ functional but without accounting for spin-orbit coupling. Our observation of the indirect band gap behavior in the *R*3*c*-NBT crystal is consistent with previous experimental and theoretical findings [19,35]. However, direct band gaps of 2.1 eV and 1.67 eV were reported by Zeng et al. [37] and Benyoussef et al. [38], respectively, using the conventional GGA–PBE approximation. Thanh et al. [39] experimentally determined optical band gap values ranging from 3.00 to 3.14 eV, which depending to the crystal growth procedures.

As depicted in Figure III.5(b) and III.5(c), both the *P*4*bm*-NBT and $Pm\bar{3}m$-NBT crystals are found to exhibit indirect band gaps with values of 3.055 eV (M–Γ) and 3.09 (X–Γ) eV, calculated using KTB–mBJ+so method, respectively. Xu et al. [40] and Baedi et al. [24] reported energy gaps of 1.01 eV (LDA) and 1.9 eV (PBE), respectively, for *P*4*bm*-NBT crystal, both of which are significantly smaller than our calculated value of 3.055 eV. This discrepancy can be attributed to the fact that GGA and LDA methods generally underestimate the band gaps of materials, leading to results that are often inconsistent with experimental data [7,41].

Consequently, the new KTB–mBJ potential significantly enhances the accuracy of computational predictions for the electronic structure of materials. It is notable that the spin-orbit interaction has only a slight influence on band gap calculations. It is obvious that the energy gap for the tetragonal (*P*4*bm*) structure, which corresponds to the medium-

temperature phase, lies between that of the high-temperature cubic phase ($Pm\bar{3}m$) and the low-temperature rhombohedral phase ($R3c$).

Table III.2: Calculated bandgaps for $Na_{0.5}Bi_{0.5}TiO_3$ (NBT) crystals in different phases using the improved TB–mBJ and KTB–mBJ functionals, without and with spin-orbit interaction.

NBT Crystals	TB–mBJ	TB–mBJ+so	KTB–mBJ	KTB–mBJ+so	Exp.	Theo.	Ref.
Rhombohedral (*R3c*)	3.236	3.212	3.308	3.292	3.30[a] – 3.18[b]	3.30[c] – 2.1[d]	[a]Ref.[35] [b]Ref.[36] [c]Ref.[19] [d]Ref.[37] [e]Ref.[40]
Tetragonal(*P4bm*)	3.175	2.951	3.043	3.055		1.01[e] – 1.9[f]	[f]Ref.[24]
Cubic (*Pm$\bar{3}$m*)	2.938	2.956	3.090	3.106			

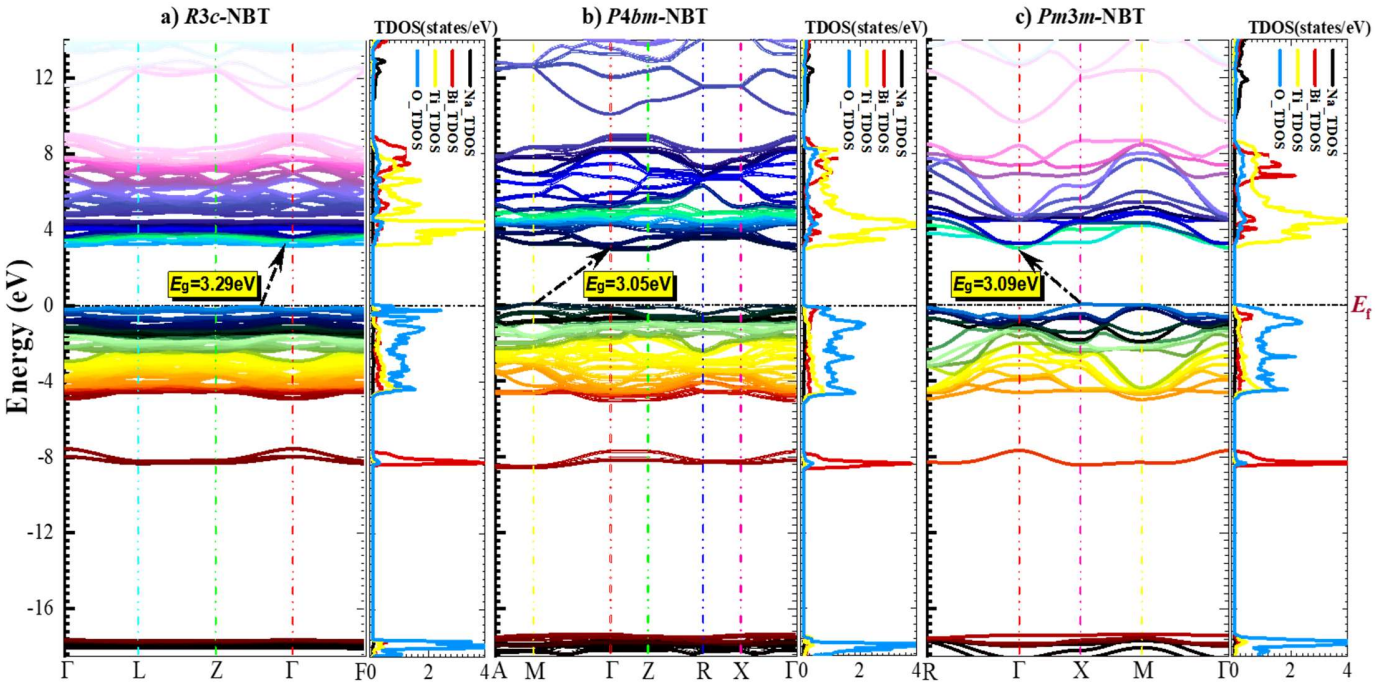

Figure III.4: Calculated band structures and density of states for (a) *R3c*-NBT, (b) *P4bm*-NBT, and (c) *Pm$\bar{3}$m*-NBT crystals, using the KTB–mBJ+so functional.

B. Density of States

Determining the density of states provides valuable insights into the origin and nature of the electronic structure of the compounds under study. Figure III.6 illustrates the computed total (TDOS) and partial (PDOS) densities of states for $Na_{0.5}Bi_{0.5}TiO_3$ (NBT) in

different crystallographic phases (*R*3*c*, *P*4*bm*, and *Pm*$\bar{3}$*m*), using the improved KTB–mBJ+so method. The curves exhibit a notable similarity in the DOS profiles across the three considered phases. Three distinct energy groups can be identified: two sub-bands in the valence band, labeled VB_{low} and VB_{high}, located below the Fermi level (EF), and the conduction band (CB). At very low energy, around –18 eV, the density of states (DOS) spectra exhibits a pronounced peak associated to the O (2s) orbitals, which is consistent with previous reports using the generalized gradient approximation (GGA) [37]. Regarding the valence band (VB), the lowest energy group, VB_{low}, situated at –8.2 eV, is primarily attributed to a sharp contribution from Bi (6s) orbitals. The higher energy group, VB_{high}, which extends from –4.8 eV to the Fermi level, is predominantly composed of O (2p) and Ti (3d) orbitals, with a minor contribution from Bi (6s) states. In the conduction band (CB), the lower energy range, from 3 to 8.8 eV, is mainly composed of Ti (3d) and Bi (6p) states, while the higher range, from 10 eV to 12 eV, is primarily contributed by Na (2p) orbitals.

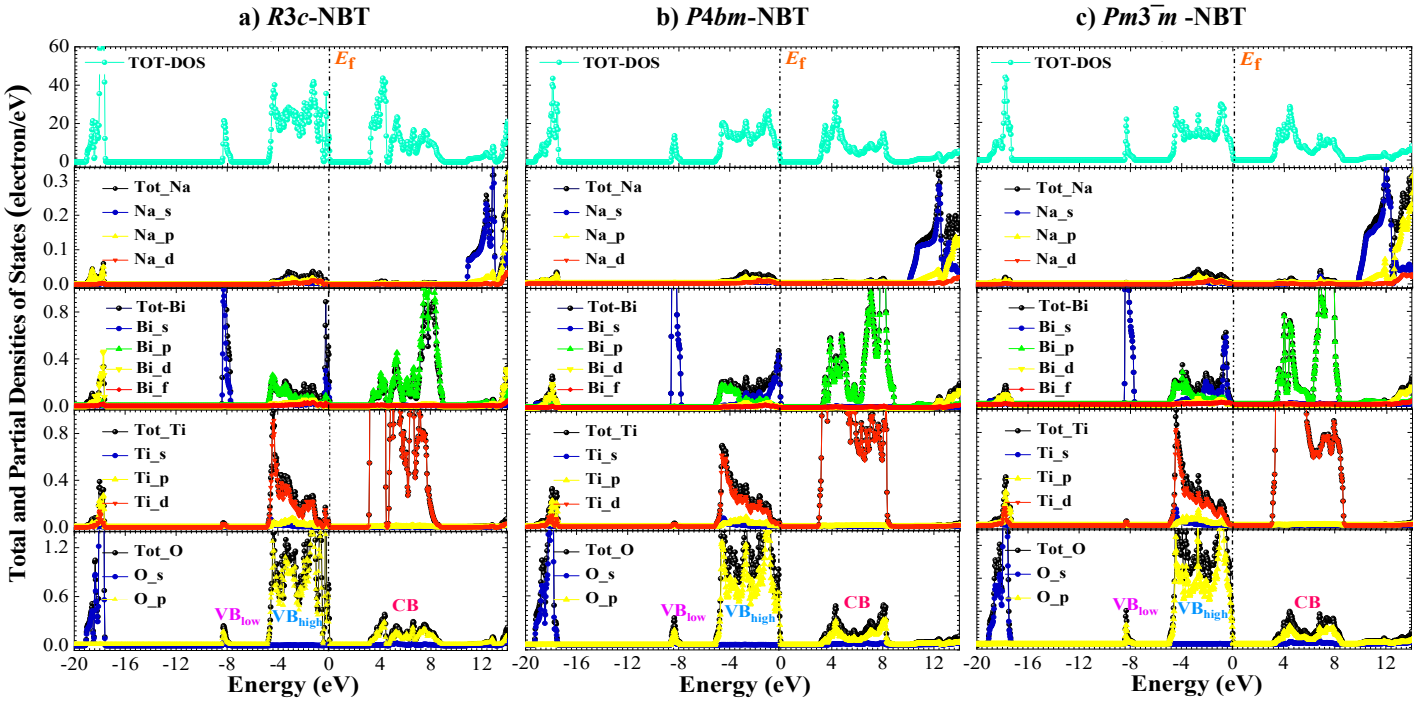

Figure III.5: Calculated total (DOS) and partial (PDOS) densities of states for (a) *R*3*c*-NBT, (b) *P*4*bm*-NBT, and (c) *Pm*$\bar{3}$*m*-NBT crystals, using the KTB–mBJ+so functional.

C. Electronic Charge Density

The distribution of electron charge density provides insight into the nature of chemical bonding among the ions in NBT crystals. Contour maps illustrating the charge density distributions for the three phases of $Na_{0.5}Bi_{0.5}TiO_3$, calculated using the KTB–mBJ+so functional, are presented in Figure III.7. Examination of these maps reveals a significant concentration of charge along the circumference of circles surrounding Na and Bi atoms, interacting with neighboring O atoms across all three structures. This observation confirms the prevalence of ionic bonds, particularly O–Na and O–Bi bonds, attributed to the substantial difference in Pauling electronegativity between O and the Na/Bi constituents. Additionally, covalent bonding between Ti and O atoms is evident in the contour maps for all structures. Furthermore, it is apparent that the bonding interaction between O and Bi atoms is stronger compared to that between O and Na atoms.

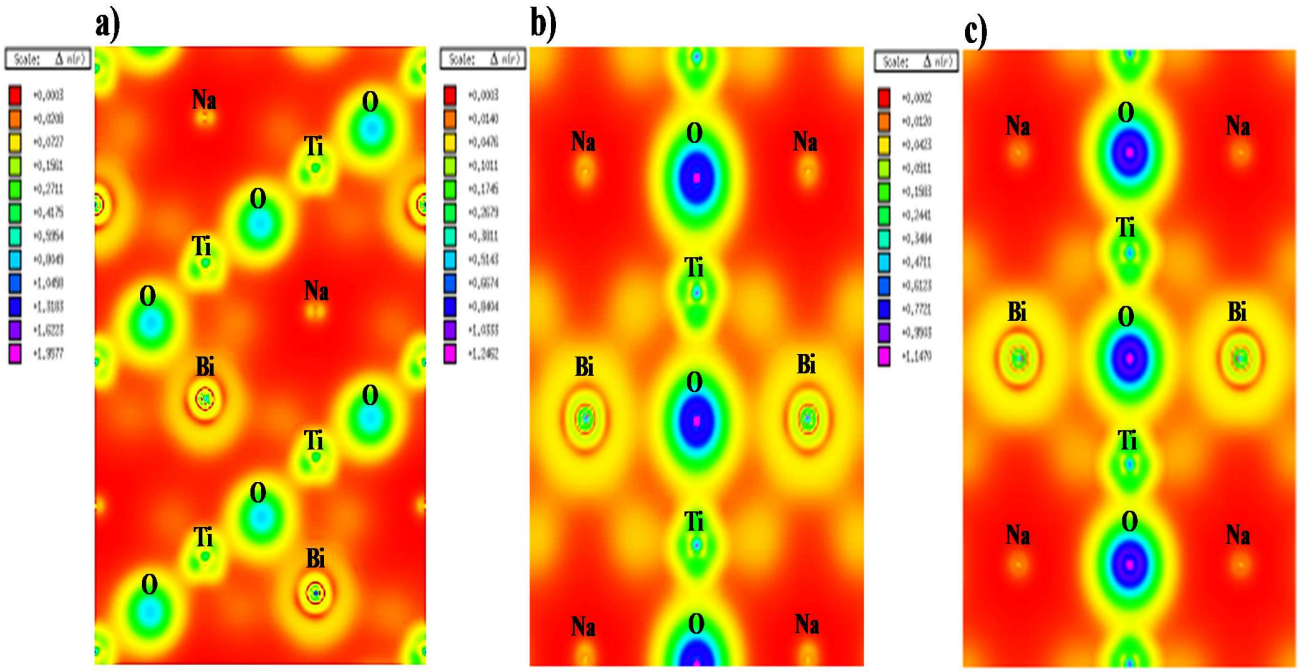

Figure-III.6: Computed charge density contours for $Na_{0.5}Bi_{0.5}TiO_3$ (NBT) in the (a) (120)-plane for *R*3*c*, (b) (100)-plane for *P*4*bm*, and (c) (110)-plane for $Pm\bar{3}m$ symmetries, using the KTB–mBJ+so functional.

III.5. Elastic and Mechanical Properties

A. Elastic Stiffness Constants (C_{ij})

Understanding elastic constants is essential for evaluating key mechanical properties of solids, such as stiffness, hardness, brittleness/ductility, stability, and bonding characteristics. In this section, we present the calculation of elastic stiffness constants (Cij) for $Na_{0.5}Bi_{0.5}TiO_3$ (NBT) crystals across their rhombohedral, tetragonal, and cubic crystallographic phases. The calculations were performed using the stress-strain method, where the total energy as a function of strain was analyzed [42,43]. This method is described by the relationship:

$$C_{ijkl} = \frac{\partial^2 E}{\partial \delta_{ij} \partial \delta_{kl}}, \tag{3}$$

where E, δ_{ij}, δ_{kl} denote the total energy, stress and strain tensors, respectively.

In the *R*3*c*, *P*4*bm*, and $Pm\bar{3}m$ symmetries, we considered six (C_{11}, C_{12}, C_{13}, C_{14}, C_{33}, C_{44}), six (C_{11}, C_{12}, C_{13}, C_{33}, C_{44}, C_{66}), and three (C_{11}, C_{12}, C_{44}) independent single elastic constants [44], respectively. There corresponding stiffness matrix notation C_{ij} are represented as flow:

$$C_{ij}(R3c) = \begin{pmatrix} C_{11} & C_{12} & C_{13} & C_{14} & 0 & 0 \\ C_{12} & C_{11} & C_{13} & -C_{14} & 0 & 0 \\ C_{13} & C_{13} & C_{33} & 0 & 0 & 0 \\ C_{14} & -C_{14} & 0 & C_{44} & 0 & 0 \\ 0 & 0 & 0 & 0 & C_{44} & C_{14} \\ 0 & 0 & 0 & 0 & C_{14} & C_{66} \end{pmatrix}, \tag{4}$$

$$C_{ij}(P4bm) = \begin{pmatrix} C_{11} & C_{12} & C_{13} & 0 & 0 & 0 \\ C_{12} & C_{11} & C_{13} & 0 & 0 & 0 \\ C_{13} & C_{13} & C_{33} & 0 & 0 & 0 \\ C_{14} & -C_{14} & 0 & C_{44} & 0 & 0 \\ 0 & 0 & 0 & 0 & C_{44} & 0 \\ 0 & 0 & 0 & 0 & 0 & C_{66} \end{pmatrix}, \tag{5}$$

$$C_{ij}(Pm\bar{3}m) = \begin{pmatrix} C_{11} & C_{12} & C_{12} & 0 & 0 & 0 \\ C_{12} & C_{11} & C_{12} & 0 & 0 & 0 \\ C_{12} & C_{12} & C_{11} & 0 & 0 & 0 \\ 0 & 0 & 0 & C_{44} & 0 & 0 \\ 0 & 0 & 0 & 0 & C_{44} & 0 \\ 0 & 0 & 0 & 0 & 0 & C_{44} \end{pmatrix}. \quad (6)$$

where, $C_{66} = \frac{C_{11} - C_{12}}{2}$.

Table III.3 summarizes the elastic constants (C_{ij}) obtained using the GGA–PBEsol and GGA–WC approximations, along with others experimental and theoretical results. The C_{ij} values obtained for the *R*3*c*-NBT crystal are higher than the experimental value reported by [45]. This discrepancy is likely due to the fact that quantum mechanical methods predict values at T = 0 K, where the crystal volume is minimized [46]. To the best of our knowledge, no other experimental studies are available to validate our computational results through comparison. Additionally, it can be observed that the *R*3*c*-NBT, *P*4*bm*-NBT, and *Pm*$\bar{3}$*m*-NBT crystals exhibit smaller C_{ij} values compared to those previously reported using the GGA–PBE approach by Bujakiewicz-Korońska et al. [46]. Therefore, the newly proposed GGA–PBEsol and GGA–WC methods are considered among the most reliable for predicting C_{ij} values that are consistent with experimental data [7,47].

The shear elastic constant C_{11} associates to the material's resistance to unidirectional compression along the [100] axis under uniaxial strain [48], while the elastic constant C_{44} corresponds the resistance to shear deformation [49]. NBT exhibits higher C_{11} values compared to C_{12} and C_{44} across the three symmetries, indicating that the crystals are more resistant to unidirectional compression than to shear deformation. Additionally, the elastic stiffness constants C_{11} and C_{33}, as well as C_{44} and C_{66}, show relatively close values due to the minor distortion in the rhombohedral structure, which aligns with experimental findings [45]. Furthermore, we propose that the NBT crystal exhibits greater rigidity in the cubic symmetry compared to the tetragonal and rhombohedral symmetries, as indicated by the highest value of C_{11} (see Table III.3). Empirical findings also show that the elastic stiffness constant C_{11} of NBT increases as the temperature approaches zero [45].

Table III.3: Presents the calculated elastic constants (C_{ij}), bulk modulus (B), shear modulus (G), Young's modulus (Y), Poisson's ratio (ν), and Frantesvich ratio (G/B) for $Na_{0.5}Bi_{0.5}TiO_3$ (NBT) in its rhombohedral, tetragonal, and cubic phases, using GGA–PBEsol and GGA–WC approximations, compared to experimental data and other theoretical studies.

Crystals		C_{11}	C_{12}	C_{13}	C_{14}	C_{33}	C_{44}	C_{66}	B	G	Y	ν	G/B
Rhomb (*R3c*)	PBEsol	266.1	120.5	71.34	−21.31	202.0	40.73	72.82	137.2	55.45	146.6	0.322	0.404
	WC	263.1	117.3	70.37	−21.46	202.2	38.48	72.92	135.7	53.95	142.9	0.324	0.397
	Expt. [45]	153.9	18.7	52.1	−1.7	168.1	82.3	67.6	95.2		138.0		
	Theo.[46]	368.8	120.3	141.1		303.5	142.1	153.6	205.1				
Tetrag (*P4bm*)	PBEsol	274.5	99.31	143.7		321.6	97.37	124.32	180.6	94.41	241.2	0.277	0.522
	WC	276.5	98.17	146.8		326.6	95.74	124.76	182.3	94.09	240.8	0.279	0.516
	Theo.[46]	328.7	96.9	115.9		318.4	95.05	115.3	168.3				
Cubic (*Pm$\bar{3}$m*)	PBEsol	330.2	117.9				91.90		188.7	97.37	249.2	0.279	0.516
	WC	329.3	112.3				93.98		184.6	99.54	253.1	0.271	0.539
	Theo.[46]	394.3	96.9				108.0		197.3				

B. Mechanical Behavior

The Born mechanical stability criteria for the cubic crystal system are expressed by the following relations [44,50]:

For the cubic crystal system:

$$C_{11}-C_{12}\rangle 0;\quad C_{11}+2C_{12}\rangle 0;\quad C_{11}\rangle 0;\quad C_{44}\rangle 0,$$

For the tetragonal crystal system:

$$C_{11}\rangle |C_{12}|;\quad 2C_{13}^2\langle C_{33}(C_{11}+C_{12});\quad C_{44}\rangle 0;\quad C_{66}\rangle 0,$$

For the rhombohedral crystal system:

$$C_{11}\rangle |C_{12}|;\quad C_{44}\rangle 0;\quad C_{13}^2\langle \frac{1}{2}C_{33}(C_{11}+C_{12});\quad C_{14}^2\langle \frac{1}{2}C_{44}(C_{11}-C_{12}).$$

The calculated elastic stiffness constants satisfy the mechanical stability criteria for the cubic, tetragonal, and rhombohedral phases, confirming that $Na_{0.5}Bi_{0.5}TiO_3$ (NBT) crystals are elastically stable under pressure.

The mechanical properties, including the bulk modulus (B), shear modulus (G), Young's modulus (Y), and Poisson's ratio (ν), for the three phases of NBT crystals were

derived from the elastic constants C_{ij} using the Voigt–Reuss–Hill (VRH) scheme [51,52]. The results are summarized in Table 3.

The bulk modulus is defined as the ratio of hydrostatic pressure to the relative change in volume, reflecting the material's resistance to fracturing. The shear modulus measures a material's ability to resist shape changes under constant volume and is indicative of its capacity for plastic deformation [53]. It can also serve as a better predictor of hardness [49]. The Young's modulus is a measure of stiffness; a high Young's modulus indicates a stiffer material [49]. Table III.3 presents nearly comparable projected values for the GGA–PBEsol and GGA–WC approximations. The calculated bulk modulus for *R*3*c*-NBT is approximately 135.7 GPa, which is slightly higher than the experimental value of 95.2 GPa [45] but significantly greater than the previous PBE estimate of 205.1 GPa. Our results indicate that *R*3*c*-NBT exhibits greater resistance to volume deformation compared to other lead-based crystals [40] which is attributed to the interactions within the Ti-O bonds [54].

The predicted values for Young's modulus (Y) and shear modulus (G) are relatively high across all three phases, indicating that the material is hard and stiff. For the *R*3*c*-NBT phase, the Young's modulus is calculated to be 142 GPa (with WC), which is in close agreement with the experimentally measured value of 135.7 GPa reported by Suchanicz et al. [45]. This value is significantly higher than that of PZT material, which has a Young's modulus of approximately 65 GPa [45]. The results demonstrate that the elastic modulus of $Na_{0.5}Bi_{0.5}TiO_3$ in the cubic phase is considerably greater than in the tetragonal and rhombohedral phases. This enhanced modulus is attributed to the strong covalent interactions between Ti and O atoms in the cubic structure, as depicted in Figure III.7 [55,56]. These findings indicate that $Na_{0.5}Bi_{0.5}TiO_3$ (NBT) possesses a robust resistance to mechanical stresses, making it an ideal candidate for applications in piezoelectric devices such as bulk acoustic wave resonators (TFBARs), transducers, and actuators [57].

The Frantesvich G/B ratio serves as a criterion for assessing the brittleness or ductility of solids [58]. A crystal is classified as ductile if the G/B ratio is less than 0.571 and as brittle if it exceeds 0.571. The calculated G/B ratios for $Na_{0.5}Bi_{0.5}TiO_3$ in all three phases are below 0.571, suggesting that the crystal is likely to be ductile. Poisson's ratio (ν) can be

used to infer the type of bonding within the material. Covalent materials typically have ν values below 0.1, while ionic materials generally have ν values around 0.25 [59]. Using the GGA-WC approach, Poisson's ratio values of 0.324, 0.279, and 0.271 were obtained for the R3c, P4bm, and $Pm\bar{3}m$ crystal symmetries, respectively, indicating ionic bonding in $Na_{0.5}Bi_{0.5}TiO_3$. However, as evidenced by the charge density distributions, $Na_{0.5}Bi_{0.5}TiO_3$ displays a combination of ionic and covalent bonding characteristics. This suggests that Poisson's ratio alone is insufficient to fully describe the bonding properties of the material.

Additionally, we examined elastic anisotropy by analyzing the directional dependence of the Young's modulus, shear modulus, and bulk modulus in $Na_{0.5}Bi_{0.5}TiO_3$ crystals. For the trigonal (class 3m), tetragonal (class 4mm), and cubic systems, the Young's modulus can be expressed as [60]:

$$Y^{tr}(\theta,\phi) = \{S_{11}\sin^4\theta + S_{33}\cos^4\theta + (2S_{13}+S_{44})\cos^2\theta\sin\theta^2 + 2S_{14}\sin\theta\cos\theta\sin\phi[3(\sin\theta\cos\phi)^2 - (\sin\theta\sin\phi)^2]\}^{-1}, \quad (7)$$

$$Y^{t}(\theta,\phi) = \{S_{11}[(\sin\theta\cos\phi)^4 + (\sin\theta\sin\phi)^4] + S_{33}\cos^4\theta + (2S_{12}+S_{66})(\sin\theta\cos\phi)^2(\sin\theta\sin\phi)^2 + (2S_{13}+S_{44})\cos^2\theta\sin^2\theta\}^{-1}, \quad (8)$$

$$Y^{c}(\theta,\phi) = \left\{S_{11} - 2\left(S_{11} - S_{12} - \frac{S_{44}}{2}\right)[(\sin\theta\cos\phi)^2(\sin\theta\sin\phi)^2 + \cos\theta^2(\sin\theta\sin\phi)^2 + \cos\theta^2(\sin\theta\cos\phi)^2]\right\}^{-1}. \quad (9)$$

For the crystals under consideration, the shear modulus can be expressed as [61]:

$$G^{tr}(\theta,\phi) = \left\{S_{44} + \left(S_{11} - S_{12} - \frac{S_{44}}{2}\right)\sin^2\theta + 2(S_{11}+S_{33}-2S_{13}-S_{44})\cos^2\theta - 4S_{14}\sin\theta\cos\theta\sin\phi[3(\sin\theta\cos\phi)^2 - (\sin\theta\sin\phi)^2]\right\}^{-1}, \quad (10)$$

$$G^{t}(\theta,\phi) = \left\{\frac{1}{2}[(S_{44}+S_{66})(\sin\theta\cos\phi)^2 + \ldots + \left[2(S_{11}+S_{33}) - 4S_{13} + \frac{1}{2}(S_{44}+S_{66}) - S_{44}\right]\cos^2\theta(\sin\theta\sin\phi)^2\right\}^{-1}, \quad (11)$$

$$G^c(\theta,\phi)=\left\{S_{44}+4\left(S_{11}-S_{12}-\frac{S_{44}}{2}\right)\left[\cos^2\theta(\sin\theta\sin\phi)^2+\cos^2\theta(\sin\theta\cos\phi)^2\right.\right.$$
$$\left.\left.+(\sin\theta\cos\phi)^2(\sin\theta\sin\phi)^2\right]\right\}^{-1}. \quad (12)$$

For crystals with 3m, 4mm, and cubic symmetries, the bulk modulus can be expressed as [62]:

$$B^{tr,t}=\left\{(S_{11}+S_{12}+S_{13})-(S_{11}+S_{12}-S_{13}-S_{33})\cos^2\theta\right\}^{-1}, \quad (13)$$

and

$$B^c=\{S_{11}+2S_{12}\}^{-1}. \quad (14)$$

We employed Eqs (7–14) to generate 3D surface plots of the bulk, shear, and Young's moduli for the rhombohedral, tetragonal, and cubic phases of $Na_{0.5}Bi_{0.5}TiO_3$ crystals, as shown in Figure III.8. The deviation of these moduli surfaces from a spherical shape provides insights into the material's elastic anisotropy. A material is considered isotropic if the moduli surfaces are spherical. The compressibility modulus data under hydrostatic pressure remains spherical, indicating that the $Na_{0.5}Bi_{0.5}TiO_3$ system is elastically isotropic in the three phases considered, consistent with previous reports [62]. Figure III.8 demonstrates that the surfaces of the shear and Young's moduli for the rhombohedral and tetragonal phases deviate from a spherical shape, suggesting elastic anisotropy in these structures. In contrast, the cubic phase shows only a slight deviation, indicating low elastic anisotropy. The shear and Young's moduli of rhombohedral crystals exhibit a significant directional dependency compared to the tetragonal and cubic structures.

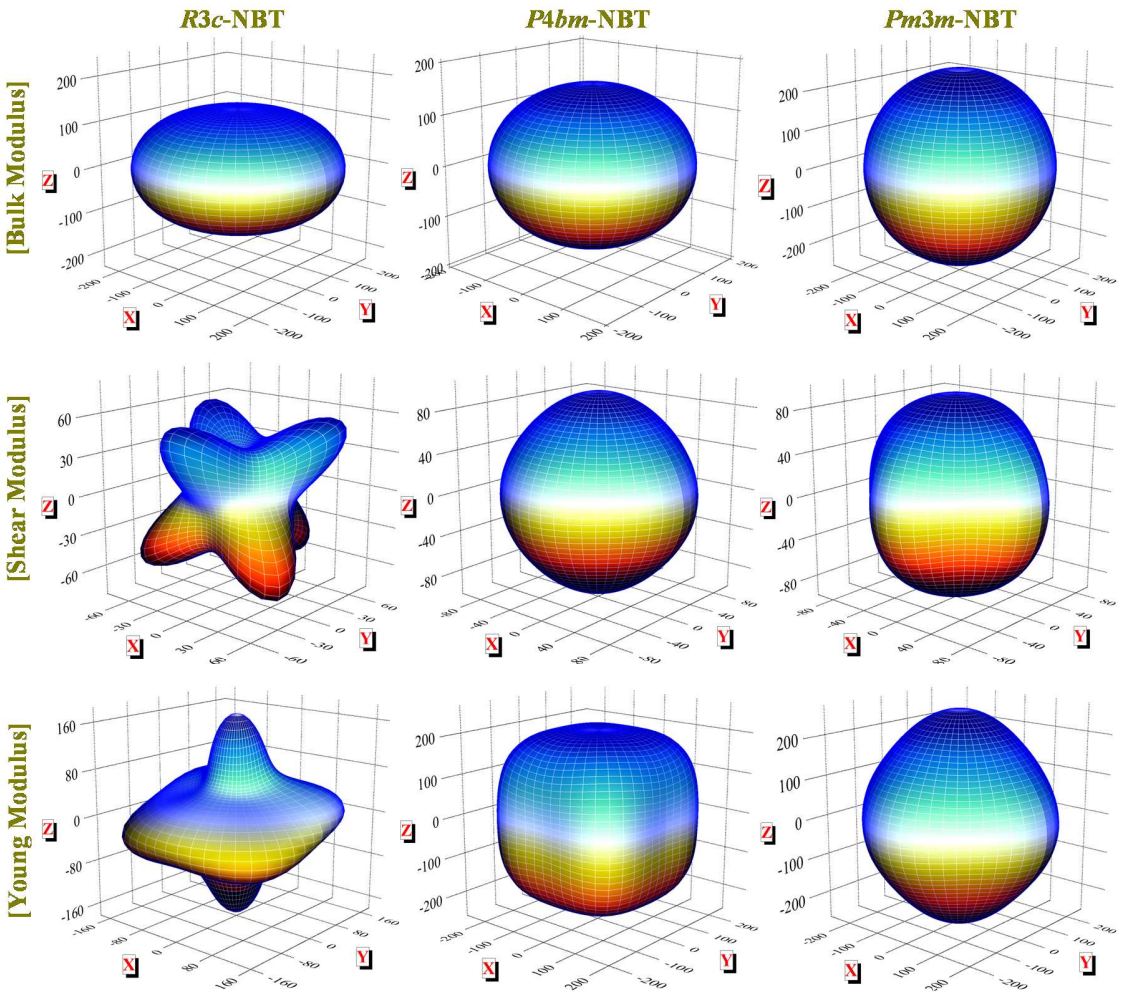

Figure III.7: Directional dependence of the bulk modulus, shear modulus, and Young's modulus for $Na_{0.5}Bi_{0.5}TiO_3$ (NBT) crystals: (a) R3c symmetry, (b) P4bm symmetry, and (c) $Pm\bar{3}m$ symmetry.

C. Sound Wave Velocities

The density (ρ) and acoustic wave velocities—longitudinal (v_l), transverse (v_t), and average (v_p)—were calculated using the GGA-PBEsol and GGA-WC approximations for the three phases of perovskite $Na_{0.5}Bi_{0.5}TiO_3$. The longitudinal (v_l), transverse (v_t), and average (v_p) acoustic velocities are determined using Napier's equations [63]. The estimated results are detailed in Table III.4. The predicted density of 6.04 g/cm³ for R3c−NBT closely matches the experimental value of approximately 6 g/cm³ [45]. This density is lower than that of PZT

ceramics, which is about 8 g/cm³ [45]. As the structure transitions to cubic ($Pm\bar{3}m$) and tetragonal (P4bm) symmetries, the density increases to 6.08 g/cm³ and 6.2 g/cm³, respectively, due to reduced porosity in the NBT structures. Table 4 shows that NBT with cubic symmetry has high acoustic wave velocities, with longitudinal (v_l), transverse (v_t), and average (v_p) velocities of approximately 7236, 4000, and 4457 m/s, respectively. These velocities decrease when the structure changes to tetragonal symmetry, with values of around 7031, 3898, and 4342 m/s, and further decrease in the rhombohedral phase, with values of approximately 5909, 3027, and 3391 m/s. The observed reduction in acoustic velocities is attributed to the increased atomic weights in these NBT crystals. To date, no experimental data are available in the literature for comparison of acoustic velocities in these phases.

Table III.4: Calculated density (ρ) in g/cm³, longitudinal (v_l), transverse (v_t), and average (v_p) acoustic wave velocities in m/s for the rhombohedral, tetragonal, and cubic phases of perovskite $Na_{0.5}Bi_{0.5}TiO_3$ (NBT).

Crystals		ρ	v_l	v_t	v_m
Rhombohedral (*R3c*)	**PBEsol**	6.04	5909	3027	3391
	WC	6.04	5862	2987	3348
	Expt. [45]	6.00			
Tetragonal (*P4bm*)	**PBEsol**	6.20	7031	3898	4342
	WC	6.19	7051	3898	4343
Cubic ($Pm\bar{3}m$)	**PBEsol**	6.08	7236	4000	4457
	WC	6.09	7215	4040	4497

III.6. Piezoelectric Properties Analysis

A. Piezoelectric and Dielectric Parameters

$Na_{0.5}Bi_{0.5}TiO_3$ (NBT) stands out as a promising lead-free piezoelectric material, ideal for use in ultrasonic transducers, actuators, sensors, and dynamic random-access memory (DRAM) [64]. The piezoelectric constants are vital for designing and modeling electronic devices, as higher values can significantly enhance device performance and improve the efficiency of converting electrical energy into mechanical energy.

In its R3c symmetry form, $Na_{0.5}Bi_{0.5}TiO_3$ (NBT) features four independent piezoelectric coefficients: e_{22}, e_{15}, e_{31} and e_{33} [65]. Conversely, NBT with P4bm symmetry has three independent piezoelectric coefficients: e_{15}, e_{31} and e_{33} [65]. Both R3c and P4bm symmetries of NBT also exhibit two independent dielectric coefficients: ϵ_{11} and ϵ_{33} [65]. The piezoelectric stress coefficients e_{ij} characterize the interaction between the electrical polarization Pi and the strain tensor ε_{ij}, as detailed by [67]:

$$e_{ijk} = \left(\frac{dP_i}{d\varepsilon_{jk}} \right), \tag{18}$$

where P_i represents the polarization vector, ε_{ij} is the strain tensor element, and i,j,k= {1, 2, 3} range over {1, 2, 3}, where 1, 2, and 3 correspond to the x, y, and z Cartesian directions, respectively.

For a rhombohedral structure, the matrix notation for e_{ij} is:

$$e_{ij} = \begin{pmatrix} 0 & 0 & 0 & 0 & e_{15} & -e_{22} \\ -e_{22} & e_{22} & 0 & e_{15} & 0 & 0 \\ e_{31} & e_{31} & e_{33} & 0 & 0 & 0 \end{pmatrix}, \tag{19}$$

For a tetragonal structure, the matrix notation for e_{ij} is:

$$e_{ij} = \begin{pmatrix} 0 & 0 & 0 & 0 & e_{15} & 0 \\ 0 & 0 & 0 & e_{15} & 0 & 0 \\ e_{31} & e_{31} & e_{33} & 0 & 0 & 0 \end{pmatrix}, \tag{20}$$

The piezoelectric coefficient d_{ij} can be derived from the piezoelectric stress tensor e_{ij} and the elastic constants C_{ij} using the following formula [67]:

$$e_{ij} = \sum_{k=1}^{6} d_{ik} C_{kj}, \tag{21}$$

In Voigt notation, the elastic constants C_i are represented with indices i, j=1, 2, 3, 4, 5, 6, while the piezoelectric tensors e_{ij} and d_{ik} use indices i=1, 2, 3 and and j, k = 1, 2, 3, 4, 5, 6.

The analytical solutions for the piezoelectric coefficients d_{ij}, obtained by solving Eq. (21) for a rhombohedral symmetry crystal, are explicitly expressed in Voigt notation as follows:

$$d_{31} = \frac{C_{33}e_{31} - C_{13}e_{33}}{(C_{11} + C_{12})C_{33} - 2C_{13}^2}, \quad (22)$$

$$d_{33} = \frac{(C_{11} + C_{12})e_{33} - 2C_{13}e_{31}}{(C_{11} + C_{12})C_{33} - 2C_{13}^2}, \quad (23)$$

$$d_{15} = \frac{(C_{11} - C_{12})e_{15} + C_{14}e_{22}}{(C_{11} - C_{12})C_{44} - C_{14}^2}, \quad (24)$$

$$d_{22} = \frac{C_{44}e_{22} + C_{14}e_{15}}{(C_{11} - C_{12})C_{44} - C_{14}^2}, \quad (25)$$

For tetragonal crystal symmetry, the analytical solutions for the piezoelectric coefficients d_{ij} are:

$$d_{31} = \frac{C_{33}e_{31} - C_{13}e_{33}}{(C_{11} + C_{12})C_{33} - 2C_{13}^2}, \quad (26)$$

$$d_{33} = \frac{(C_{11} + C_{12})e_{33} - C_{13}e_{31}}{(C_{11} + C_{12})C_{33} - 2C_{13}^2}, \quad (27)$$

$$d_{15} = \frac{e_{15}}{C_{44}}. \quad (28)$$

The piezoelectric coefficients (e_{ij}, d_{ij}) and static dielectric tensors (ϵ_{ij}) for both the rhombohedral and tetragonal phases of $Na_{0.5}Bi_{0.5}TiO_3$ crystals were calculated using density functional perturbation theory (DFPT) [15] within the plane-wave pseudopotential framework and the GGA–PBE exchange potential. The results are summarized in Table III.5.

The piezoelectric coefficients for the R3c-NBT system are e_{31}= 1.94 C/m², e_{15}= 3.40 C/m², and e_{33}= 3.01 C/m², which are notably lower compared to those of the P4bm-NBT crystal, where the values are 9.84 C/m², 7.18 C/m², and 11.61 C/m², respectively. The d_{33} piezoelectric constant for R3c-NBT is 21.22 pC/N, which is less than the experimental values of 72.18 pC/N [67] and 75.24 pC/N [68]. The d_{31} value is 8.93 pC/N, lower than the experimental measurement of 15.0 pC/N [69]. On the other hand, the d_{15} value of 96.4

pC/N for R3c-NBT is relatively close to the experimental value of 87.3 pC/N [69]. The d_{22} value is 21.2 pC/N. It is important to note that the GGA–PBE approximation within DFT tends to underestimate piezoelectric coefficients, as noted by other researchers [8,70]. For the P4bm-NBT crystal, the piezoelectric coefficients are d_{31}= – 51.3 pC/N, d_{15} = 101.0 pC/N, and d_{33} = 81.8 pC/N. These values are significantly higher than those for R3c-NBT, likely due to the greater distortion and higher permittivity (ϵ_{33}) of the tetragonal NBT structure [48], as corroborated by Wan et al. [70]. The relatively modest piezoelectric properties are attributed to the challenges in effectively poling the perovskite $Na_{0.5}Bi_{0.5}TiO_3$ (NBT) due to its high conductivity and large coercive field [69,71]. Compared to conventional perovskite ferroelectrics like $PbZr_xTi_{1-x}O_3$ (410 pC/N [72]), $Ba_{1-x}Sr_xTiO_3$ (133 pC/N [73]), and $K_{0.5}Na_{0.5}NbO_3$ (160 pC/N [74]), the piezoelectric coefficients of NBT are relatively small. However, they are comparable to those of $BaTiO_3$ (90 pC/N [75]) and $PbTiO_3$ (79.1 pC/N [75]), and are substantially higher than those of semiconductor materials such as AlN (~5.6 pC/N [76]), GaN (~3.1 pC/N [77]), $Sc_{0.43}Al_{0.57}N$ (~24.6 pC/N [78]), $Y_{0.5}In_{0.5}N$ (~23.31 pC/N [79]), and $Y_{0.3t-0.625}N$ (~17.5 pC/N [47]). Thus, lead-free $Na_{0.5}Bi_{0.5}TiO_3$ remains a strong candidate for advanced piezoelectric devices such as BAW resonators and RF filters [80]. Additionally, NBT with tetragonal symmetry exhibits high static dielectric tensors, with ϵ_{11} = 274.8 and ϵ_{33} = 163.5, making it a promising option for dynamic random-access memory (DRAM) applications [81]. In contrast, the dielectric tensors for NBT in rhombohedral symmetry are lower, with ϵ_{11} = 48.93 and ϵ_{33} = 20.42, aligning with previous theoretical values of 43.81 and 31.37, respectively [18].

Table III.5: Computed values for piezoelectric strain coefficients (d_{ij}, in pC/N), piezoelectric stress coefficients (e_{ij}, in C/m^2) and dielectric constants (ϵ_{ij}) for ferroelectric $Na_{0.5}Bi_{0.5}TiO_3$ (NBT) crystals.

Crystals		d_{22}	d_{15}	d_{31}	d_{33}	e_{22}	e_{15}	e_{31}	e_{33}	ϵ_{11}	ϵ_{33}
Rhombohedral (R3c)	**PBE**	21.2	96.4	–8.93	21.2	1.55	3.40	–1.94	3.01	48.93	20.42
	Expt. [69]		87.3	–15.0	72.9						
	[75]				72.1						
	[68]				75.2						
	Theor. [18]									43.81	31.37
Tetragonal (P4bm)	**PBE**		101.0	–50.3	81.1		9.84	–7.18	11.61	274.8	163.5

B. Directional Dependence of the Piezoelectric Coefficient

The longitudinal piezoelectric coefficient d_{33}^* (in pm/V) provides insight into how the piezoelectric response of a crystal depends on its orientation [82]. For the tetragonal system (class 4mm), this coefficient in any given direction, as a function of the angle θ from the polar axis, can be described by [51]:

$$d_{33}^*(\theta) = \cos\theta \sin^2\theta d_{31} + \cos\theta \sin^2\theta d_{15} + \cos^3\theta d_{33} \quad (29)$$

For the rhombohedral system (class 3m), the piezoelectric coefficient d_{33}^* depends on two Euler angles, θ and ϕ. It is expressed by the following relation [51]:

$$d_{33}^*(\theta,\phi) = \cos\theta \sin^2\theta \sin^2\phi(d_{15} + d_{31}) + \sin^3\theta \cos\phi(3\sin^2\phi - \cos^2\phi)d_{22} + \cos^3\theta d_{33} \quad (30)$$

We compute the orientation dependence of the piezoelectric coefficients using Eqs. (29) and (30) for both the rhombohedral (R3c) and tetragonal (P4bm) phases of $Na_{0.5}Bi_{0.5}TiO_3$ (NBT) crystals, as depicted in Figure III.9.

The surface forms of $d_{33}^*(\theta,\phi)$ for the rhombohedral and tetragonal phases of $Na_{0.5}Bi_{0.5}TiO_3$ (NBT) are comparable to those of other perovskite ferroelectrics with similar point groups, such as $BaTiO_3$ [83,84], $PbTiO_3$ [83], and PZT [84]. In the rhombohedral phase, NBT exhibits pronounced piezoelectric anisotropy due to ferroelectric-ferroelectric phase transitions [85], as shown in Figure III.9(a). Figure III.9(b) illustrates the relatively mild piezoelectric anisotropy in the tetragonal phase of NBT. Additionally, the data in Figure III.9 indicates that the maximum piezoelectric response for tetragonal symmetry occurs along the [001] polar direction, suggesting that P4bm-NBT behaves as an extender ferroelectric. In contrast, for rhombohedral symmetry, the highest piezoelectric response is observed away from the vertical polar direction, indicating that R3c-NBT functions as a rotator ferroelectric. This behavior is attributed to the significantly larger shear coefficient d_{15} compared to the longitudinal coefficient d_{33} in R3c-NBT, resulting in a stronger piezoelectric response away from the polar axis, unlike in P4bm-NBT. This

finding is consistent with the observations of Davis et al. [83] and Damjanovic et al. [84] regarding $BaTiO_3$ and $PbTiO_3$.

Rotator ferroelectrics include materials like PMN-33PT, $BaTiO_3$, $KNbO_3$, and PZN-9PT, whereas $PbTiO_3$ is classified as an extender ferroelectric [83]. For the rhombohedral NBT system, we calculate a value of d_{33}^{*} = 39.24 pC/N for the [69] direction (with ϕ = 0°and θ = 54.74°), nearly twice the mono-domain value of (d_{33} = 21.2 pC/N). The value of d_{33}^{*} for the [001] direction is 26.72 pC/N for (with ϕ = 60° and θ = 35.26°). These values are smaller than the measured value of 131 pC/N [86], which is about twice the mono-domain experimental value of 72 pC/N reported by Fujii et al. [86]. For the tetragonal NBT crystal, we obtain d_{33}^{*} = 46.59 pC/N for the $[69]_c$ direction (with ϕ = 90°, θ = 45°), and d_{33}^{*} = 35.96 pC/N for the $[111]_c$ direction (with ϕ = –45°, θ = –54.74°). Thus, domain engineering enhances the longitudinal piezoelectric coefficient d_{33}^{*} in the rotator ferroelectric R3c-NBT, whereas the piezoelectric coefficient in the extender ferroelectric P4bm-NBT peaks along the polar axis. davis et al. [75] provide a comprehensive description of domain-engineered structures and the relevant Euler angles (ϕ and θ) for coordinate transformations across different crystal point groups.

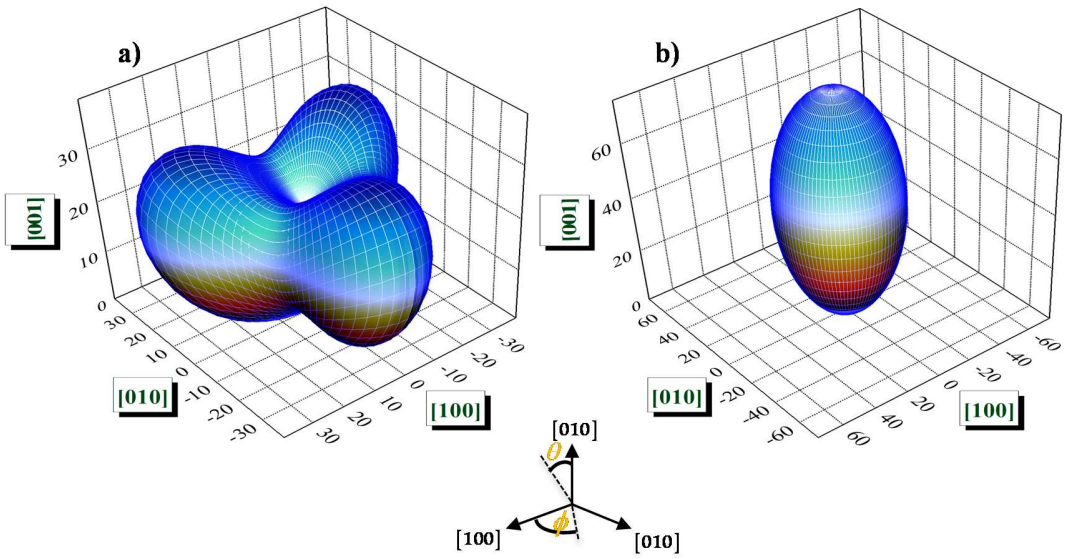

Figure III.8: Orientation dependence of $d_{33}^{*}(\theta,\phi)$ in (a) rhombohedral and (b) tetragonal phases of $Na_{0.5}Bi_{0.5}TiO_3$ (NBT) crystals. The minimum and maximum piezoelectric constants are observed along the [010] direction. The coordinate system corresponds to the crystallographic axes.

III.7. Thermodynamic Properties

In this section, the Gibbs2 code, developed by Blanco et al. [87], is utilized to analyze thermodynamic properties such as volume (V), bulk modulus (B), specific heat (Cv), thermal expansion (α), entropy (S), and Debye temperature (ΘD) for the $Na_{0.5}Bi_{0.5}TiO_3$ crystal in its rhombohedral (R3c) phase, within the temperature range of 0–1200 K. These thermodynamic properties are derived using the quasi-harmonic Debye model, which calculates energy-volume points [88]. In this model, the Gibbs free energy G* (V,P,T) is expressed as follows:

$$G^{*}(V,P,T) = E(V) + PV + A_{Vib}\left[\Theta_{D}(V),T\right], \tag{31}$$

where $E(V)$ represents the total energy per unit cell PV is the hydrostatic pressure term, $\Theta_D(V)$ is the Debye temperature, and A_{Vib} denotes the vibrational Helmholtz free energy.

The vibrational Helmholtz free energy can be expressed as follows [87]:

$$A_{vib}(\Theta_D,T) = nKT\left[\frac{9\Theta_D}{8T} + 3\ln\left(1-e^{\frac{-\Theta_D}{T}}\right) - D\left(\frac{\Theta_D}{T}\right)\right], \tag{32}$$

where n is the number of atoms per unit cell, and $D(\Theta_D/T)$ denotes the Debye integral. For an isotropic solid with a Poisson's ratio σ, the Debye temperature Θ_D is expressed as:

$$\Theta_D = \frac{\hbar}{K}\left[6\pi^2 V^{1/2} n\right]^{1/3} f(\sigma)\sqrt{\frac{B_s}{M}}, \tag{33}$$

where M represents the molecular mass per unit cell, and B_S is the adiabatic bulk modulus, which is estimated using the static compressibility:

$$B_s \cong B(V) = V\frac{d^2E(V)}{dV^2}, \tag{34}$$

The function $f(\sigma)$ is provided in references [89,90]. Thus, the minimum of the non-equilibrium Gibbs function, $G^*(V, P, T)$, can be determined by differentiating it with respect to the volume V:

$$\left[\frac{\partial G^*(V,P,T)}{\partial V}\right]_{P,T} = 0, \tag{35}$$

By solving Eq. (35), the thermal equation of state (*EOS*) $V(P, T)$ can be determined. The heat capacity $C_v(T)$ and the coefficient of thermal expansion α are given by [52]:

$$C_v = 3nK\left[4D\left(\frac{\theta_D}{T}\right) - \frac{3\Theta_D/T}{e^{\Theta_D/T}-1}\right], \tag{36}$$

$$\alpha = \frac{\gamma C_v}{B_T V}, \tag{37}$$

The Grüneisen parameter γ has several equally valid formulations. Some of these can be defined as follows:

$$\gamma = V\left(\frac{dP}{dE}\right)_V = -\frac{d\ln\Theta_D(V)}{d\ln(V)}, \tag{38}$$

B_T is the isothermal bulk modulus, defined by the equilibrium thermodynamic relation [87]:

$$B_T = -V\left(\frac{\partial P}{\partial V}\right)_T. \tag{39}$$

A. Pressure and Temperature Effects on Volume (V) and Bulk Modulus (B)

Figure III.10(a) illustrates how volume varies with temperature at different pressures. The volume shows a steady increase with temperature, though the rate of increase is quite

gradual. At zero pressure, the volume is approximately 2375 bohr^3, decreasing to about 1994 bohr^3 (P = 50 GPa) at a pressure of 50 GPa. Conversely, the bulk modulus B rises significantly with pressure, from 184 GPa at 0 GPa to 414 GPa at 50 GPa at ambient temperature (300 K), but slightly decreases to 175 GPa as the temperature increases to 600 K, as shown in Figure III.10(b). This observation suggests that the effect of reducing pressure on the material is similar to that of increasing temperature, indicating that higher temperatures lead to a decrease in the hardness of the crystals.

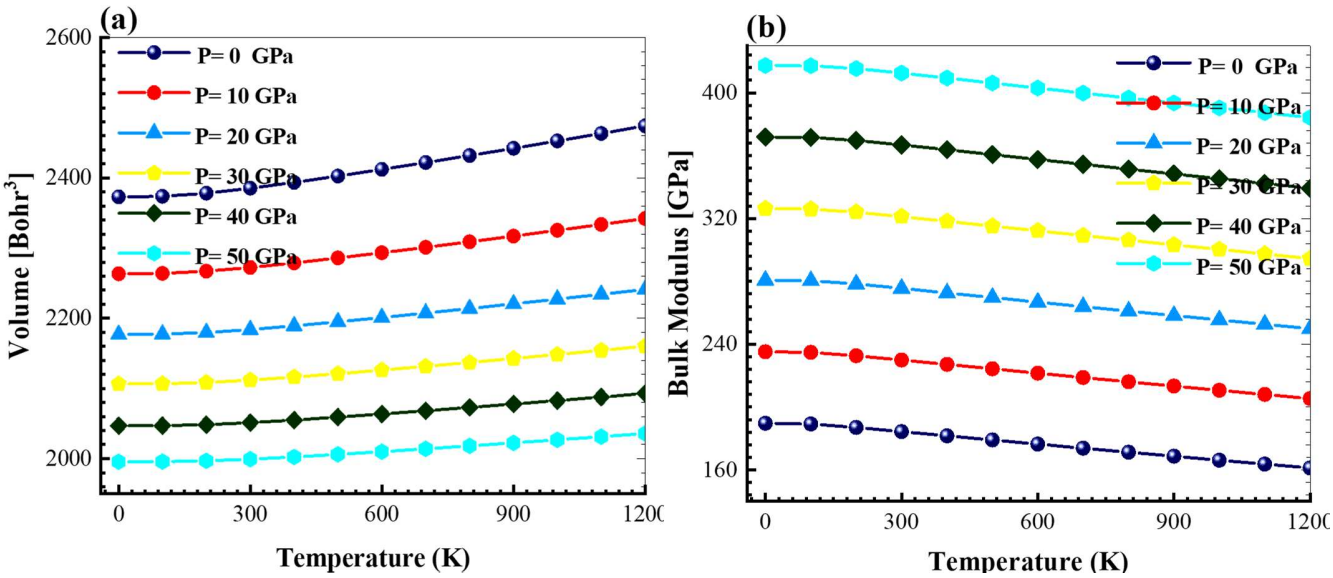

Figure III.9: Variation of (a) volume V and (b) compressibility modulus B with temperature under different pressures for the rhombohedral $Na_{0.5}Bi_{0.5}TiO_3$ crystal.

B. Specific Heat (*Cv*)

Heat capacity measures a material's ability to store heat as temperature changes and provides insights into various properties, such as lattice vibrations, which are crucial for many applications [91]. As shown in Figure III.10(a), the volume remains relatively stable with temperature changes. Consequently, we focus on the heat capacity at constant volume, *Cv* , in this section. Figure III.11(a) illustrates the variation of *Cv* with temperature at different pressures. At T=0 K, *Cv* is zero. At low temperatures (T < 800 K), *Cv* increases rapidly with

temperature, reflecting the Debye model's approximation. At higher temperatures, *Cv* becomes nearly temperature-independent and approaches a saturation value of 727.3 J/mol·K. This behavior, which aligns with the Dulong–Petit law, indicates that at high temperatures, thermal energy excites all phonon modes, a common characteristic of solids.

C. Thermal Expansion (α)

As the temperature of a material increases, its configuration changes, a phenomenon known as thermal expansion, denoted by "α". Figure III.11(b) illustrates the variation of thermal expansion α\alphaα with temperature at different pressures. As shown, α increases rapidly between 0 K and 400 K. Beyond this range, α continues to rise but at a slower, nearly linear rate, eventually reaching a constant value at higher temperatures. In this temperature range, α decreases sharply with increasing pressure, dropping from 4.0×10^{-5} K^{-1} at P= 0 GPa to 2.0×10^{-5} K^{-1} at P = 50 GPa. This decrease indicates that as the atoms gain kinetic energy, they vibrate and move more, increasing the interatomic distances and thus the material's expansion. However, applied pressure constrains the expansion of bond lengths, thereby reducing the overall thermal expansion.

According to standard classifications based on the coefficient of thermal expansion:

- Low expansion: $\Theta < \alpha <$ 2.10^{-6} K^{-1}.
- Intermediate expansion: 2.10^{-6} $K^{-1} < \alpha < 8.10^{-6}$ K^{-1}
- Strong expansion: $\alpha > 8.10^{-6}$ K^{-1}

Based on these classifications, our calculations suggest that the rhombohedral NBT system belongs to the strong expansion material group.

D. Entropy (S)

Entropy (S), an extensive property, measures the level of molecular disorder or randomness within a system. Figure III.11(c) illustrates how entropy S varies with temperature under different pressures. At very low temperatures, S increases sharply as the temperature T rises, primarily due to vibrational excitations from acoustic vibrations.

However, as pressure increases, S decreases gradually. For instance, at T = 300 K, entropy S decreases from 535 J/mol·K at 0 GPa to 322 J/mol·K at 50 GPa.

E. Debye Temperature (Θ_D)

The Debye temperature (Θ_D) is a crucial parameter in condensed matter physics, used to derive thermal properties of crystal structures. It represents the maximum vibrational energy of the system, where high-frequency modes possess energy on the order of k_{BT} and are effectively frozen at temperatures below Θ_D [92]. Figure III.11(d) presents the variation of Θ_D with temperature for different pressures in $Na_{0.5}Bi_{0.5}TiO_3$ crystals. At 0 K and 0 GPa, the Debye temperature is relatively high at 623.9 K, indicating that the $Na_{0.5}Bi_{0.5}TiO_3$ system in its rhombohedral phase is elastically stiff. At room temperature (300 K) and 0 GPa, Θ_D slightly decreases to 617.9 K. However, Θ_D increases significantly with pressure, reaching 900 K at 50 GPa. This suggests that pressure has a more pronounced effect on Θ_D and, consequently, the hardness of the NBT crystal than temperature.

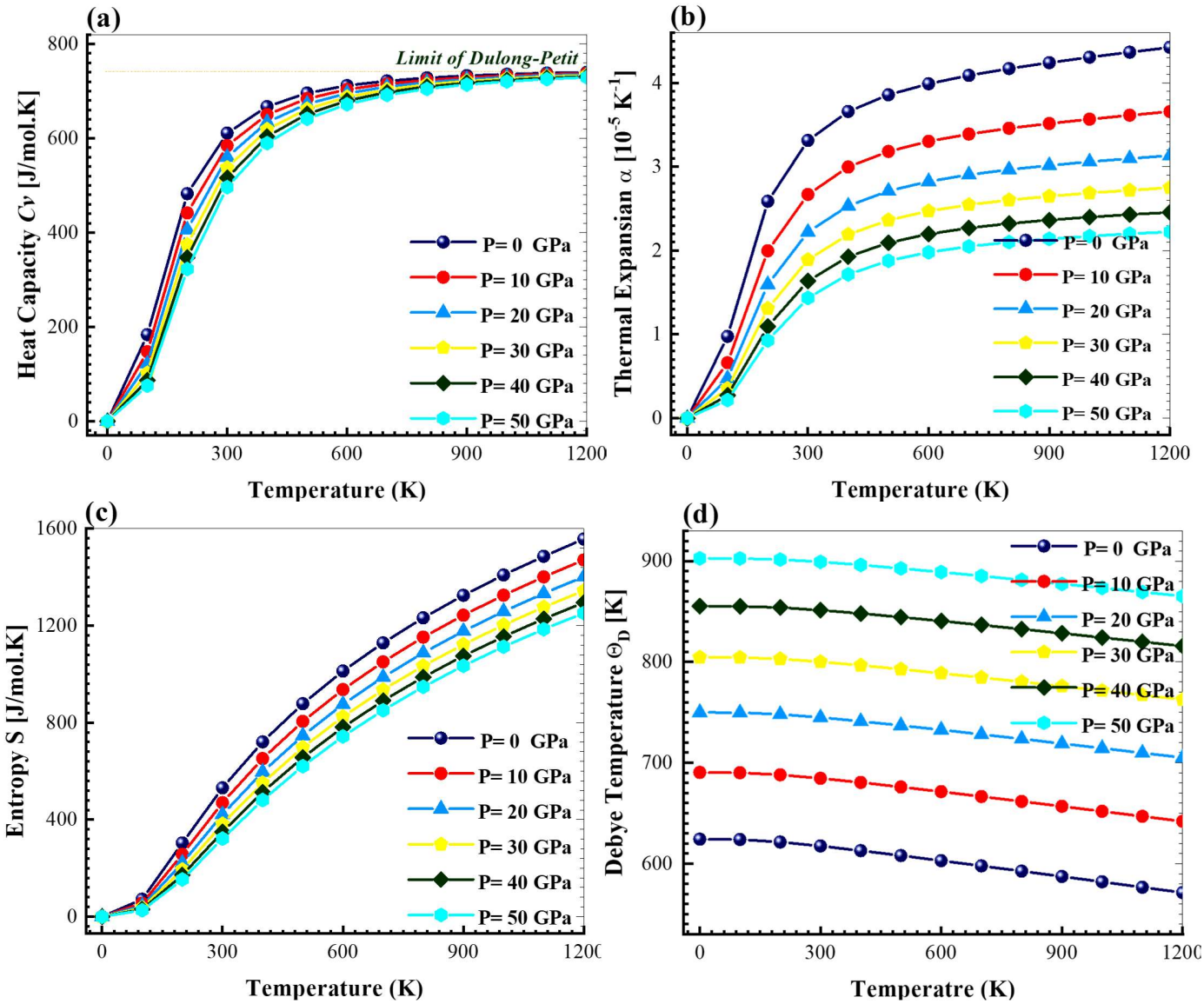

Figure III.10: Variation of (a) thermal capacity *Cv*, (b) thermal expansion α, (c) entropy S, and (d) Debye temperature Θ_D with temperature under different pressures for the rhombohedral $Na_{0.5}Bi_{0.5}TiO_3$ crystal.

III.8. Thermoelectric Properties

The primary cause of excessive energy consumption is the loss of more than 60% of energy as wasted heat. Thermoelectricity, first discovered by Thomas Seebeck [93], offers a method to harness this wasted energy by directly converting excess heat into usable power. Identifying effective and environmentally friendly thermoelectric materials is a key focus for scientists and industry professionals aiming to generate green energy from waste heat. The performance of a thermoelectric material is quantified by the dimensionless figure of merit, ZT, defined as follows:

$$ZT = \frac{S^2\sigma}{\kappa}T, \tag{40}$$

where S (V/K) denotes the Seebeck coefficient, σ $(\Omega ms)^{-1}$ represents the electrical conductivity, and κ $(Wm^{-1}K^{-1}s^{-1})$ is the total thermal conductivity, which includes contributions from both electrons and the lattice:

$$\kappa = \kappa_{el} + \kappa_{latt} \tag{41}$$

The Seebeck coefficient can be derived from the electron density of states and the effective masses of the charge carriers using the following relationship:

$$S = \frac{8\pi^2 k_B^2}{3eh^2} m^* T \left(\frac{\pi}{3n}\right)^{2/3}. \tag{42}$$

where k_B denotes the Boltzmann constant, e represents the elementary charge, h is the Planck constant, m^* refers to the effective mass of the carriers at the Fermi level, n is the concentration of the majority carriers and T is the temperature.

We examine, in this section, the thermoelectric (TE) properties of the $Na_{0.5}Bi_{0.5}TiO_3$ crystals across rhombohedral (R3c), tetragonal (P4bm), and cubic ($Pm\bar{3}m$) symmetries as a function of temperature up to 900 K. These properties include electrical conductivity (σ/τ), thermal conductivity (κ/τ), Seebeck coefficient (S), figure of merit (ZT), and thermopower. All these quantities are computed using the BoltzTraP2 code, which applies the Boltzmann semi-classical theory with a constant relaxation time approximation. In this framework, the relaxation time τ is set to 10^{-14} s [94].

A. Seebeck Coefficient (S)

The Seebeck coefficient (S) reflects the ability of electrons to transport heat and electric current, defined as the ratio of the voltage change (ΔV) to the temperature change (ΔT) [95]. A positive Seebeck coefficient suggests that the dominant charge carriers in the material are holes [96,97], identifying it as a p-type semiconductor. Figure III.12(a) displays the computed Seebeck coefficient for the $Na_{0.5}Bi_{0.5}TiO_3$ crystals across the three crystal phases as a function of temperature. For both tetragonal and cubic phases, the Seebeck coefficient initially increases with temperature until reaching a peak, beyond which it declines due to the thermal excitation of minority carriers. Conversely, in the rhombohedral phase, the Seebeck coefficient decreases with rising temperature. The tetragonal phase exhibits the highest Seebeck coefficient, reaching approximately 201.42 μV/K at T = 500 K, compared to about 173.6 μV/K in the cubic phase at T = 800 K and 158.6 μV/K in the rhombohedral phase at T = 100 K. At room temperature (T = 300 K), the Seebeck coefficients are approximately 185.3 μV/K for the tetragonal phase, 150.3 μV/K for the cubic phase, and 142.3 μV/K for the rhombohedral phase.

B. Electrical Conductivity (σ/τ)

Electrical conductivity (σ) is influenced by the concentration and mobility of charge carriers. Figure III.12(b) illustrates the variation of σ/τ with temperature (T). Since the BoltzTraP2 code calculates σ relative to the relaxation time (τ), we incorporate τ by multiplying it with a constant value previously specified. At room temperature (T = 300 K), the cubic phase exhibits a notable σ/τ value of approximately 1.54×10^{19} $(\Omega\cdot m)^{-1}$. In comparison, the tetragonal and rhombohedral phases show values of about 3.65×10^{18} $(\Omega\cdot m)^{-1}$ and 3.85×10^{18} $(\Omega\cdot m)^{-1}$, respectively. As depicted in Figure III.12(b), σ/τ initially increases with temperature and accelerates at higher temperatures, peaking at approximately 2.82×10^{19} $(\Omega\cdot m)^{-1}$ for the cubic phase. At 900 K, the values for the tetragonal and rhombohedral phases are about 1.09×10^{19} $(\Omega\cdot m)^{-1}$ and 3.65×10^{18} $(\Omega\cdot m)^{-1}$, respectively. These high electrical conductivity values confirm that $Na_{0.5}Bi_{0.5}TiO_3$, a lead-free perovskite, is an excellent electrical conductor [98].

C. Thermal Conductivity (κ/τ)

Thermal conductivity in materials arises from two primary sources: phonons, which conduct heat through lattice vibrations, and electrons, which transfer heat as charge carriers [99]. Among these, electronic thermal conductivity (κ_{el}) is typically more substantial than vibrational (phonon) conductivity (κ_{Latt}). Figure III.12(c) presents the electronic thermal conductivity, expressed as κ_{el}/τ, for the three phases of $Na_{0.5}Bi_{0.5}TiO_3$ crystals as a function of temperature. The κ_{el}/τ values increase with temperature up to 900 K due to the rising concentration of electrons, which enhances collisions and, consequently, thermal conductivity. In the rhombohedral phase, κ_{el}/τ shows a modest increase from 0 to 2.85×10^{13} $W\cdot m^{-1}\cdot K^{-1}\cdot s^{-1}$ by 900 K. In the tetragonal phase, thermal conductivity rises more noticeably from 0 to 1.36×10^{14} $W\cdot m^{-1}\cdot K^{-1}\cdot s^{-1}$ at 900 K. The cubic phase, however, exhibits a rapid increase in κel/τ with temperature, reaching approximately 3.53×10^{14} $W\cdot m^{-1}\cdot K^{-1}\cdot s^{-1}$ at 900 K.

D. Power Factor

The power factor (PF), or thermal power, is calculated $S^2\,\sigma/\tau$. Figure III.12(d) illustrates the power factor for $Na_{0.5}Bi_{0.5}TiO_3$ crystals across different phases. The power factor increases with temperature, peaking at high temperatures (900 K). In the cubic phase, the PF reaches approximately 8.52×10^{11} $W\cdot m^{-1}\cdot K^{-2}\cdot s^{-1}$. The tetragonal phase shows a PF of about 4.06×10^{11} $W\cdot m^{-1}\cdot K^{-2}\cdot s^{-1}$, while the rhombohedral phase has a lower value of around 5.09×10^{10} $W\cdot m^{-1}\cdot K^{-2}\cdot s^{-1}$. These results indicate that the lead-free perovskite $Na_{0.5}Bi_{0.5}TiO_3$ exhibits significant thermal power, with values on the order of 10^{11} $W\cdot m^{-1}\cdot K^{-2}\cdot s^{-1}$, positioning it as an excellent thermoelectric material [100].

E. Figure of Merit (ZT)

The figure of merit (ZT) is a key indicator of the potential of thermoelectric materials, with higher ZT values reflecting better performance. A high ZT value is typically associated with a high Seebeck coefficient (S) and low lattice thermal conductivity (κ), as

indicated by Eq. (40), which are essential for efficient thermoelectric systems [101]. Figure III.12(e) displays the ZT values as a function of temperature for the three phases of $Na_{0.5}Bi_{0.5}TiO_3$ crystals. The ZT increases with temperature, peaking at approximately 2.76 at 700 K for the tetragonal phase, 2.16 at 900 K for the cubic phase, and 1.96 at 400 K for the rhombohedral phase. Beyond these temperatures, ZT tends to decrease due to a decline in the Seebeck coefficient and a sharp rise in thermal conductivity. At room temperature (T = 300 K), the R3c-NBT crystal achieves the highest ZT value of about 1.94, followed by the P4bm-NBT crystal at approximately 1.62, and the $Pm\bar{3}m$-NBT crystal at around 1.16. These results suggest that the lead-free $Na_{0.5}Bi_{0.5}TiO_3$ perovskite is a promising candidate for thermoelectric generators and the development of cost-effective, environmentally friendly energy harvesters.

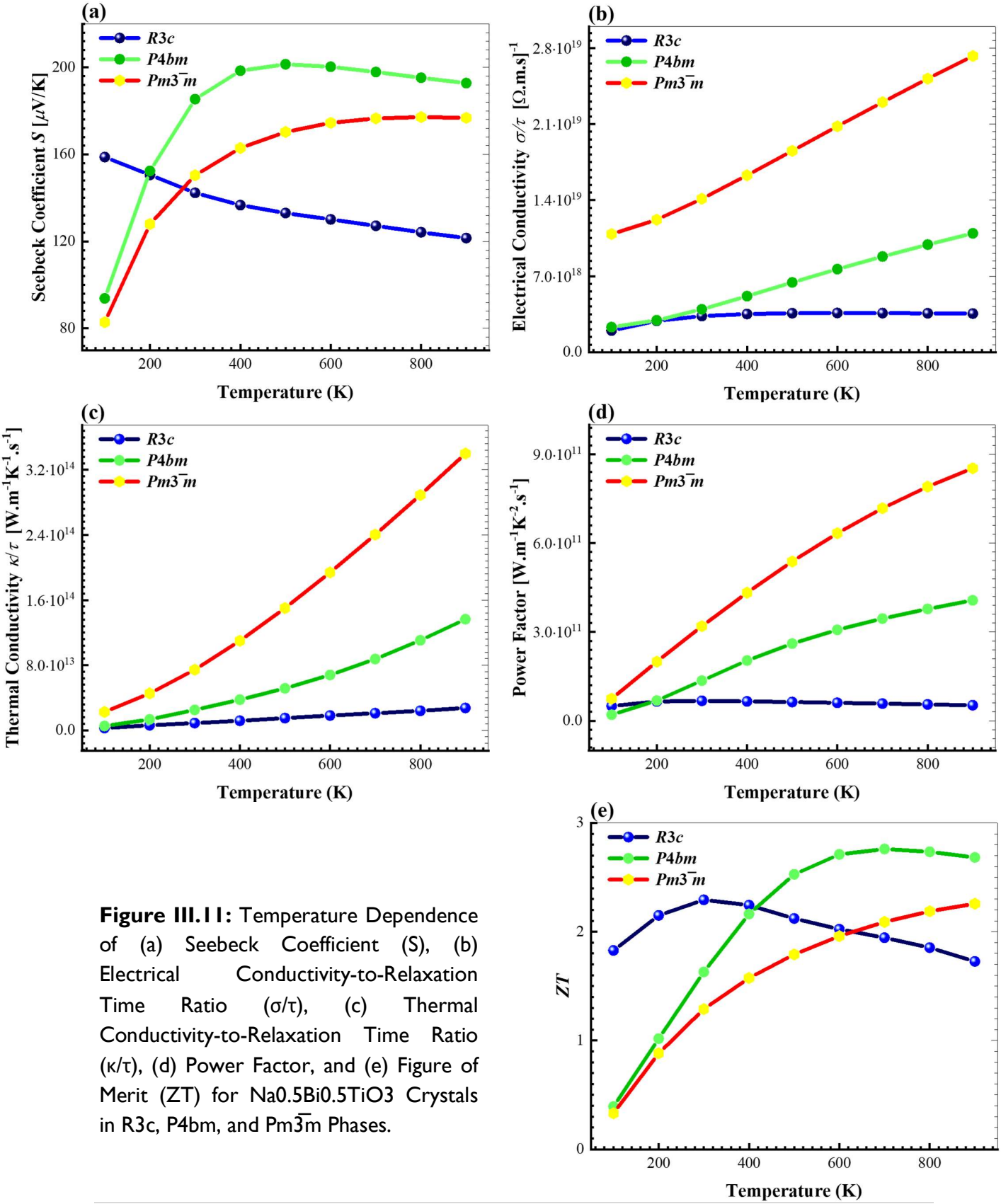

Figure III.11: Temperature Dependence of (a) Seebeck Coefficient (S), (b) Electrical Conductivity-to-Relaxation Time Ratio (σ/τ), (c) Thermal Conductivity-to-Relaxation Time Ratio (κ/τ), (d) Power Factor, and (e) Figure of Merit (ZT) for Na0.5Bi0.5TiO3 Crystals in R3c, P4bm, and Pm3̄m Phases.

III.9. Conclusion

In this chapter, we have utilized advanced ab initio DFT computational methods to explore key properties of lead-free $Na_{0.5}Bi_{0.5}TiO_3$ (NBT) perovskite, including structural stability, electronic structure, elasto-mechanical characteristics, piezoelectricity, thermodynamics, and thermoelectric performance across its rhombohedral (R3c), tetragonal (P4bm), and cubic ($Pm\bar{3}m$) phases. Our computed lattice parameters are consistent with experimental data. The formation energy and phonon dispersion analyses affirm the thermodynamic and dynamic stability of the R3c-NBT phase. The KTB–mBJ+so potential accurately predicts the indirect band gaps for all three phases of NBT. Analysis of the electron charge density reveals a combination of ionic (O–Na and O–Bi) and covalent (O–Ti) bonding characteristics. The elastic constants and moduli (B, G, and Y) indicate that $Na_{0.5}Bi_{0.5}TiO_3$ crystals are mechanically robust, with the R3c-NBT phase exhibiting notable anisotropy in its elastic properties. The ferroelectric P4bm-NBT phase shows superior piezoelectric and dielectric coefficients compared to R3c-NBT. Our findings demonstrate that pressure has a more substantial impact on the Debye temperature than temperature itself. The thermoelectric properties of NBT crystals indicate impressive performance, with high electrical conductivity, a substantial figure of merit, and low thermal conductivity. Consequently, lead-free $Na_{0.5}Bi_{0.5}TiO_3$ (NBT) perovskite emerges as a highly promising material for advanced piezoelectric devices and future green energy harvesting applications.

References

[1] P. Hohenberg, W. Kohn, Inhomogeneous Electron Gas, Phys. Rev. B 136 (1964) 864, https://doi.org/10.1103/PhysRev.136.B864.

[2] W. Kohn, L.J. Sham, Self-Consistent Equations Including Exchange and Correlation Effects, Phys. Rev. A 140 (1965) 1133, https://doi.org/10.1103/PhysRev.140.A1133.

[3] P. Blaha, K. Schwarz, F. Tran, R. Laskowski, G.K.H. Madsen and L.D. Marks, WIEN2k: An APW+ lo Program for Calculating the Properties of Solids, J. Chem. Phys. 152 (2020) 074101, https://doi.org/10.1063/1.5143061.

[4] F. Tran, P. Blaha, Accurate Band Gaps of Semiconductors and Insulators with a Semilocal Exchange-Correlation Potential, Phys. Rev. Lett. 102 (2009) 226401, https://doi.org/10.1103/PhysRevLett.102.226401.

[5] J.P. Perdew, A. Ruzsinszky, G.I. Csonka, O.A. Vydrov, G.E. Scuseria, et al., Restoring the Density-Gradient Expansion for Exchange in Solids and Surfaces, Phys. Rev. Lett. 100 (2008) 136406, https://doi.org/10.1103/PhysRevLett.100.136406.

[6] Z. Wu, R.E. Cohen, More Accurate Generalized Gradient Approximation for Solids, Phys. Rev. B 73 (2006) 235116, https://doi.org/10.1103/PhysRevB.73.235116.

[7] A. Assali, F. Kanouni, Q. Zou, R. Khenata, Optical Characteristics of Dilute Gallium Phosphide Bismide: Promising Material for Near-Infra Photonic Device Applications, Physics Letters A 384 (2020) 126147, https://doi.org/10.1016/j.physleta.2019.126147.

[8] A. Assali, F. Kanouni, F. Laidoudi, F. Arab, M'hamedBouslama, Structural and Electromechanical Properties of Sr-Substituted Barium Titanate (BST) as Potential Material for High Performance Electroacoustic Devices, Materials Today Communications 25 (2020) 101643, https://doi.org/10.1016/j.mtcomm.2020.101643.

[9] D. Koller, F. Tran, and P. Blaha, Improving the Modified Becke-Johnson Exchange Potential, Phys. Rev. B 85 (2012) 155109, https://doi.org/10.1103/PhysRevB.85.155109.

[10] F. Tran, P. Blaha, Accurate band gaps of semiconductors and insulators with a semilocal exchange-correlation potential, Phys. Rev. Lett. 102 (2009), 226401, https://doi.org/10.1103/PhysRevLett.102.226401.

[11] A. Boubaia, A. Assali, S. Berrah, H. Bennacer, I. Zerifi, A. Boukortt, Band Gap and Emission Wavelength Tuning of Sr-doped BaTiO3 (BST) Perovskites for High-Efficiency Visible-Light Emitters and Solar Cells, Materials Science in Semiconductor Processing 130 (2021) 105837, https://doi.org/10.1016/j.mssp.2021.105837.

[12] J. Monkhorst, J.D. Pack, Special points for Brillouin-zone integrations, Phys. Rev. 13 (1976) 5188, https://doi.org/10.1103/PhysRevB.13.5188.

[13] D. Vanderbilt, Soft self-consistent pseudopotentials in a generalized eigenvalue formalism, Phys. Rev. B 41, (1990) 7892, https://doi.org/10.1103/PhysRevB.41.7892.

[14] M. Segall, P.J. Lindan, M. Probert, C. Pickard, P. Hasnip, S. Clark, M. Payne, First-principles simulation: ideas, illustrations and the CASTEP code, J. Phys. Condens. Matter 14 (2002) 2717, https://doi.org/10.1088/0953-8984/14/11/301.

[15] S. Baroni, P. Giannozzi, A. Testa, Green's-function approach to linear response in solids, Phys. Rev. Lett. 58 (1987) 1861,https://doi.org/10.1103/PhysRevLett.58.1861.

[16] G.O. Jones, P.A. Thomas, Investigation of the structure and phase transitions in the novel a-site substituted distorted perovskite compound Na0.5Bi0.5TiO3, Acta Crystallogr. Sect. B: Struct. Sci. 58 (2002) 168–178, https://doi.org/10.1107/ S0108768101020845.

[17] F.D. Murnaghan, The Compressibility of Media Under Extreme Pressures, Proc. Natl. Acad. Sci. USA 30 (1944) 244–247.

[18] M.K. Niranjan, T. Karthik, S. Asthana, J. Pan, V. Umesh, Waghmare, Theoretical and experimental investigation of Raman modes, ferroelectric and dielectric properties of relaxor Na0.5Bi0.5TiO3, J. Appl. Phys. 113 (2013), 194106, https:// doi.org/10.1063/1.4804940.

[19] W. Chatta, B. Lagoun, H. Lidjici, A. Chadli, A. Cheriet, H. Farh, H. Khemakhem, K. Salah, TB-mBJ calculations of structural and optoelectronic properties of the rhombohedral phase of bismuth sodium titanate (Bi0.5Na0.5)TiO3, Solid State Phenom. 297 (2019) 165–172, https://doi.org/10.4028/www.scientific.net/SSP.297.165.

[20] A. Assali, M. Bouslama, A.H. Reshak, L. Chaabane, Highly desirable semiconducting materials for mid-ir optoelectronics: dilute bismide $InAs_{1-x}Bi_x$ alloys, Mater. Res. Bull. 95 (2017) 588–596, https://doi.org/10.1016/j.materresbull.2017.06.011.

[21] A. Assali, M. Bouslama, L. Chaabane, A. Mokadem, F. Saidi, Structural and opto-electronic properties of $InP_{1-x}Bi_x$ bismide alloys for MID−infrared optical devices: A DFT + TB-mBJ study, Phys. B Condens. Matter 526 (2017) 71–79, https://doi.org/10.1016/j.physb.2017.09.058.

[22] A. Assali, M. Bouslama, A.H. Reshak, S. Zerroug, H. Abid, Electronic structure and optical properties of dilute boron-bismide quaternary alloys BxGa1–xAs1–yBiy/ GaAs for infrared optoelectronic devices, Optik 135 (2017) 57–69, https://doi. org/10.1016/j.ijleo.2017.01.059.

[23] F. Semari, R. Boulechfar, F. Dahmane, A. Abdiche, R. Ahmed, S.H. Naqib, A. Bouhemadou, R. Khenata, X.T. Wang, Phase Stability, Mechanical, Electronic and Thermodynamic Properties of the Ga3Sc Compound: An *Ab-initio* Study, Inorganic Chemistry Communications 122 (2020) 108304, https://doi.org/10.1016/j.inoche.2020.108304.

[24] F. Baedi, H. Mircholi, G. Moghadamn, Study of electronic and optical properties of $Bi_{0.5}Na_{0.5}TiO_3$, $BiTiO_3$, NaTiO3 crystals using full potential linear argumented plane wave method, Optik 126 (2015) 1505–1509, https://doi.org/10.1016/j. ijleo.2014.04.092.

[25] E. Yu, & Y. Pan, Influence of Noble Metals on the Electronic and Optical Properties of LiH Hydride: First-principles Calculations, International Journal of Hydrogen Energy 46 (2021) 35342–35350, https://doi.org/10.1016/j.ijhydene.2021.08.095.

[26] S. Chen, Y. Pan, Noble Metal Interlayer-doping Enhances the Catalytic Activity of 2H–MoS2 from First-principles Investigations, International Journal of Hydrogen Energy 46 (2021) 21040–21049, https://doi.org/10.1016/j.ijhydene.2021.03.202.

[27] S. Chen and Y. Pan, Influence of Group III and IV Elements on the Hydrogen Evolution Reaction of MoS2 Disulfide, J. Phys. Chem. C. 125 (2021) 11848–11856, https://doi.org/10.1021/acs.jpcc.1c03152.

[28] S. Baroni, S. D. Gironcoli, A. D. Corso, and P. Giannozzi, Phonons and Related Crystal Properties from Density-Functional Perturbation Theory, Rev. Mod. Phys. 73 (2001) 515, https://doi.org/10.1103/RevModPhys.73.515.

[29] K.M. Rabe and P. Ghosez, First-Principles Studies of Ferroelectric Oxides. In Physics of Ferroelectrics, Springer-Verlag, Berlin, 2007, pp. 117, https://doi.org/10.1007/978-3-540-34591-6_4.

[30] D.I. Bilc, R. Orlando, R. Shaltaf, G.-M. Rignanese, J. ´I˜niguez, P. Ghosez, Hybrid exchange-correlation functional for accurate prediction of the electronic and structural properties of ferroelectric oxides, Phys. Rev. 77 (2008), 165107, https://doi.org/10.1103/PhysRevB.77.165107.

[31] C. Wang, S. Liang, J. Cui, X. Wang, Y. Wei, First-principles study of the mechanical and thermodynamic properties of Al4W, Al5W and Al12W under pressure, Vacuum 169 (2019), 108844, https://doi.org/10.1016/j.vacuum.2019.108844.

[32] Y. Pan, Cr concentration driving the structural, mechanical, and thermodynamic properties of Cr-Al compounds from first-principles calculations, Int. J. Quant. Chem. 119 (2019), e25943, https://doi.org/10.1002/qua.25943

[33] G.O. Jones and P.A. Thomas, The Tetragonal Phase of $Na_{0.5}B_{i0.5}TiO_3$–a new Variant Of ThePerovskite Structure, ActaCrystallographica Section B: Structural Science 56 (2000) 426–430, https://doi.org/10.1107/S0108768100001166.

[34] V. Dorcet, G. Trolliard, P. Boullay, Reinvestigation of phase transitions in Na0.5Bi0.5TiO3 by TEM. Part I: first order rhombohedral to orthorhombic phase transition, Chem. Mater. 20 (2008) 5061–5073, https://doi.org/10.1021/ cm8004634.

[35] M. Bousquet, J.-R. Ducl`ere, E. Orhan, A. Boulle, C. Bachelet, et al., Optical properties of an epitaxial Na0.5Bi0.5TiO3 thin film grown by laser ablation: experimental approach and density functional theory calculations, J. Appl. Phys. 107 (2010), 104107, https://doi.org/10.1063/1.3400095.

[36] A.P.B. Selvadurai, V. Pazhnivelu, B.K. Vasanth, C. Jagadeeshwaran, R. Murugaraj, Investigation of structural and optical spectroscopy of 5% Pr doped (Bi0.5Na0.5) TiO3 ferroelectric ceramics: site depended study, J. Mater. Sci. Mater. Electron 26 (2015) 7655–7665, https://doi.org/10.1007/s10854-015-3405-5.

[37] M. Zeng, S.W. Or, H.L.W. Chan, First-principles study on the electronic and optical properties of Na0.5Bi0.5TiO3 lead-free piezoelectric crystal, J. Appl. Phys. 107 (2010), 043513, https://doi.org/10.1063/1.3309407

[38] M. Benyoussef, H. Zaari, J. Belhadi, A. Lahmar, Y.E. Amraoui, H. Ez-Zahraouy, M. E. Marssi, Electrical and Structural Properties of Pure and Dysprosium Doped Na0.5Bi0.5TiO3 system: DFT and Monte Carlo simulation, (2020), arXiv preprint arXiv:2003.03978.

[39] L.T.H. Thanh, N.B. Doan, L.H. Bac, D.V. Thiet, S. Cho, P.Q. Bao, D.D. Dung, Making room-temperature ferromagnetism in lead-free ferroelectric Bi0.5Na0.5TiO3 material, Mater. Lett. 186 (2017) 239–242, https://doi.org/ 10.1016/j.matlet.2016.09.105.
[40] Y.-N. Xu, W.Y. Ching, Electronic structure of (Na½Bi½)TiO3 and Its solid solution with BaTiO3, Philos. Mag. Part B 80 (2000) 1141–1151, https://doi.org/10.1080/ 13642810008208587.
[41] A. Assali, M. Bouslama, Novel BTlGaN semiconducting materials for infrared opto-electronic devices, Infrared Phys. Technol. 81 (2017) 175–181, https://doi. org/10.1016/j.infrared.2017.01.006.
[42] J. Li, K. Yamanaka, A. Chiba, Influence of interatomic interactions on the mechanical properties of face-centered cubic multicomponent Co-Ni-Cr-Mo Alloys, Materialia 12 (2020), 100742, https://doi.org/10.1016/j.mtla.2020.100742.
[43] Y. Pan, The structural, mechanical and thermodynamic properties of the orthorhombic TMAl (TM= Ti, Y, Zr and Hf) aluminides from first-principles calculations, Vacuum 181 (2020), 109742, https://doi.org/10.1016/j.vacuum.2020.109742.
[44] F. Mouhat, F.-X. Coudert, Necessary and sufficient elastic stability conditions in various crystal systems, Phys. Rev. B 90 (2014), 224104, https://doi.org/ 10.1103/PhysRevB.90.224104.
[45] J. Suchanicz, Elastic constants of Na0.5Bi0.5TiO3 single crystal, J. Mat. Sci. 7 (2002) 489–491, https://doi.org/10.1023/A:1013705204937.
[46] R. Bujakiewicz-Koro´nska, Y. Natanzon, Determination of elastic constants of Na0.5Bi0.5TiO3 from Ab initio calculations, Phase Transit. 81 (2008) 1117–1124, https://doi.org/10.1080/01411590802460833.
[47] A. Assali, F. Laidoudi, R. Serhane, F. Kanouni, O.-k. Mezilet, Highly enhanced electro-acoustic properties of YAlN/sapphire based surface acoustic wave devices for next generation of microelectromechanical systems, Mater. Today Commun. 26 (2021), 102067, https://doi.org/10.1016/j.mtcomm.2021.102067
[48] O. Zywitzki, T. Modes, S. Barth, H. Bartzsch, P. Frach, Effect Of scandium content on structure and piezoelectric properties of AlScN films deposited by reactive pulse magnetron sputterin, Surf. Coat. Technol. 309 (2017) 417, https://doi.org/ 10.1016/j.surfcoat.2016.11.08.
[49] A. Yildirim, H. Koc, E. Deligoz, First-principles study of the structural, elastic, electronic, optical, and vibrational properties of intermetallic Pd2Ga, Chin. Phys. B 21 (2012), 037101, https://doi.org/10.1088/1674-1056/21/3/037101
[50] M. Born, K. Huang, Dynamical Theory of Crystal Lattices, Oxford University Press, New York, 1988.
[51] J. Nye, J.F. Lindsay, R.B. Physical Properties of Crystals: Their Representation by Tensors and Matrices, Clarendon Press, Oxford, UK, 1985.
[52] R. Hill, The elastic behaviour of a crystalline aggregate, Proc. Phys. Soc. Sect. A 65 (1952) 349–354, https://doi.org/10.1088/0370-1298/65/5/307.
[53] J. Chang, X. Zhou, K. Liu, N. Ge, Structural, elastic, mechanical and thermodynamic properties of HfB4 under high pressure, R. Soc. Open. Sci. 7 (2018), 180701, https://doi.org/10.1098/rsos.180701
[54] Y. Pan, D.L. Pu, E.D. Yu, Structural, electronic, mechanical and thermodynamic properties of Cr–Si binary silicides from first-principles investigations, Vacuum 185 (2021), 110024, https://doi.org/10.1016/j.vacuum.2020.110024.
[55] D.L. Pu, Y. Pan, Influence of high pressure on the structure, hardness and brittle-to-ductile transition of NbSi2 ceramics, Ceram. Int. 47 (2021) 2311–2318, https://doi.org/10.1016/j.ceramint.2020.09.073.
[56] Y. Pan, Role of hydrogen on the structural stability, mechanical and thermodynamic properties of the cubic TM3Si silicides, Int. J. Hydrog. Energy 46 (2021) 28338–28345, https://doi.org/10.1016/j.ijhydene.2021.06.038.
[57] A. Vorobiev, S. Gevorgian, Intrinsically switchable thin film bulk acoustic wave resonators, Appl. Phys. Lett. 104 (2014), 222905, https://doi.org/10.1063/ 1.4881141.
[58] I.N. Frantsevich, F.F. Voronov, S.A. Bokuta, Elastic Constants and Elastic Moduli of Metals and Insulators Handbook, Naukova Dumka, Kiev, Ukraine, 1982.
[59] V.V. Bannikov, I.R. Shein, A.L. Ivanovskii, Electronic structure, chemical bonding and elastic properties of the first thorium-containing nitride perovskite TaThN3, Phys. Status Solidi Rapid Res. Lett. 3 (2007) 89, https://doi.org/10.1002/ pssr.200600116.
[60] R. Hill, The elastic behaviour of a crystalline aggregate, Proc. Phys. Soc. Sect. A 65 (1952) 349–354, https://doi.org/10.1088/0370-1298/65/5/307.
[61] RW. Voigt, Lehrbuch der Kristallphysik, Vieweg+Teubner Verlag, 1966, https ://doi.org/10.1007/978–3-663–15884-4.
[62] J. Nye, J.F. Lindsay, R.B. Physical Properties of Crystals: Their Representation by Tensors and Matrices, Clarendon Press, Oxford, UK, 1985.

[63] E. Schreiber, O.L. Anderson, N. Soga, Elastic Constants and their Measurement, McGraw-Hill, New York, 1973.
[64] K. Shibata, R. Wang, T. Tou, J. Koruza, Applications of lead-free piezoelectric materials, MRS Bull. 43 (2018) 612–616, https://doi.org/10.1557/mrs.2018.180.
[65] R.E. Newnham, Properties of Materials, Anisotropy, Symmetry, Structure, Published in the United States by Oxford University Press Inc., New York © Oxford University Press, 2005.
[66] S. Konabe, T. Yamamoto, Piezoelectric coefficients of Bulk 3R transition metal dichalcogenides, Jpn. J. Appl. Phys. 56 (2017), 098002, https://doi.org/ 10.7567/JJAP.56.098002.
[67] M. Davies, E. Aksel, J.L. Jonesw, Enhanced high-temperature piezoelectric coefficients and thermal stability of Fe-and Mn-substituted Na0.5Bi0.5TiO3 ceramics, J. Am. Ceram. Soc. 94 (2011) 1314–1316, https://doi.org/10.1111/ j.1551-2916.2011.04441.x.
[68] Y. Takagi, H. Nagata, T. Takenaka, Effects of quenching on bending strength and piezoelectric properties of (Bi0.5Na0.5)TiO3 Ceramics, J. Asian Ceram. Soc. (2020), https://doi.org/10.1080/21870764.2020.1732020.
[69] Y. Hiruma, H. Nagata, T. Takenaka, Thermal depoling process and piezoelectric properties of bismuth sodium titanate ceramics, J. Appl. Phys. 105 (2009), 084112, https://doi.org/10.1063/1.3115409.
[70] L.F. Wan, T. Nishimatsu, S.P. Beckman, The structural, dielectric, elastic, and piezoelectric properties of KNbO3 from first-principles methods, J. Appl. Phys. 111 (2012), 104107, https://doi.org/10.1063/1.4712052.
[71] Y.S. Sung, J.M. Kim, J.H. Cho, T.K. Song, M.H. Kim, T.G. Park, Effects of Bi nonstoichiometry in (Bi0.5+*x*Na)TiO3 ceramics, Appl. Phys. Lett. 98 (2011), 012902, https://doi.org/10.1063/1.3525370.
[72] M. Akiyama, T. Kamohara, K. Kano, A. Teshigahara, Y. Takeuchi, N. Kawahara, Enhancement of piezoelectric response in scandium aluminum nitride alloy thin films prepared by dual reactive cosputtering, Adv. Mater. 21 (2009) 593–596, https://doi.org/10.1002/adma.200802611.
[73] V. Tomara, P.A. Jhab, P. Singh, Effect of Processing Conditions on The Piezoelectric Constant and Curie Temperature of Ba0.7Sr0.3TiO3 Piezoelectric Ceramics, In AIP Conference Proceedings (Vol. 2009, No. 1, p. 020009). AIP Publishing LLC, https://doi.org/10.1063/1.5052078.
[74] D. Wang, K. Zhu, H. Ji, J. Qiu, Two-Step Sintering of the Pure K0.5Na0.5NbO3 Lead-Free Piezoceramics and Its Piezoelectric Properties. Ferroelectrics 392 (20091) 120–126, https://doi.org/10.1080/00150190903412622.
[75] M. Davis, D. Damjanovic, D. Hayem, N. Setter, Domain engineering of the transverse piezoelectric coefficient in perovskite ferroelectrics, J. Appl. Phys. 98 (2005), 014102, https://doi.org/10.1063/1.1929091.
[76] E.M. Muensit, Goldys, I.L. Guy, Shear piezoelectric coefficients of gallium nitride and aluminum nitride, Appl. Phys. Lett. 75 (1999) 3965, https://doi.org/ 10.1063/1.125508.
[77] C.M. Lueng, H.L.W. Chan, C. Surya, C.L. Choy, Piezoelectric coefficient of aluminum nitride and gallium nitride, J. Appl. Phys. 88 (2000) 5360–5363, https://doi.org/10.1063/1.1317244.
[78] M. Akiyama, T. Kamohara, K. Kano, A. Teshigahara, Y. Takeuchi, N. Kawahara, Enhancement of piezoelectric response in scandium aluminum nitride alloy, thin films prepared by dual reactive cosputtering, Adv. Mater. 21 (2009) 593, https:// doi.org/10.1002/adma.200802611.
[79] C. Tholander, J. Birch, F. Tasnadi, L. Hultman, J. Palisaitis, P.O.Å. Persson, J. Jensen, P. Sandstrom, B. Alling, A. ˇZukauskaitˆ e, Ab initio calculations and experimental study of piezoelectric $Y_xIn_{1-x}N$ thin films deposited using reactive magnetron sputter epitaxy, Acta Mater. 105 (2016) 199–206, https://doi.org/ 10.1016/j.actamat.2015.11.050.
[80] T. Yanagitani, J. Jia, ScAlN polarization inverted resonators and enhancement of kt2 in New YbAlN Materials for BAW Devices (In). IEEE International Ultrasonics Symposium (IUS), IEEE, 2019, pp. 894–899, https://doi.org/10.1109/ ULTSYM.2019.8925786 (In).
[81] T. Horikawa, N. Mikami, T. Makita, J. Tanimura, M. Kataoka, K. Sato, et al., Dielectric properties of (Ba,Sr)TiO3 thin films deposited By RF sputtering, Jpn. J. Appl. Phys. 32 (1993) 4126, https://doi.org/10.1143/JJAP.32.4126.
[82] A.L. Kholkin, N.A. Pertsev, A.V. Goltsev, Piezoelectricity and crystal symmetry, piezoelectricity and crystal symmetry (In). Piezoelectric and Acoustic Materials for Transducer Applications, Springer,, Boston, MA, 2008, pp. 17–38 (In).
[83] M. Davis, M. Budimir, D. Damjanovic, N. Setter, Rotator and extender ferroelectrics: importance of the shear coefficient to the piezoelectric properties of ferroelectrics: importance of the shear coefficient to the piezoelectric properties of domain-engineered crystals and ceramics, J. Appl. Phys. 101 (2007), 054112, https://doi.org/10.1063/1.2653925.
[84] D. Damjanovic, M. Budimir, M. Davis, N. Setter, Piezoelectric anisotropy: enhanced piezoelectric response along nonpolar directions in perovskite crystals, J. Mater. Sci. 41 (2006) 65–76, https://doi.org/10.1007/s10853-005-5925-5.

[85] M. Budimir, D. Damjanovic, N. Setter, Piezoelectric anisotropy–phase transition relations in perovskite single crystals, J. Appl. Phys. 94 (2003) 6753–6761, https://doi.org/10.1063/1.1625080.
[86] I. Fujii, Y. Ito, T. Suzuki, T. Wada, Ferroelectric and piezoelectric properties of (Bi1/2Na1/2)TiO3–BiFeO3 ceramics, J. Mater. Res. 31 (2016) 28–35, https://doi. org/10.1557/jmr.2015.315.
[87] M.A. Bianco, E. Francisco, V. Luana, GIBBS: isothermal-isobaric thermodynamics of solids from energy curves using A Quasi-harmonic debye model, Comput. Phys. Commun. 158 (2004) 57–72, https://doi.org/10.1016/j.comphy.2003.12.001.
[88] A. Otero-de-la-Roza, V. Lua˜na, GIBBS2: a new version of the quasi-harmonic model code. I. Robust treatment of the static data, Comput. Phys. Commun. 182 (2011) 1708–1720, https://doi.org/10.1016/j.cpc.2011.04.016.
[89] E. Francisco, J.M. Recio, M.A. Blanco, A.M. Pendas, Quantum-mechanical study of thermodynamic and bonding properties of MgF2, J. Phys. Chem. A 102 (1998) 1595–1601, https://doi.org/10.1021/jp972516j.
[90] E. Francisco, M.A. Blanco, G. Sanjurjo, Atomistic simulation of SrF2 polymorphs, Phys. Rev. B 63 (2001), 094107, https://doi.org/10.1103/PhysRevB.63.094107.
[91] S.A. Mir, S. Yousuf, D.C. Gupta, First principle study of mechanical stability, magneto-electronic and thermodynamic properties of double perovskites: A2MgWO6 (A = Ca, Sr), Mater. Sci. Eng. C. 250 (2019) 1–10, https://doi.org/10. 1016/j.mseb.2019.114434.
[92] S. Tariq, A. Ahmed, S. Saad, S. Tariq, Structural, electronic and elastic properties of the cubic CaTiO3 under pressure: A DFT Study, AIP Adv. 5 (2015), 077111, https://doi.org/10.1063/1.4926437.
[93] H.J. Goldsmid, Introduction to Thermoelectricity, Second ed., Springer Series in Materials Science, 2016, https://doi:10.1007/978-3-662-49256-7.
[94] A.Q. Seh, D.C. Gupta, Exploration of highly correlated co-based quaternary heusler alloys for spintronics and thermoelectric applications, Int. J. Energy Res. 43 (2019) 8864–8877, https://doi.org/10.1002/er.4853.
[95] A.Q. Seh, D.C. Gupta, Quaternary heusler alloys a future perspective for revolutionizing conventional semiconductor technology, J. Alloy. Compd. 871 (2021), 159560, https://doi.org/10.1016/j.jallcom.2021.159560
[96] E.S. Toberer, A.F. May, C.J. Scanlon, G.J. Snyder, Thermoelectric properties of *p*-type LiZnSb: assessment of ab initio calculations, J. Appl. Phys. 105 (2009), 063701, https://doi.org/10.1063/1.3091267.
[97] N.A. Noor, M.B. Saddique, B.U. Haq, A. Laref, M. Rashid, Investigations of half-metallic ferromagnetism and thermoelectric properties of cubic XCrO3 (X= Ca, Sr, Ba) compounds via first-principles approaches, Phys. Lett. A 382 (2018) 3095–3102, https://doi.org/10.1016/j.physleta.2018.07.045.
[98] H. Bi, F. Huang, J. Liang, Y. Tang, X. Lü, X. Xie, M. Jiang, Large-scale preparation of highly conductive three dimensional graphene and its applications in CdTe solar cells, J. Mater. Chem. 21 (2011) 17366–17370, https://doi.org/10.1039/ C1JM13418C.
[99] G.J. Snyder, E.S. Toberer, Complex thermoelectric materials, Nat. Mater. 7 (2008) 105–114, https://doi.org/10.1038/nmat2090.
[100] F. Zareef, M. Rashid, A.A.H. Ahmadini, T. Alshahrani, N.A. Kattan, A. Laref, Optoelectronic and thermoelectrical and mechanical properties of CdLu2X4 (X = S, Se) using first-principles calculations for energy harvesting applications, Mater. Sci. Semicond. Process. 127 (2021), 105695, https://doi.org/10.1016/j. mssp.2021.105695.
[101] M. Sajjad, N. Singh, J.A. Larsson, Bulk and monolayer bismuth oxyiodide (BiOI): excellent high temperature P-type thermoelectric materials, AIP Adv. 10 (2020), 075309, https://doi.org/10.1063/1.5133711.

Exploring the Emergent Piezoelectric and Thermoelectric Properties of Novel YAlN Semiconductor Alloys

Chapter IV

IV.1. Introduction

The major advancements in numerical computation method, particularly the Full-Potential Linearized Augmented Plane Wave (FP-LAPW) method within the framework of Density Functional Theory (DFT), play a crucial role in the accurate investigation and prediction of various semiconductor material properties. The discovery of new materials such as $Sc_xAl_{1-x}N$, $Cr_xAl_{1-x}N$, and $Y_xAl_{1-x}N$, which are formed by doping AlN with transition metals (TM = Sc, Cr, Y), presents significant opportunities to enhance optoelectronic and piezo-thermoelectric performance. These enhancements are particularly relevant for advanced optoelectronics, potentially extending the spectral range from the infrared-visible to the deep ultraviolet spectrum, as well as for the development of electroacoustic devices operating at high frequencies.

In this chapter, we investigated the structural, electronic, thermodynamic, and thermoelectric properties of yttrium aluminum nitride, $Y_xAl_{1-x}N$, semiconductor alloys in the wurtzite structure for yttrium concentration ranging from $0 \leq x \leq 0.375$, employing the powerful FP-LAPW method within DFT. These calculations were performed using various approaches such as the modern GGA–PBEsol and *n*KTB–mBJ approximations. We first calculated the structural properties to obtain information on the macroscopic and chemical structure of the materials. The knowledge of the structural properties then allowed us to predict other interesting properties such as electronic, thermoelectric, piezoelectric, etc.

IV.2. Methodological Details

The structural and electronic characteristics of wurtzite $Y_xAl_{1-x}N$ alloys have been demonstrated using ab initio calculations based on a Full Potential Linear Augmented Plane Wave (FP–LAPW) method [1] within DFT theory [2] as incorporated in the WIEN2K package [3]. To optimize the structural parameters, the new Perdew-Berke-Ernzerhof for solids (PBEsol) approach [4] based on generalized gradient approximation (GGA) was used to treat the exchange-correlation potential, which is known for its efficiency in the prediction of structural parameters and agrees well with experiments [5]. To examine the

electronic structure, such as band structure, density of states, and charge density, the modified semi-local Becke-Johnson exchange potential recently established by Koller-Tran-Blaha (*n*KTB–mBJ) [6] was used. This modern approach is actually considered one of the best tools to obtain energy bandgaps with high accuracy for various types of semiconductors and insulators, in better agreement with experiments and comparable to those of high-cost hybrid functionals and GW methods [7,8]. In addition, for elastic constants calculations, we applied the Ultrasoft Vanderbilt pseudopotential [9] and PBEsol-GGA [4] as implemented in the Cambridge Serial Total Energy Package (CASTEP) [10]. The piezoelectric response of the considered alloys was determined using density functional perturbation theory (DFPT) [11] with the Plane-Wave Pseudopotential method and PBEsol for the exchange-correlation term.

In the WIEN2K package, the interstitial region, the basis function is expanded up to $R_{MT} \times K_{max} = 7$, where R_{MT} is the middle radius of the spheres muffin-tin and K_{max} is the highest value of the vector wave. The charge density, potential, and wave functions inside the muffin-tin spheres are expanded with an angular momentum up to $l_{max} = 10$. The R_{MT} values of 1.9, 1.85, and 1.64 a.u. are chosen for Y, Al, and N, respectively. The states [Kr] $4d^1\ 5s^2$, [Ne] $3s^2\ 3p^1$, and $1s^2\ 2s^2\ 2p^3$ for Y, Al, and N, respectively, are treated as the valence states. In the CASTEP code, a self-consistent field (SCF) tolerance of 5.0×10^{-6} eV/atom was employed, with the residual force minimized to below 0.01 eV/Å, the residual bulk stress reduced to less than 0.02 GPa, and atomic displacements constrained to within 0.001 Å. The plane-wave cutoff energy was set to 520 eV to ensure the convergence of calculations. In the irreducible wedge of the Brillouin zone, we use Monkhorst-Pack [12] meshes of 40 (a grid of 8 × 8 × 8) special *k*-points for undoped Al and 16 (a grid of 4 × 4 × 2) for doped $Y_xAl_{1-x}N$ alloys.

Along this study, we consider $Y_xAl_{1-x}N$ crystals (with x up to 0.375) to crystalize in the hexagonal wurtzite structure, consistent to previous works [13,14]. To model theses crystals, we adopt 32-atom super-cells ($Y_nAl_{1-n}N_{16}$) based on a (2 × 2 × 2) conventional hexagonal wurtzite unit cell.

In Figure-IV.1, we display the crystallographic structures for hexagonal wurtzite $Y_xAl_{1-x}N$ for x = 0, 0.062, 0.125, 0.25, and 0.375. The atomic configurations shown in Figure-IV.1 are the most energetically stable [15]. To achieve structural stability, all doped material structures were fully relaxed, and consequently, the atoms were positioned in their equilibrium positions by minimizing the forces on the atoms using a self-consistent FP-LAPW calculation via the MIN program implemented in the WIEN2K code.

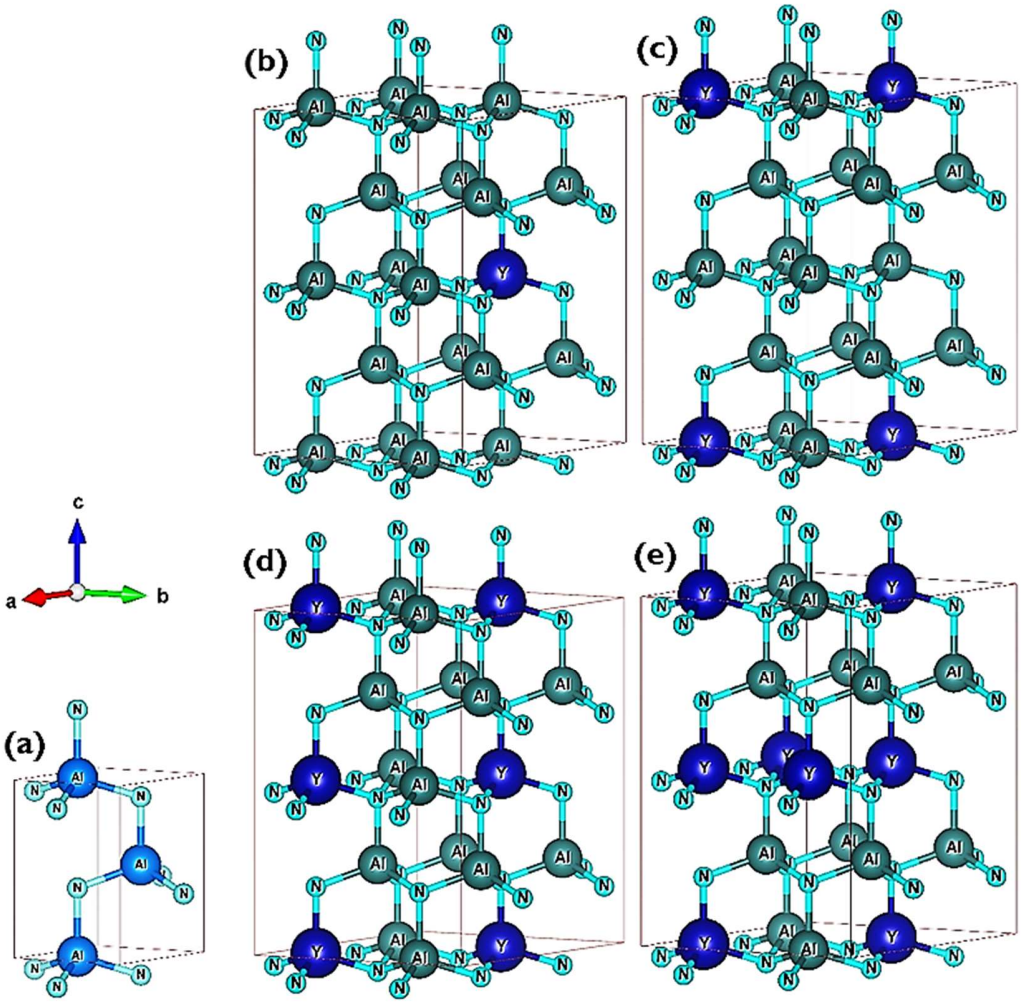

Figure-IV.1. Crystallographic structures of wurtzite $Y_xAl_{1-x}N$ alloys for x= 0 (a) (unit cell), 0.062 (b), 0.125 (c), 0.25 (d), and 0.375 (e) (2a×2b×2c supercell).

IV.3. Structural Properties and Lattice Stabilities

A. Ground-State Structural Parameters

In the first step of this study, we have optimized and determined the ground-state structural parameters of $Y_xAl_{1-x}N$ alloys in their equilibrium hexagonal wurtzite phase using the GGA-PBEsol functional within FP–LAPW method for yttrium concentrations (x) of 0, 0.062, 0.125, 0.25, and 0.375. Recent experimental studies have demonstrated that $Y_xAl_{1-x}N$ thin films can be grown with yttrium concentrations up to 11.6% [16] and 22% [17].

The results for the lattice parameters (a_0, c_0), c_0/a_0 ratio, volume (V_0), and bulk modulus (B_0) at T = 0 K and P = 0 GPa are presented in Table 1, along with comparative computational values and experimental data. A good agreement was achieved between the present values and those obtained experimentally for the binary AlN compound, with lattice parameters of 3.11 Å, 4.98 Å, and a c_0/a_0 ratio of 1.601 [14,18]. The calculated values of a_0 = 3.204 Å and c_0 = 5.06 Å within GGA-PBEsol for the $Y_{0.125}Al_{0.875}N$ alloy are in close agreement with the measured values of 3.20 Å and 5.04 Å reported at x = 0.13 [14]. In contrast, previous calculations using standard approaches like GGA-PBE have overestimated these lattice parameters, as reported by Montes et al. [13] and Xie et al. [15]. It is well known that conventional GGA-PBE within DFT theory typically overestimates lattice parameters [19,20]. This underscores the advantage of using the GGA-PBEsol functional for more accurate calculations. As shown in Table IV-1, the bulk modulus decreases from 200.4 GPa at x = 0 to 163.2 GPa at x = 0.375. This indicates that $Y_xAl_{1-x}N$ crystal becomes less resistant to compressibility as Y substitutes for the Al atom.

Table IV.1: Calculated equilibrium lattices parameters (Å), c_0/a_0 ratio, volume (Å^3), bulk modulus, and formation energy (ΔE_f) (eV) for wurtzite $Y_xAl_{1-x}N$ alloys with yttrium contents ($0 \leq x \leq 0.375$).

Y-contents		a_0 (Å)	c_0 (Å)	c_0/a_0	V_0 (Å^3)	B_0 (GPa)	ΔE_f (eV)
AlN	**PBEsol**	3.113	4.983	1.600	335.49	200.4	-
	Expt. [14,18,21]	3.11	4.98	1.601			
	Theo. PP-PBE [15]	3.13	5.02	1.603	340.564		
	FP-PBE [13]	3.138	5.027	1.602	21.435		
$Y_{0.0625}Al_{0.9375}N$	**PBEsol**	3.155	5.031	1.594	348.59	193.0	–3.966
	Theo. PP-PBE [15]	3.17	5.08	1.602	354.321		
$Y_{0.125}Al_{0.875}N$	**PBEsol**	3.204	5.060	1.579	361.98	186.3	–4.027
	Theo. PP-PBE [15]	3.22	5.10	1.584	367.823		
$Y_{0.25}Al_{0.750}N$	**PBEsol**	3.290	5.141	1.577	385.30	174.9	–4.062
	Theo. PP-PBE [15]	3.33	5.19	1.559	392.358		
	FP-PBE [13]	3.352	5.346	1.595	26.012		
$Y_{0.375}Al_{0.625}N$	**PBEsol**	3.375	5.256	1.557	411.52	163.2	–4.092

Figure IV.2 represent the variation of the lattice parameters (a_0 and c_0) of $Y_xAl_{1-x}N$ alloys as a function of yttrium concentration. It is observed that a_0 increases approximately linearly with increasing *x*, exhibiting a slight upward bowing with a parameter of −0.08597 Å. In contrast, c_0 deviates significantly from the linear Vegard's rule [22], showing a substantial bowing of −0.5715 Å. These bowing effects can be primarily attributed to the lattice mismatch between the parent binaries AlN and YN, as well as the relaxation influences on the Al–Y and N–Y bond lengths. The increase in lattice parameters with Y content is due to the larger ionic radius of Y^{+3} (≈1.019 Å) compared to that of Al^{+3} (≈0.535 Å) [23].

In addition, as observed in Figure IV.2(a) and IV.2(b), the evolution of lattice parameters in $Y_xAl_{1-x}N$ is in better agreement with experimental results [14,16,17] compared to those from other classical DFT calculations [13,14,15,16]. A similar trend in lattice parameters (a_0, c_0) with varying Sc content has recently been observed in $Sc_xAl_{1-x}N$ films, as reported in the experimental work by Dinh et al. [24]. Figure IV.3 clearly shows that the total energy decreases as yttrium content increases, signifying an enhancement in the energetic stability of the $Y_xAl_{1-x}N$ systems.

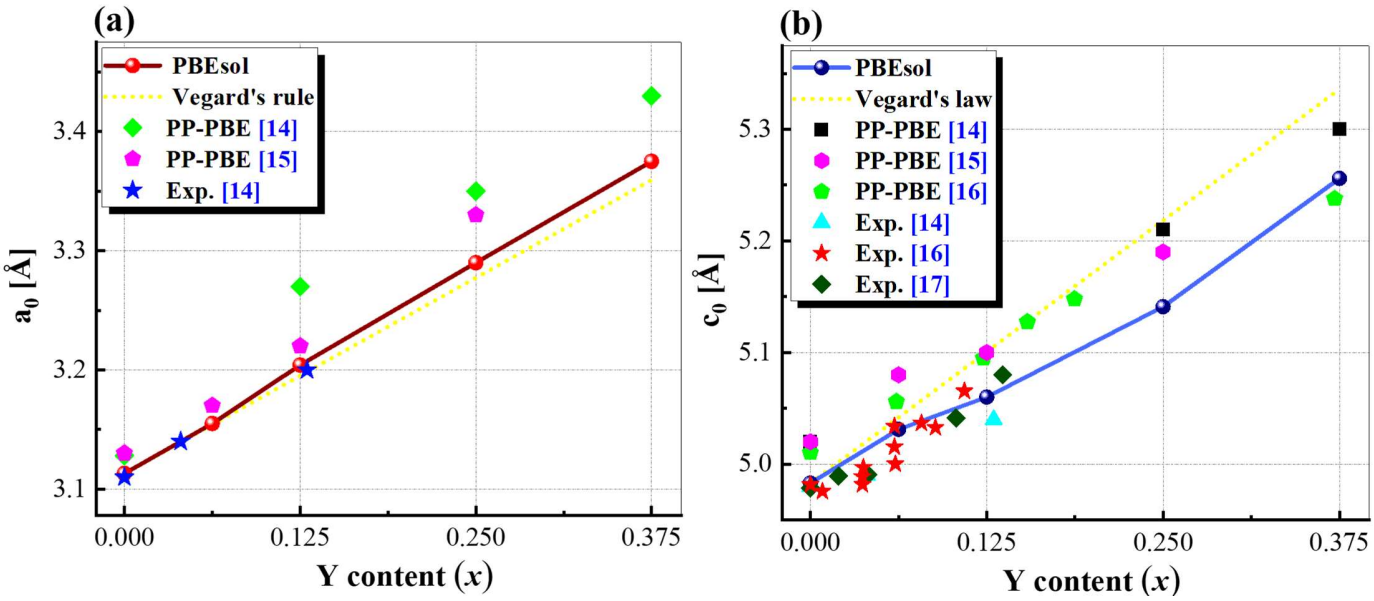

Figure IV.2. Variation of lattice parameters a_0 (a) and c_0 (b) as a function of yttrium composition for wurtzite $Y_xAl_{1-x}N$ alloys.

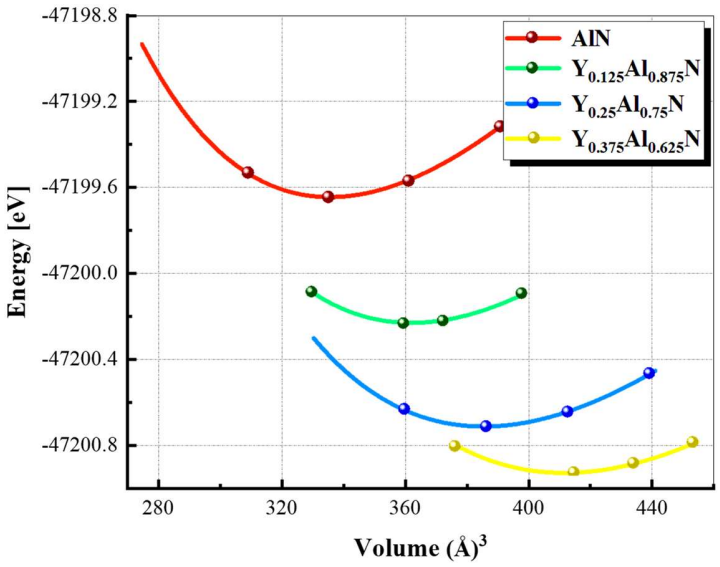

Figure IV.3. Variation of total energy as a function of volume for wurtzite $Y_xAl_{1-x}N$ alloys with x values of 0, 0.062, 0.125, 0.25, and 0.375. The solid lines denote the fit of Murnaghan's equation of state to the data.

B. Lattice Stability

To ensure structural stability, the thermodynamic and dynamical stabilities of doped wurtzite $Y_xAl_{1-x}N$ alloys were examined through formation energy and phonon frequency calculations [25,26].

Firstly, we computed the formation energy (ΔE_f) of doping YAlN alloys using the flowing relationship [27] :

$$\Delta E_f = E_{YAlN}^{dop} - E_{AlN}^{parent} - \sum m_i \mu_i \quad (1)$$

Where E_{YAlN} and E_{AlN} are the total energy of doping YAlN and the pure AlN, respectively. m_i denotes the number of atoms related to pure AlN, and μ_i are the chemical potentials of the corresponding atoms in their bulk phases.

As shown in Table IV-1, the obtained values of ΔE_f are –3.966, –4.027, –4.062, –4.092 eV for x= 0.062, 0.125, 0.25, and 0.375, respectively. These negative values signify the thermodynamic stability of $Y_xAl_{1-x}N$ systems across the full range of yttrium concentrations. It is also observed that ΔE_f decreases as yttrium content increases, indicating that $Y_xAl_{1-x}N$ crystals can be grown more easily experimentally, consistent with previous experimental work [16,17]. Consequently, yttrium doping enhances the thermodynamic stability of $Y_xAl_{1-x}N$ crystals.

Secondly, to evaluate dynamical stability, we calculated the phonon frequencies of $Y_xAl_{1-x}N$ alloys with x = 0, 0.125, 0.25, and 0.375 using density functional perturbation theory (DFPT) [28] and the local density approximation (LDA). LDA is a more efficient tool for computing phonon frequencies and generally provides better agreement with experimental results [29]. The absence of imaginary phonon frequencies indicates that the crystal is dynamically stable [30]. In contrast, negative values correspond to imaginary frequencies, which are associated with unstable modes. The computed phonon dispersion spectra along high-symmetry directions are displayed in Figure IV.4. The absence of imaginary phonon frequencies in the curves suggests dynamic stability of $Y_xAl_{1-x}N$ crystals across the entire yttrium concentration range of 0 to 0.375.

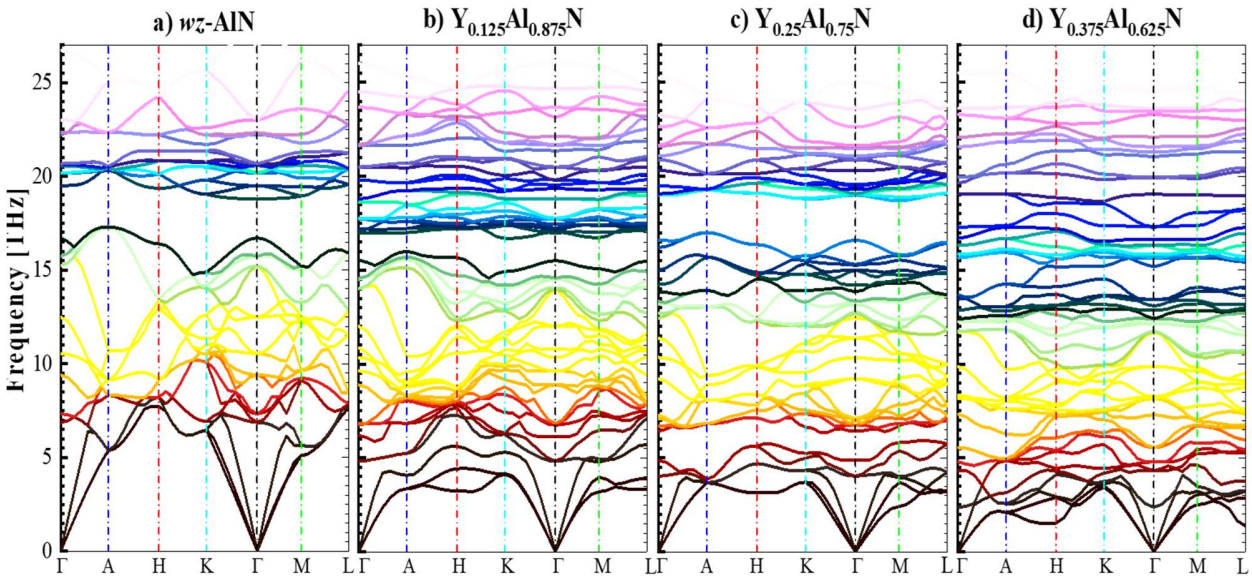

Figure IV.4. Computed phonon dispersions for wurtzite $Y_xAl_{1-x}N$ alloys with concentrations x = 0, 0.125, 0.25, and 0.375 along high-symmetry directions.

IV.4. Electronic Structure

A. Bandgap

Understanding the electronic structure of materials is crucial for determining their suitability for applications in photonic devices. In this section, we investigate the electronic structure of wurtzite $Y_xAl_{1-x}N$ compounds with varying yttrium concentrations ($0 \leq x \leq 0.375$). This study includes an analysis of the bandgap, density of states, and bonding charge density. The calculations were performed using self-consistent scalar relativistic FP-LAPW methods, with the exchange and correlation effects treated using the newly developed *n*KTB–mBJ exchange potential.

Table IV-2 summarizes the bandgap results along with previous DFT calculations and experimental data. The direct bandgap ($E\Gamma-\Gamma$) of pure AlN was calculated to be 6.104 eV, which is in close agreement with the measured value of 6.2 eV reported by Sedrine et al. [17] and Adachi [21]. This result obtained using *n*KTB–mBJ is an improvement over the

5.385 eV value obtained using the original TB–mBJ functional [13], and significantly better than the previous values of 4.028 eV [15], 4.11 eV [31], 3.98 eV [32], and 4.1 eV [33] derived from the standard PBE (GGA) approach. Our calculated bandgaps using the *n*KTB–mBJ approach for $Y_xAl_{1-x}N$ compounds (see Table IV-2) are overestimated than those reported in previous studies using the TB-mBJ (López-Pérez et al. [13]) and PBE (GGA) (Xie et al. [15]) methods. The *n*KTB–mBJ functional is nowadays considered one of the most accurate schemes for predicting bandgaps across a wide range of materials, including semiconductors and insulators, with performance comparable to more expensive methods such as GW and hybrid functionals [3]. Both the *n*KTB–mBJ functional and its origin the TB–mBJ have been successfully employed to explore the characteristics of emergence optoelectronic materials, such as III–V bismides semiconductors {InSbBi [34], GaPBi [35], InAsBi [36], InPBi [37], BTlGaN [38], BGaAsBi [39], BInGaN [40]}, and perovskites crystals {$BaSrTiO_3$ [7], Na_2AgAsX_6 (X = Cl, Br) [8]}.

Table IV-2: Calculated direct {$E_{\Gamma-\Gamma}$} and indirect {$E_{M-\Gamma}$, $E_{K-\Gamma}$} bandgaps for wurtzite $Y_xAl_{1-x}N$ alloys with yttrium contents ($0 \leq x \leq 0.375$) using *n*KTB–mBJ functional.

Y-contents		Bandgaps *n*KTB–mBJ	Theor. values	Exp.
AlN	$E_{\Gamma-\Gamma}$	6.104	5.385[a] - 4.028[b] - 4.11[c]	6.2[d,e]
	$E_{M-\Gamma}$	6.288	5.961[a]	
	$E_{K-\Gamma}$	6.427		
$Y_{0.062}Al_{0.937}N$	$E_{\Gamma-\Gamma}$	5.441	3.421[b]	
	$E_{M-\Gamma}$	5.195		
	$E_{K-\Gamma}$	5.215		
$Y_{0.125}Al_{0.875}N$	$E_{\Gamma-\Gamma}$	5.219	3.091[b]	
	$E_{M-\Gamma}$	4.946		
	$E_{K-\Gamma}$	4.941		
$Y_{0.25}Al_{0.75}N$	$E_{\Gamma-\Gamma}$	4.672	4.231[a] - 2.712[b]	
	$E_{M-\Gamma}$	4.505	3.885[a]	
	$E_{K-\Gamma}$	4.449		
$Y_{0.375}Al_{0.625}N$	$E_{\Gamma-\Gamma}$	3.850		
	$E_{M-\Gamma}$	4.171		
	$E_{K-\Gamma}$	4.159		

[a]Ref.(TB–mBJ) [13], [b]Ref. (PBE) [15], [c]Ref. (PBE) [31], [d]Ref. (Exp.) [17], [e]Ref. (Exp.) [21].

Figure IV.5 shows the calculated band structures of wurtzite $Y_xAl_{1-x}N$ alloys with concentrations x = 0, 0.125, 0.25, and 0.375 along high-symmetry directions of the Brillouin zone (BZ) using *n*KTB–mBJ functional. As seen in Figure IV.5 (a) and IV.5 (d), for pure AlN and $Y_{0.375}Al_{0.625}N$ alloy, the valence band maximum (VB_{max}) and the conduction band minimum (CB_{min}) are both located at the Γ point of the BZ, signifying that these materials exhibit a direct bandgap character. Analysis by spectroscopic ellipsometry (SE) of $Y_xAl_{1-x}N$ at x = 0.22 indicates that it is a direct bandgap semiconductor with an E_g of 4.5 eV [17]. It can be observed from Figure IV.5 (b) and IV.5 (c) that the bandgap becomes indirect for $Y_{0.0625}Al_{0.875}N$ at M→Γ transition, and for $Y_{0.125}Al_{0.875}N$ and $Y_{0.25}Al_{0.75}N$ systems at K→Γ transition. Figure IV.6 shows the variation of direct (Γ→Γ) and indirect (M→Γ, K→Γ) bandgaps as a function of yttrium doping in wurtzite$Y_xAl_{1-x}N$ compounds. A decrease in the direct bandgap (Γ→Γ) from 6.10 eV in AlN to 3.85 eV in$Y_{0.375}Al_{0.625}N$ is clearly observed, which is consistent with the experimental data showing a bandgap reduction from 6.2 eV (x = 0) to 4.5 eV (x = 0.22) [18]. Baeumler et al. [41] recently observed a similar reduction in bandgap for wurtzite $Al_{1-x}Sc_xN$, with E_g decreasing from 6.06 eV for AlN to 5.0 eV for $Al_{0.75}Sc_{0.25}N$. The bandgap in $Al_{1-x}Sc_xN$ remains direct up to x = 0.23 [41] and x = 0.25 [42,43]. Additionally, as shown in Figure IV.6, the curves indicate two bandgap transitions in wurtzite $Y_xAl_{1-x}N$: the first transition is from a direct (Γ→Γ) to an indirect (M→Γ) bandgap at a lower yttrium concentration of x = 0.029 (E_g = 5.78 eV), and the second transition is from an indirect (K→Γ) to a direct (Γ→Γ) bandgap at x = 0.29 (E_g = 4.38 eV). *As a result*, wurtzite $Y_xAl_{1-x}N$ (x= 0–0.375) exhibits a bandgap that corresponds to wavelengths ranging from 203 to 322 nm, making it a potential material for promising applications in near and deep ultraviolet optoelectronics, such as LEDs [40,44].

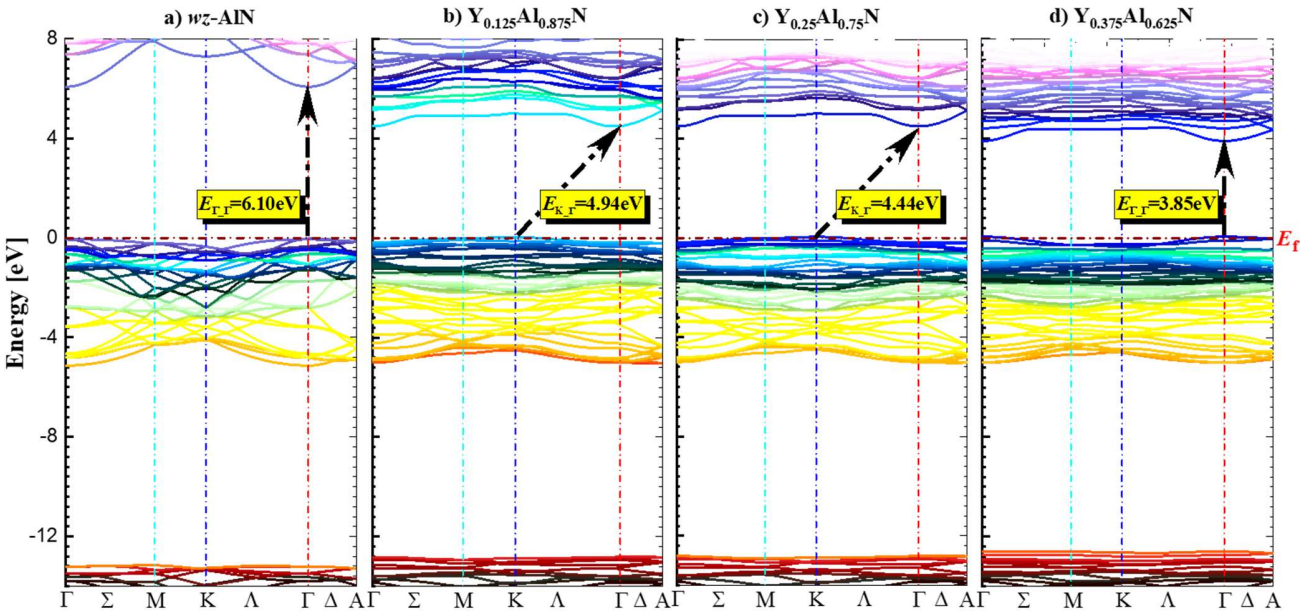

Figure IV.5. Calculated band structures for wurtzite $Y_xAl_{1-x}N$ alloys with concentrations x = 0 (a), 0.125 (b), 0.25 (c), and 0.375 (d) along high-symmetry directions using *n*KTB–mBJ functional.

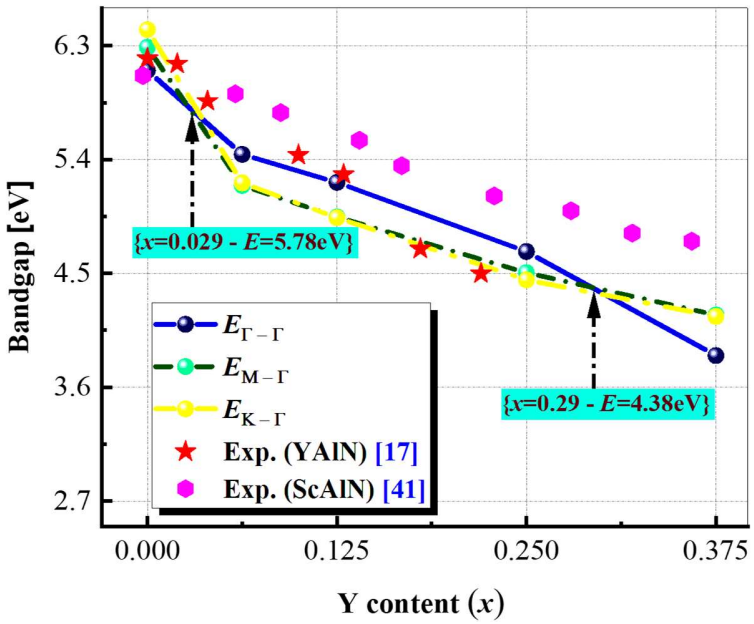

Figure IV.6. Calculated direct $E_{\Gamma-\Gamma}$ and indirect $E_{M-\Gamma}$, $E_{K-\Gamma}$ bandgaps as a function of yttrium composition for wurtzite $Y_xAl_{1-x}N$ alloys using *n*KTB–mBJ functional. The bandgap transitions from direct to indirect at x = 0.029 and then back to direct at x = 0.29.

B. Density of States (DOS)

In order to characterize the electronic band structures of wurtzite$Y_xAl_{1-x}N$ alloys under study, we calculated the partial density of states (PDOS) and the total density of states (TDOS) using the *n*KTB–mBJ functional for compositions x = 0.125, 0.25, and 0.375. The results are presented in Figure IV.7, for an energy range from –5.8 eV to +6.8 eV.

The TDOS profiles in Figure IV.7(a), IV.7(b), and IV.7(c) show a similar overall pattern for the three compounds. We can distinguish two main energy groups: one localized in the valence band (VB) (below the Fermi level (E_F)) and the other in the conduction band (CB) (above E_F). In the valence band region, the TDOS exhibits two sub-bands. The lower sub-band, arising in the energy range from –5.8 to –3.7 eV, is composed mainly of Al_3s states with a slight admixture of N_2p states. The higher sub-band, located between –3.7 eV and 0 eV, is dominated by Al_3p states, with a significant contribution from N_2p and Y_4d orbitals near the Fermi level (E_F), consistent with previous findings [15]. The conduction band (CB) is mainly formed by Y_4*d* states, with partial participation from Al_3*p* states. A shift in the CB to lower energies is clearly observed as yttrium is incorporated into $Y_xAl_{1-x}N$, which leads to a decrease in the bandgap energy.

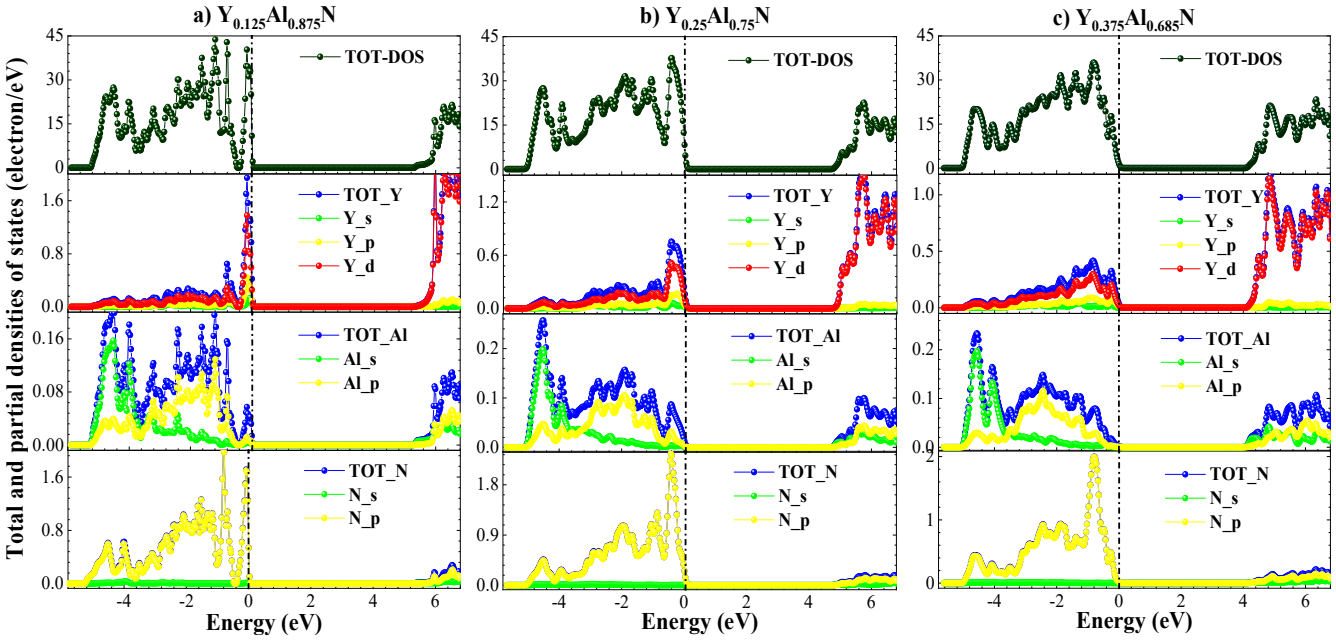

Figure IV.7. Calculated partial density of states (PDOS) and total density of states (TDOS) for wurtzite $Y_xAl_{1-x}N$ alloys with x = 0.125 (a), 0.25 (b), and 0.375 (c) using *n*KTB–mBJ functional.

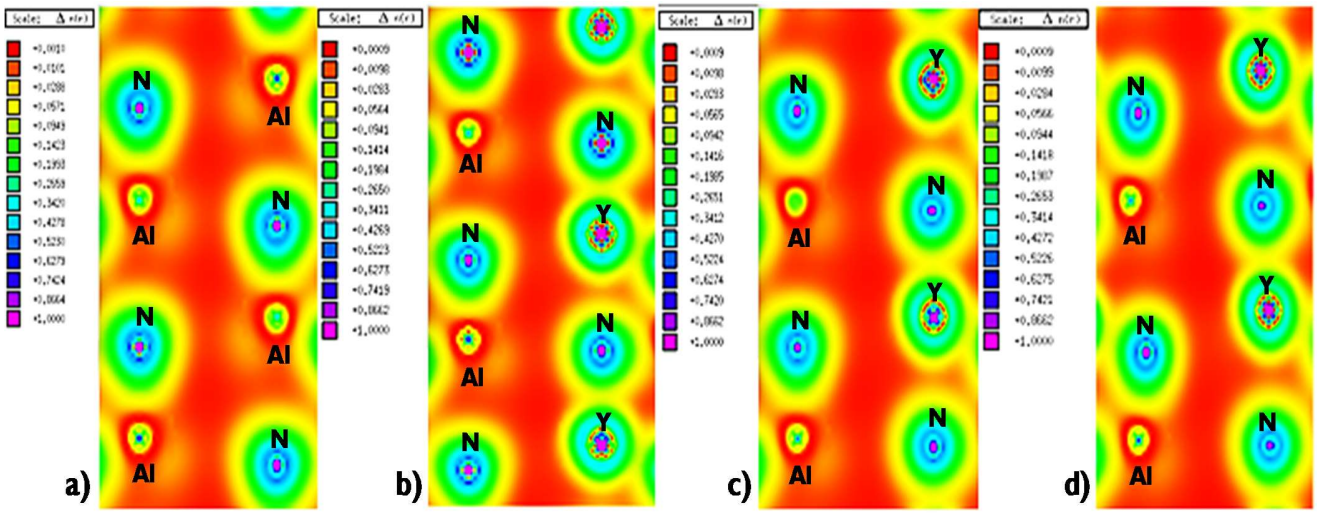

Figure IV.8. Charge density maps in the (4-20) plane for wurtzite $Y_xAl_{1-x}N$ alloys for compositions: (a) x= 0, (b) x= 0.125, (c) x= 0.25, and (d) x= 0.375 from *n*KTB–mBJ functional.

C. Electronic Charge Density

The electron charge density is a useful tool that used for understanding the nature of chemical bonds between the different elements that constitute a solid. Using the *n*KTB–mBJ functional, we calculated and plotted the 2D bonding charge density distributions projected onto the (4 -2 0) plane for wurtzite $Y_xAl_{1-x}N$ alloys with yttrium compositions of 0, 0.125, 0.25, and 0.375, as shown in Figure IV.8. In Figure IV.8(b), IV.8(c), and IV.8(d), the charge distribution around the Y atoms and their neighboring N atoms in the Y-125, Y-25, and Y-375 alloys exhibits a circular form, indicating that the bonding between Y and N atoms is ionic in nature. In contrast, the charge distribution around the Al atoms and their neighboring N atoms deviates slightly from a circular shape, indicating a covalent bond character between the Al–N ions. This may stem from the differences in Pauling electronegativity between the neighboring ions [7,34].

IV.5. Elastic and Mechanical Properties

Here, we calculated the elastic constants (C_{11}, C_{12}, C_{13}, C_{33} and C_{44}) of wurtzite $Y_xAl_{1-x}N$ alloys using PBEsol approximation within Ultrasoft Vanderbilt pseudopotential method. The procedure for extracting these constants is detailed by Boonchun et al. [45]. The resulting values are presented in Table IV-3 along with previous DFT calculations and available experimental data. For pure AlN, our values with the PBEsol approximation are C_{11} = 372 GPa, C_{12} = 127 GPa, C_{13} = 98 GPa, C_{33} = 343 GPa, and C_{44} = 109 GPa. These values closely match the measurements reported by Tsubouchi et al. [46] and McNeil et al. [47], and are more accurate than those reported by Wright [48] and Kim et al. [49] using LDA approximation. In contrast, the C_{ij} values for $Y_xAl_{1-x}N$ compounds are found to be larger than those from recent PBE-GGA calculations by Manna et al. [50], which generally the C_{ij} constants [51].

Table IV-3: Calculated elastic constants (C_{ij}) in GPa, bulk modulus (B) in GPa, shear modulus (G) in GPa, Young's modulus (Y) in GPa, Poisson's ratio (ν) and Frantesvich ratio (G/B_0) for wurtzite $Y_xAl_{1-x}N$ crystals ($0 \leq x \leq 0.375$) using PBEsol approximation.

Y-contents		C_{11}	C_{12}	C_{13}	C_{33}	C_{44}	B	G	Y	ν	G/B_0
AlN	PBEsol	372	127	98	343	109	192	118	295	0.24	0.61
	Expt. [46]	345	125	120	395	118	201			0.22 [21]	
	[47]	411	149	99	389	125	210				
	Theo. [48]	396	137	108	373	116	207		294		
	[49]	398	140	127	382	96	218				
$Y_{0.0625}Al_{0.9375}N$	PBEsol	329	122	104	320	95	180	100	255	0.26	0.55
$Y_{0.125}Al_{0.875}N$	PBEsol	299	126	107	305	88	176	90	232	0.27	0.51
	Theo. [48]				232						
$Y_{0.25}Al_{0.750}N$	PBEsol	244	122	110	263	75	156	70	183	0.30	0.44
	Theo. [48]				144						
$Y_{0.375}Al_{0.625}N$	PBEsol	209	103	114	224	56	145	53	143	0.33	0.37

Figure IV.9 illustrates the dependency of elastic constants on yttrium composition in $Y_xAl_{1-x}N$ alloys within the x range of 0 to 0.375. A decrease in elastic constants is observed as the yttrium dopant concentration increases, with values decreasing from C_{11} = 372 GPa, C_{12} = 127 GPa, C_{33} = 343 GPa, and C_{44} = 109 GPa in pure AlN to 209 GPa, 103 GPa, 224 GPa, and 56 GPa in $Y_{0.375}Al_{0.625}N$, respectively. This corresponds to reductions of approximately 43%, 18%, 34%, and 48% compared to pure AlN. In contrast, C_{13} increases by 14% with the addition of yttrium, rising from 98 GPa at x = 0 to 114 GPa at x = 0.375. We conclude that wurtzite $Y_xAl_{1-x}N$ alloys exhibit elastic behavior comparable to that demonstrated experimentally in $Sc_xAl_{1-x}N$ and $Y_xIn_{1-x}N$ crystals [47,50]. Similarly, a theoretical decrease in C_{33} was reported for $Y_xIn_{1-x}N$, reducing from 205 GPa (at x = 0) to 94 GPa (at x = 0.5), corresponding to a reduction of approximately 54%. This decrease is higher than the 34% reduction observed in $Y_xAl_{1-x}N$ at x = 0.375 in this work but lower than the 64% decrease reported in $Sc_xAl_{1-x}N$, where C_{33} decreases from 367 GPa (at x = 0) to 131 GPa (at x = 0.5). Additionally, Kurz et al. [52] recently observed experimentally that C_{ij} values decrease with Sc doping in $Sc_xAl_{1-x}N$ (for x up to 0.32), with reductions of approximately 26% for C_{11}, 43% for C_{33}, and 20% for C_{44}, while C_{13} increases with x.

To assess mechanical stability, we analyzed the compliance of the elastic constants C_{ij} of wurtzite $Y_xAl_{1-x}N$ crystals with the Born mechanical stability criteria, given as [53]:

$$C_{11} > 0, \quad (C_{11} - C_{12}) > 0, \quad C_{44} > 0, \quad (C_{11} + C_{12})\, C_{33} > 2C_{11}^2.$$

Our calculated C_{ij} values satisfy these mechanical stability criteria, indicating that $Y_xAl_{1-x}N$ crystals are mechanically stable for across the full range of yttrium concentrations ($0 \le x \le 0.375$).

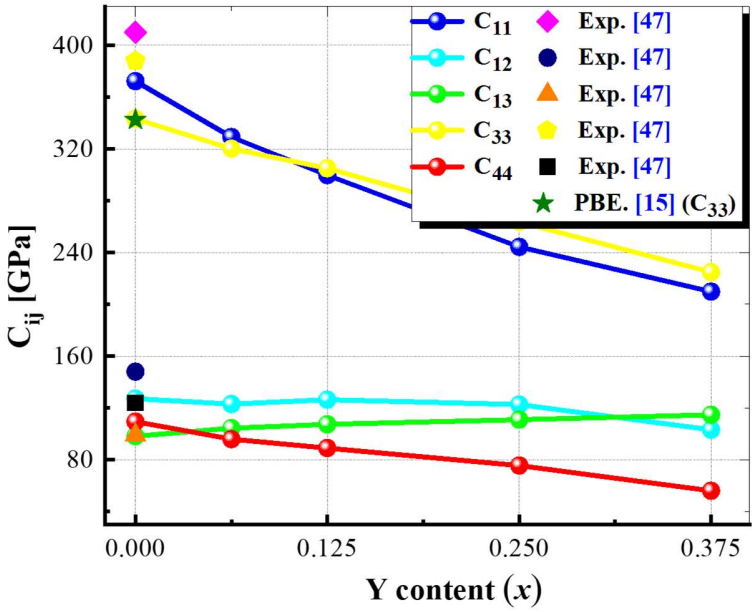

Figure-IV.9. Dependency of elastic constants (C_{ij}) on yttrium composition in $Y_xAl_{1-x}N$ alloys.

Additionally, using Voigt–Reuss theory [54,55], the calculated elastic constants (C_{ij}) are then used to determine supplementary mechanical properties for $Y_xAl_{1-x}N$ polycrystals, such as the bulk modulus (B), shear modulus (G), Young's modulus (Y), and Poisson's ratio (ν).

In a hexagonal crystal, the Voigt bulk modulus B_v and shear modulus G_v are expressed by

$$B_v = \left(\frac{1}{9}\right)\left[2(c_{11} + c_{12}) + c_{33} + 4c_{13}\right] \quad (2)$$

$$G_v = \left(\frac{1}{30}\right)\left[c_{11} + c_{12} + 2c_{33} - 4c_{13} + 12c_{44} + 12c_{66}\right] \quad (3)$$

The *R*euss bulk modulus B_R and shear modulus G_R are given as:

$$B_R = \left\{(c_{11} + c_{12})c_{33} - 2c_{12}^2\right\}/(c_{11} + c_{12} + 2c_{33} - 4c_{13}) \quad (4)$$

$$G_R = \frac{\left(\frac{5}{2}\right)\left\{\left[(c_{11} + c_{12})c_{33} - 2c_{12}^2\right]c_{44}c_{66}\right\}}{\left\{3B_v c_{44}c_{66} + \left[(c_{11} + c_{12})c_{33} - 2c_{12}^2\right](c_{44} + c_{66})\right\}} \quad (5)$$

where $c_{66} = (c_{11} - c_{12})/2$.

The bulk modulus B_0 and shear modulus G are done by the *V*oigt–*R*euss–*H*ill scheme [56] as the arithmetic averages

$$B = \frac{B_v + B_R}{2} \quad (6)$$

$$G = \frac{G_v + G_R}{2} \quad (7)$$

The Young's modulus (Y) and Poisson's ratio (ν) are given by

$$Y = \frac{9BG}{3B + G} \quad (8)$$

$$\nu = \frac{3B - 2G}{6B + 2G} \quad (9)$$

Table 3 summarizes the results for the bulk modulus (B_0), shear modulus (G), Young's modulus (Y), Poisson's ratio (ν), and Frantesvich ratio (G/B_0) for wurtzite $Y_xAl_{1-x}N$ alloys. For pure AlN, the calculated values of the bulk modulus and Young's modulus are 192.3 GPa and 294.5 GPa, respectively, which are in good agreement with the experimental results reported in [21,47].

The shear modulus (G) serves as a criterion for the hardness of a solid, the Young's modulus (Y) is associated with stiffness [57], and the bulk modulus (B) is linked to

compressibility. As shown in Table IV-3, $Y_xAl_{1-x}N$ crystals exhibit reasonably high G and Y values, signifying significant hardness and stiffness. The value of B (with *x* up to 0.125) is also higher than that of steel (~160 GPa) [58]. Moreover, the mechanical properties, such as the shear modulus (G), Young's modulus, bulk modulus (B) in $Y_xAl_{1-x}N$, are found to decrease with increasing yttrium content, as shown in Table 4. This suggests that $Y_xAl_{1-x}N$ tends to be less stiff and more compressible compared to pure AlN crystals, as revealed in Table IV-3.

The Frantesvich G/B ratio is a measure a solid's brittleness or ductility [59]. A crystal is considered ductile when G/B < 0.571 and brittle when G/B > 0.571. Our results (see Table IV-3) indicate that the $Y_xAl_{1-x}N$ crystal undergoes a transition from brittleness to ductility as *x* increases to approximately 0.04.

The Poisson's ratio (*v*) is a parameter often used for explain the nature of crystal's bonds. For *v* values less than ~ 0.1, the crystal is typically covalent, whereas values close to 0.25 are characteristic of ionic crystals [60]. The obtained values of ν (see Table 3) range from 0.24 to 0.33 for $0 \leq x \leq 0.375$, indicating that $Y_xAl_{1-x}N$ alloys exhibit a strong ionic bond character.

To analyze the elastic anisotropy in $Y_xAl_{1-x}N$ crystals, we plotted 3D anisotropic surfaces of the bulk modulus (B), shear modulus (G), and Young's modulus (Y) in Figure-IV.10, using the equations described in [61]. The degree of elastic anisotropy can be defined by the extent to which the contours deviate from a spherical shape. The 3D surfaces of the bulk modulus that are typically spherical indicate lower directional dependence. However, the surfaces of Young's modulus deviate significantly from a spherical form compared to those of the shear modulus, indicating that the Young's modulus exhibits high elastic anisotropy. Figure IV.10 also shows that the anisotropies of the shear and Young's moduli are only slightly affected by yttrium doping in $Y_xAl_{1-x}N$ crystals.

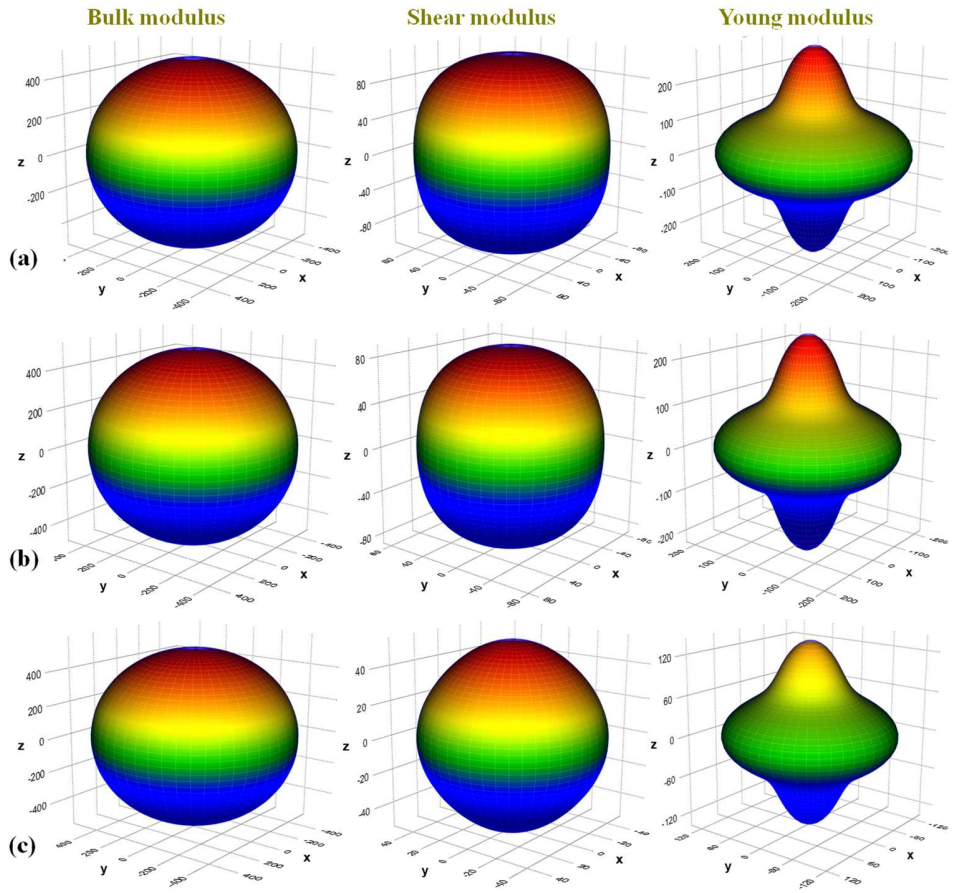

Figure IV.10. 3D anisotropic surface plots of bulk modulus, shear modulus, and Young's modulus for wurtzite $Y_xAl_{1-x}N$ alloys with compositions x = 0 (a), 0.125 (b), and (c) 0.375.

Furthermore, using the calculated elastic moduli, additionally physical quantities, such as Debye temperature, density (ρ) and sound velocities (v_l, v_t, v_m) for wurtzite $Y_xAl_{1-x}N$ crystals with varying yttrium contents were determined.

The Debye temperature (Θ_D) is a significant factor often used to extract the thermal parameters of solids. It quantifies the maximum value of vibration energies. High-frequency modes contribute energy of approximately k_BT, and these modes become 'frozen' at temperatures below Θ_D [62].

Debye temperature (Θ_D) is calculated from acoustic wave velocity (v_m) using the formula [63]:

$$\Theta_D = \frac{h}{k}\left[\frac{3n}{4\pi}\left(\frac{N_A\rho}{M}\right)\right]^{1/3} v_m \tag{10}$$

where h is Plank's constant, k is Boltzmann's constant, ρ is the density, M is molecular weight in g/mol, N_A is Avogadro number, and n is the number of atoms in the formula unit.

The average of the acoustic wave velocity (v_m) is expressed by

$$v_m = \left[\frac{1}{3}\left(\frac{2}{v_t^3}+\frac{1}{v_l^3}\right)\right]^{1/3} \tag{11}$$

where v_l and v_t are the longitudinal and transversal acoustic wave velocities, respectively, which are obtained using Napier's equations [64]:

$$v_l = \left(\frac{3B+4G}{3\rho}\right)^{1/2} \tag{12}$$

$$v_t = \left(\frac{G}{\rho}\right)^{1/2} \tag{13}$$

For pure AlN, the value of ρ is found to be 3.21 g/cm³ using the PBEsol functional, which is in close agreement with the measured values of 3.23 g/cm³ [52] and 3.26 g/cm³ [65], as well as the previously calculated value of 3.21 g/cm³ [52]. The calculated value of Θ_D is 914 K, which is slightly smaller than the measured value of 988 K at 300 K [21]. Our values for the longitudinal and transverse sound velocities are 10454 m/s and 6084 m/s, respectively. These are in good agreement with the experimental results of 10900 m/s [21] (10880 m/s [66]) and 6070 m/s [21], respectively.

Figure IV.11 shows the evolution of Debye temperature (Θ_D), density (ρ) and sound velocities (v_l, v_t, v_m) as a function of yttrium composition for wurtzite $Y_xAl_{1-x}N$ crystals. The Debye temperature (Θ_D) can be also used to assess a material's hardness. A material is considered hard if it has a high Debye temperature [67]. As depicted in Figure IV.11(a), Θ_D ranges from 519 to 914 K for $0 \le x \le 0.375$, indicating significant hardness. It decreases with

increasing yttrium content. Contrary, as observed in Figure IV.11(a), the density ρ increases to 3.74 g/cm^3 for x = 0.375, due to a decrease in porosity in $Y_xAl_{1-x}N$ crystals. A decrease in sound velocities with increasing x is also observed, as shown in Figure IV.11(b). For $Y_{0.375}Al_{0.625}N$, the velocities v_l, v_t and v_m are 7609 m/s, 3789 m/s and 4251 m/s, respectively. These values may influence sound propagation velocities in acoustic wave devices [68]. Although, a decrease in longitudinal wave velocity (v_l) has been experimentally observed in CrAlN, ScAlN, and MgZrAlN crystals with the incorporation of transition metal elements. Despite the decrease in velocity, these materials offer high electromechanical coupling, making them promising for advanced high-frequency electroacoustic devices [66,69]. We suggest that the decrease in Debye temperature in $Y_xAl_{1-x}N$ is due to the reduction in acoustic wave velocities and the increase in atomic weights.

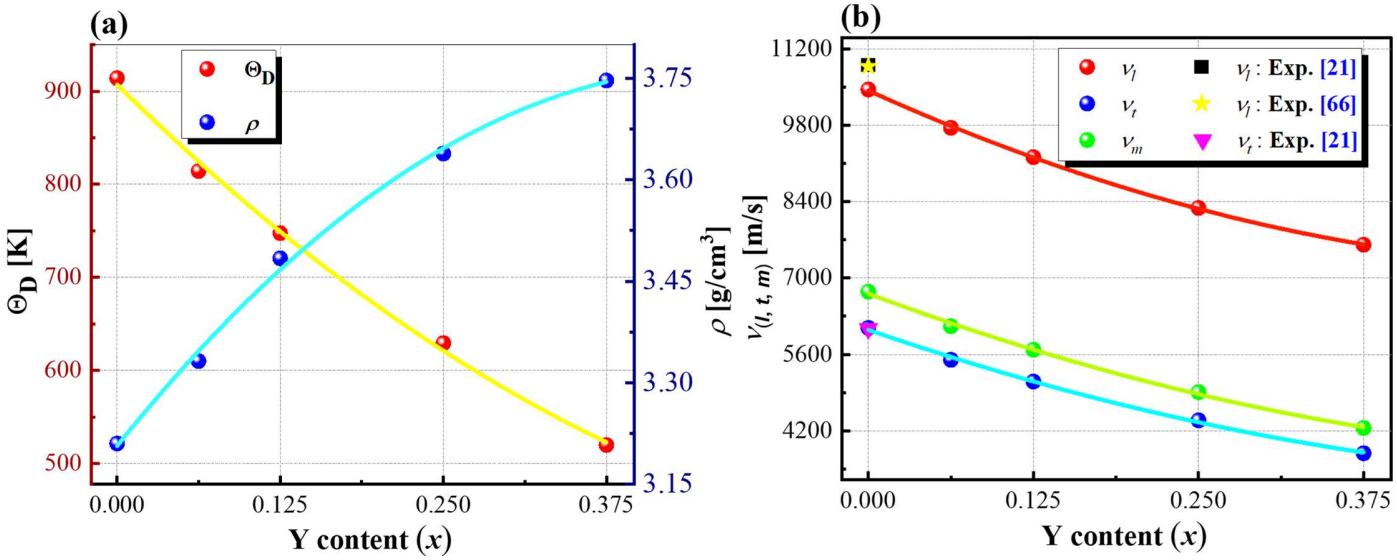

Figure IV.11. Debye temperature (Θ_D), and density (ρ) (a), and sound velocities (v_l, v_t, v_m) (b), versus yttrium composition in wurtzite $Y_xAl_{1-x}N$ alloys.

IV.6. Piezoelectric Properties

The wurtzite symmetry for $Y_xAl_{1-x}N$ systems is characterized by three independent piezoelectric coefficients: d_{15}, d_{31} and d_{33}, along with two independent dielectric tensor components: ε_{11} and ε_{33}.

We aim to calculate the piezoelectric stress tensors (e_{ij}) and static dielectric tensors (ε_{ij}) using a self-consistent Density Functional Perturbation Theory (DFPT) [11] within the plane-wave pseudopotential framework, where the exchange potential is treated using the PBEsol approximation.

The piezoelectric stress tensor e_{ij} (in units of C/m^2) is expressed by the flowing formula [70]:

$$e_{ij}^{T} = -\left(\frac{\partial \sigma_j}{\partial E_i}\right)_{\varepsilon,T} \tag{14}$$

where σ denotes the stress tensor and E represents the electric filed.

The piezoelectric strain tensor elements d_{ij} can then be extracted from the determined piezoelectric stress tensors e_{ij} and the elastic stiffness matrix C_{ij}, using the following formula [71]:

$$e_{ij} = \sum_{k} d_{ik} C_{kj} \tag{15}$$

Here, C_{ij} represents the elastic constants at a constant electric field, and e_{ij} and d_{ij} are the piezoelectric tensors.

The d_{ij} parameter is essential for evaluating the performance of materials in electroacoustic device applications [71].

Table IV-4 summarizes the results for piezoelectric strain tensors d_{ij}, the piezoelectric stress matrix e_{ij}, and the static relative dielectric tensor ε_{ij} for wurtzite $Y_xAl_{1-x}N$ alloys using the PBEsol approximation. Our PBEsol calculations for *wz*-AlN show better agreement with experimental results [72–74] compared to those obtained using the PBE-GGA [16,50,71] and LDA [51] methods. It is notable that the PBE-GGA approach generally underestimates the piezoelectric coefficients, particularly d_{31} and d_{33} [75,76]. The results for e_{ij} in *wz*-AlN are

e_{15} = –0.30 C/m^2, e_{31} = –0.60 C/m^2, and e_{33} = 1.52 C/m^2, which are in good agreement with the PBEsol values of –0.30 ± 0.22 C/m^2, –0.54 ± 0.05 C/m^2, and 1.52 ± 0.43 C/m^2, respectively, as recently reported by Kurz et al. [52]. The ε_{ij} values in $Y_xAl_{1-x}N$ are also found to be in better agreement with measured data [72]. These values increase slightly with yttrium content. This indicates that the PBEsol approach can accurately and effectively predict the piezoelectric properties of the materials under study.

Table IV-4: Computed piezoelectric strain constants (d_{ij}) in pC/N, piezoelectric stress constants (e_{ij}) in C/m^2, and static dielectric constants (ε_{ij}) for wurtzite $Y_xAl_{1-x}N$ crystals.

Y-contents			d_{15}	d_{31}	d_{33}	e_{15}	e_{31}	e_{33}	ε_{11}	ε_{33}
AlN	**PBEsol**		–2.74	–2.33	5.76	–0.30	–0.60	1.52	3.79	5.10
	Expt.	[72]	–4.07	–2.65	5.33	–0.48	–0.58	1.55	4.71	4.93
		[73,74]	3.6	–2.1	5.6		–0.58	1.46		
	Theo.	[16]	2.90	–2.1	5.0		–0.64	1.46		
		[71]			5.4			1.8		
		[50, 51]			5.15					
$Y_{0.0625}Al_{0.9375}N$	**PBEsol**		–4.37	–3.09	7.49	–0.42	–0.62	1.68	3.98	5.18
	Theo.	[16]		–2.90	6.7		–0.59	1.54		
$Y_{0.125}Al_{0.875}N$	**PBEsol**		–4.94	–3.60	8.35	–0.44	–0.64	1.78	4.41	5.26
	Theo.	[16]		–3.70	7.8		–0.63	1.62		
		[50]			8.03			1.53		
$Y_{0.25}Al_{0.750}N$	**PBEsol**		–6.48	–5.15	11.2	–0.49	–0.66	1.88	5.00	5.47
	Theo.	[16]		–6.80	15.2		–0.63	1.8		
		[50]			15.2			1.7		
$Y_{0.375}Al_{0.625}N$	**PBEsol**		–11.0	–8.65	17.5	–0.62	–0.70	1.95	5.30	5.77
	Theo.	[16]		–9.60	21.5		–0.68	1.92		

The piezoelectric stress e_{33} and strain d_{33} coefficients dependency on yttrium composition is depicted in Figure IV.12. As shown in Figure IV.12(a) and Table IV-4, the piezoelectric stress tensors (e_{ij}) increase more significantly with the composition *x* compared

to other theoretical results [16,50]. The piezoelectric coefficients (d_{ij}) also show significant increases in $Y_{0.375}Al_{0.625}N$, d_{33}= 17.5 pC/N, d_{15}= −11.07 pC/N, and d_{31}= −8.65 pC/N, as displayed in Figure IV.2(b). These values represent approximately 300%, 400%, and 370% higher, respectively, compared to those of pure AlN crystals. This enhancement in d_{ij} coefficients is principally due to a significant distortion of the wurtzite symmetry in $Y_xAl_{1-x}N$ systems.

A similar phenomenon was observed in $Al_{1-x}Sc_xN$ crystals, as reported by Zywitzki et al. [77]. This can also be explained by the fact that the piezoelectric stress elements (e_{ij}) increase while the elastic constants (C_{ij}) decrease simultaneously with increasing Y content in $Y_xAl_{1-x}N$. Additionally, the value of d_{33} ≈ 17.5 pC/N in $Y_{0.375}Al_{0.625}N$ is comparable to that reported for alternatives such as $Sc_{0.33}Al_{0.67}N$ (≈ 23.6 pC/N) [77], $Sc_{0.4}Al_{0.6}N$ (≈ 20.1 pC/N) [78], $Sc_{0.42}Al_{0.625}N$ (≈ 19.0 pC/N) [79], $Sc_{0.43}Al_{0.57}N$ (≈ 24.6 pC/N) [80], $Sc_{0.5}Al_{0.5}N$ (≈ 26.13 pC/N) [81], $Y_{0.5}In_{0.5}N$ (≈ 23.31 pC/N) [82]. It is much higher than that reported for $Ta_{0.051}Al_{0.946}N$ (≈ 8.2 pC/N) [83].

As a result, the dramatic improvement in piezoelectric coefficients for the novel $Y_xAl_{1-x}N$ systems was demonstrated experimentally in [82,16]. This enhancement leads to a significant improvement in the electromechanical coupling coefficient, thereby boosting the performance of advanced MEMS (micro-electromechanical systems) components, such as sensors, actuators, resonators, and RF filters, particularly those based on surface acoustic wave (SAW) and bulk acoustic wave (BAW) devices [84].

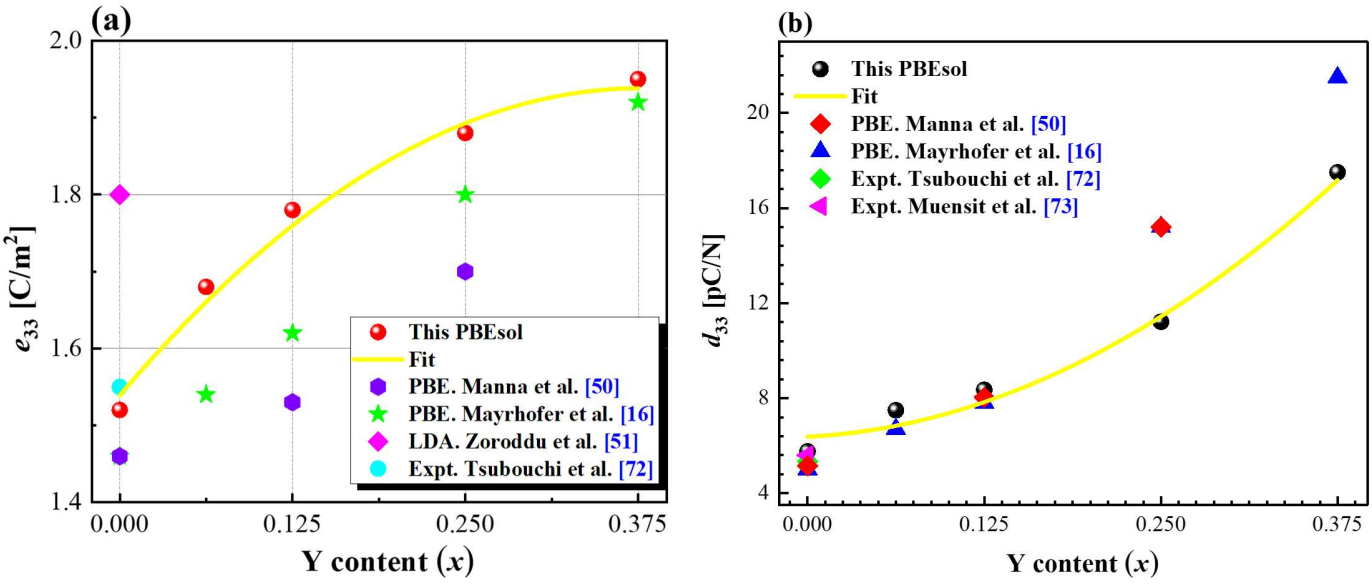

Figure IV.12. Piezoelectric stress constants (e_{ij}) (a), and piezoelectric strain constants (d_{ij}) as a function of yttrium content in wurtzite $Y_xAl_{1-x}N$ alloys.

IV.7. Thermodynamic Properties

In this section, using Gibbs2 package [85] based on the Debye quasi-harmonic model, we analyzed the influence of pressure and temperature on thermodynamic properties of $Y_xAl_{1-x}N$ alloys with the composition x ranging from 0 to 0.375. The properties studied include volume (V_0), compressibility modulus (B_0), specific heat (C_v), thermal expansion (α), entropy (S) and Debye temperature (Θ_D). The Gibbs2 package is employed to understand the thermal characteristics of alloys across a temperature range of 0–1000 K, utilizing energy-volume data obtained from ab initio simulations within the PBEsol (GGA) framework. The thermodynamic parameters calculated at 300 K for $Y_xAl_{1-x}N$ crystals, at pressures of 0 GPa, 20 GPa, and 50 GPa, and concentrations x ranging from 0 to 0.375, are listed in Table IV-5.

The obtained bulk modulus (B_0) for pure AlN at zero pressure and ambient temperature is approximately 194.83 GPa, which is in agreement with the value calculated by Ramírez-Montes et al. [13], approximately 195 GPa. In contrast, our result of the bulk

modulus $Y_{0.25}Al_{0.75}N$, which is 169.53 GPa at 300 K and 0 GPa, is slightly larger than the value of 150 GPa reported in [13]. A similar thermal behavior was in (YAlN) crystals with a rock-salt structure [13,86]. Generally, an increase in volume results in a decrease in the bulk modulus because the crystal's size (volume) affects its compressibility.

Figure IV.13 shows the dependence of the volume (V_0) and compressibility modulus (B_0) on temperature for wurtzite $Y_xAl_{1-x}N$ crystals with *x* ranging from 0 to 0.375. As depicted in Figure IV.13(a), V_0 gradually increases with temperature. Conversely, Figure IV.13(b) illustrates that B_0 decreases with rising temperature at zero pressure. This indicates that yttrium doping in $Y_xAl_{1-x}N$ crystals influences their resistance to deformation and compression.

Table IV-5. Computed thermodynamic parameters—bulk modulus (B_0, in GPa), heat capacity at constant volume (C_V, in $J \cdot mol^{-1} \cdot K^{-1}$), entropy (S, in $J \cdot mol^{-1} \cdot K^{-1}$), Debye temperature ($\Theta_D$, in K), and thermal expansion coefficient (α, in K^{-1})—at 300 K and various pressures for $Y_xAl_{1-x}N$ crystals.

Y-contents		P=0 GPa	P=20 GPa	P=50 GPa
AlN	B_0	194.832	272.199	388.353
	C_V	531.100	465.978	389.888
	S	345.355	268.528	198.525
	Θ_D	895.270	1044.23	1229.60
	α	2.36608	1.62007	1.04144
$Y_{0.125}Al_{0.875}N$	B	181.108	258.401	374.465
	C_V	572.032	508.870	433.466
	S	405.422	316.920	236.478
	Θ_D	802.960	945.580	1121.34
	α	2.53967	1.73599	1.12312
$Y_{0.25}Al_{0.750}N$	B	169.539	249.663	370.009
	C_V	604.236	541.286	465.312
	S	461.818	359.291	267.835
	Θ_D	729.570	872.300	1045.78
	α	2.80078	1.87660	1.20068
$Y_{0.375}Al_{0.625}N$	B	159.057	233.625	345.622
	C_V	629.254	573.061	503.520
	S	513.154	407.084	310.446
	Θ_D	671.330	800.630	957.750
	α	2.69255	1.85077	1.22081

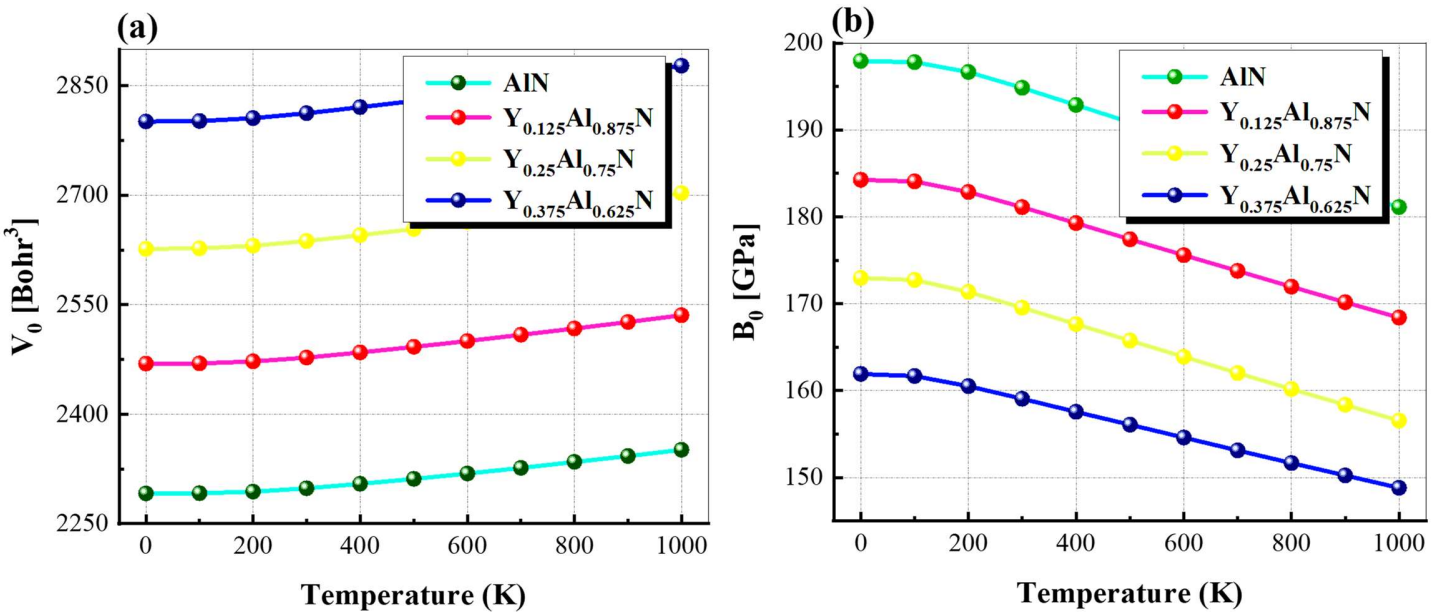

Figure IV.13. Dependence of volume (V_0) (a), and compressibility modulus (B_0) (b) on temperature under pressure for wurtzite $Y_xAl_{1-x}N$ crystals.

Figure IV.14 depicts the variation of the thermal capacity (C_V), thermal expansion (α), entropy (S) and Debye temperature (Θ_D) as a function of temperature (at P = 0 GPa) for wurtzite $Y_xAl_{1-x}N$ crystals with $0 \leq x \leq 0.375$. Figure IV.14(a) shows that C_V increases with rising temperature and reaches the Dulong-Petit limit, approaching a maximum close to the $3NK_B$ constant, where N = 32 atoms in the $Y_xAl_{1-x}N$ supercell. The C_V value exceeds 780 $J \cdot mol^{-1} \cdot K^{-1}$. The increase in C_V at low temperatures can be attributed to an anharmonic approximation of the Debye model. In contrast, at higher temperatures, the capacitance approaching the Dulong-Petit limit is due to the diminishing anharmonic effects. Like in all solids, the thermal energy induces exciting all modes of phonons at high temperatures. Our calculated values for pure AlN using PBEsol are larger than those reported by Ramírez-Montes et al. [13] using PBE, but lower than the values obtained by Fu et al. [87]. In $Y_xAl_{1-x}N$ alloys, the values of C_V are found to be larger than the others of the ternary mixed $N_xAs_{1-x}Ga$, as demonstrated by Souheyla et al. [88]. Moreover, it can be observed in Figure

IV.14(a) that the capacitance (C_V) increases slightly with yttrium doping in $Y_xAl_{1-x}N$, indicating a modest influence.

The thermal expansion curves (α) in Figure IV.14(b) show an increase with temperature, which is directly proportional to the yttrium content for temperatures up to 300K. At high temperatures (T > 300 K), the highest α value is correspond to the $Y_{0.25}Al_{0.75}N$, approximately 3.81 × 10^{-5} K^{-1}. Additionally, α is observed to decrease with pressure, as shown in Table IV-5. The increase in α can be explained by the expansion of interatomic distances caused by increased heat transfer (*higher kinetic energy of atoms*), while its decrease is due to an increase in bond energy, which limits bond length expansion. For pure *wz*-AlN (T = 1000 K), the obtained α value is approximately 3.6 × 10^{-5} K^{-1}, which is consistent with the α value of the AlN rock-salt phase reported by Noudjoud et al. [86]. The α values for $Y_xAl_{1-x}N$ at ambient temperature (T = 300 K, P = 0 GPa) are as follows (see Table IV-5): 2.36 × 10^{-5} K^{-1}, 2.53 × 10^{-5} K^{-1}, 2.80 × 10^{-5} K^{-1}, 2.69 × 10^{-5} K^{-1} for x = 0, 0.125, 0.25 and 0.375, respectively. We infer that $Y_{0.25}Al_{0.75}N$ exhibits superior thermal expansion compared to the other alloys.

Entropy (S) reflects the level of molecular disorder in a solid, with higher values signifying greater disorder. Figure IV.14(c) clearly shows an increase in entropy (S) with rising temperature at zero pressure in wurtzite $Y_xAl_{1-x}N$ alloys, displaying a nonlinear behavior. Entropy (S) also increases with yttrium doping in $Y_xAl_{1-x}N$, leading to greater disorder in these alloys. Table IV-IV-5 shows that entropy (S) decreases with pressure at a given temperature. The values of S for $Y_xAl_{1-x}N$ at T = 300 K and P = 0 GPa are 345.35 $J \cdot mol^{-1} \cdot K^{-1}$, 405.42 $J \cdot mol^{-1} \cdot K^{-1}$, 461.81 $J \cdot mol^{-1} \cdot K^{-1}$, and 513.15 $J \cdot mol^{-1} \cdot K^{-1}$ for x = 0, 0.125, 0.25, and 0.375, respectively. We observe that $Y_xAl_{1-x}N$ has the highest S values and exhibits greater disorder during heating compared to similar III–V materials, such as $N_xAs_{1-x}Ga$ (S ≈ 30–84 $J \cdot mol^{-1} \cdot K^{-1}$) [88] and $Al_xGa_{1-x}As$ (100–170 $J \cdot mol^{-1} \cdot K^{-1}$) [89].

The Debye temperature (Θ_D) is a measure of the heat capacity in solids at low temperatures ($T << \Theta_D$). As the temperature increases from absolute zero, the atoms in the solid gradually vibrate more intensely until they reach Θ_D, where they achieve their

maximum possible vibrational modes. Figure IV.14(d) shows a slight decrease in Θ_D for $Y_xAl_{1-x}N$ with temperature in the range of 0–1000 K. For *wz*-AlN, Θ_D decreases from 900.0 K to 859.8 K as the temperature increases. Additionally, Θ_D is observed to decrease with increasing yttrium content (see Figure IV.14(d)), which impacts the hardness of $Y_xAl_{1-x}N$ crystals. The predicted Θ_D values for $Y_xAl_{1-x}N$ are relatively high, approximately 895.27 K, 802.96 K, 725.52 K, and 675 K for x = 0, 0.125, 0.25, and 0.375, respectively, which confirms the elastic hardness of crystals. These results are consistent with our earlier findings regarding the elastic constants. The Θ_D values for pure AlN and $Y_{0.25}Al_{0.75}N$ are somewhat lower than those reported in [13]. Our resulting value for pure AlN of Θ_D = 900.0 K (at T = 0 K) is much lower than the experimental data of 940 K reported by Bruls et al. [90] and the calculated value (LDA) of 804.13 K by Fu et al. [91]. We find that $Y_xAl_{1-x}N$ is less hard compared to AlGaN [91], $Cr_{0.9}Al_{0.1}N$ (845 K) [92], and $Ti_{0.36}Al_{0.64}N$ (907 K) [92], but harder than AsGaN [88], which has Θ_D in the range of approximately 706.22–323.21 K at (x = 0–1).

Grüneisen parameter (γ) is a dimensionless quantity that approximates the relationship between phonon frequency and volume, reflecting the anharmonic effects in crystals [93]. It can also associate mechanical and thermal properties through elasticity moduli and their pressure derivatives [94]. Therefore, there are various valid formulations of the Grüneisen parameter [94,95]. Figure IV.15 illustrates the dependence of γ on pressure (at 300 K) and temperature (at 0 GPa) for wurtzite $Y_xAl_{1-x}N$ crystals. As shown in Figure IV.15(a) and IV.15 (b), γ remains constant and is unaffected by pressure and temperature variations. For pure AlN, γ varies from approximately 1.78033 to 1.78034, consistent with previous findings from Li et al. [96] (1.7) and Feng et al. [97] (1.5). For $Y_xAl_{1-x}N$, γ is less than 2, ranging from 1.7 (for x = 0.375) to 1.85 (for x = 0.25).

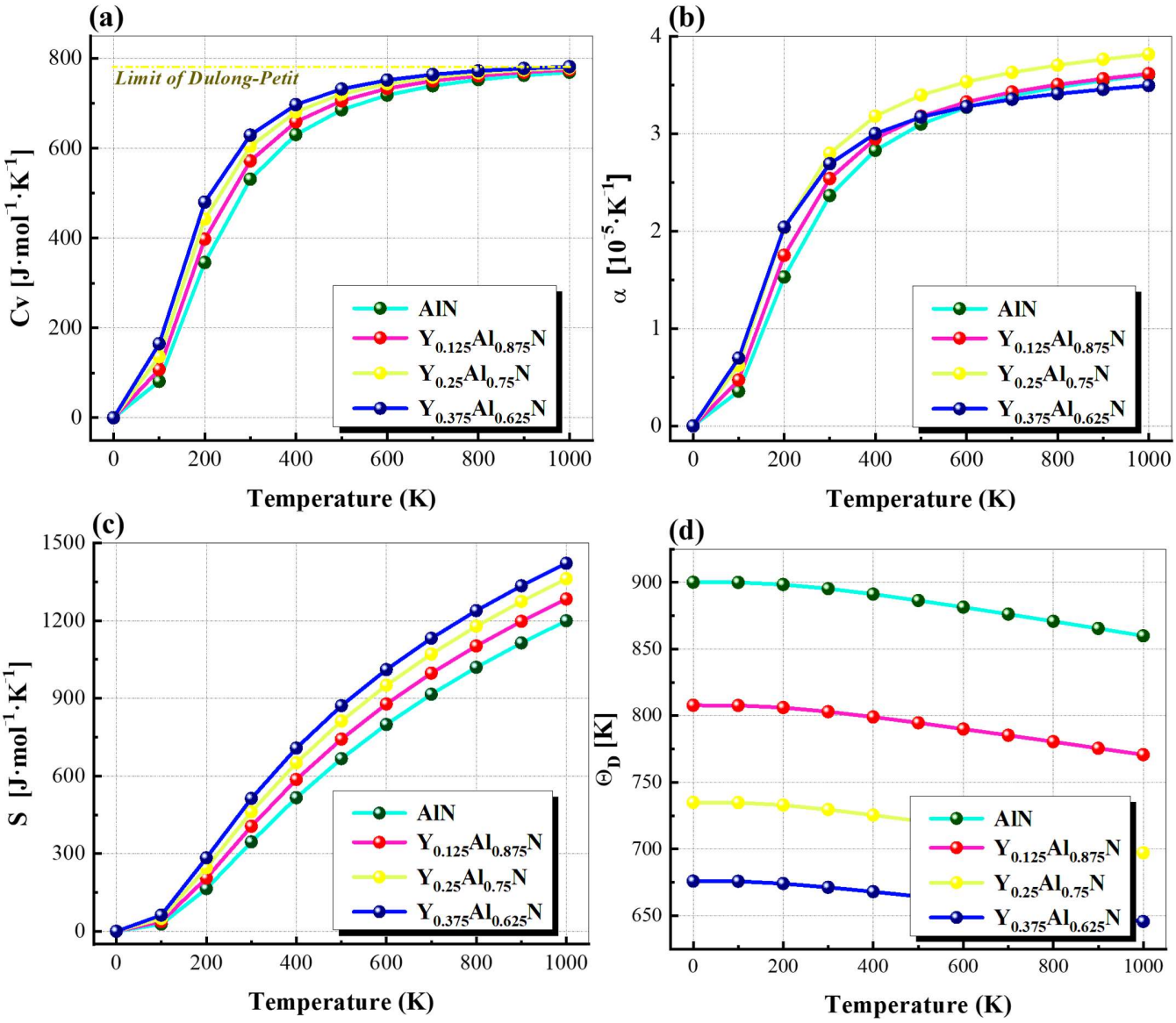

Figure IV.14. Calculated thermal capacity (C_v) (a), thermal expansion (α) (b), entropy (S) (c), and Debye temperature (Θ_D) (d) as a function of temperature under pressure for wurtzite $Y_xAl_{1-x}N$ alloys.

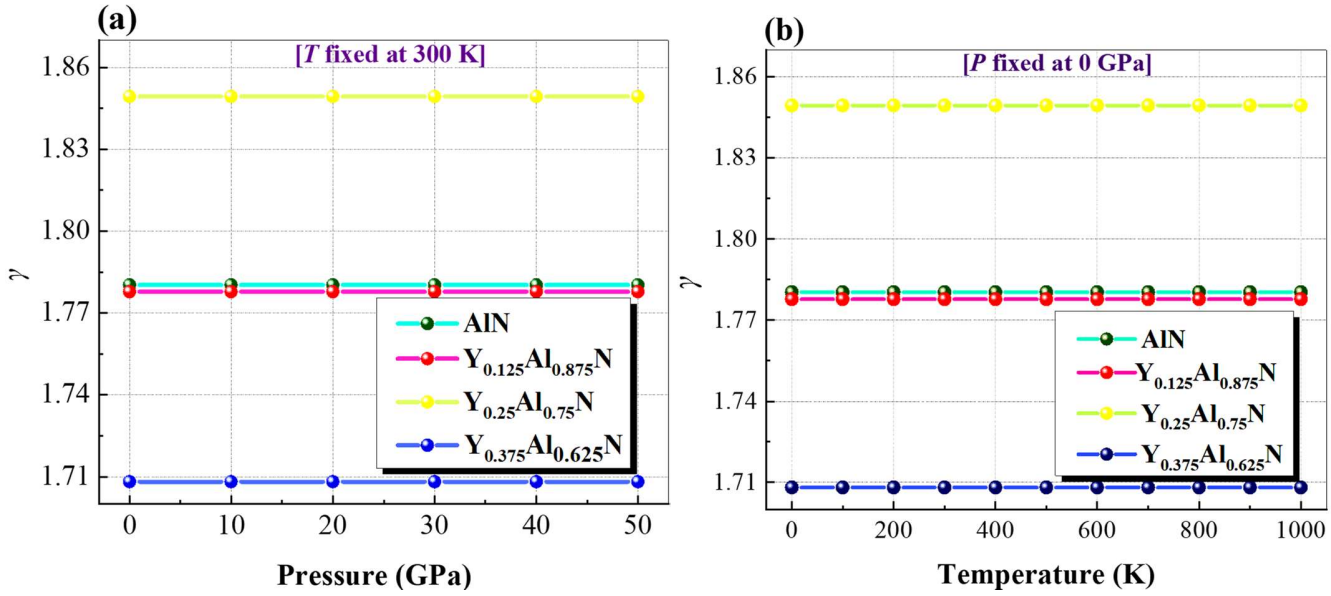

Figure IV.15. Calculated Grüneisen parameter (γ) as a function of pressure (a), and temperature (b) for wurtzite $Y_xAl_{1-x}N$ crystals.

IV.8. Thermoelectric Properties

The thermoelectric (TE) properties of wurtzite $Y_xAl_{1-x}N$ crystals, with varying Y concentrations (x) ranging from 0 to 0.375, were investigated using the Boltzmann transport theory as implemented in the BoltzTraP code [98]. These properties include Seebeck coefficient (S), electrical conductivity (σ/τ), electronic thermal conductivity (κ_{el}/τ), power factor (PF), and figure of merit (ZT). All calculations are performed using the constant relaxation time approximation (τ) for the charge carriers near the Fermi level, over a temperature range of 0–1000 K. The thermoelectric quantities dependency on temperature are plotted in Figure IV.16. The aims of this study is to enhance the performance of III–V material-based thermoelectric devices, which currently have a limited capacity to convert waste heat into electrical energy due to their low figure of merit (ZT).

The Seebeck coefficient (S) offers insights into the type of majority carriers (n-type or p-type) present in the valence/conduction bands of materials. It is strongly associated with the density of states (DOS) near the valence band maximum (VBM) and conduction band

minimum (CBM). A higher DOS near the VBM indicates a p-type material, whereas a higher DOS near the CBM suggests an n-type material. All alloys exhibit a sharp rise near the VBM as shown in Figure IV.7 of the electronic section, suggesting that $Y_xAl_{1-x}N$ semiconductors may display p-type behavior. The Seebeck coefficient as a function of temperature for $Y_xAl_{1-x}N$ alloys at x = 0, 0.125, 0.25, and 0.375 is presented in Figure IV.16(a). We observed that S is positive for all alloys, indicating that holes are the majority charge carriers in these materials, as previously mentioned. Figure IV.16(a) shows that S reaches a maximum value at high temperatures due to the bipolar effect, which arises from the electronic excitation from the valence band to the conduction band [99–102].

Thermal excitation generally increases the concentration of minority carriers while the majority carrier concentration leaving largely unchanged. The Seebeck coefficients produced by these minority carriers oppose those of the majority carriers, leading to a decrease in the total Seebeck coefficient. This reduction is unfavorable for thermoelectric power generation [103]. To avoid the excitation of minority carriers, a material must possess both temperature stability and a wide bandgap. We found that $Y_xAl_{1-x}N$ alloys meet these criteria, ensuring that the total Seebeck coefficient is not significantly affected by opposing Seebeck coefficients. The highest S values for $Y_xAl_{1-x}N$ are as follows: 216 μV/K (1000K), 215 μV/K (200K), 214 μV/K (600K), and 200 μV/K (500K) for x = 0, 0.125, 0.25 and 0.375 respectively. At ambient temperature, the values are 108 μV/K, 191 μV/K, 199 μV/K, and 209 μV/K for $Y_xAl_{1-x}N$ for x equal to 0, 0.375, 0.25, and 0.125, respectively. Moreover, as observed (see Figure IV.16(a)), there is an enhancement in the Seebeck coefficient (S) with increasing Y concentration (x). The $Y_{0.125}Al_{0.875}N$ alloy exhibits higher S values at low temperatures (100–300 K) but shows a decrease as the temperature rises (400–700 K). In contrast, $Y_{0.125}Al_{0.875}N$ demonstrates a significant increase in S within the temperature range of 400–800 K. Also, S value shows the smallest increase in the $Y_{0.375}Al_{0.625}N$ alloy compared to the other two concentrations, rising up to 400 K and then decreasing. At high temperatures (~1000 K), pure AlN exhibits a higher Seebeck coefficient (S) than the $Y_xAl_{1-x}N$ alloys.

Figure IV.16(b) show that electrical conductivity (σ/τ) increases with temperature across the entire range of yttrium concentrations. Since the BoltzTraP package extracts the thermoelectric quantities with respect to τ, it is assumed to be constant in calculations. At ambient temperature, the obtained σ/τ values are are 1.34×10^{18} $(\Omega.m.s)^{-1}$, 2.84×10^{18} $(\Omega.m.s)^{-1}$, 1.56×10^{18} $(\Omega.m.s)^{-1}$ and 1.73×10^{18} $(\Omega.m.s)^{-1}$ for x = 0, 0.125, 0.25, and 0.375, respectively. The $Y_{0.125}Al_{0.875}N$ alloy exhibits the highest electrical conductivity among the alloys. Our σ/τ values for pure AlN are superior than those reported in the literature: Kusunose et al. [104] reported approximately 6×10^{1} $(\Omega \cdot m \cdot s)^{-1}$ at temperatures above 1000 K, Zheng et al. [105] reported about 8×10^{-4} $(\Omega \cdot m \cdot s)^{-1}$ at 300 K, and Liu et al. [106] reported around 2.7×10^{-2} $(\Omega \cdot m \cdot s)^{-1}$.

The power factor (PF) is directly related to the electrical conductivity and Seebeck coefficient, as it is proportional to $S^2\sigma/\tau$. The results of S and σ/τ suggest that $Y_xAl_{1-x}N$ exhibits significant power factor (PF) values, as presented in Figure IV.16(c). The calculated power factor values at room temperature for $Y_xAl_{1-x}N$ alloys, with respect to τ, are 7.67×10^{10} $W \cdot m^{-1} \cdot K^{-2} \cdot s^{-1}$, 1.24×10^{11} $W \cdot m^{-1} \cdot K^{-2} \cdot s^{-1}$, 5.38×10^{10} $W \cdot m^{-1} \cdot K^{-2} \cdot s^{-1}$, and 5.57×10^{10} $W \cdot m^{-1} \cdot K^{-2} \cdot s^{-1}$ for x = 0, 0.125, 0.25, and 0.375, respectively. Based on these performance results, wurtzite $Y_xAl_{1-x}N$ can be classified as an excellent thermoelectric material.

Thermal conductivity (κ/τ) is attributed to charge carriers and is described by two components: electronic thermal conductivity (κ_{el}) and lattice thermal conductivity (κ_{latt}), such that $\kappa = \kappa_{el} + \kappa_{latt}$. It should be noted that the BoltzTraP code determines only the electronic part of thermal conductivity, expressed in terms of the relaxation time τ (κ_{el}/τ). The electron transport heat can be written as $\kappa_{el} = L\sigma T$, where L is the Lorenz factor. Figure IV.16(d) depicts that κ_{el}/τ increases with temperature and decreases with increasing Y content. The lowest κ_{el}/τ value is exhibited by $Y_{0.25}Al_{0.75}N$ in the temperature range of 100–600 K, and by $Y_{0.25}Al_{0.75}N$ at temperatures ≥ 600 K. The obtained κ_{el}/τ values for $Y_xAl_{1-x}N$ at T = 300 K are 2.67×10^{13} $W \cdot m^{-1} \cdot K^{-1} \cdot s^{-1}$, 5.09×10^{13} $W \cdot m^{-1} \cdot K^{-1} \cdot s^{-1}$, 2.52×10^{13} $W \cdot m^{-1} \cdot K^{-1} \cdot s^{-1}$, and 2.72×10^{13} $W \cdot m^{-1} \cdot K^{-1} \cdot s^{-1}$ for x = 0, 0.125, 0.25 and 0.375, respectively. Experimental data for the total thermal conductivity (κ) of pure AlN reported in the literature are as follows: Slack

et al. [107] measured 319 $W \cdot m^{-1} \cdot K^{-1} \cdot s^{-1}$ at room temperature, Qiao et al. [108] reported 41.56 $W \cdot m^{-1} \cdot K^{-1} \cdot s^{-1}$, Duan et al. [109] found 155 $W \cdot m^{-1} \cdot K^{-1} \cdot s^{-1}$, Lee et al. [110] also recorded 155 $W \cdot m^{-1} \cdot K^{-1} \cdot s^{-1}$, and Watari et al. [111] obtained 220 $W \cdot m^{-1} \cdot K^{-1} \cdot s^{-1}$ at temperatures above 1000 K. Our thermal conductivity (κ_{el}/τ) values for pure AlN show a similarity to those of other III-nitrides, such as InN (120 $W \cdot m^{-1} \cdot K^{-1} \cdot s^{-1}$) [112] and GaN (177 $W \cdot m^{-1} \cdot K^{-1} \cdot s^{-1}$) [113]. Additionally, the κ_{el}/τ results for $Y_xAl_{1-x}N$ crystals are comparable to those of other III–V ternary compounds, such as $Tb_xAl_{1-x}N$ [114], $Al_xGa_{1-x}N$ [115,116], $In_xGa_{1-x}N$ [116], $In_xAl_{1-x}N$ [116,117], and $In_xGa_{1-x}Sb$ [118].

The dimensionless figure of merit, ZT, given as $ZT = (S^2\sigma T)/\kappa$ (where T represents the absolute temperature), quantifies the performance of thermoelectric materials. As shown in Figure IV.16 (e), the ZT values of wurtzite $Y_xAl_{1-x}N$ alloys range from 0.3 to 0.9 over the temperature range of 100–1000 K. The maximum ZT value for these alloys remains below 1.

The ZT values for $Y_xAl_{1-x}N$ alloys under varying temperatures are quite close to the experimental results reported for similar ternary semiconductors, such as $In_xGa_{1-x}Sb$ [119] (0.62 at 573K), $In_xGa_{1-x}N$ [120] (0.34 at 873K), and $Al_xIn_{1-x}N$ [117] (0.53 at 300K). Moreover, the ZT value for pure AlN, approximately 0.73 at 1000 K, is in good agreement with measured data for binary compounds, including InN (0.92 at 300K) [121], GaN (0.35 at 900K) [116], and ZnSb (0.7), InSe (0.4), GeTe (0.9), PbSe (1.2), PbTe (1), PbS (0.7), and InSb (0.51) [122–127]. Hoverer, the ZT value of approximately 0.72 at 900 K for AlN is much higher than the 0.15 value reported by Sztein et al. [116] at the same temperature.

The most prominent commercially available thermoelectric materials today are based on bismuth telluride, with a figure of merit (ZT) of approximately 1.0 [128]. These alloys have maintained their prominence for the past two decades, and it is unlikely that significant improvements in thermoelectric efficiency will be achieved through alloys alone [129]. Nonetheless, the novel $Y_xAl_{1-x}N$ ternary semiconductors alloys with specific compositions remain a promising alternative for applications in renewable energy systems, such as thermoelectric generators.

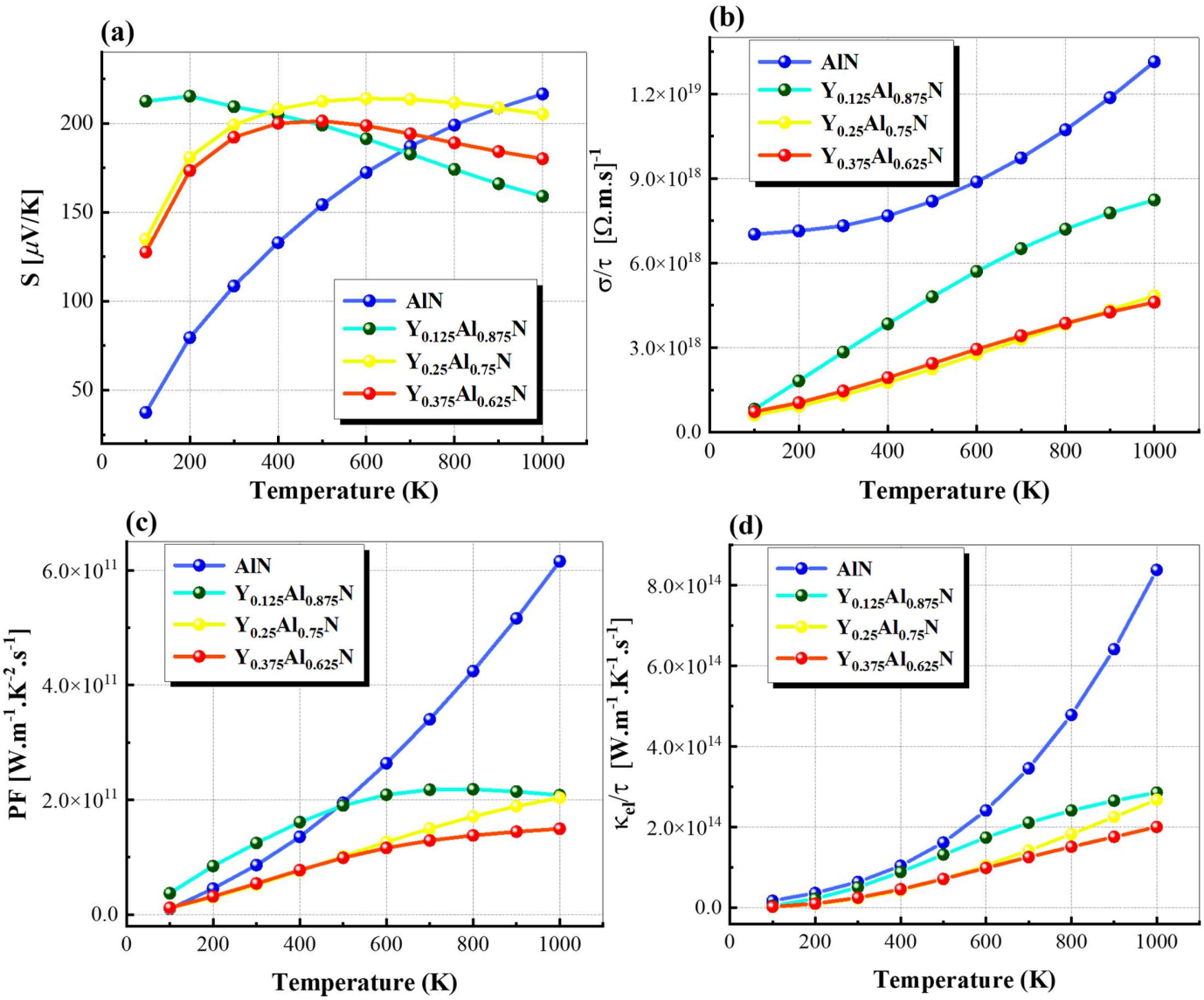
(a)
S [μV/K]
Temperature (K)
AlN
Y0.125Al0.875N
Y0.25Al0.75N
Y0.375Al0.625N
(b)
σ/τ [Ω.m.s]-1
Temperature (K)
(c)
PF [W.m-1.K-2.s-1]
Temperature (K)
(d)
κel/τ [W.m-1.K-1.s-1]
Temperature (K)

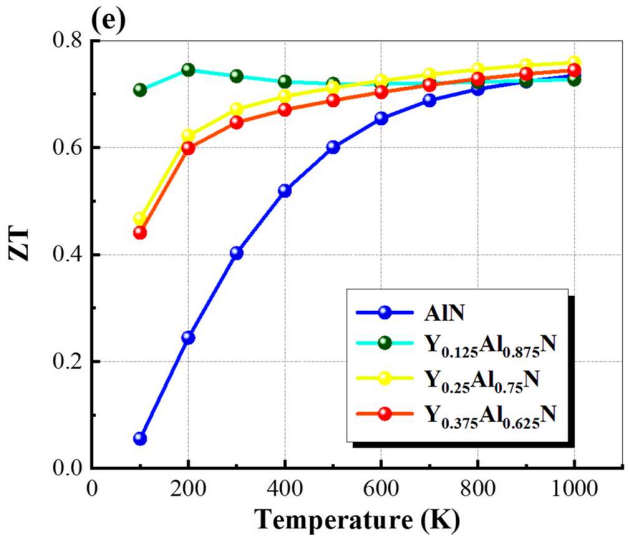

Figure IV.16. Dependence of Calculated Seebeck coefficient (S) (a), electrical conductivity (σ/τ) (b), electronic thermal conductivity (κ_{el}/τ) (c), power factor (PF) (d), and figure of merit (ZT) (e) as a function of temperature for wurtzite $Y_xAl_{1-x}N$ crystals.

IV.9. Conclusion

In this chapter, the key characteristics of novel $Y_xAl_{1-x}N$ crystals (with $0 \leq x \leq 0.375$) were explored, including their structural, electronic, elastic, piezoelectric, thermodynamic, and thermoelectric properties, using precise Ab Initio DFT calculations. By employing the newly proposed PBEsol approach, we obtained ground-state structural parameters for $Y_xAl_{1-x}N$ alloys that are in excellent agreement with experimental data. Formation energy and frequency dispersion calculations confirmed that these alloys exhibit both thermodynamic and dynamic stability across the full range of Y concentrations. The $Y_xAl_{1-x}N$ alloys are expected to have a direct bandgap energy that can be tuned from 6.10 eV (for x = 0) down to 3.85 eV (for x = 0.375), covering wavelengths of approximately 203–322 nm in the ultraviolet spectrum. These crystals also demonstrate excellent thermoelectric performance, with a high figure of merit of 0.75, making them promising candidates for green energy conversion devices and UV optoelectronics. Furthermore, Y doping significantly enhances the piezoelectric coefficients of $Y_xAl_{1-x}N$, indicating its potential for high-performance MEMS applications, particularly in high-sensitivity sensing and future mobile telecommunications.

References

[1] P. Hohenberg, W. Kohn, Inhomogeneous electron gas, Phys. Rev. B 136 (1964) 864, https://doi.org/10.1103/PhysRev.136.B864.

[2] W. Kohn, L.J. Sham, Self-consistent equations including exchange and correlation effects, Phys. Rev. A 140 (1965) 1133, https://doi.org/10.1103/PhysRev.140. A1133.

[3] P. Blaha, K. Schwarz, F. Tran, R. Laskowski, G.K.H. Madsen, L.D. Marks, WIEN2k: an APW+ lo program for calculating the properties of solids, J. Chem. Phys. 152 (2020), 074101, https://doi.org/10.1063/1.5143061.

[4] J.P. Perdew, A. Ruzsinszky, G.I. Csonka, O.A. Vydrov, G.E. Scuseria, et al., Restoring the density-gradient expansion for exchange in solids and surfaces, Phys. Rev. Lett. 100 (2008), 136406, https://doi.org/10.1103/PhysRevLett.100.136406.

[5] A. Assali, F. Kanouni, F. Laidoudi, F. Arab, M'hamed Bouslama, structural and electromechanical properties of Sr-substituted barium titanate (BST) as potential material for high performance electroacoustic devices, Mater. Today Commun. 25 (2020), 101643, https://doi.org/10.1016/j.mtcomm.2020.101643.

[6] D. Koller, F. Tran, P. Blaha, Improving the modified Becke-johnson exchange potential, Phys. Rev. B 85 (2012), 155109, https://doi.org/10.1103/ PhysRevB.85.155109.

[7] A. Boubaia, A. Assali, S. Berrah, H. Bennacer, I. Zerifi, A. Boukortt, Band gap and emission wavelength tuning of Sr-doped BaTiO3 (BST) perovskites for highefficiency visible-light emitters and solar cells, Mater. Sci. Semicond. Process. 130 (2021), 105837, https://doi.org/10.1016/j.mssp.2021.105837.

[8] Samir Charef, Abdenacer Assali, Abdelkader Boukortt, Optoelectronic and thermoelectric properties of novel double halide perovskites Na_2AgAsX_6 (X = Cl, Br) for efficient green solar cells, Mater. Today Commun. 38 (2024), 108065, https://doi.org/10.1016/j.mtcomm.2024.108065.

[9] D. Vanderbilt, Soft self-consistent pseudopotentials in a generalized eigenvalue formalism, Phys. Rev. B 41,(1990)7892, https://doi.org/10.1103/PhysRevB.41.7892.

[10] M. Segall, P.J. Lindan, M. Probert, C. Pickard, P. Hasnip, S. Clark, M. Payne, First-principles simulation: ideas, illustrations and the CASTEP code, J. Phys.: Condens. Matter 14 (2002) 2717, https://doi.org/10.1088/0953-8984/14/11/301.

[11] S. Baroni, P. Giannozzi, A. Testa, Green's-function approach to linear response in solids, Phys. Rev. Lett. 58(1987)1861,https://doi.org/10.1103/PhysRevLett.58.1861.

[12] H.J. Monkhorst, J.D. Pack, Special points for Brillouin-zone integrations, Phys. Rev. 13 (1976) 5188, https://doi.org/10.1103/PhysRevB.13.5188.

[13] L. Ramírez-Montes, W. López-Pérez, A. González-García & R. González-Hernández, Structural, optoelectronic, and thermodynamic properties of $Y_xAl_{1-x}N$ semiconducting alloys, J. Mater. Sci. 51 (2016) 2817–2829, https://doi.org/10.1007/s10853-015-9590-z.

[14] A. Žukauskaite, C. Tholander, J. Palisaitis, P.O. Persson, V. Darakchieva, N. Ben Sedrine, F. Tasnádi, B. Alling, J. Birch, L. Hultman, $Y_xAl_{1-x}N$ thin films, J. Phys. D. Appl. Phys. 45 (2012) 422001, https://doi.org/10.1088/0022-3727/45/42/422001.

[15] Y. Xie, Y. Cai, Y. Liu, Y. Zhao, S. Guo, C. Sun, S. Liu, Electronic structure and optical properties of YAlN: a first-principles study, Phys. Status Solidi B 257 (2020), 1900678, https://doi.org/10.1002/pssb.201900678.

[16] P.M. Mayrhofer, H. Riedl, H. Euchner, M. Stöger-Pollach, P.H. Mayrhofer, A. Bittner, Microstructure and piezoelectric response of $Y_xAl_{1-x}N$ thin films, Acta Materialia 100 (2015) 81–89, https://doi.org/10.1016/j.actamat.2015.08.019.

[17] N.B. Sedrine, A. Žukauskaitė, J. Birch, J. Jensen, L. Hultman, S. Schöche, M. Schubert and V. Darakchieva, Infrared dielectric functions and optical phonons of wurtzite $Y_xAl_{1-x}N$ ($0 \leqslant x \leqslant 0.22$), J. Phys. D. Appl. Phys. 48 (2015) 415102, doi:10.1088/0022-3727/48/41/415102

[18] M.A. Moram, M.E. Vickers, X-ray diffraction of III-nitrides, Rep. Prog. Phys. 72 (2009), 036502, https://doi.org/10.1088/0034-4885/72/3/036502.

[19] Kahina Ouali, Abdenacer Assali, Salim Benaissa, Lyes Benharrat, Smail Berrah, Electronic structure and optical properties of tin (IV) doped transparent perovskite crystal BaTiO3 for efficient visible optoelectronic devices and solar cells, Materials Mater. Today Commun. 35 (2023) 106035, https://doi.org/10.1016/j.mtcomm.2023.106035.

[20] P. Haas, F. Tran, P. Blaha, Calculation of the lattice constant of solids with semilocal functionals, Phys. Rev. B 79 (2009), 085104, https://doi.org/10.1103/ PhysRevB.79.085104.

[21] S. Adachi, Properties of Group-IV, III–V and II–VI Semiconductors, John Wiley & Sons Ltd., Chichester, UK, 2005.

[22] L. Vegard, Die konstitution der mischkristalle und die raumfüllung der atome, Z. Phys. 5 (1) (1921) 17–26, https://doi.org/10.1007/BF01349680.

[23] R.D. Shannon, Revised Effective Ionic Radii and Systematic Studies of Interatomic Distances in Halides and Chalcogenides, Published in Acta Crystallographica, USA, 1976, pp. 751–767. A32.

[24] Duc V. Dinh, J. Lähnemann, L. Geelhaar, O. Brandt, Lattice parameters of $Sc_xAl_{1-x}N$ layers grown on GaN(0001) by plasma-assisted molecular beam epitaxy, Appl. Phys. Lett. 122 (2023) 152103, https://doi.org/10.1063/5.0137873 .

[25] Y. Pan, S. Chena, Y. Jia, First-principles investigation of phonon dynamics and electrochemical performance of TiO2-x oxides lithium-ion batteries, Int. J. Hydrogen Energy 45 (2020) 6207–6216, https://doi.org/10.1016/j. ijhydene.2019.12.211.

[26] Y. Pan, Structural prediction and overall performances of CrSi2 disilicides: DFT investigations, ACS Sustainable Chem. Eng. 8 (2020) 11024–11030, https://doi. org/10.1021/acssuschemeng.0c04737.

[27] Y. Pan, W.M. Guan, The hydrogenation mechanism of PtAl and IrAl thermal barrier coatings from first-principles investigations, Int. J. Hydrogen Energy 45 (2020) 20032–20041, https://doi.org/10.1016/j.ijhydene.2020.04.290.

[28] S. Baroni, S.D. Gironcoli, A.D. Corso, P. Giannozzi, Phonons and related crystal properties from density-functional perturbation theory, Rev. Mod. Phys. 73 (2001) 515, https://doi.org/10.1103/RevModPhys.73.515.

[29] K.M. Rabe, P. Ghosez, First-principles studies of ferroelectric oxides, in: Physics of Ferroelectrics, Springer-Verlag, Berlin, 2007, p. 117.

[30] C. Wang, S. Liang, J. Cui, X. Wang, Y. Wei, First-principles study of the mechanical and thermodynamic properties of Al4W, Al5W and Al12W under pressure, Vacuum 169 (2019), 108844, https://doi.org/10.1016/j.vacuum.2019.108844.

[31] Z. Tai, C. Yang, X. Hu, Y. Xie, Structural and optical properties of Er-doped AlN, Integrated Ferroelectrics Int. J. 192 (2018) 154–163, https://doi.org/10.1080/ 10584587.2018.1521664.

[32] H. Momida, A. Teshigahara, T. Oguchi, Strong enhancement of piezoelectric constants in $Sc_xAl_{1-x}N$: first-principles calculations, AIP Adv. 6 (2016), 065006, https://doi.org/10.1063/1.4953856.

[33] M. Zhu, L. Hua, F. Xiong, First principles study on the structural, electronic, and optical properties of Sc-doped AlN, Russ. J. Phys. Chem. 88 (2014) 722–727, https://doi.org/10.1134/S0036024414040177.

[34] I. Zerifi, A. Assali, A. Boukortt, L. Chaabane, First-principles investigation on narrow bandgap $InSb_{1-x}Bi_x$ dilute bismide alloys for highly efficient longwavelength infrared optoelectronics, Infrared Phys. Technol. 125 (2022), 104319, https://doi.org/10.1016/j.infrared.2022.104319.

[35] A. Assali, F. Kanouni, Zou Qin, R. Khenata, Optical characteristics of dilute gallium phosphide bismide: promising material for near-infra photonic device Applications, Phys. Lett. 384 (2020) 126147, https://doi.org/10.1016/j. physleta.2019.126147.

[36] A. Assali, M. Bouslama, A.H. Reshak, L. Chaabane, Highly desirable semiconducting materials for mid-ir optoelectronics: dilute bismide $InAs_{1-x}Bi_x$ alloys, Mater. Res. Bull. 95 (2017) 588–596, https://doi.org/10.1016/j. materresbull.2017.06.011.

[37] A. Assali, M. Bouslama, L. Chaabane, A. Mokadem, F. Saidi, Structural and optoelectronic properties of $InP_{1-x}Bi_x$ bismide alloys for mid− infrared optical devices: a DFT + TB-mBJ study, Physica B 526 (2017) 71–79, https://doi.org/10.1016/j. physb.2017.09.058.

[38] A. Assali, M. Bouslama, Novel BTlGaN semiconducting materials for infrared optoelectronic devices, Infrared Phys. Technol. 81 (2017) 175–181, https://doi.org/10.1016/j.infrared.2017.01.006.

[39] A. Assali, M. Bouslama, A.H. Reshak, S. Zerroug, H. Abid, Electronic structure and optical properties of dilute boron-bismide quaternary alloys $B_xGa_{1-x}As_{1-y}Bi_y$/GaAs for infrared optoelectronic devices, Optik 135 (2017) 57–69, https://doi.org/ 10.1016/j.ijleo.2017.01.059.

[40] A. Assali, M. Bouslama, H. Abid, S. Zerroug, M. Ghaffour, F. Saidi, L. Bouzaiene, K. Boulenouar, Optoelectronic properties of cubic $B_xIn_yGa_{1-x-y}N$ alloys matched to gan for designing quantum well lasers: first-principles study within mBJ exchange potential, Mater. Sci. Semicond. Process. 36 (2015) 192–203, https:// doi.org/10.1016/j.mssp.2015.03.033.

[41] M. Baeumler, Y. Lu, Nicolas Kurz, L. Kirste, M. Prescher, T. Christoph, J. Wagner, A. Žukauskaitė, ˙ O. Ambacher, Optical constants and band gap of wurtzite $Al_{1-x}Sc_xN/Al_2O_3$ prepared by magnetron sputter epitaxy for scandium concentrations up to x = 0.41, J. Appl. Phys. 126 (2019) 045715, https://doi.org/ 10.1063/1.5101043.

[42] S. Saada, S. Lakel, K. Almi, Optical, electronic and elastic properties of ScAlN alloys in WZ and ZB phases: prospective material for optoelectronics and solar cell applications, Superlattice. Microst. 109 (2017) 915–926, https://doi.org/10.1016/ j.spmi.2017.06.025.

[43] S. Zhang, D. Holec, W.Y. Fu, C.J. Humphreys, M.A. Moram, Tunable optoelectronic and ferroelectric properties in Sc-based III-nitrides, J. Appl. Phys. 114 (2013) 133510, https://doi.org/10.1063/1.4824179.

[44] K. Orita, S. Yoshida, Semiconductor light-emitting element, U.S. Patent Application No. 12/866 (2010) 436.

[45] A. Boonchun, W.R.L. Lambrecht, First-principles study of the elasticity, piezoelectricity, and vibrational modes in $LiGaO_2$ compared with ZnO and GaN, Phys. Rev. B 81 (2010) 235214, Phys. Rev. B 82, 079904 (2010).

[46] K. Tsubouchi, K. Sugai, and N. Mikoshiba, in 1981 Ultrasonics Symposium, edited by B. R. McAvoy, Vol. 1, p. 375, IEEE, New York, 1981.

[47] L.E. McNeil, M. Grimsditch, and R. H. French, Vibrational spectroscopy of aluminum nitride, J. Am. Ceram. Soc.76 (1993)1132, https://doi.org/10.1111/j.1151-2916.1993.tb03730.x.

[48] A. F. Wright, Elastic properties of zinc-blende and wurtzite AlN, GaN, and InN, J. Appl. Phys. 82 (1997)2833, https://doi.org/10.1063/1.366114.

[49] K. Kim, W. R. L. Lambrecht, and B. Segall, Elastic constants and related properties of tetrahedrally bonded BN, AlN, GaN, and InN, Phys. Rev. B 53 (1996) 16310, https://doi.org/10.1103/PhysRevB.53.16310.

[50] S. Manna, K.R. Talley, P. Gorai, J. Mangum, A. Zakutayev, G.L. Brennecka, V. Stevanović, and C.V. Ciobanu, Enhanced Piezoelectric Response of AlN via CrN Alloying, Phys. Rev. Appl. 9 (2018) 34026, https://doi.org/10.1103/PhysRevApplied.9.034026.

[51] A. Zoroddu, F. Bernardini, and P. Ruggerone, First-principles prediction of structure, energetics, formation enthalpy, elastic constants, polarization, and piezoelectric constants of AlN, GaN, and InN: Comparison of local and gradient-corrected density-functional theory, Phys. Rev. B 64 (2001) 045208, https://doi.org/10.1103/PhysRevB.64.045208.

[52] N. Kurz, A. Ding, D.F. Urban, Y. Lu, L. Kirste, N.M. Feil, A. Žukauskaitė, O. Ambacher, Experimental determination of the electro-acoustic properties of thin film AlScN using surface acoustic wave resonators, J. Appl. Phys. 126 (2019) 075106, https://doi.org/10.1063/1.5094611.

[53] J. Nye, Physical Properties of Crystals: Their Representation by Tensors and Matrices, Oxford University Press, 1985.

[54] J. Nye, J.F. Lindsay, R.B. Physical Properties of Crystals: Their Representation by Tensors and Matrices; Clarendon Press: Oxford, UK, 1985.

[55] L.-W Shi, Y.-Feng Duan, L.-X. Qin, Structural stability and elastic properties of wurtziteTIN in under hydrostatic pressure, Chin. Phys. LETT. 27 (2010) 080505, https://doi.org/10.1088/0256-307X/27/8/080505.

[56] R. Hill, the Elastic Behaviour of a Crystalline Aggregate. Proc. Phys. Soc. Sect. A65 (1952) 349–354, https://doi.org/10.1088/0370-1298/65/5/307.

[57] A. Yildirim, H. Koc, E. Deligoz, First-principles study of the structural, elastic, electronic, optical, and vibrational properties of intermetallic Pd_2Ga, Chin. Phys. B 21 (2012) 037101, https://doi.org/10.1088/1674-1056/21/3/037101.

[58] H. Han, Density-functional theory study of the effect of pressure on the elastic properties of CaB_6, Chin. Phys. B 22 (2013) 077101, https://doi.org/10.1088/1674-1056/22/7/077101.

[59] I.N. Frantsevich, F.F. Voronov, S.A. Bokuta, Elastic Constants and Elastic Moduli of Metals and Insulators Handbook, Naukova Dumka, Kiev, Ukraine, 1982.

[60] V.V. Bannikov, I.R. Shein and A.L. Ivanovskii, Electronic structure, chemical bonding and elastic properties of the first thorium-containing nitride perovskite $TaThN_3$, Phys. Status Solidi Rapid Res. Lett. 3 (2007) 89, https://doi.org/10.1002/pssr.200600116.
[61] L.A. Valdez, M.A. Caravaca, R.A. Casali, Ab-initio study of elastic anisotropy, hardness and volumetric thermal expansion coefficient of ZnO, ZnS, ZnSe in wurtzite and zinc blende phases, Journal of Physics and Chemistry of Solids 134 (2019) 245–254, https://doi.org/10.1016/j.jpcs.2019.05.019.
[62] S. Tariq, A. Ahmed, S. Saad, and S. Tariq, Structural, electronic and elastic properties of the cubic $CaTiO_3$ under pressure: A DFT study, AIP Advances 5 (2015) 077111, https://doi.org/10.1063/1.4926437.
[63] E.V. Degtyareva, L. Verba, N. Gulko et al., Inorg. Mater. 13 (1977) 853. http://doi.org/10.1103/PhysRevB.68.184108.
[64] E. Schreiber, O.L. Anderson, N. Soga, Elastic Constants and their Measurement, McGraw-Hill, New York, 1973.
[65] K.M. Taylor and C. Lenie, Some properties of aluminum nitride, J. Electrochem. Soc. 107 (1960)308–314, https://doi.org/10.1149/1.2427686.
[66] M. Suzuki and S. Kakio, IEEE International Ultrasonics Symposium (IUS), Glasgow, Scotland, 2019.
[67] J.P. Poirier, Introduction to The Physics of the Earth's Interior, Cambridge University Press, Second edition, 2000.
[68] A. Ioachim, M.I. Toacsan, M.G. Banciu, L. Nedelcu, C. Plapcianu, H.V. Alexandru, C. Berbecaru, D. Ghetu, G. Stoica and R. Ramer, Frequency Agile BST Materials for Microwave Applications, Journal of Optoelectronics and Advanced Materials5 (2003) 1389–1393.
[69] T. Yokoyama, Y. Iwazaki, Y. Onda, T. Nishihara, Y. Sasajima, and M. Ueda, Effect of Mg and Zr co-doping on piezoelectric AlN thin films for bulk acoustic wave resonators, IEEE Trans. Ultrason. Ferroelectr. Freq. Contr. 61(2014)1322, https://doi.org/10.1109/TUFFC.2014.3039.
[70] M. Jong, W. Chen, H. Geerlings, M. Asta & K.A. Persson, A database to enable discovery and design of piezoelectric materials, Scientific Data 2 (2015)150053, https://doi.org/10.1038/sdata.2015.53.
[71] F. Bernardini and V. Fiorentini, First-principles calculation of the piezoelectric tensor d⇊ of III–V nitrides, Appl. Phys. Lett. 80 (2002) 4145, https://doi.org/10.1063/1.1482796.
[72] K. Tsubouchi and N. Mikoshiba, Zero-temperature-coefficient SAW devices on AlN epitaxial films, IEEE Trans. on Sonics and Ultrasonics SU 32 (1985) 634.
[73] S. Muensit, E.M. Goldys, and I.L. Guy, Shear piezoelectric coefficients of gallium nitride and aluminum nitride, Appl. Phys. Lett. 75 (1999)3965, https://doi.org/10.1063/1.125508.
[74] I.L. Guy, S. Muensit, and E. M. Goldys, Extensional piezoelectric coefficients of gallium nitride and aluminum nitride, Appl. Phys. Lett. 75 (1999) 4133, https://doi.org/10.1063/1.125560.
[75] A. Assali, F. Kanouni, F. Laidoudi, F. Arab, M. Bouslama, Mater. Today Commun. 25 (2020) 101643, https://doi.org/10.1016/j.sna.2020.111980.
[76] L.F. Wan, T. Nishimatsu, and S.P. Beckman, The structural, dielectric, elastic, and piezoelectric properties of $KNbO_3$ from first-principles methods, Journal of Applied Physics 111 (2012) 104107, https://doi.org/10.1063/1.4712052.
[77] O. Zywitzki, T. Modes, S. Barth, H. Bartzsch, and P. Frach, Effect of scandium content on structure and piezoelectric properties of AlScN films deposited by reactive pulse magnetron sputterin, Surf. Coat. Technol. 309 (2017) 417, https://doi.org/10.1016/j.surfcoat.2016.11.08 .
[78] T. Tabaru , M. Akiyama , Residual stress reduction in piezoelectric $Sc_{0.4}Al_{0.6}N$ films by variable-pressure sputtering from 0.4 to 1.0 Pa, Thin Solid Films 692 (2019) 137625, https://doi.org/10.1016/j.tsf.2019.137625
[79] M. Akiyama, T. Tabaru, K. Nishikubo, A. Teshigahara And K. Kano, Preparation of scandium aluminum nitride thin films by using scandium aluminum alloy sputtering target and design of experiments, Journal of the Ceramic Society of Japan 118 (2010) 1166–1169, https://doi.org/10.2109/jcersj2.118.1166.
[80] M. Akiyama, T. Kamohara, K. Kano, A. Teshigahara, Y. Takeuchi, N. Kawahara, Enhancement of Piezoelectric Response in Scandium Aluminum Nitride Alloy, Thin Films Prepared by Dual Reactive Cosputtering, Adv. Mater. 21 (2009) 593, https://doi.org/10.1002/adma.200802611.

[81] M.A. Caro, S. Zhang, T. Riekkinen, M. Ylilammi, M.A. Moram, O. Lopez-Acevedo, J. Molarius, T. Laurila, Piezoelectric coefficients and spontaneous polarization of ScAlN, J. Phys. Condens. Matter 27 (2015) 245901, https://doi.org/10.1088/0953-8984/27/24/245901.

[82] C. Tholander, J. Birch, F. Tasnadi, L. Hultman, J. Palisaitis, P.O.Å. Persson, J. Jensen, P. Sandstrom, B. Alling, A. Žukauskaitė, Ab initio calculations and experimental study of piezoelectric $Y_xIn_{1-x}N$ thin films deposited using reactive magnetron sputter epitaxy, Acta Materialia 105 (2016) 199–206, https://doi.org/10.1016/j.actamat.2015.11.050.

[83] H. Liu, F. Zeng, G. Tang, F. Pan, Enhancement of piezoelectric response of diluted Ta doped AlN, Applied Surface Science 270 (2013)225–230, https://doi.org/10.1016/j.apsusc.2013.01.005.

[84] T. Yanagitani and T. Shimidzu, US Patent Application 20190089325, May. 2016.

[85] M.A. Bianco, E. Francisco, V. Luana, GIBBS: isothermal-isobaric thermodynamics of solids from energy curves using A Quasi-harmonic debye model, Comput. Phys. Commun. 158 (2004) 57–72, https://doi.org/10.1016/j.comphy.2003.12.001.

[86] N. Lebga, S. Daoud, X.W. Sun, N. Bioud, A. Latreche, Mechanical and thermophysical properties of cubic rock-salt AlN under high pressure, J. Electron. Mater. 47 (7) (2018) 3430–3439, https://doi.org/10.1007/s11664-018-6169-x.

[87] J.Q. Fu, T.L. Song1, X.X. Liang, G.J. Zhao, First-principle studies of phonons and thermal properties of AlN in wurtzite structure, J. Phys. Conf. 574 (2015) 012046, https://doi.org/10.1088/1742-6596/574/1/012046.

[88] S. Gagui, S. Ghemid, H. Meradji, B. Zaidi, Bakhtiar Ul Haq, R. Ahmed, B. Hadjoudja, B. Chouial, First-principles predictions on structural stability, electronic, optical, and thermal properties of semiconductors GaN_xAs_{1-x}: materials for Futuristic Optoelectronic Energy Devices, https://doi.org/10.21203/rs.3.rs848653/v1, 2021.

[89] O. Nemiri, F. Oumelaz, A. Boumaza, S. Ghemid, H. Meradji, W.K. Ahmed, R. Khenata, X. Wang, Structural, electronic and thermal properties of $Al_xGa_{1-x}As$ ternary alloys: insightsfrom DFT study, J. Mol. Graph. Model. 92 (2019) 140–146, https://doi.org/10.1016/j.jmgm.2019.07.011.

[90] R.J. Bruls, H.T. Hintzen, G. de With, R. Metselaar, The temperature dependence of the Young's modulus of MgSiN2, AlN and Si3N4, J. Eur. Ceram. Soc. 21 (2001) 263–268, https://doi.org/10.1016/S0955-2219(00)00210-7.

[91] J. Fu, T. Song, X. Liang, G. Zhao, Composition dependence of phonon and thermodynamic properties of the ternary AlGaN mixed crystal, Results Phys. 14 (2019) 102505, https://doi.org/10.1016/j.rinp.2019.102505.

[92] V. Moraes, H. Riedl, R. Rachbauer, S. Kolozsvari, ´ M. Ikeda, L. Prochaska, S. Paschen, P.H. Mayrhofer, Thermal conductivity and mechanical properties of AlN-based thin films, J. Appl. Phys. 119 (2016) 225304, https://doi.org/10.1063/ 1.4953358.

[93] Zhang, S. Sun, T. Xu, T. Zhang, Temperature dependent Grüneisen parameter, Sci. China Technol. Sci. 62 (2019) 1565–1576, https://doi.org/10.1007/ s11431-019-9526-3.

[94] L. Vo˘cadlo, J.P. Poirer, G.D. Price, Grüneisen parameters and isothermal equations of state, Am. Mineral. 85 (2) (2000) 390–395, https://doi.org/10.2138/am-2000- 2-319.

[95] F.D. Stacey, J.H. Hodgkinson, Thermodynamics with the Grüneisen parameter: fundamentals and applications to high pressure physics and geophysics, Phys. Earth Planet. In. 286 (2018) 42–68, https://doi.org/10.1016/j.pepi.2018.10.006.

[96] Q. Li, X. Yang, F. Peng, G. Yang, T. Han, L. Fang, Q. Hu, L. Xie, X. Chen, Y. Zou, Elasticity, mechanical and thermal properties of submicron h-AlN: in-situ high pressure ultrasonic study, J. Eur. Ceram. Soc. 41 (2021) 4788–4793, https:// doi:10.1016/j.jeurceramsoc.2021.03.056.

[97] B. Feng, Y. Zhou, C. Peng, X. Li, J. Liu, Vibration assisted hot-press sintering of AlN ceramics, J. Am. Ceram. Soc. 98 (2015) 1711–1713, https://doi.org/10.1111/ jace.13591.

[98] Georg K.H. Madsen, David J. Singh, BoltzTraP. A code for calculating bandstructure dependent quantities, Comput. Phys. Commun. 17 (2006) 67–71, https:// doi.org/10.1016/j.cpc.2006.03.007.

[99] JH. Bahk, A. Shakouri, Enhancing the thermoelectric figure of merit through the reduction of bipolar thermal conductivity with heterostructure barriers, Appl. Phys. Lett. 105 (5) (2014) 52106, https://doi.org/10.1063/1.4892653.

[100] L.D. Zhao, H.J. Wu, S.Q. Hao, C.I. Wu, X.Y. Zhou, K. Biswas, J.Q. He, T.P. Hogan, C. Uher, C. Wolverton, V.P. Dravid, M.G. Kanatzidis, All-scale hierarchical thermoelectrics: MgTe in PbTe facilitates valence band convergence and suppresses bipolar thermal transport for high performance, Energy Environ. Sci. 6 (2013) 3346, https://doi.org/10.1039/C3EE42187B.

[101] J.J. Gong, A.J. Hong, J. Shuai, L. Li, Z.B. Yan, Z.F. Ren, J.-M. Liu, Investigation of the bipolar effect in the thermoelectric material CaMg 2 Bi 2 using a first-principles study, Phys. Chem. Chem. Phys. 18 (2016) 16566, https://doi.org/10.1039/ C6CP02057G.

[102] J.H. Bahk, A. Shakouri, Minority carrier blocking to enhance the thermoelectric figure of merit in narrow-band-gap semiconductors, Phys. Rev. B 93 (2016) 165209, https://doi.org/10.1103/PhysRevB.93.165209.

[103] Y. Rao, Y. Rao, C.Y. Zhao, S. Ju, High thermoelectric performance in metastable phase of silicon: a first-principles study, Appl. Phys. Lett. 120 (2022) 163901, https://doi.org/10.1063/5.0087730.

[104] T. Kusunose, T. Sekino, K. Niihara, Production of a grain boundary phase as conducting pathway in insulating AlN ceramics, Acta Mater. 55 (18) (2007) 6170–6175, https://doi.org/10.1016/j.actamat.2007.07.025.

[105] J. Zheng, Y. Yang, B. Yu, X. Song, X. Li, Oriented aluminum nitride onedimensional nanostructures: synthesis, structure evolution, and electrical properties, 0001, ACS Nano 2 (1) (2008) 134–142, https://doi.org/10.1021/ nn700363t.

[106] F. Liu, Z.J. Su, F.Y. Mo, L. Li, Z.S. Chen, Q.R. Liu, et al., Controlled synthesis of ultra-long AlNnanowires in different densities and in situ investigation of the physical properties of an individual AlNnanowire, Nanoscale 3 (2011) 610–618, https://doi.org/10.1039/c0nr00586j.

[107] G.A. Slack, R.A. Tanzilli, R.O. Pohl, J.W. Vandersande, The intrinsic thermal conductivity of AlN, J. Phys. Chem. Solid. 48 (1987) 641–647, https://doi.org/ 10.1016/0022-3697(87)90153-3.

[108] L. Qiao, H. Zhou, C. Li, Microstructure and thermal conductivity of spark plasma sintering AlN ceramics, Mater. Sci. Eng. B 99 (2003) 1–3, https://doi.org/ 10.1016/S0921-5107(02)00429-4.

[109] W. Duan, S. Li, G. Wang, R. Dou, L. Wang, Y. Zhang, H. Lic, H. Tan, Thermal conductivities and mechanical properties of AlN ceramics fabricated by three dimensional printing, J. Eur. Ceram. Soc. 40 (2020) 3535–3540, https://doi.org/ 10.1016/j.jeurceramsoc.2020.04.004.

[110] H.M. Lee, K. Bharathi, D.K. Kim, Processing and characterization of aluminum nitride ceramics for high thermal conductivity, Adv. Eng. Mater. 16 (2014) 655–669, https://doi.org/10.1002/adem.201400078.

[111] K. Watari, K. Ishizaki, F. Tsuchiya, Phonon scattering and thermal conduction mechanisms of sintered aluminium nitride ceramics, J. Mater. Sci. 28 (1993) 3709–3714, https://doi.org/10.1007/BF00353168.

[112] A.X. Levander, T. Tong, K.M. Yu, J. Suh, D. Fu, R. Zhang, et al., Effects of point defects on thermal and thermoelectric properties of InN, Appl. Phys. Lett. 98 (2011) 012108, https://doi.org/10.1063/1.3536507.

[113] J. Zou, D. Kotchetkov, A.A. Balandin, D.I. Florescu, F.H. Pollak, Thermal conductivity of GaN films: effects of impurities and dislocations, J. Appl. Phys. 92 (5) (2002) 2534–2539, https://doi.org/10.1063/1.1497704.

[114] A.T. Wieg, Y. Kodera, Z. Wang, T. Imai, C. Dames, J.E. Garay, Visible photoluminescence in polycrystalline terbium doped aluminum nitride (Tb:AlN) ceramics with high thermal conductivity, Appl. Phys. Lett. 101 (2012) 111903, https://doi.org/10.1063/1.4751856.

[115] A. Kafi, F.D. Khodja, F. Saadaoui, S. Chibani, A. Bentayeb, M.D. Khodja, Structural, elastic, electronic and thermoelectric properties of $Al_xGa_{1-x}N$ (x = 0, 0.125, 0.375, 0.625, 0.875 and 1) semiconductors, Mater. Sci. Semicond. Process. 113 (2020) 105049, https://doi.org/10.1016/j.mssp.2020.105049.

[116] A. Sztein, J. Haberstroh, J.E. Bowers, S.P. DenBaars, S. Nakamura, Calculated thermoelectric properties of $In_xGa_{1-x}N$, $In_xAl_{1-x}N$, and $Al_xGa_{1-x}N$, J. Appl. Phys. 113 (18) (2013) 183707, https://doi.org/10.1063/1.4804174.

[117] H. Tong, J. Zhang, G. Liu, J.A. Herbsommer, G.S. Huang, N. Tansu, Thermoelectric properties of lattice-matched AlInN alloy grown by metal organic chemical vapor deposition, Appl. Phys. Lett. 97 (2010), 112105, https://doi.org/10.1063/ 1.3489086.

[118] V.N. Kumar, M. Arivanandan, T. Koyoma, et al., Effects of varying indium composition on the thermoelectric properties of $In_xGa_{1-x}Sb$ ternary alloys, Appl. Phys. A 122 (2016) 885, https://doi.org/10.1007/s00339-016-0409-9.

[119] V.N. Kumar, Y. Hayakawa, H. Udono, Y. Inatomi, An Approach to optimize the thermoelectric properties of III–V Ternary InGaSb crystals by defect engineering via point defects and microscale compositional segregations, Inorg. Chem. 58 (2019) 11579–11588, https://doi.org/10.1021/acs.inorgchem.9b01430.
[120] A. Sztein, H. Ohta, J.E. Bowers, S.P. DenBaars, S. Nakamura, High temperature thermoelectric properties of optimized InGaN, J. Appl. Phys. 110 (2011) 123709, https://doi.org/10.1063/1.3670966.
[121] M. Yeganeh, F. Kafi, A. Boochani, Thermoelectric properties of InN graphene-like nanosheet: a first principle study, Superlattice. Microst. 138 (2020) 106367, https://doi.org/10.1016/j.spmi.2019.106367.
[122] D.-B. Xiong, N.L. Okamoto, H. Inui, Enhanced thermoelectric figure of merit in ptype Ag-doped ZnSb nanostructured with Ag3Sb, Scripta Mater. 69 (2013) 397–400, https://doi.org/10.1016/j.scriptamat.2013.05.029.
[123] Y. Zhai, Q. Zhang, J. Jiang, T. Zhang, Y. Xiao, S. Yang, G. Xu, Thermoelectric properties of $In_{1.3-x}Sn_xSe$ prepared by spark plasma sintering method, J. Alloys Compd. 553 (2013) 270–272, https://doi.org/10.1016/j.jallcom.2012.11.139.
[124] D. Wu, L.-D. Zhao, S. Hao, Q. Jiang, F. Zheng, J.W. Doak, H. Wu, H. Chi, Y. Gelbstein, C. Uher, C. Wolverton, M. Kanatzidis, J. He, Origin of the high performance in GeTe-based thermoelectric materials upon Bi2Te3 doping, J. Am. Chem. Soc. 136 (2014) 11412–11419, https://doi.org/10.1021/ja504896a.
[125] H. Wang, Z.M. Gibbs, Y. Takagiwa, G.J. Snyder, Tuning bands of PbSe for better thermoelectric efficiency, Energy Environ. Sci. 7 (2014) 804–811, https://doi.org/ 10.1039/c3ee43438a.
[126] H. Wang, Y. Pei, A.D. LaLonde, G.J. Snyder, Heavily doped p-type PbSe with high thermoelectric performance: an alternative for PbTe, Adv. Mater. 23 (2011) 1366–1370, https://doi.org/10.1002/adma.201004200.
[127] H. Wang, E. Schechtel, Y. Pei, G.J. Snyder, High thermoelectric efficiency of n-type PbS, Adv. Energy Mater. 3 (2013) 488–495, https://doi.org/10.1002/ aenm.201200683.
[128] G.J. Snyder, E.S. Toberer, Complex thermoelectric materials, Nat. Mater. 7 (2008) 105–114, https://doi.org/10.1038/nmat2090.
[129] M.S. Dresselhaus, G. Chen, M.Y. Tang, R. Yang, H. Lee, D. Wang, Z. Ren, J.- P. Fleurial, P. Gogna, New directions for low-dimensional thermoelectric materials, Adv. Mater. 19 (2007) 1–12, https://doi.org/10.1002/adma.200600527.

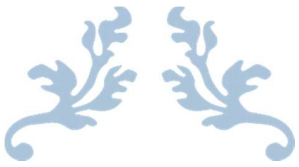

GENERAL CONCLUSION

In this thesis, we have investigated the high-performance potential of two eco-friendly materials, ferroelectric Sodium Bismuth Titanate ($Na_{0.5}Bi_{0.5}TiO_3$, NBT) and non-ferroelectric Yttrium-doped Aluminum Nitride ($Y_xAl_{1-x}N$) alloys, by evaluating their key electronic, elastic, piezoelectric, dielectric, thermodynamic, and thermoelectric properties to enhance their applicability in various innovative technological domains. The Full-Potential Linearized Augmented Plane Wave (FP-LAPW) method, based on Density Functional Theory (DFT), was employed using advanced approximation techniques such as GGA-PBEsol and *n*KTB-mBJ to determine and analyze the physical properties of NBT in rhombohedral (R3c), tetragonal (P4bm), and cubic ($Pm\bar{3}m$) phases, as well as $Y_xAl_{1-x}N$ alloys in the wurtzite structure with Yttrium concentrations ranging from 0 to 37.5%. Our computational results exhibit good agreement with available experimental data and findings from other theoretical studies.

In the case of the NBT perovskite, the R3c phase was found to be the most stable structure. Calculations of formation energy and phonon dispersion confirmed the thermodynamic and dynamic stability of NBT across all three phases. Additionally, the results indicate a sequence of ferroelectric phase transitions, starting from the rhombohedral phase and progressing to the tetragonal and cubic structures with increasing temperature.

The analysis of the elastic properties obtained from plane wave pseudo-potential method and GGA-PBEsol exchange potential, including elastic constants (C_{ij}) and elastic moduli (bulk modulus B, shear modulus G, and Young's modulus Y), indicates that NBT crystals exhibit greater hardness and mechanical stability. Among the different phases, the rhombohedral R3c-NBT crystal demonstrates stronger anisotropy in its elastic moduli compared to the other two NBT phases. Additionally, using a self-consistent density functional perturbation theory (DFPT) method with the GGA-PBEsol approximation, the results predict superior piezoelectric and dielectric properties for the tetragonal P4bm-NBT system, with a higher piezoelectric coefficient (d_{33} = 81.1 pC/N) and dielectric constant (ϵ_{33} = 163.5), in contrast to the rhombohedral R3c-NBT system, which shows lower values (d_{33} = 21.2 pC/N and ϵ_{33} = 20.42). The thermodynamic calculations using the Gibbs2 code reveal that pressure has a more significant impact on the Debye temperature than temperature. Furthermore, BoltzTraP2 computations show that NBT materials exhibit a high Seebeck coefficient, high electrical

conductivity, and a high figure of merit (ZT), coupled with low thermal conductivity. These properties make NBT crystals highly suitable for thermoelectric applications.

In the case of $Y_xAl_{1-x}N$ semiconductor alloys, the GGA-PBEsol results show that the variation of the lattice parameter a_0 increases almost linearly with increasing the Y content (x) with a marginal upward bowing parameter of $b = -0.08597$. As for the parameter c_0, it deviates strongly from the linear Vegard's rule, exhibiting a significant bowing of – 0.5715, which is in good agreement with experimental results. Analysis of the formation energy, phonon dispersion, and elastic and mechanical properties demonstrates that the wurtzite $Y_xAl_{1-x}N$ alloys (for $0 \leq x \leq 0.375$) are dynamically, thermodynamically, elastically, and mechanically stable. Furthermore, the Debye temperature results obtained from Gibbs2 calculations indicate that the $Y_xAl_{1-x}N$ alloys exhibit high elastic hardness.

The results obtained using the newly developed modified Becke-Johnson (nKTB-mBJ) potential within the FP-LAPW method reveal a direct bandgap energy of 3.85 eV for Yttrium-doped [$Y_xAl_{1-x}N$] alloys at x = 0.375. This bandgap corresponds to the ultraviolet spectrum range (~203–322 nm). The piezoelectric properties obtained using the DFPT and PBEsol methods predict an increase in the piezoelectric constant, with d_{33} rising from 5.76 pC/N for binary AlN to 21.5 pC/N for the ternary $Y_{0.375}Al_{0.625}N$. Moreover, $Y_xAl_{1-x}N$ crystals demonstrate excellent thermoelectric performance, featuring a high figure of merit (ZT ~ 0.76 for x= 0.25) that makes them suitable for thermoelectric applications. They present a promising alternative to the widely used commercial material bismuth telluride (Bi_2Te_3) at elevated temperatures, as suggested by BoltzTraP calculations.

In conclusion, the present ab initio calculations for Sodium Bismuth Titanate [$Na_{0.5}Bi_{0.5}TiO_3$] and Yttrium Aluminum Nitride [$Y_xAl_{1-x}N$] have yielded excellent results. These findings suggest that both materials are highly suitable candidates and could serve as effective alternatives to conventional materials currently used in the market. This potential positions them as exciting avenues for further research, motivating researchers to pursue both theoretical and experimental studies on these promising materials for green energy and high-performance devices in the future.

Recommendations for Future Works

1. Based on the promising theoretical results obtained for the materials mentioned in this work (such as $Na_{0.5}Bi_{0.5}TiO_3$ (NBT) and $Y_xAl_{1-x}N$ alloys), experimental work is a possible next important step.

2. In appendix A, we mentioned how to calculate the thermal conductivity $\kappa_{lattice}$ and the relaxation time τ to calculate the exact value of ZT. Given the great interest of theoretical results in guiding and supporting experimental results, we propose to conduct a comparative study to calculate the exact value of figure of merit ZT for the two mentioned materials in this work (including $Na_{0.5}Bi_{0.5}TiO_3$ (NBT) and $YxAl_{1-x}N$ alloys).

3. Explore the performance of new eco-friendly materials suited for enhancing the efficiency of energy conversion and storage systems, as well as thermoelectric generators, with the goal of optimizing their use in renewable energy technologies. This would involve assessing the potential of materials such as $Na_{0.5}Bi_{0.5}TiO_3$ (NBT) and $YxAl_{1-x}N$ alloys for high-efficiency applications in green energy systems.

4. Integrate into local manufacturing efforts of materials such as Aluminum Nitride (AlN) and Zinc Oxide (ZnO), as well as microelectronic components, by leveraging sophisticated techniques available at the national level. This initiative aims to promote the development of advanced electronic and piezoelectric devices, contributing to the local microelectronics industry.

APPENDIX A

How to calculate the exact value of ZT ?

The figure of merit, denoted as ZT, is a dimensionless parameter used to quantify the efficiency of thermoelectric materials. The efficiency of these materials lead to a good performance for the thermoelectric devices.

As we know, it is defined by the following equation:

$$ZT = \frac{S^2 \sigma T}{\kappa} \quad (1)$$

Where:

- **S** is the Seebeck Coefficient (V/K).
- **σ** is the Electrical Conductivity (Ω/m).
- **T** is the Absolute Temperature in kelvin (K).
- **κ** is the Thermal Conductivity (W/m ·K).

1. Thermal Conductivity

Thermal conductivity, κ is given by two terms, electronic κ_{el} and thermal κ_{latt} as:

$$\kappa = \kappa_{el} + \kappa_{latt} \quad (2)$$

The BoltzTrap code can calculate only κ_{el} . Therfore, the code takes the value of $\kappa_{Latt} \sim 0$.

In this case, we can say that the ZT calculated using the BoltzTrap code is incomplete and is expressed in terms of κ_{Latt}.

To find the exact value of ZT, it must be calculated κ_{Latt}, we can use the Slack equation [1]:

$$\kappa_{Latt} = A \frac{M \, \theta_D^3 \, V^{1/3}}{\gamma^2 \, T \, n^{2/3}} \quad (3)$$

Where:

M: Average atomic mass;

θ: Debye Temperature;

V: Vomule;

n: Atoms number;

T: Temperature;

γ: Gruneisen parameter; which given by :

$$\gamma = \frac{9-12(v_t/v_l)^2}{2+4(v_t/v_l)^2} \quad (4)$$

A: The constant calculated as follow:

$$A = \frac{2.43\times10^{-8}}{1-\frac{0.514}{\gamma}+\frac{0.228}{\gamma^2}} \quad (5)$$

Lattice thermal conductivity can be calculated by using *ShengBTE code*. [2]

ShengBTE (Sheng Boltzmann Transport Equation) is a software package designed to solve the Boltzmann Transport Equation for phonons, primarily aimed at calculating the lattice contribution to the thermal conductivity in bulk crystalline solids. The latest update of this software ShengBTE v1.5.1 released in March, 2024 [2].

2. *The Relaxation Time* τ

The BoltzTraP code facilitates the computation of transport properties by adopting a constant relaxation time (τ) approximation. While the Seebeck coefficient (S) remains unaffected by τ, the electrical conductivity (σ), thermal power ($S^2\sigma$) and electronic thermal conductivity (κ_e) are represented as σ/τ , $S^2\sigma/\tau$ and κ_e/τ, respectively. Consequently, temperature-dependent variations in τ for charges carries are considered to enhance the accuracy of thermoelectric property predictions.

We can say in this case that the relaxation time τ is the second factor that must be taken into consideration to calculate the exact value of ZT.

In the works done in this thesis, the usual constant value of relaxation time τ was taken, which it's about 10^{-14} s.

The value of τ are calculated by utilizing the Bardeen and Shockley formula [3] given as follow:

$$\tau = \frac{(8\pi)^{1/2}\hbar^4 C_{ii}}{3(m_d^* k_B T)^{3/2} E_d^2} \quad (6)$$

Where ħ is the reduced Planck constant; C_{ii} is the elastic constant; E_d is the deformation potential and m_d^* is the density of states (DOS) effective mass.

The elastic constants C_{ii} are computed by the quadratic polynomial fit of the total energy variation under strains as:

$$C_{ii} = \frac{1}{V_0}\frac{\partial^2 E}{\partial\left(\frac{\Delta a}{a_0}\right)^2} \tag{7}$$

Where V_o is the equilibrium volume and E is the total energy of the system, a_0 is the equilibrium lattice parameter and $\Delta a = a - a_0$ is the lattice distortion.

The deformation potential E_d for holes and electrons is calculated based on the change in energy at the edge (E_{edge}) of the VBM and the CBM caused by uniaxial deformation defined by :

$$E_d = \frac{\partial^2 E_{edge}}{\partial\left(\frac{\Delta a}{a_0}\right)^2} \tag{8}$$

The band effective mass in both valence and conduction bands under the parabolic approximation is defined by the curvature of the band in k-space as:

$$m_b^* = \frac{\hbar^2}{\left(\frac{\partial^2 E}{\partial k^2}\right)} \tag{9}$$

The density of states (DOS) effective mass is calculated using the formula:

$$m_d^* = N_v^{2/3} m_b^* \tag{10}$$

Where the band degeneracy $N_v = \sum_i N_b^i N_0^i$, and N_b is the number of bands contributing and N_o is the number of symmetry related pockets in the first Brillouin zone.

Reference

[1] Slack G.A , Nonmetallic crystals with high thermal conductivity, (1973) J. Phys. Chem. Solids 34 321, https://doi.org/10.1016/0022-3697(73)90092-9

[2] ShengBTE [WWW Document], n.d. URL https://www.shengbte.org/ (accessed 7.15.25).

[3] Bardeen J and Shockley W (1950) Phys. Rev. 80 72,

Scientific Productions

- **Publications:**

  - O. Mezilet, A. Assali, S. Benaissa, S. Meskine, A. Boukortt, L. Chaabane, *Electronic Structure, Thermodynamics and Thermoelectric Properties of $Y_xAl_{1-x}N$ Semiconductor Alloys for New Promising Optoelectronics and Energy Conversion: Ab Initio Study*, *Materials Science in Semiconductor Processing* 163 (2023) 107571, https://doi.org/10.1016/j.mssp.2023.107571.

  - O. Mezilet, A. Assali, S. Meskine, A. Boukortt, M.S. Halati, *New Insights into The Piezoelectric, Thermodynamic and Thermoelectric Properties of Lead-free Ferroelectric Perovskite $Na_{0.5}Bi_{0.5}TiO_3$ from Ab Initio Calculations*, *Materials Today Communications* 31 (2022) 103371, https://doi.org/10.1016/j.g.2022.103371.

  - A. Assali, F. Laidoudi, R. Serhane, F. Kanouni, O. Mezilet, *Highly Enhanced Electro-acoustic Properties of YAlN/Sapphire Based Surface Acoustic Wave Devices for Next Generation of Microelectromechanical Systems*, *Materials Today Communications* 26 (2021) 102067, https://doi.org/10.1016/j.mtcomm.2021.102067.

- **Communications:**

  - O. Mezilet, A. Assali, S. Meskine, On the understanding of the electronic properties of Na0.5Bi0.5TiO3 ferroelectric perovskite: ADFT perspective, Poster, IC-SEAM'21, April 2021, Ouargla, Algeria.

  - O. Mezilet, A. Assali, S. Meskine, Electronic properties of yttrium aluminum nitride (YxAl1−xN) alloys: A first-principles study, October 2022, Ouargla, Algeria.

  - O. Mezilet, A. Assali, S. Meskine, A. Boukortt, Propriétés piézoélectriques de la perovskite sans plomb titane de sodium et de bismuth, Poster, CNPMA'2021, 2021, Algiers, Algeria.

  - O. Mezilet, A. Assali, S. Meskine, A. Boukortt, Highly desired lead-free perovskite Bi(1/5)Na(1/5)TiO3 material for thermoelectric devices, Poster, NC-PVMD'21, 2021, Bechar, Algeria.

  - O. Mezilet, A. Assali, S. Meskine, A. Boukortt, Structural, dielectric, and piezoelectric properties of lead-free sodium bismuth titanate perovskite ferroelectric, Poster, CNLPM2022, 2022, Eltaref, Algeria.

- **Workshop Organized**

  - 1st national workshop on WIEN2K, Mostaganem – Algeria, December 2019.